SANDIA REPORT
SAND2007-6218
Unlimited Release
Printed October 2007

Development of Design and Simulation Model and Safety Study of Large-Scale Hydrogen Production Using Nuclear Power

Sal B. Rodriguez, Randall O. Gauntt, Randy Cole, Katherine McFadden, Fred Gelbard, Tom Drennen, Len Malczynski, Billy Martin, David L. Y. Louie, Louis Archuleta, Mohamed El-Genk, Jean-Michel Tournier, Flor Espinoza, Karen Vierow, Kevin Hogan, Shripad T. Revankar, and Seungmin Oh

Prepared by
Sandia National Laboratories
Albuquerque, New Mexico 87185 and Livermore, California 94550

Sandia is a multiprogram laboratory operated by Sandia Corporation,
a Lockheed Martin Company, for the United States Department of Energy's
National Nuclear Security Administration under Contract DE-AC04-94AL85000.

Issued by Sandia National Laboratories, operated for the United States Department of Energy by Sandia Corporation.

Available to DOE and DOE contractors from
U.S. Department of Energy
Office of Scientific and Technical Information
P.O. Box 62
Oak Ridge, TN 37831

Telephone: (865) 576-8401
Facsimile: (865) 576-5728
E-Mail: reports@adonis.osti.gov
Online ordering: http://www.osti.gov/bridge

Available to the public from
U.S. Department of Commerce
National Technical Information Service
5285 Port Royal Rd.
Springfield, VA 22161

Telephone: (800) 553-6847
Facsimile: (703) 605-6900
E-Mail: orders@ntis.fedworld.gov
Online order: http://www.ntis.gov/help/ordermethods.asp?loc=7-4-0#online

SAND2007-6218
Unlimited Release
Printed October 2007

Development of Design and Simulation Model and Safety Study of Large-Scale Hydrogen Production Using Nuclear Power

Sal B. Rodriguez, Randall O. Gauntt, Randy Cole, Katherine McFadden,
Fred Gelbard, Tom Drennen, Len Malczynski, and William J. Martin
Sandia National Laboratories
Albuquerque, New Mexico 87185-0748

David L. Y. Louie and Louis Archuleta
OMICRON Safety and Risk, Inc.
Albuquerque, New Mexico 87110

Mohamed El-Genk, Jean-Michel Tournier, and Flor Espinoza
University of New Mexico
Albuquerque, New Mexico 87131

Karen Vierow and Kevin Hogan
Texas A & M University
College Station, Texas 77843-3133

Shripad T. Revankar and Seungmin Oh
Purdue University
West Lafayette, Indiana 47907

Abstract

Before this LDRD research, no single tool could simulate a very high temperature reactor (VHTR) that is coupled to a secondary system and the sulfur iodine (SI) thermochemistry. Furthermore, the SI chemistry could only be modeled in steady state, typically via flow sheets. Additionally, the MELCOR nuclear reactor analysis code was suitable only for the modeling of light water reactors, not gas-cooled reactors. We extended MELCOR in order to address the above deficiencies. In particular, we developed three VHTR input models, added generalized, modular secondary system components, developed reactor point kinetics, included transient thermochemistry for the most important cycles [SI and the Westinghouse hybrid sulfur], and developed an interactive graphical user interface for full plant visualization. The new tool is called MELCOR-H2, and it allows users to maximize hydrogen and electrical production, as well as enhance overall plant safety. We conducted validation and verification studies on the key models, and showed that the MELCOR-H2 results typically compared to within less than 5% from experimental data, code-to-code comparisons, and/or analytical solutions.

TABLE OF CONENTS

LIST OF FIGURES

LIST OF TABLES

ACRONYMS AND ABBREVIATIONS

AIChE	American Institute of Chemical Engineers
ANS	American Nuclear Society
ASME	American Society of Mechanical Engineers
CBC	Closed Brayton Cycle
CFD	computational fluid dynamics
CPU	central processing unit
CV	control volume
DLOFC	depressurized loss of forced cooling
DOE	Department of Energy
GT-MHR	Gas-Turbine, Modular Helium Reactor
GUI	graphical user interface
H_2O	water
H_2SO_4	sulfuric acid
HI	hydrogen iodide
HI	hydrogen iodine
HS	heat structure
HTGR	high-temperature gas-cooled reactor
HyS	hybrid sulfur
I_2	iodine
IAEA	International Atomic Energy Agency
IHX	intermediate heat exchangers
INL	Idaho National Laboratory
JAEA	Japanese Atomic Energy Agency
JAERI	Japan Atomic Energy Research Institute
LWR	light water reactor
NERI	Nuclear Energy Research Initiative
NGNP	Next Generation Nuclear Reactor
NRC	Nuclear Regulatory Commission
PBMR	Pebble Bed Modular Reactor
PJA	prompt jump approximation
PWR	pressurized water reactor
RC	reaction chamber

SI	sulfur iodine
SIMPLEC	SIMPLE-Consistent
SNL	Sandia National Laboratories
SO_2	sulfur dioxide
SO_3	sulfur trioxide
STP	standard test and pressure
UNM-ISNPS	University of New Mexico – Institute of Space and Nuclear Power Studies
VHTR	very high temperature reactor
WHEC	World Hydrogen Energy Conference

EXECUTIVE SUMMARY

The Department of Energy (DOE) is expediting its search for economical, reliable fuel sources that produce minimal greenhouse gases. Among these are very high temperature reactors (VHTRs) that are suitable for large-scale production of hydrogen. The VHTRs are coupled to a secondary system (for the generation of electricity) and to a thermochemical cycle (for the production of hydrogen). The sulfur iodine (SI) thermochemical cycle is a top choice due to its high efficiency. The Westinghouse hybrid sulfur (HyS) cycle is another leading contender. For convenience, the coupled system is referred as a nuclear-hydrogen (nuclear-H_2) plant or VHTR-SI plant whenever the thermochemical cycle is SI. Currently, there are two leading VHTR core designs: the pebble bed and prismatic core.

For FY07, we completed a multipurpose tool, MELCOR-H2, capable of modeling nuclear-H_2 plants in both steady state and transient mode. Our effort focused on the following key areas:

- Development of input models for a pebble bed core, a prismatic core, and a full-plant VHTR-SI.
- Secondary system components (turbines, compressors, intermediate heat exchangers, and generators),
- Transient chemical cycles (e.g., SI and HyS),
- Reactor point kinetics model,
- Validation and verification of the models, and
- Development of an interactive graphical user interface (GUI) for system output visualization and interactive modification of system parameters during simulations.

We endeavored to produce modular, generalized system components that can be linked as desired by the analyst/designer. Thus, the uniqueness of our modeling approach is that MELCOR-H2 is not limited to an *ad hoc* configuration for the primary system, the secondary system, or chemistry cycle. Instead, because of MELCOR-H2's generalized and modular approach, the configuration possibilities are practically infinite; that is, the modular, generalized nature of MELCOR-H2 allows the analyst/designer to explore any desired system configurations. This approach serves to enhance plant safety, efficiency, and profitability.

As a result of our research, every component shown in Figure ES-1 can now be modeled dynamically using MELCOR-H2. The figure shows our VHTR-SI input model.

Figure ES-2 shows a summary of the latest MELCOR-H2 models, their status, and key results. In the discussion that follows, we will briefly discuss the models, as well as their validation and verification.

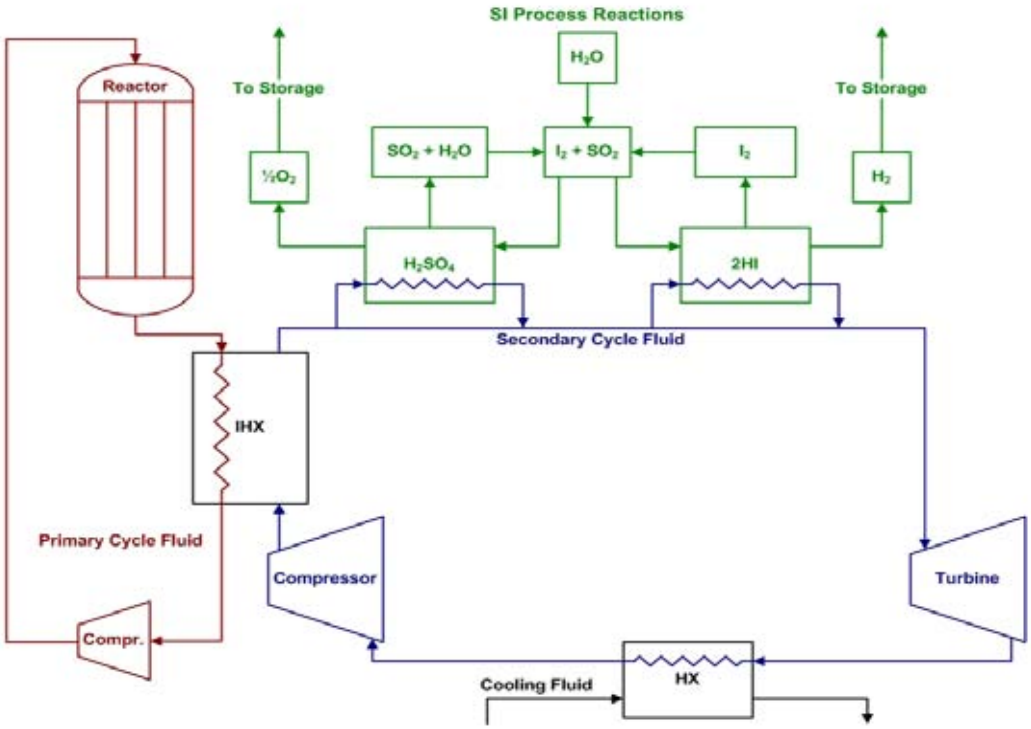

Figure ES-1. MELCOR-H2 input model of a pebble bed reactor coupled to a secondary system and a sulfur iodine cycle (VHTR-SI model).

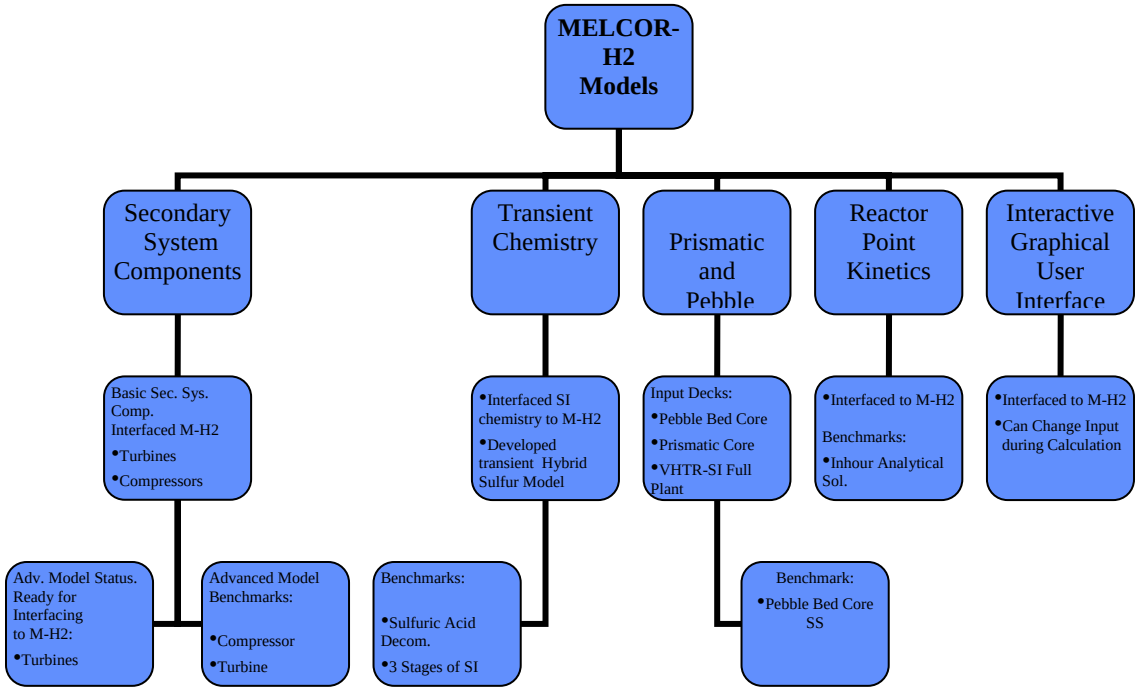

Figure ES-2. Summary of the latest MELCOR-H2 models, their status, and key results.

This is the first time that the SI chemistry equations have been modeled in transient mode. The literature shows that previous attempts were done in steady state by using mostly spreadsheets. In addition, the search showed that there were no simulations where a thermochemical cycle was coupled with a detailed nuclear reactor model.

The transient MELCOR-H2 SI chemistry model consists of the three chemical reaction sections:

1. decomposition of sulfuric acid (H_2SO_4),

2. decomposition of hydrogen iodide (HI) (hydriodic acid when dissolved in water), and

3. the Bunsen reaction, which is the low-temperature reconstitution of the two acids. This is shown in Figure ES-3.

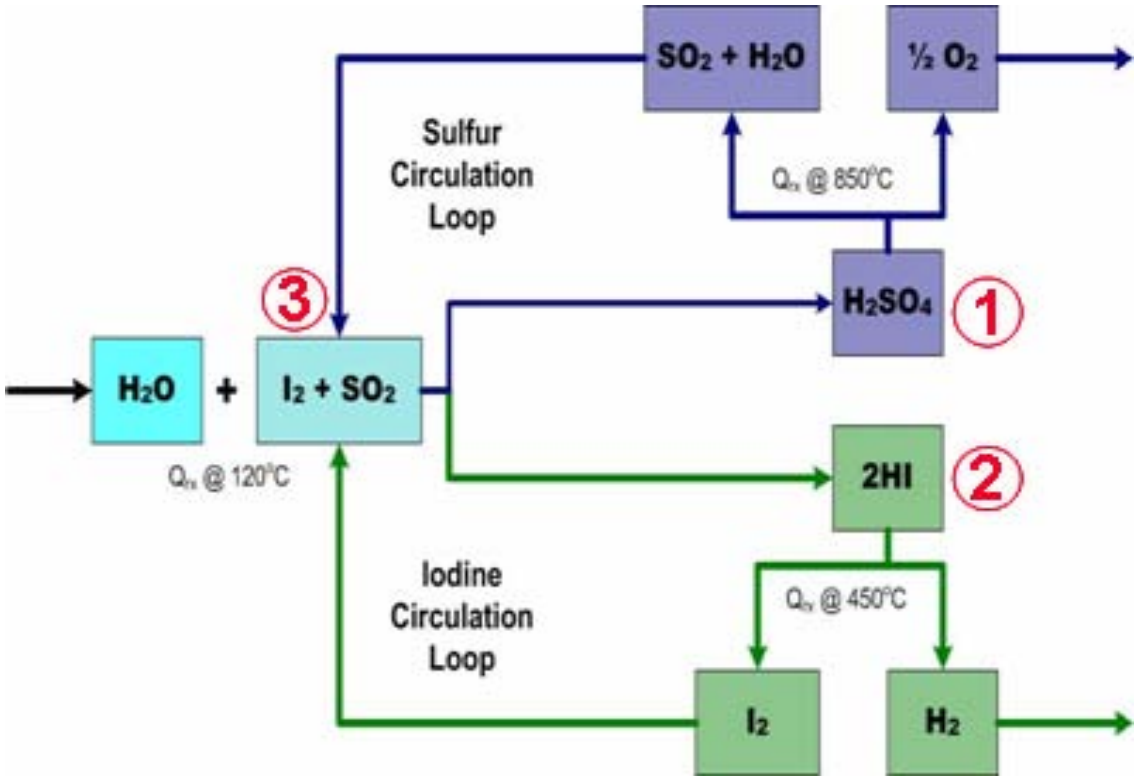

Figure ES-3. Schematic of the transient SI chemistry model.

In order to test the adequacy of our models, we simulated two sets of experiments: the Sandia National Laboratories (SNL) Sulfuric Acid Decomposition Experiments and the Japan Atomic Energy Research Institute (JAERI) SI Experiment. Our results showed that MELCOR-H2 output was mostly within 5% or less of measured data. These results are shown in Figures ES-4 and ES-5, respectively.

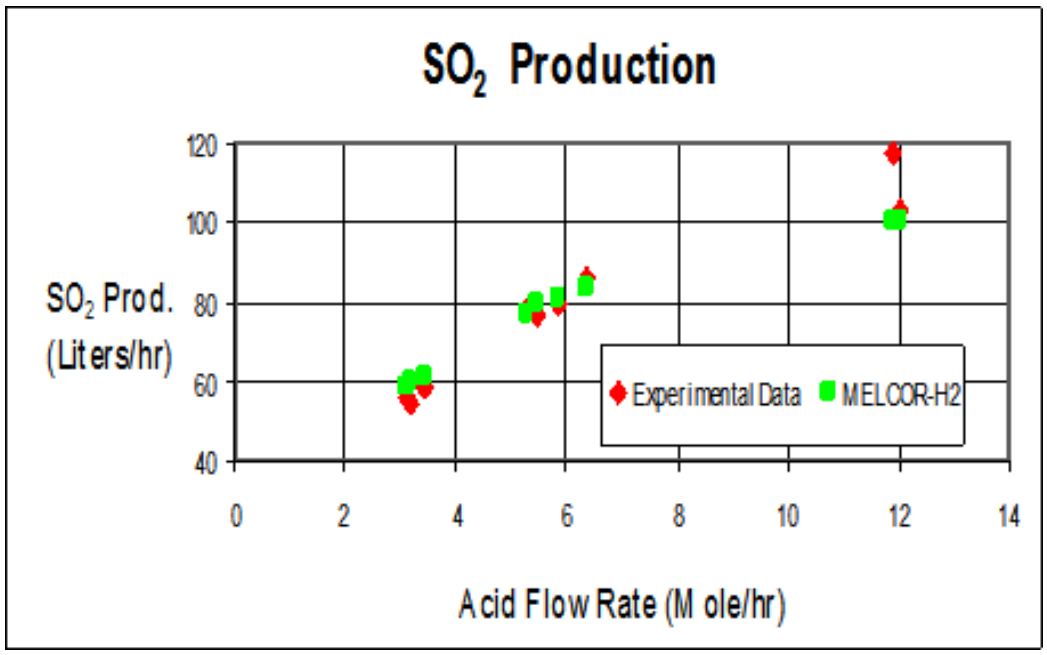

Figure ES-4. Comparison between measured and calculated SO_2 production rates for the SNL sulfuric acid decomposition experiments.

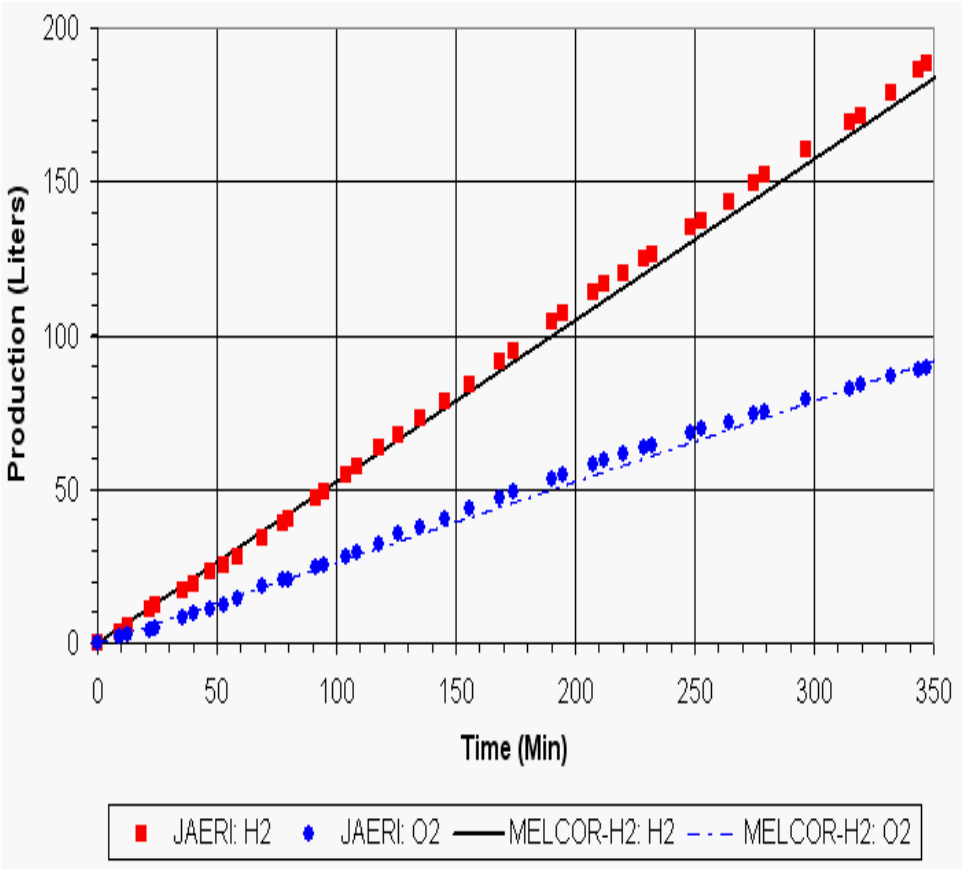

Figure ES-5. Comparison between measured and calculated hydrogen and oxygen production for the JAERI SI experiment.

Our point kinetics model uses Padé polynomials in order to approximate the exponents of matrices. The model was interfaced to MELCOR-H2 for the calculation of reactivity changes in the reactor core. We benchmarked the model against the exact Inhour solution, with the comparison showing that the point kinetics model output and the analytical solution differed by much less than 1%, as shown in Figure ES-6.

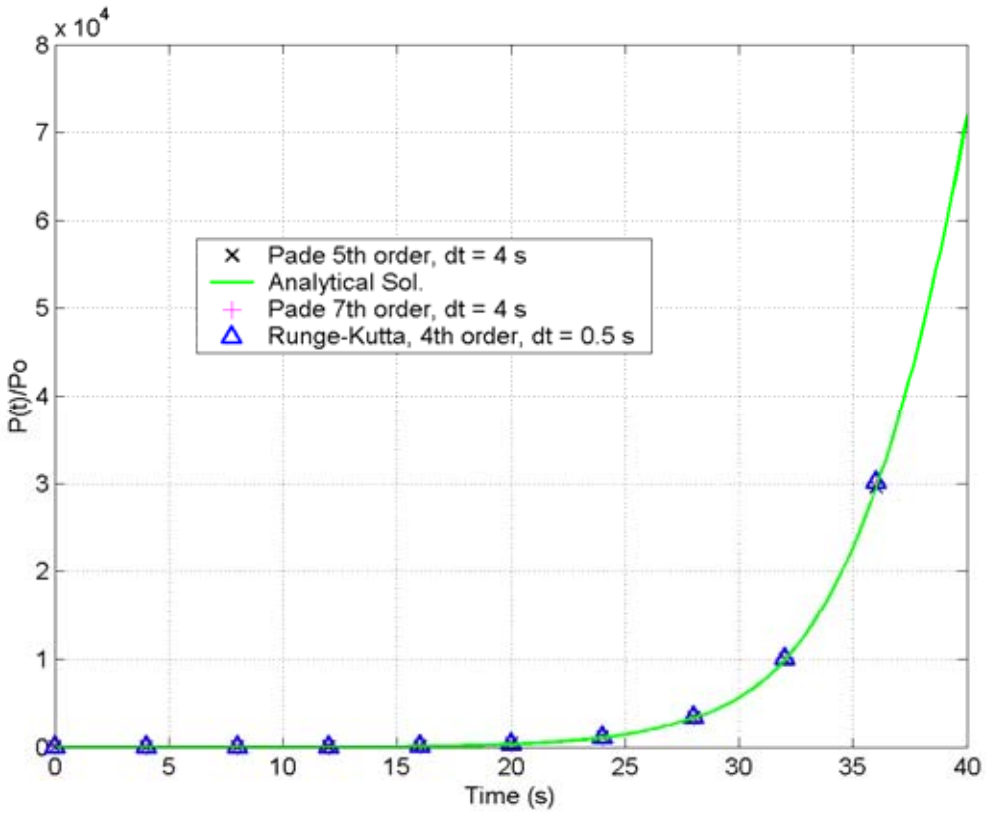

Figure ES-6. Comparison of MELCOR-H2 Padé point kinetics model with the exact Inhour solution for the case of $1.0 step reactivity insertion ($\Lambda = 10^{-2}$ s).

In addition, we tested the point kinetics model against the prompt jump approximation (PJA). We ran various calculations with Λ ranging from 10^{-5} to 10^{-2} s. As expected, the smaller Λ was, the closer the calculation compared against the PJA. By the time $\Lambda=10^{-5}$, the PJA and computed solution were nearly identical, as shown by Figure ES-7.

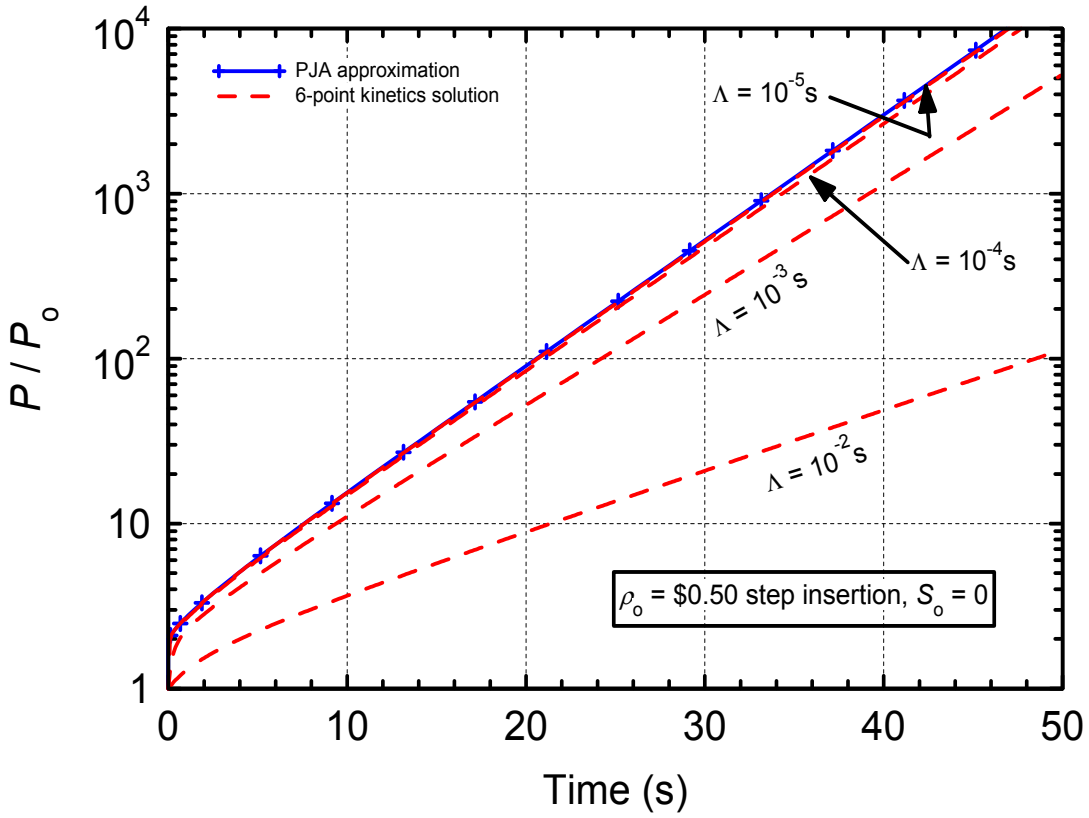

Figure ES-7. Comparison of MELCOR-H2 point kinetics model with the prompt jump approximation for the case of $0.50 step reactivity insertion.

The advanced turbine and compressor models were benchmarked against the Japanese Atomic Energy Agency (JAEA) models. Table ES-1 shows a comparison between their models and ours. Note that the results typically differed by much less than 5%.

Table ES-1. MELCOR-H2 Turbine and Compressor Simulations vs. JAEA Calculations

Parameter	JAEA	MELCOR-H2
Compressor Exit Temperature (K)	410.00	409.40
Compressor Exit Pressure (MPa)	7.11	7.16
Compressor Work (MW)	251.00	253.60
Turbine Exit Temperature (K)	891.00	893.20
Turbine Exit Pressure (MPa)	3.68	3.62
Turbine Work (MW)	530.00	527.60

We also developed an input model of a pebble bed core, and used MELCOR-H2 to run the model to steady state. We compared the output against values found in the literature. Table ES-2 shows that most MELCOR-H2 output compared well within 5% of

the literature values for the helium mass flow rate, core pressure drop, core coolant temperature rise, and maximum fuel temperature.

Table ES-2. MELCOR-H2 Output vs. Literature for a Pebble Bed Core at Steady State

Parameter	MELCOR-H2	Literature
Helium Mass Flow Rate (kg/s)	130	129
Core ΔP (MPa)	0.17	0.175
Core Coolant ΔT (K)	394	400
Maximum Fuel Temperature, Ring 2 (K)	1,330	1,373

In addition, we ran several steady state and transient calculations using the VHTR-SI model. For example, we ran a startup transient where the reactor and secondary system were allowed to reach steady state. At this point, the system parameters such as pressure, temperature, mass flow rate, etc., were nearly constant. Then, as the SI chemistry was activated, there was a significant secondary system pressure drop. This drop was caused by the heat demand imposed by the decomposition of the sulfuric and hydriodic acid in the thermochemistry loop. As the heat was removed, the secondary system temperature decreased, and hence the pressure dropped; see the left side of Figure ES-8. The right side shows the cumulative hydrogen production. The SI cycle was activated at 1000 s, after the system parameters had reached near constant values.

Notice that the secondary system pressure drop can be sufficiently large to cause a reactor scram, so the thermochemical loop activation must be done carefully. This, as well as other calculations, shows the importance of modeling the VHTR-SI in transient mode. Only such analysis will allow analysts to investigate potential system feedbacks in this promising, yet complex, nuclear-H_2 plant.

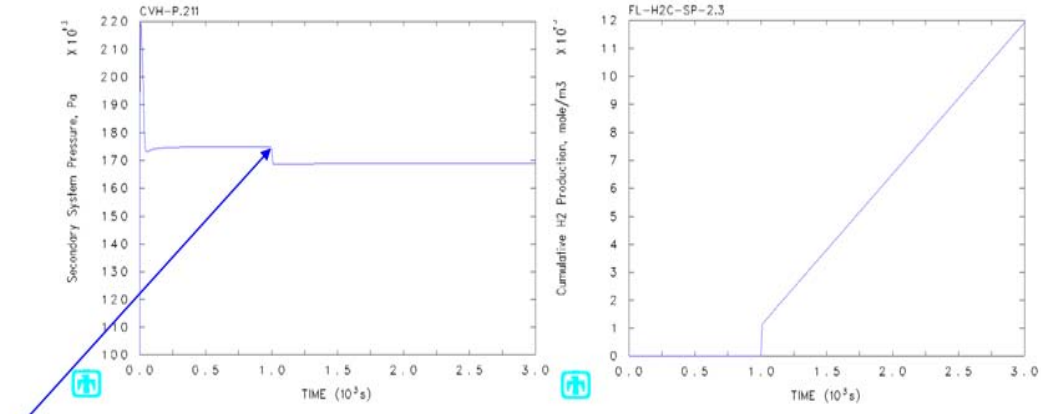

Figure ES-8. Impact on secondary system pressure as SI chemistry is activated.

As a final test of the entire VHTR-SI plant, we conducted a simulation whereby we allowed the system to proceed to a pseudo steady state, and we thereafter activated the SI chemistry at 300 s. Then, we inserted 10 cents worth of positive reactivity into the reactor at 400 s. Note that this is a hypothetical VHTR-SI plant model, so this simulation is therefore intended primarily as a demonstration of capabilities.

Key primary system parameters such as total core energy, fuel temperature, reactor inlet and outlet temperature, pressure, and mass flow rate are presented in FiguresES-9 through ES-13, respectively. Figures ES-14 and ES-15 show the secondary system pressure and mass flow rate, while the cumulative hydrogen generation is shown in Figure ES-16.

Notice that the reactor underwent an exponential rise in total energy as the reactivity was inserted (Figure ES-9). As the core energy increased, the temperatures increased (e.g., fuel, core inlet and outlet; see Figures ES-10 and ES-11, respectively). Because of the reactor's negative temperature reactivity coefficient, there was a subsequent energy reduction and therefore a temperature drop. The calculation was stopped at this point.

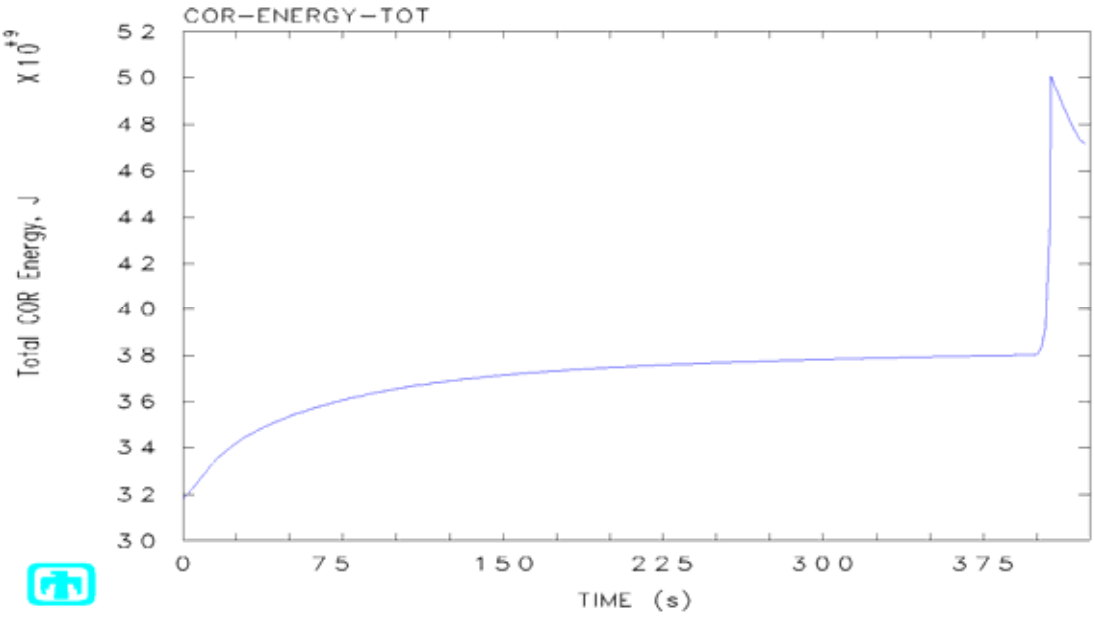

Figure ES-9. Total core energy.

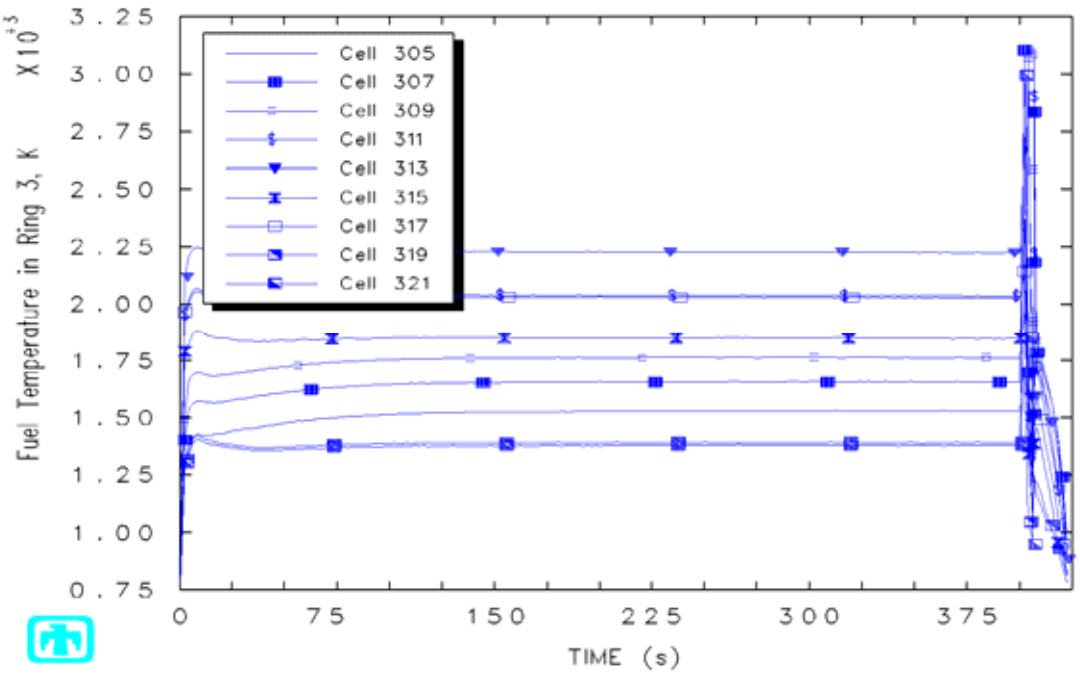

Figure ES-10. Fuel temperature in Ring 3.

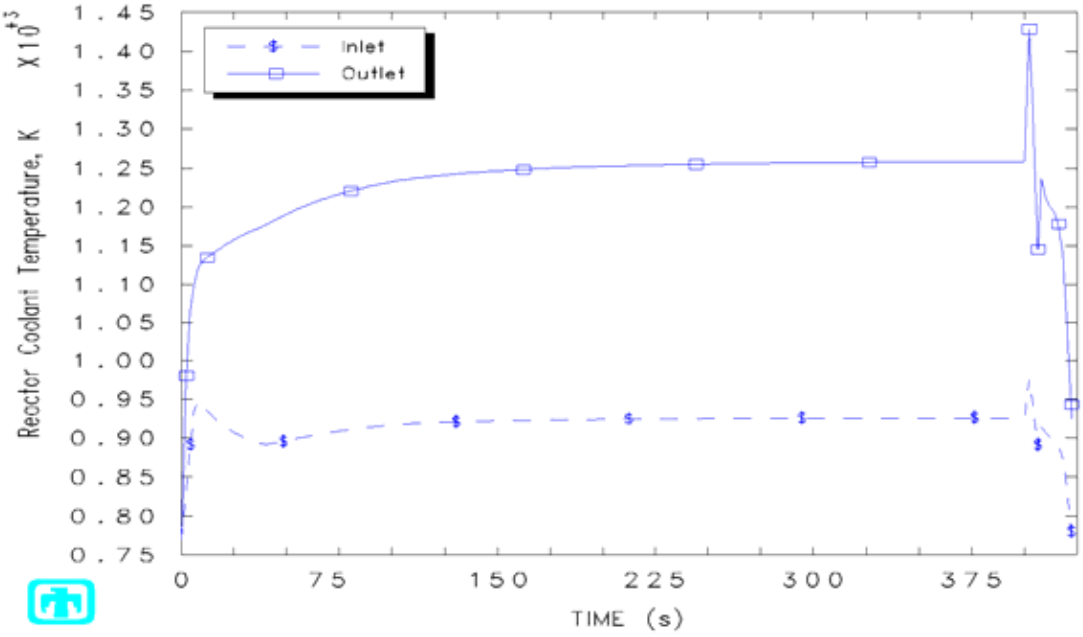

Figure ES-11. Reactor coolant temperatures.

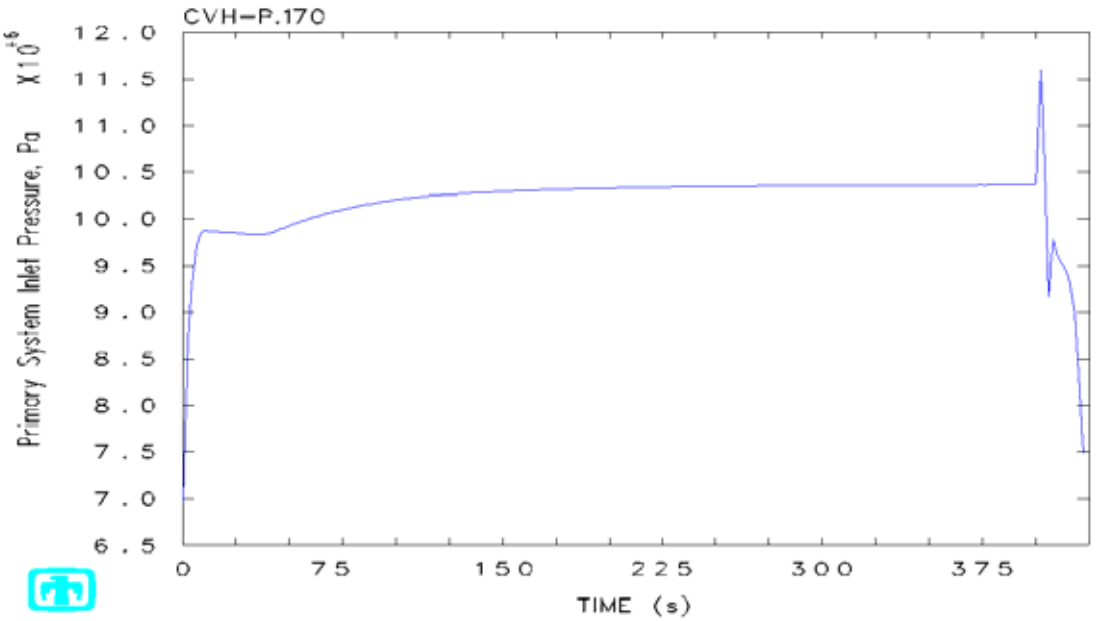

Figure ES-12. Primary system inlet pressure.

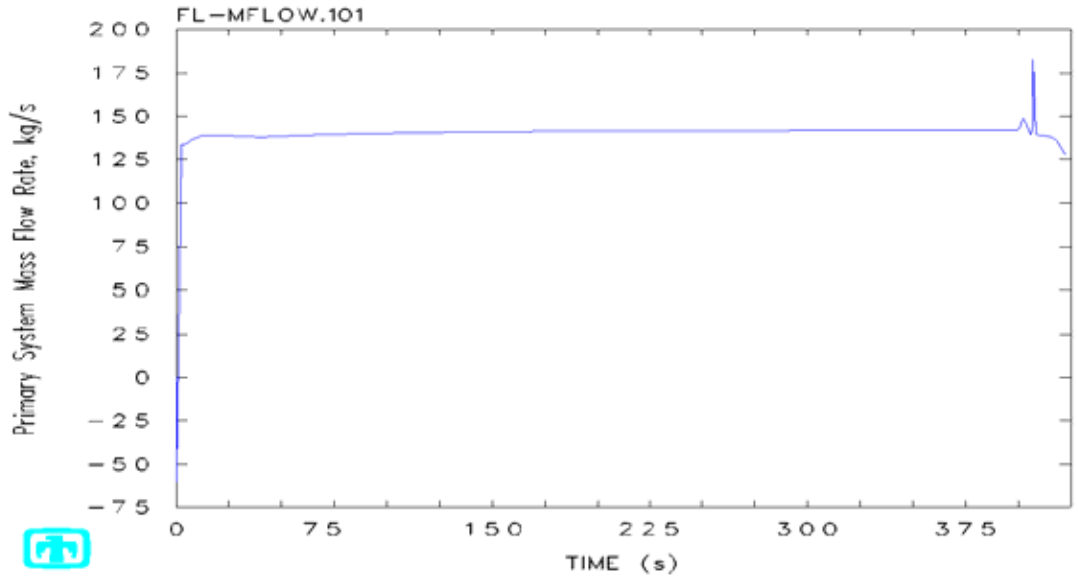

Figure ES-13. Primary system mass flow rate.

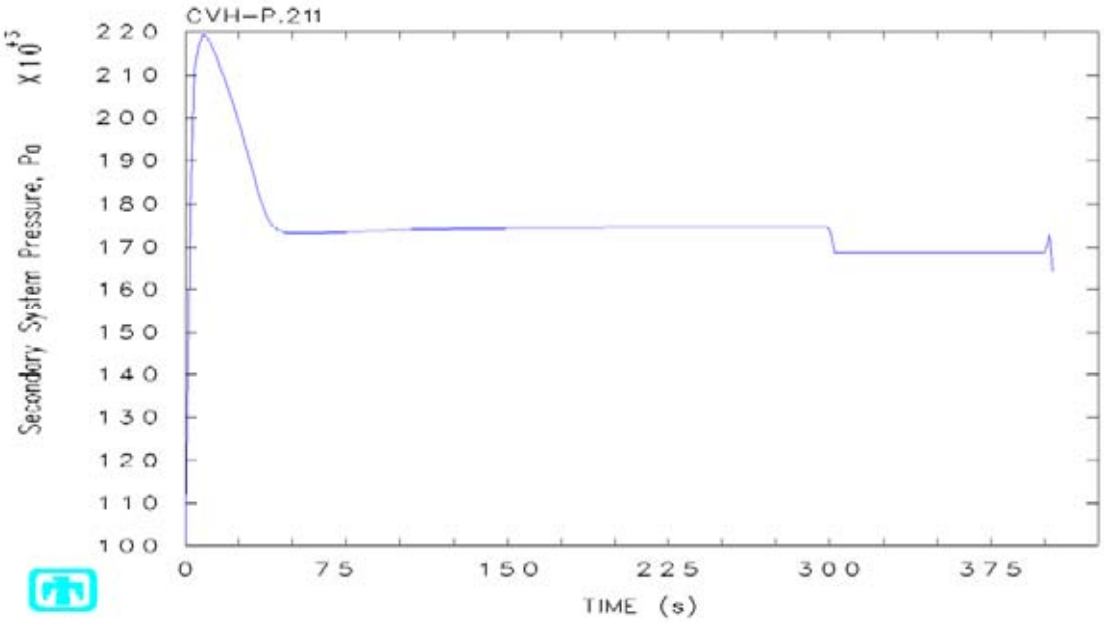

Figure ES-14. Secondary system pressure.

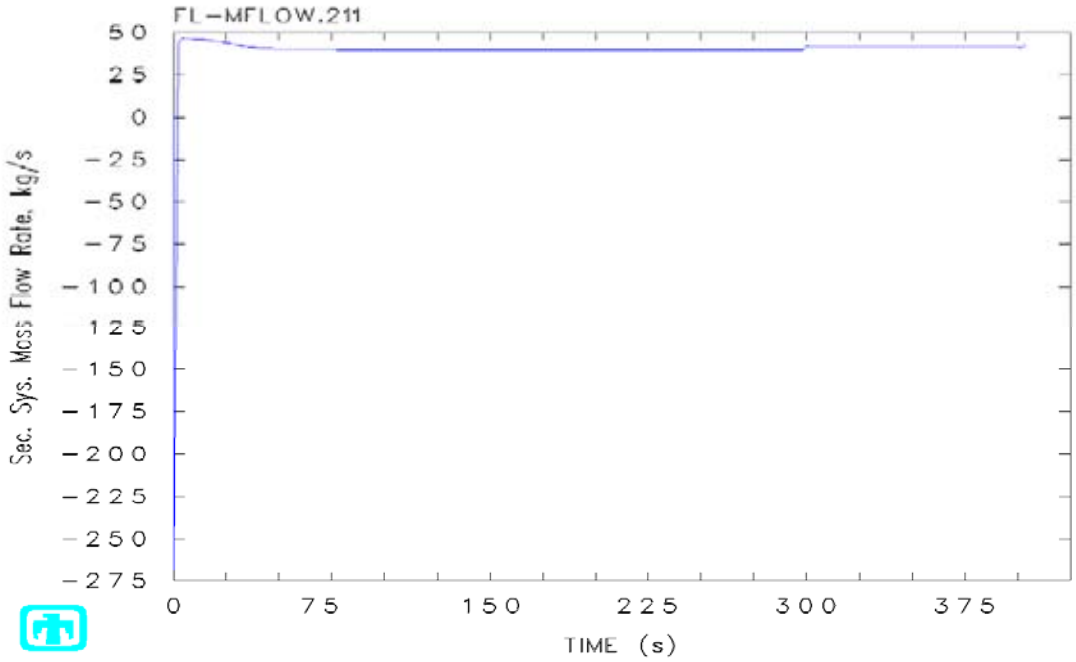

Figure ES-15. Secondary system mass flow rate.

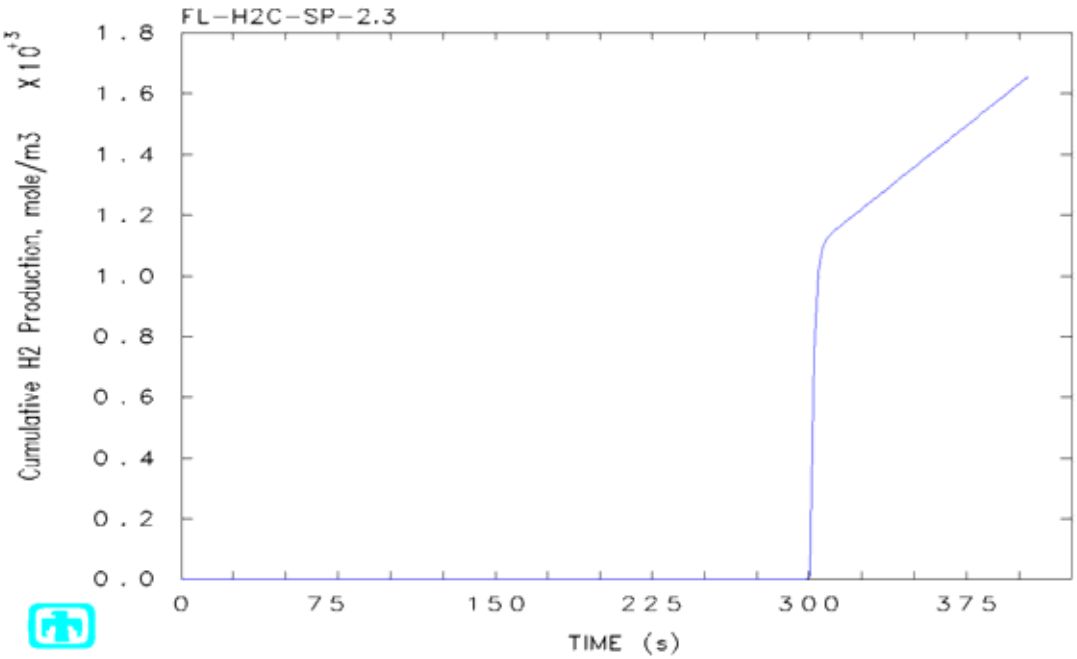

Figure ES-16. Cumulative hydrogen production.

For ease of system design and analysis, a GUI was interfaced to MELCOR-H2. The GUI can be used to display parameters such as system pressure, temperature, hydrogen production, plant efficiency, chemical inventory, and so on. Additionally, because the GUI is dynamic, it allows the analyst/designer to observe the hydrogen plant behavior as a function of time as key parameters are being calculated. The user may modify an input parameter while running a calculation, and immediately observe how that parameter change affects the system's behavior. Figure ES-17 shows a set of six parameters. Notice that at approximately 125 s into the transient, an input parameter (a convective heat transfer coefficient) was changed, thereby causing a change in the system response, as shown by the green arrows.

Through our three-year research effort, we published 15 papers at national and international conferences through the American Nuclear Society (ANS), the American Society of Mechanical Engineers (ASME), the American Institute of Chemical Engineers (AIChE), the World Hydrogen Energy Conference (WHEC), etc. Additionally, papers were also presented and/or published to DOE and NRC personnel, the MELCOR Code Assessment Program, Tri-Laboratory Engineering conferences, and the Sandia Technical Magazine. Figure ES-18 summarizes the impact of this research towards the United States and SNL. Because of MELCOR-H2's unique ability to dynamically model the entire, fully coupled VHTR-SI plant, the United States, through SNL, is now the world leader in the VHTR-SI modeling effort. MELCOR-H2 brings the United States one step closer to achieving the goal of energy independence. In addition, as a result of the pebble bed model simulations, the Nuclear Regulatory Commission awarded SNL close to $650,000 in FY07 for VHTR model development.

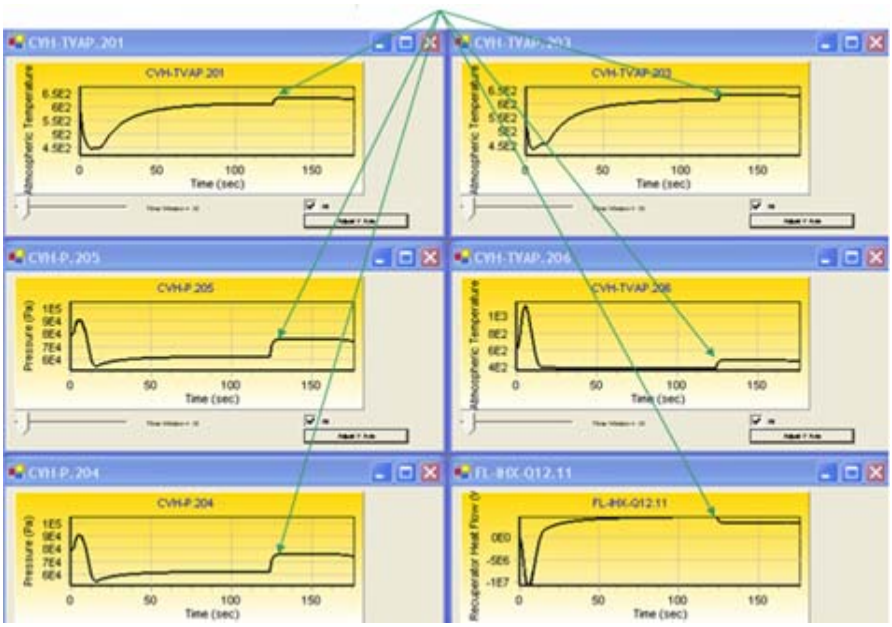

Figure ES-17. Demonstration of the interactive GUI.

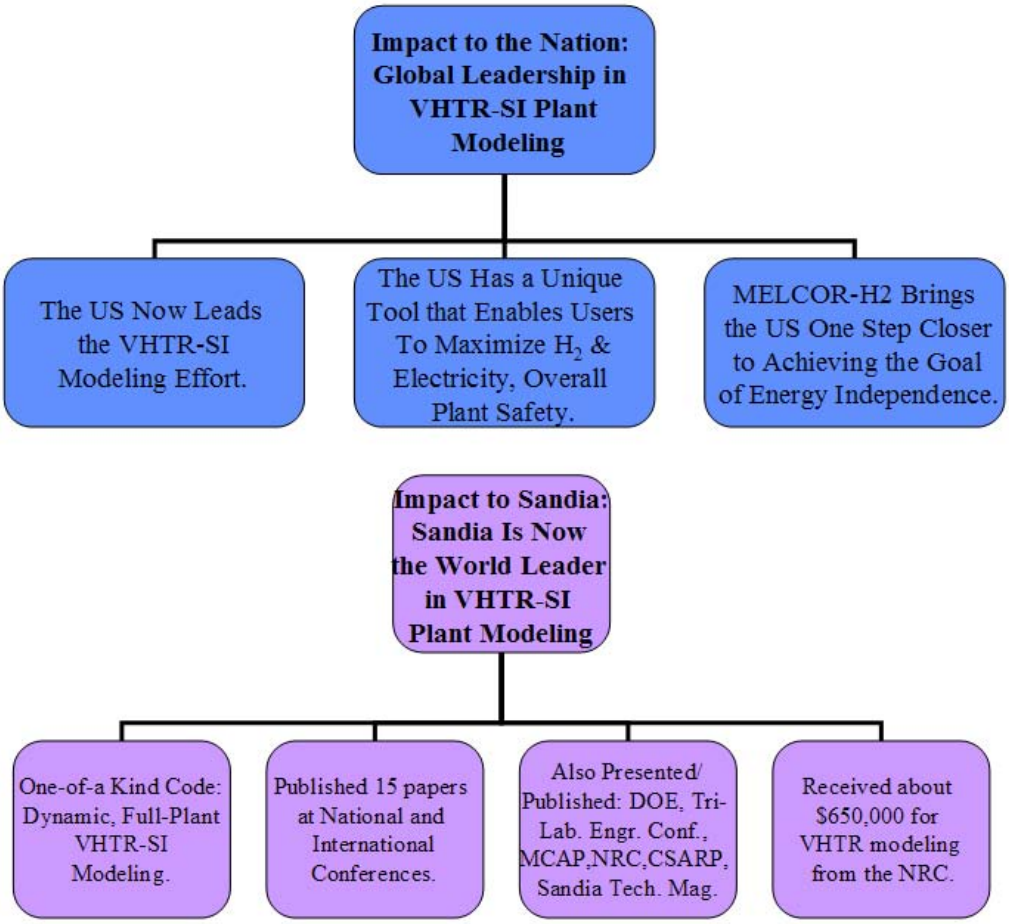

Figure ES-18. Impact to the US and SNL.

Figure ES-19 shows a summary of the interested parties for MELCOR-H2. The list includes U.S. government organizations, national laboratories, universities, and foreign countries, as well as domestic companies.

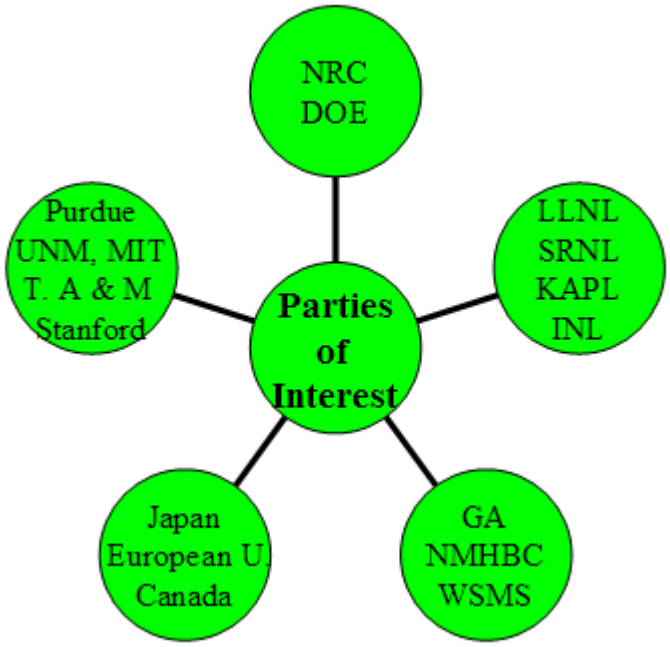

Figure ES-19. MELCOR-H2 parties of interest.

The following is a summary of transients/analysis that can now be performed with MELCOR-H2:

- Loss of flow accidents
  - primary system
  - secondary system
- Chemical leaks from the chemistry loop
  - H_2, SO_2, H_2SO_4, etc.
  - H_2 deflagration
- Air ingress, graphite oxidation
- System feedback, core reactivity effects, system perturbations
- Maximization of
  - H_2 production
  - Electrical output
- Modeling of system startup, turbine, and compressor transients, plant design changes, etc.

In summary, recent MELCOR-H2 advances have resulted in a versatile tool that is suitable for maximizing the generation of hydrogen and electricity from VHTRs, as well as enhancing their safety.

- It is now possible to model the entire, fully coupled nuclear/hydrogen plant in dynamic mode.
- MELCOR-H2 includes
  - Transient SI chemistry models that have been benchmarked,
  - Generalized, modular secondary system components (turbines, compressors, heat exchangers, and generators); the turbines and compressors have been benchmarked,
  - Reasonable ability to model prismatic and pebble bed reactors; some validation and verification has been done,
  - Reactor point kinetics, with model validation, and
  - Interactive GUI.
- Scores of safety/design analysis scenarios can be considered with a single code.

1. INTRODUCTION

Analysis of a very high temperature reactor-sulfur iodine (VHTR-SI) system shows that each plant can produce about 420,000,000 kg of hydrogen per year (at an *in situ* cost of $1.38/kg) and generate close to 600 MW of electricity in the process. One kilogram of hydrogen has the energy equivalence of one gallon of gasoline. Thus, VHTR-SI plants can be considered as domestic oil plants, which need not have to entirely replace petroleum—in particular, it would be economically advantageous if VHTR-SI plants produced sufficient hydrogen such that the oil supply/demand curve is favorably impacted. That is, a significant supply of hydrogen means less petroleum would be needed, with a subsequent reduction in energy prices due to supply and demand.

During FY07, we continued the development of MELCOR-H2, a tool suitable for the analysis of large-scale nuclear-H_2 plants. The work scope included the design and analysis of the nuclear and chemical components, as well as the development of generalized and modular computational models for the nuclear reactor, the secondary system, and the chemical loop. Our work scope focused upon developing a fully transient, fully coupled, modular tool for the design and analysis of nuclear/hydrogen plants.

1.1 Research Strategy

The overall flow of the MELCOR-H2 research strategy is found in Figure 1-1. It consisted principally of a continuous process that began with literature search, followed by the enhancement of the nuclear reactor analysis code, MELCOR. Rather than "reinvent the wheel," we began with MELCOR, which is a safety analysis code being developed by Sandia National Laboratories (SNL) for the Nuclear Regulatory Commission (NRC). We added basic model components, tested them, and then proceeded by adding more advanced models. MELCOR-H2 also adhered to the MELCOR philosophy of developing modular, generalized components that can be used as required by the analyst. We subsequently performed validation and verification of the majority of the models in order to gain confidence in MELCOR-H2.

As noted in Figure 1-1, this three-year effort included three SNL departments, three universities, and one contractor. Because of the extensive amount of research that was conducted by all the involved parties, we divided this report into five self-contained chapters. The Introduction, with a discussion about research strategy and a brief conclusion, is found in this chapter. Chapter 2 discusses the VHTR models, while the SI and HyS chemistry are found in Chapter 3. The secondary system components are documented in Chapter 4. Finally, the point kinetics and interactive graphical user interface (GUI) were combined into Chapter 5.

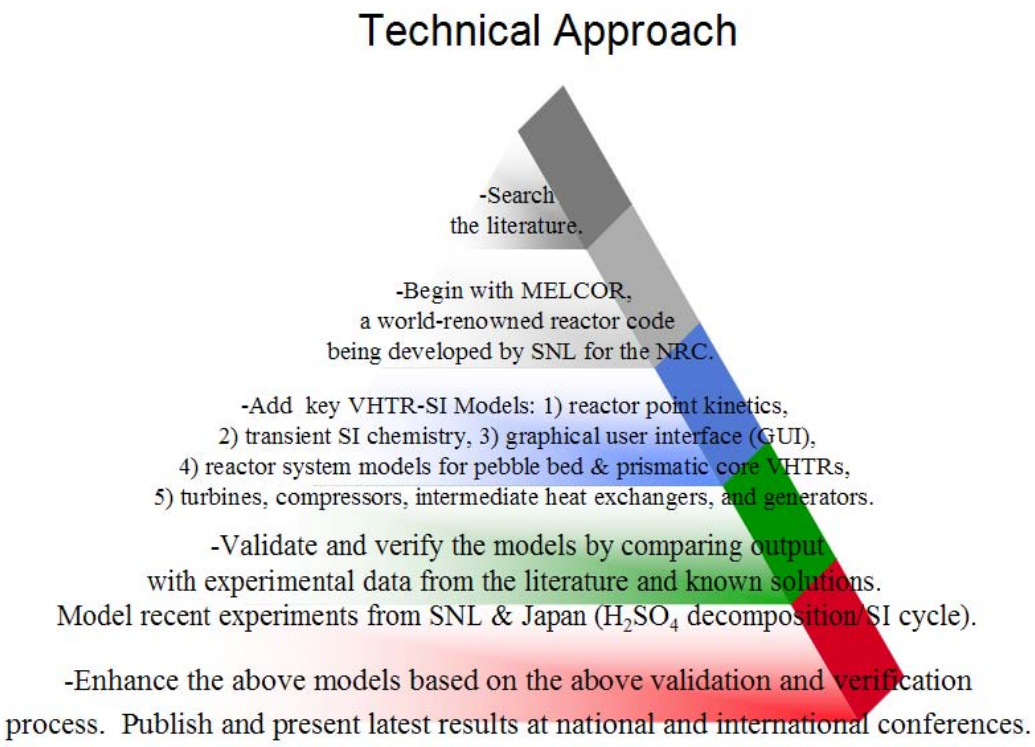

Figure 1-1. MELCOR-H2 technical approach.

1.2 Conclusion

Energy security is an important issue for US national security and economic well-being. New concepts, ideas, and technologies are needed to improve the security and reliability of energy infrastructure and to reduce dependence on imported energy. MELCOR-H2 supports the Department of Energy's (DOE's) National Security Mission through the development of technology and application of this technology towards the safe and economic production of hydrogen as a carrier of energy. Because MELCOR-H2 was designed to simulate the fully coupled nuclear/hydrogen plant in both transient and steady state mode, it is now at the forefront for the design and analysis of such plants.

Recent MELCOR-H2 advances have resulted in a versatile tool that is suitable for maximizing the generation of hydrogen and electricity from VHTRs, as well as enhancing their safety.

- It is now possible to model the entire, fully coupled nuclear/hydrogen plant in dynamic mode.
- MELCOR-H2 includes
  - Transient SI chemistry models that have been benchmarked,
  - Modular secondary system components (turbines, compressors, heat exchangers, and generators); the turbines and compressors have been benchmarked,

  - Reasonable ability to model prismatic and pebble bed reactors; some validation and verification has been done,
  - Reactor point kinetics, with model validation,
  - Modular, generalized model components, and
  - Interactive GUI.
- Scores of safety/design analysis scenarios can now be considered with a single code.

Fifteen papers were published as a result of our MELCOR-H2 research. Consequently, U.S. government organizations, national laboratories, universities, and foreign countries, as well as domestic companies, are interested in MELCOR-H2. We expect to copyright the SI chemistry models and to eventually incorporate all the models into a public release of the code. This will result in the availability of the MELCOR-H2 models in no fewer than 100 user communities throughout the world.

Certainly, the VHTR community would benefit tremendously from the development of additional MELCOR-H2 models and research.

2. VHTR MODELING

2.1 Chapter 2 Highlights

Two tasks are documented herein regarding the simulation of VHTRs with the MELCOR-H2 code.

Task 1: Improvement of PBMR Modeling

The MELCOR-H2 input model developed in the previous year for the Pebble Bed Modular Reactor (PBMR) was modified to allow for improved simulations of its behavior.

The focus of PBMR modeling was placed on the prediction of the pebble radial temperature distribution. A detailed evaluation was performed of the applicability of the lumped capacitance modeling approach for the pebbles. This investigation revealed that the lumped capacitance approach is not valid in several parts of the core region under many conditions. This conclusion is significant because safety issues are involved. First, the pebble center temperature must be known to determine the peak fuel temperature and second, the pebble surface temperature must be accurately estimated to enable accurate heat transfer calculations from the pebbles to the coolant.

Theoretical models for conduction through a sphere were implemented into the PBMR model via Control Functions. The first model predicts pebble temperatures at steady state and includes internal heat generation. The second model predicts the transient pebble temperatures when the pebble is exposed to a sudden change in boundary conditions. Results showed the importance of modeling the radial temperature distribution through the fuel pebbles. The pebble surface temperatures obtained from the new modeling were generally shown to be lower than the sphere isothermal temperatures predicted using the lumped capacitance model.

Implementation of the models into the MELCOR-H2 source is recommended. The Control Function input was excessively lengthy because the calculation methods had to be programmed for each control volume containing pebbles. The current limitations of each model are discussed and future work tasks are identified. Addition of a heat generation term to the second method and incorporation of radiative heat transfer analysis to both methods are of high priority.

Other issues were investigated as continuation of the PBMR deck submitted in September 2006. PBMR calculations in FY06 had been showing an overprediction of fueled pebble temperatures. This problem was partially eliminated with the use of a MELCOR 1.8.5 executable with double-precision (64-bit) accuracy. Predicted steady-state temperatures remain above the fuel failure temperature of 1600^{o}C. Possible causes are uncertainties in fuel properties, missed flow, and heat transfer details due to the large control volume sizes and the lack of a proper radiation heat transfer model. Suggestions for further research into these aspects are provided.

The PBMR input deck was intended to be converted to a double-precision version of MELCOR 1.8.6 that includes the MCH and IHX software. The PBMR input deck supplied by the contractor to SNL in September 2006 was updated by SNL. For the experience, attempts were made by the contractor to update the deck from 1.8.5 to 1.8.6 for use in other parts of this task.

The deck after it had been run through the Input Deck Converter and the diagnostic errors are included in this report.

The radially inward flow issue was not resolved. The same conclusion was reached as in the previous year, namely that the small radial flow patterns observed with and without a heated core have a nodalization dependency. This is not an issue for the prismatic gas-cooled reactor modeling because the coolant flow within the core is restricted to one-dimensional flow through vertical coolant channels.

Methods for modeling the radiation heat transfer that potentially require changes to the MELCOR-H2 source were considered. Discussions concluded that the view factors for radiative heat transfer are dependent on the control volume and core cell sizes and the local pebble packing fraction. Data for comparison against estimated view factors were not obtained in a literature search.

Task 2: High-Temperature Prismatic Reactor Input Deck Development

A new MELCOR-H2 input deck was developed for a high-temperature, gas-cooled prismatic reactor based on design data from a literature survey. The literature survey is included in this report.

The Next Generation Nuclear Reactor (NGNP) design published by Idaho National Laboratory (INL) was selected as the reference design for this input deck development. The point design report provides some data on the reactor design, which is based on Gas-Turbine, Modular Helium Reactor (GT-MHR) designs by General Atomics. Data from General Atomics reports supplement those in the INL report. Data not available from any public reports were estimated and the justifications of these estimations are documented herein.

An initial MELCOR-H2 deck was built as a simplified model of the coolant through an annular core region and the inner and outer graphite reflectors. Control volumes were set up for the gas coolant flow and the reflectors were modeled by heat structures. The purpose of this deck was to demonstrate MELCOR-H2's ability to model passive cooling by thermal conduction through these graphite reflectors. Demonstration calculations showed that heat flowed from the hotter core region into the inner graphite reflector and towards the reactor boundary through the outer reflector.

In discussion with the developers, the subcontractor found that this deck could not be used to faithfully model the core and various components in and around the core region. The strategy was modified to model the graphite fuel elements and reflectors with core cells. The hexagonal graphite blocks are modeled as "clad." The reactor type was declared a pressurized water reactor (PWR). The upper and lower reflectors also presented difficulties for the original model.

A second input deck was developed for the new modeling strategy. The control volume and heat structure input was debugged; however, difficulties were encountered with debugging of the lower head. The subcontractor's current experience of MELCOR 1.8.6 lower head modeling is insufficient, particularly with regard to modeling the bypass flows and null cells in the lower head. The debugging effort is ongoing with the focus on devising techniques to properly associate radial rings in the lower plenum of the prismatic reactor with components above the

bottom of active fuel. No MELCOR-H2 deficiencies have been encountered with respect to prismatic gas-cooled reactor modeling.

A description of a RELAP5 input model for the passive heat removal system, the Reactor Cavity Cooling System, was found in the literature survey. Design data for the passive cooling system is scarce, with a particular deficiency of data needed for the radiative heat transfer modeling. As a future work task, a simplified model will be developed as a place holder.

The simplified input deck and experimental results are included in this report. The detailed input deck and results of the debugging procedure for the core cells are included. As soon as a working input deck of the prismatic reactor is available, it will be transmitted.

2.2 Introduction

2.2.1 Task Descriptions

Task 1: Improvement of PBMR modeling

The MELCOR-H2 input model was modified to allow for improved simulations of the PBMR behavior. Focus was on the radial temperature distributions within the pebbles, the overprediction of the fuel pebble temperatures, and the unexplained radial flows that appear in the core region.

- A model for predicting the radial temperature distribution within a pebble was implemented via Control Functions.
- The fuel temperature overpredictions of FY06 were investigated by running with a higher-precision version of MELCOR 1.8.5.
- The FY06 PBRM input model was run on a double-precision version of MELCOR 1.8.5 to investigate any contribution of numerical accuracy on energy balances. Attempts were made to convert the input deck to a version of MELCOR 1.8.6.
- Methods for modeling the radiation heat transfer that potentially require changes to the MELCOR-H2 source were discussed.
- The radially-inward flow of coolant within the core region that had been observed in the FY06 model was investigated.

Deliverables:

- A MELCOR-H2 PBMR input deck converted to 1.8.6
- MELCOR-H2 code modifications (None were made. All changes were implemented via input.)
- MELCOR-H2 input deck modifications

Completion Date: September 1, 2007

Task 2: High-temperature prismatic reactor input deck development

A MELCOR-H2 input deck will be developed for a high-temperature prismatic reactor based on design data from a literature survey to be performed. Key output will be compared with any available data.

- A literature survey was performed to acquire the most recently available design data on the VHTR and other prismatic high-temperature gas-cooled reactors.
- An appropriate design was selected and a strategy for estimating data that is not available determined.
- A MELCOR-H2 input deck for a prismatic, gas-cooled reactor was developed.

Deliverables:

- Literature survey to obtain high-temperature prismatic reactor design data
- MELCOR-H2 input deck for a high-temperature prismatic reactor

Completion Date: September 1, 2007

2.2.2 Suitability of MELCOR-H2 for Modeling GEN IV Gas-Cooled Reactors

MELCOR-H2 possesses a number of features that render the code uniquely qualified for analysis of modern gas-cooled reactor designs. Originally a fast-running, simplified code for plant risk assessment, MELCOR-H2 is the successor to the Source Term Code Package (Gieseke, 1986). MELCOR-H2 retains some features of the earlier code versions that render it especially appropriate for the proposed work. In particular, "sensitivity coefficients," which are user-controlled input parameters, allow the user to vary physics model parameters for sensitivity studies. The ability to implement these changes without necessitating reprogramming of the code itself makes MELCOR-H2 an ideal testing code.

The Control Volume-Flow Path concept and the Control Function features render MELCOR-H2 a flexible code with which to model Generation IV reactors. There are no restrictions to pre-defined components such as "Pipe" and "Vessel" components. The code can be extended to various systems without creating a new version of the code executable for each design. The Control Volume-Flow Path approach allows for simulation of reactor volumes of any geometry. Therefore the helium flow channels and unique core geometries of high-temperature reactors may be represented by control volumes and flow path connections without code modifications.

The Control Functions permit programming within input files to simulate reactor controls and test new physics models. These Control Functions also allow for a code user to test new physics models via changes to the input only. Control Functions have access to a large number of code parameters as arguments, providing a creative user with many opportunities. In this report, a model is described that determines the pebble radial temperature distribution and was able to draw upon code-calculated parameters via Control Functions.

For pebble bed reactors, the fuel pebbles may be modeled as the "Particulate Debris" fuel component, with newly-assigned thermal properties in the input.

Code assessment performed during FY06 revealed that the current helium property formulation is appropriate under gas-reactor conditions. The code had been written in such a manner that replacing the light water coolant with a gas coolant also did not require any code modifications. Finally, the user is given the ability to redefine core materials, thereby enabling graphite to be a core material.

Other reactor systems codes were considered for the reference code. SCDAP/RELAP5 may not be as suitable because it is not able to model events outside of the reactor pressure vessel. The MAAP4 code has fixed components and a new code version is required when geometry changes are made to standard reactor designs.

2.3 Task 1: Improvement of PBMR Modeling

2.3.1 Pebble Temperature Radial Distribution Model

2.3.1.1 Applicability of Lumped Capacitance Modeling for Pebble Bed Reactors

MELCOR-H2 was originally developed for light water reactor severe accident analysis. Light water reactors mainly use fuel rod bundles with cylindrical UO_2 pellets instead of the TRISO fuel. TRISO fuel is not modeled in the core package of the code. In the current MELCOR-H2 PBMR deck, the TRISO fuel is modeled by the particulate debris phase (Hogan, 2006).

MELCOR-H2 employs the lumped capacitance method to solve for particulate debris temperatures, an assumption which is likely valid for dispersed-phase rubble formed during core degradation. The basic premise behind the lumped capacitance method is that thermal conduction through the heat transfer medium under consideration is large with respect to the thermal conduction away from the medium. In this case, the thermal gradients are small and the medium may be considered isothermal.

In the case of pebbles for a PBMR, the heat transfer medium has a relatively large diameter (6 cm) and some of the constituents of the pebbles do not have a high thermal conductivity. Experimentally measured temperatures of pebbles exposed to high burnup and high temperatures show that the temperature difference between a pebble center and a pebble surface can be over 150 °C (Futterer et al., 2004).

The initial motivation for careful scrutiny of the applicability of the lumped capacitance method arose during analysis with the MELCOR-H2 PBMR model by Hogan (2006). The PBMR model using the particulate debris model overpredicted the fuel temperature by a significant amount in some core cells. In fact, steady-state temperatures predicted by the lumped capacitance method were higher than the expected values following a depressurized loss of forced convection.

The high temperatures were later found to be due in large part to an error in the solution of the energy equation (see Section 2.3.2). In conjunction with the energy balance study, consideration was given to appropriate temperatures to pass to the CVH for heat removal analysis. The large discrepancy in fuel temperatures is a significant drawback when using the model for severe accident analysis. Further study was therefore required to better estimate fuel center and surface temperatures during steady state and transient conditions. This formulation described below

focuses on predicting a temperature distribution profile in the fuel pebbles during steady state and transient conditions.

Fuel integrity is the basis of severe accident analysis. Fuel temperature is the leading factor in determining the failure of fuel pebbles in most analysis. Air ingress during depressurized loss of forced coolant accident is another important event that requires a better estimate of fuel surface temperature to calculate graphite oxidation rates. The rate of air entering the reactor and interacting with hot graphite in the fuel and structures is a function of the surface temperature among other parameters. To better predict the oxidation rate and the energy generation from oxidation reactions, correct fuel surface temperature estimation is a priority. Fuel pebble center point temperature is needed for severe accident analysis since it is the basis for determining fuel failure by overheating.

The current PBMR model results for steady-state showed that the energy transfer between the core to the coolant is accurate. The formulation that is used in this chapter is based on using the coolant properties to solve for the fuel pebble temperature and compare it with MELCOR-H2 lumped capacitance fuel temperature.

The Biot number, which is a ratio of thermal conduction resistance to thermal convection resistance, must be 0.1 or less for the lumped capacitance method to be valid (Incropera and DeWitt, 2002). The validity of this method is in question for the conditions of the flow in high-temperature gas-cooled reactors. For this purpose, evaluating the Biot number across the reactor core is important. The Biot number is calculated using Equation (2-1).

$$Bi = \frac{h \quad L^*}{k_{fuel}} \tag{2-1}$$

L^* is the characteristic length. It is defined as the volume of the body divided by the surface area of the body. For a sphere, it equals $\frac{1}{6}$ of the diameter.

The nodalization of the PBMR model submitted at the end of FY06 is shown in Figure 2-1 for reference. This model has been used in the following calculations.

Figures 2-2 and 2-3 show the Biot number results for different control volumes (CVs) in the reactor during steady state operation. Results show that some of the control volumes have flows of Biot numbers less than 0.1 while others do not meet the Biot number criteria. These results confirm that most of the reactor conditions during steady state do not meet the lumped capacitance validity limit to calculate fuel temperatures. The reason behind the differences in flow properties at different locations in the reactor can be attributed to the complex geometry of the flow around fuel pebbles and the location of fueled pebbles. Many phenomena are involved, including complex mixing behavior accompanied with large temperature gradient. This results in significant differences in thermal and dynamic properties of the flow at different locations of the reactor core.

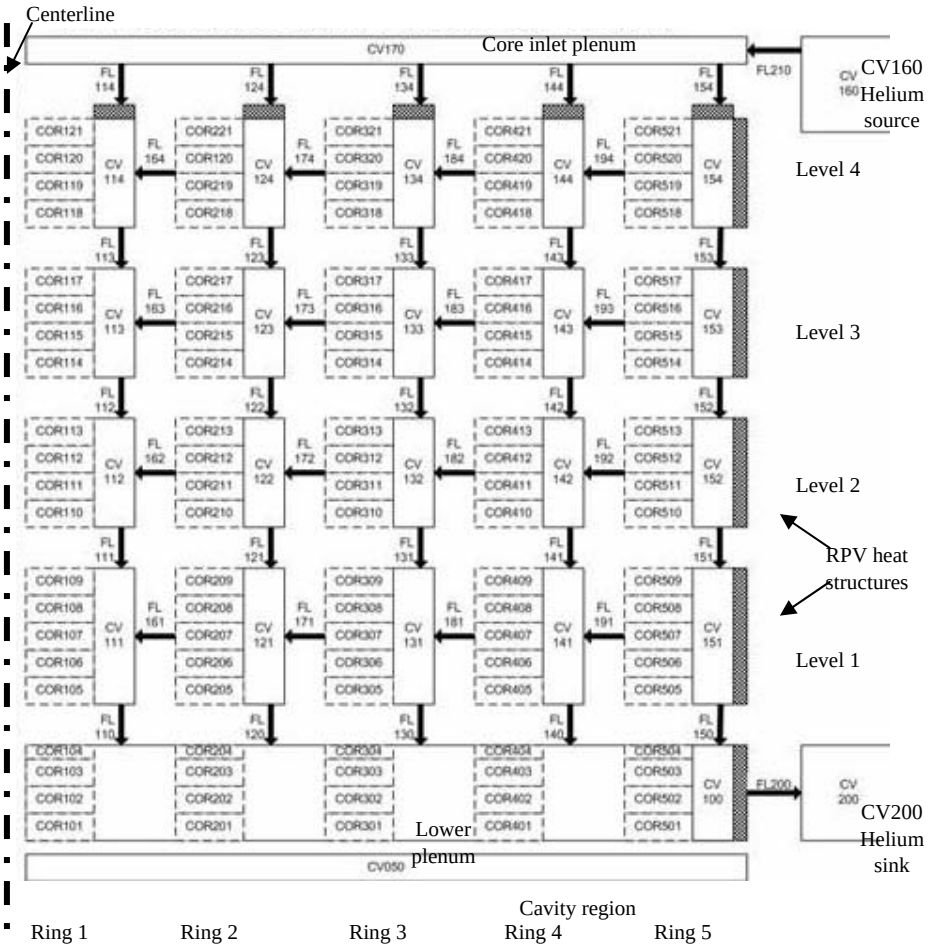

Figure 2-1. PBMR nodalization for MELCOR-H2 model (Hogan, 2006).

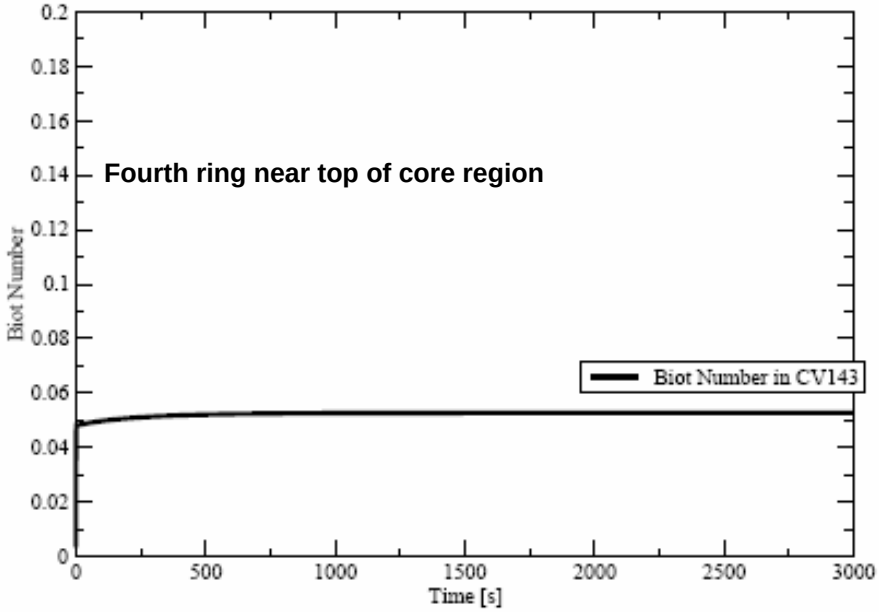

Figure 2-2. Biot number in CV 143.

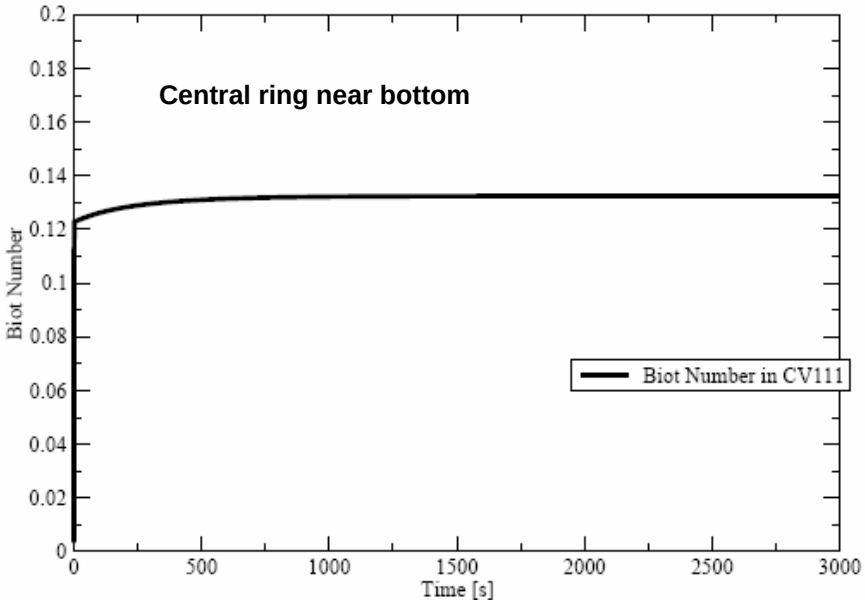

Figure 2-3. Biot number in CV 111.

Two methods are discussed in this section for estimating the center and surface temperatures of fuel pebbles. The first uses correlations for conduction and convection heat transfer around the sphere and solves for the steady state pebble temperatures. The second method is based on an approximate numerical solution for the heat equation in spherical coordinates under transient conditions. The methods acquire information from MELCOR-H2 about the fluid conditions in each control volume around the pebbles. This limits the calculation to one radial temperature distribution per control volume. As a result, all pebbles in each control volume will be assumed to have identical temperature distributions.

2.3.1.2 Analysis Method for Steady State Radial Temperature Profile

Heat transfer in packed bed involves three main heat transfer methods. Each fuel pebble experiences conduction heat transfer inside the pebble and from the fuel pebble to adjacent pebbles and convection heat transfer by coolant flow, as well as radiation heat transfer from the fuel pebble to the surrounding vicinity of fuel and structure.

In this approximate analysis, the fuel pebble is assumed to be isolated from other fuel pebbles. This assumption eliminates other heat transfer methods and only accounts for convective heat transfer to the primary coolant. In reality, conduction heat transfer in a packed bed core is an important method of heat transfer in high-temperature gas-cooled reactors. However, advanced methods would require three-dimensional capabilities with a three-dimensional thermal network for the full reactor simulation that is beyond this research scope. A three-step formulation is presented here:

- Approximation of maximum fuel temperature difference between the pebble center and the surface temperatures, ΔT, by a conduction calculation within the pebble.

- Solving for the convection heat transfer coefficient, *h*, using coolant properties around the fuel pebble.
- Solving for the fuel pebble surface temperature using the obtained heat transfer coefficient and then estimation of the center temperature using ΔT from the first step.

The difference between the surface temperature and the center temperature of the fuel pebble can be obtained by solving the one-dimensional heat equation for a spherical geometry with uniform heat generation and symmetrical surface conditions (Incropera and DeWitt, 2002). Equation (2-2) describes the heat rate as function of radial location in the pebble. This equation assumes that the heat generation occurs uniformly throughout the pebble. It also assumes that the fuel pebble has constant thermal conductivity.

$$q(r)=\frac{\dot{q}4\pi r^3}{3}=\frac{4\pi k_{fuel}\left[\frac{\dot{q}r_2^2}{6k_{fuel}}\left(1-\frac{r_1^2}{r_2^2}\right)+\left(T_{s,2}-T_{s,1}\right)\right]}{\frac{1}{r_1}-\frac{1}{r_2}} \tag{2-2}$$

The equation calculates *q*, the heat rate, at a specific radial location, *r*, given the total heat generation rate per pebble, $\dot{q}$. For this analysis, $T_{s,1}$ is the temperature at a point very close to the pebble center (r_1 = 0.000001) and $T_{s,2}$ is the fuel pebble surface temperature. Rearranging the terms in Equation (2-2), one can approximate the temperature difference, ΔT, as shown in Equation (2-3).

$$\Delta T=T_{s,1}-T_{s,2}=\frac{1}{12}\frac{3qr_2-2qr_1-4\dot{q}\pi r_2^4+6\dot{q}\pi r_2^3 r_1}{\pi r_1 r_2 k_{fuel}} \tag{2-3}$$

The reference model that is used in this research is based on the 268 MWth power PBMR (Reitsma, 2004). The number of fuel pebbles in the core is estimated to be 330,000 pebbles (Nichols, 2001). For the approximate fuel temperature calculation, it is assumed that the full generated power in the reactor is distributed evenly among the fuel pebbles. In reality, the power profile in the reactor varies axially and radially. The power distribution is important in determining the hot spots in the reactor. The maximum temperatures are more likely to occur where the power profile is the highest in the core and the coolant has the highest temperature or lowest flow rate. Heat rate generated per pebble can be approximated by dividing the total generated power by the number of fuel pebbles (Equation (2-4)).

$$\dot{q}=\frac{Normal\ Operation\ Power}{Number\ of\ Fuel\ Spheres\times Volume}=\frac{268MW}{330{,}000\times\frac{4}{3}\pi R^3} \tag{2-4}$$

where *R* is the fuel pebble radius (0.06 m).

The thermal conductivity for the fuel in a PBMR can be calculated as a function fuel temperature using the correlation by No (2001) in Equation (2-5). This is an empirical correlation for an

average fuel thermal conductivity for fuel pebbles in a packed bed as a function of fuel temperature.

$$k_{fuel}=1.1536\text{-}4 \quad (T\text{-}T_{\circ}) \tag{2-5}$$

where T_o is the reference temperature of 273.16 K and k_{fuel} is in units of W/(m K). A plot of pebble bed thermal conductivity is shown in Figure 2-4 over a range of temperatures.

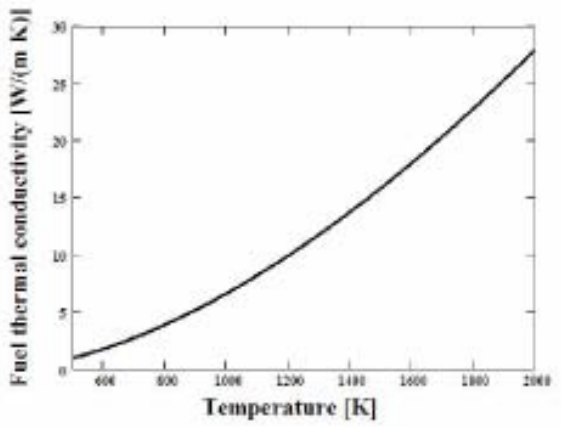

Figure 2-4. Thermal conductivity in pebble bed versus fuel temperature.

In past calculations, the PBMR fuel bed thermal conductivity has been averaged to 20 W/(m K) (Reitsma, 2004). The average value seems reasonable given the reactor operation temperatures.

Taking r_2 as the radius at the surface of the sphere and r_1 as very close to the center, The only unknowns left in equation are $T_{s,1}$ and $T_{s,2}$, or ΔT. Solution of Equation (2-3) results in a range of ΔT from 107.71 K to 53.81 K using k_{fuel} equals 10 W/(m K) and 20 W/(m K) respectively. The power profile along the core varies compared to average normalized power from 0.0 to 1.39 (Reitsma, 2004). This variation in the axial power leads to a maximum fuel temperature difference $\Delta T = 149.718K$ using k_{fuel} equals 20 W/(m K) at the location of greatest power. The temperature difference between the surface and the center of the pebble seems reasonable compared to the irradiation experiment data of Futterer et al., 2004. Irradiation experiments on fuel pebbles showed a temperature difference as large as about 150 K between the pebble center and the pebble surface.

For a steady state condition, one can solve for an isolated fuel pebble surface temperature by using the formulation for steady state forced convection around a sphere in Equation (2-6).

$$Q = h\ A\ (T_s - T_{\infty}) \tag{2-6}$$

where q represents power in watts (average pebble power), h is the local heat transfer coefficient, and A is the surface area of the fuel pebble. H can be calculated using the definition of Nu number given the thermal conductivity of the coolant and the diameter of the sphere (Equation (2-7)).

$$Nu = \frac{hD}{k_{He}} \tag{2-7}$$

To calculate the heat transfer coefficient, *Nu* number is calculated as a function of *Re* and *Pr*. A correlation for forced convection around a spherical element can be used for this purpose, as shown in Equation (2-8) (Gauntt et al., 2005).

$$Nu = 2.0 + 0.6 Re^{1/2} Pr^{1/3} \tag{2-8}$$

To calculate the Reynolds number, viscosity of helium as a function of temperature is estimated as below (Bird et al., 1960).

$$\mu = 2.6693\text{-}6 \frac{\sqrt{MT}}{\sigma^2 \Omega_\mu} \tag{2-9}$$

and the kinematic viscosity is given by Equation (2-10).

$$\nu = \frac{\mu_{He}}{\rho} \tag{2-10}$$

where μ is in *kg*/(*m s*), *T* is the temperature in K, σ and Ω_μ are slowly varying functions of the dimensionless temperature KT/ε as explained in Bird et al. (1960). For the approximate calculations presented here, σ and Ω_μ are assumed constants. The available data for Ω_μ are limited to a maximum temperature of 1020 K. The value of Ω_μ has been interpolated beyond the table for a temperature of 1173 K (reactor outlet temperature). This resulted in $\Omega_\mu = 0.5745$ for helium using $\sigma = 2.576\ A$.

The thermal conductivity k_{He} for helium can be calculated using Equation (2-11) from Bird et al. (1960).

$$k = 1.9891 \cdot 10^{-2} \frac{\sqrt{T/M}}{\sigma^2 \Omega_k} \tag{2-11}$$

where k is $\frac{cal}{s\ m\ K}$, σ in *A*° and $\Omega_K = \Omega_\mu$.

The Reynolds number can be then calculated using Equation (2-12).

$$Re = \frac{vD}{\nu} \tag{2-12}$$

where D is the diameter of the fuel pebble, 0.06 m. The specific heat of helium can be taken as a constant for this calculation. The thermal diffusivity of the helium gas can be calculated as follows:

$$\alpha = \frac{k_{He}}{\rho C_{p_{He}}} \tag{2-13}$$

Pr number is then calculated as follows:

$$Pr = \frac{\nu}{\alpha} \tag{2-14}$$

Equations (2-7) and (2-8) can now be solved for the local heat transfer coefficient, h. Equation (2-6) leads to the pebble surface temperature, T_S. The fuel center temperature is then calculated using the surface temperature of the pebble and ΔT, which was calculated by Equation (2-3).

This methodology for calculating the fuel pebble surface temperature has been implemented into the MELCOR-H2 PBMR input deck as Control Functions. The Control Functions avoid the need for source code changes and enable testing by other than the code developers. Several variables that MELCOR-H2 outputs by default have been used as model input. These variables are coolant velocity, density, and temperature (T_∞) of each control volume.

This method contains a few limitations and approximations. The homogeneous pebble assumption for the TRISO fuel is valid because the fuel pebble is constructed of thousands of very small fuel elements distributed in the fueled region of the pebble. However, the heat generation in the fuel pebble is not generated uniformly throughout the sphere. The fuel microspheres are distributed evenly in all but the outer coatings of the fuel pebble, as shown in Figure 2-5. The spatial heat generation assumption may affect the accuracy of the temperature profile inside the fuel pebble. The above method has also assumed no conduction heat transfer from the fuel pebble to other pebbles. It assumes that heat is being removed by the coolant only.

The methods above of using the control volume properties to estimate fuel temperature limits the estimated fuel temperature to one value per control volume. Regardless of how many core cells are attached to each control volume, the estimated temperature using this method will be the same for all core cells attached to any given control volume.

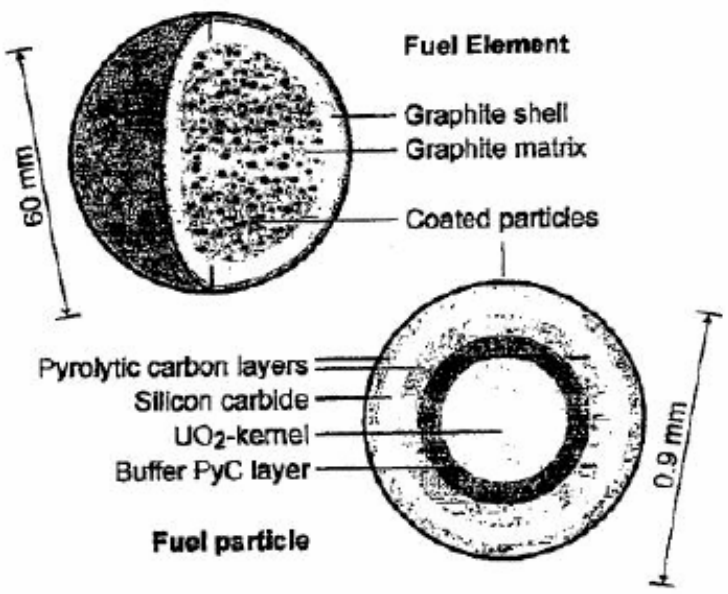

Figure 2-5. TRISO fuel microspheres (Nichols, 2001).

The results are shown in Figures 2-6 through 2-17 for the Ring 1 (containing only unfueled graphite pebbles), Ring 3 (containing 50% unfueled and 50% fueled graphite pebbles), and Ring 5 (containing 100% fueled graphite pebbles), control volumes and their associated core cells. The pebble surface temperatures calculated using this method are in good overall agreement with MELCOR's calculated particulate debris (isothermal sphere) temperatures in the corresponding core cells. The calculated surface temperatures are generally less than MELCOR's highest fuel temperature in the control volume. Exceptions to this are some control volumes in the central Ring 1 containing unfueled graphite pebbles. The bottom region of the core also displays calculated surface temperatures close to MELCOR's fuel temperatures. The maximum calculated surface temperature during steady state was in CV 132. However, MELCOR's highest fuel temperature was still higher in this control volume. The overprediction of fuel temperatures in some control volumes is discussed in the next section of this report.

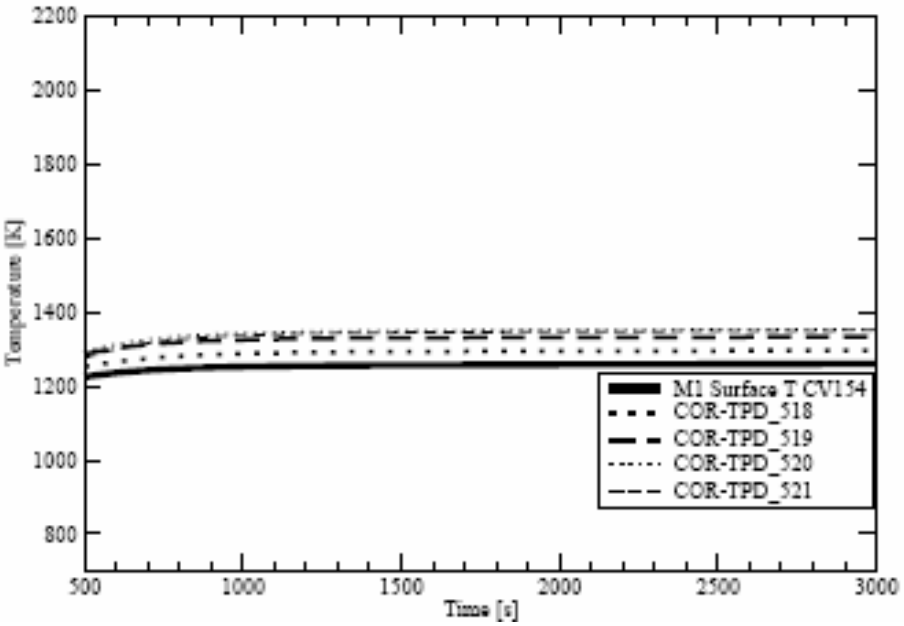

Figure 2-6. Pebble surface temperature vs. isothermal pebble temperature in CV 154.

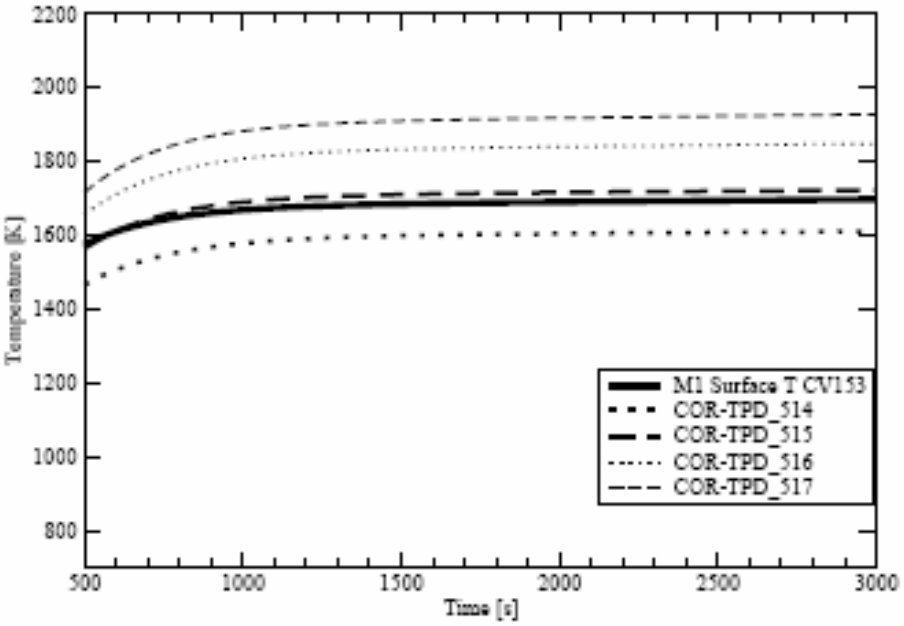

Figure 2-7. Pebble surface temperature vs. isothermal pebble temperature in CV 153.

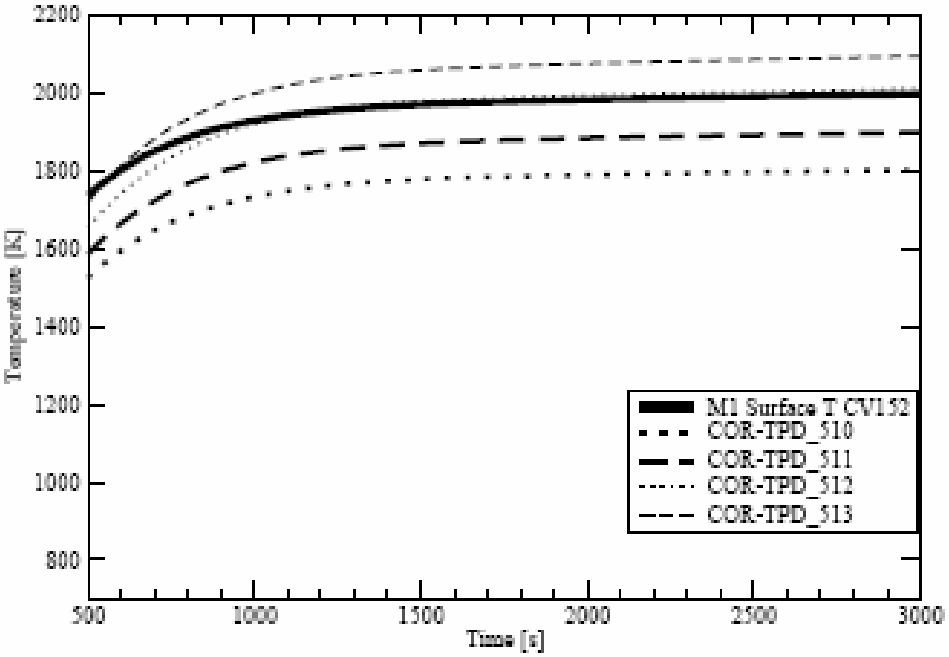

Figure 2-8. Pebble surface temperature vs. isothermal pebble temperature in CV 152.

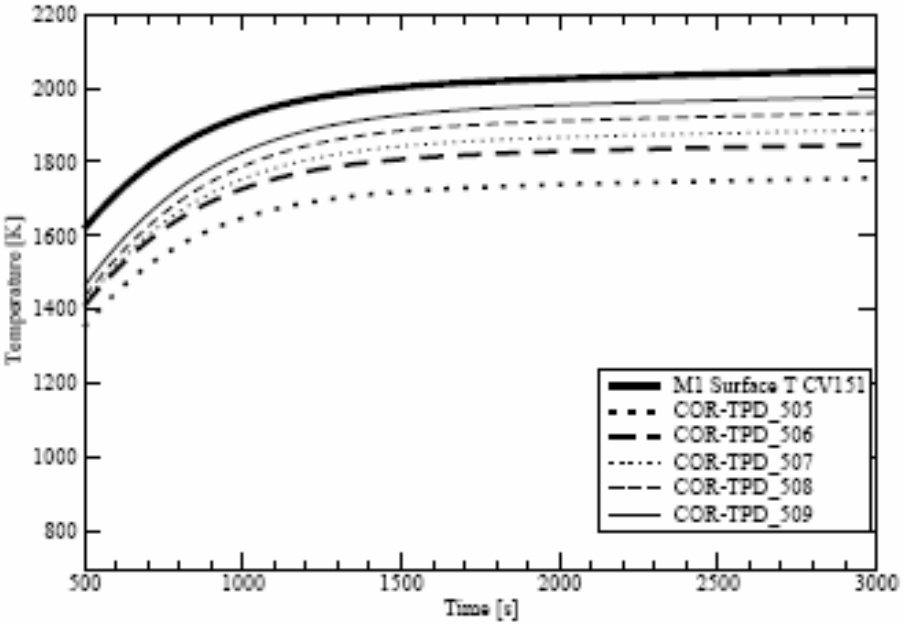

Figure 2-9. Pebble surface temperature vs. isothermal pebble temperature in CV 151.

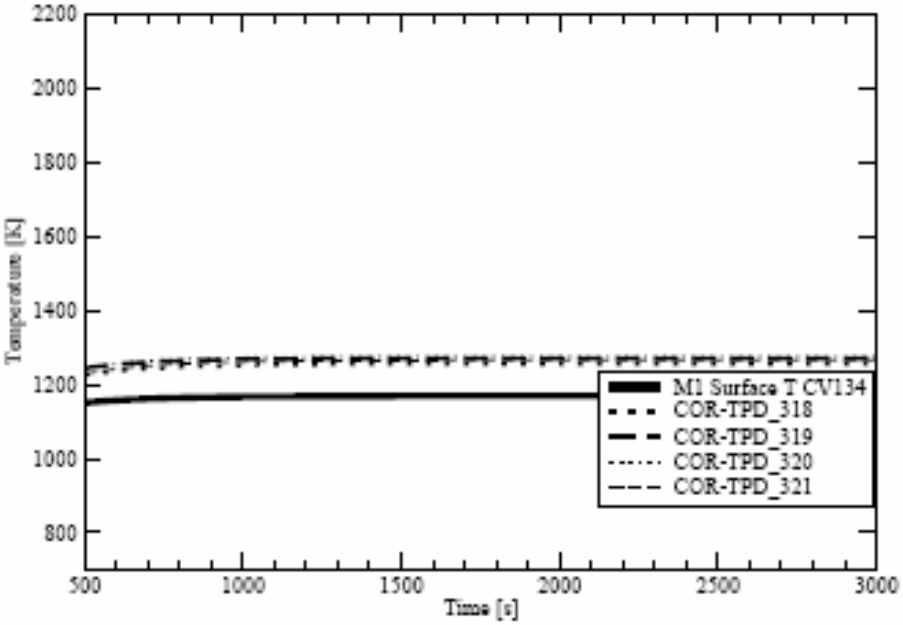

Figure 2-10. Pebble surface temperature vs. isothermal pebble temperature in CV 134.

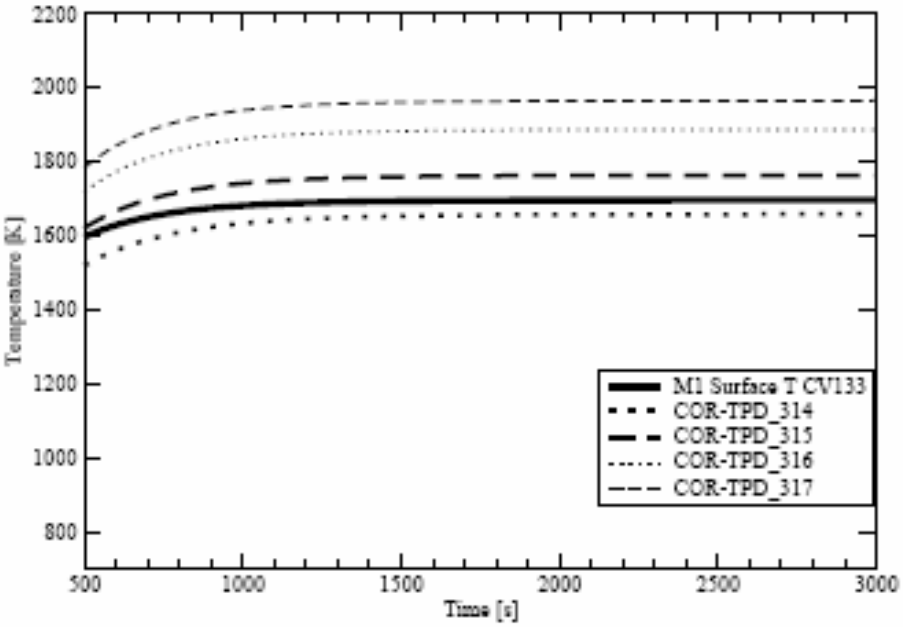

Figure 2-11. Pebble surface temperature vs. isothermal pebble temperature in CV 133.

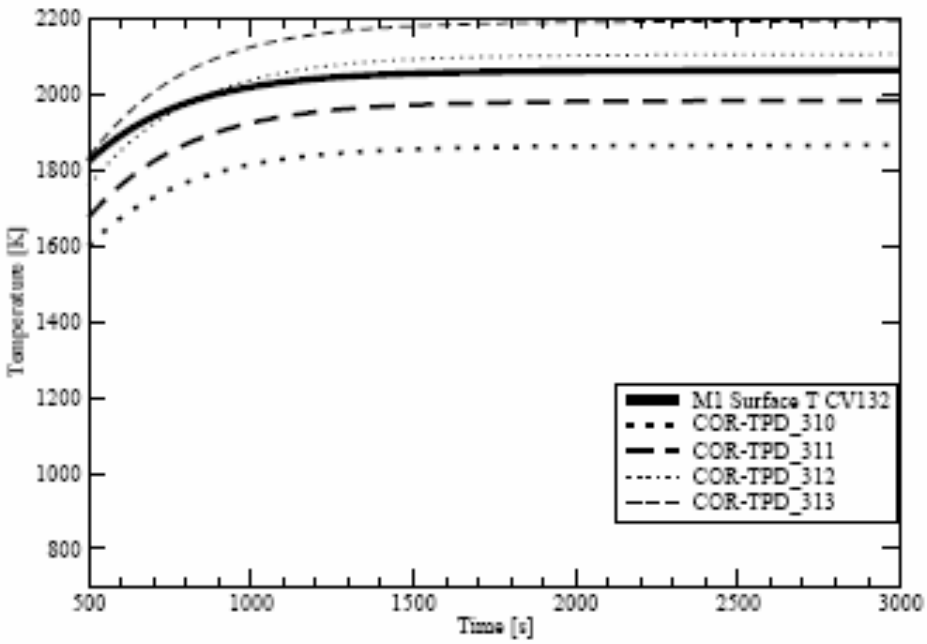

Figure 2-12. Pebble surface temperature vs. isothermal pebble temperature in CV 132.

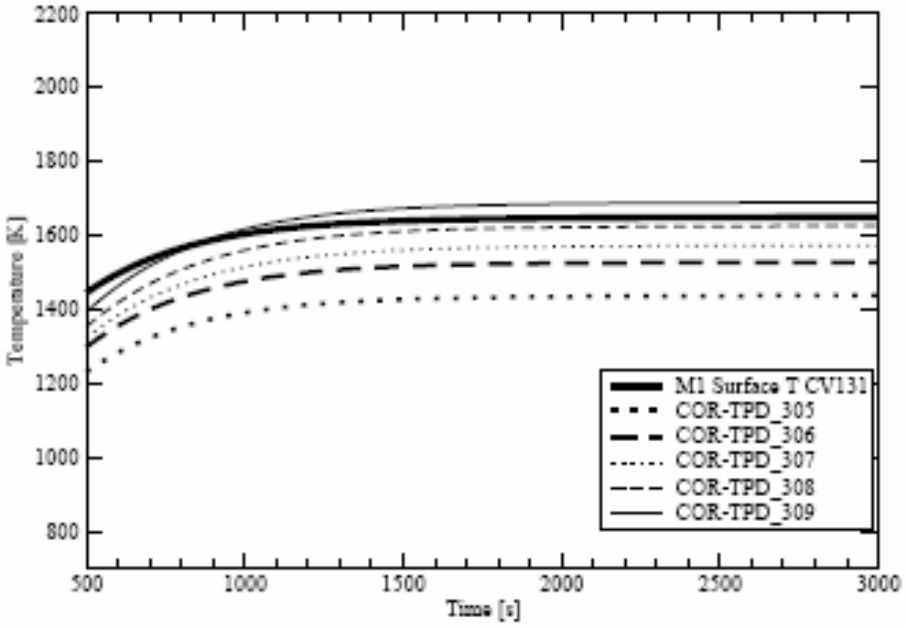

Figure 2-13. Pebble surface temperature vs. isothermal pebble temperature in CV 131.

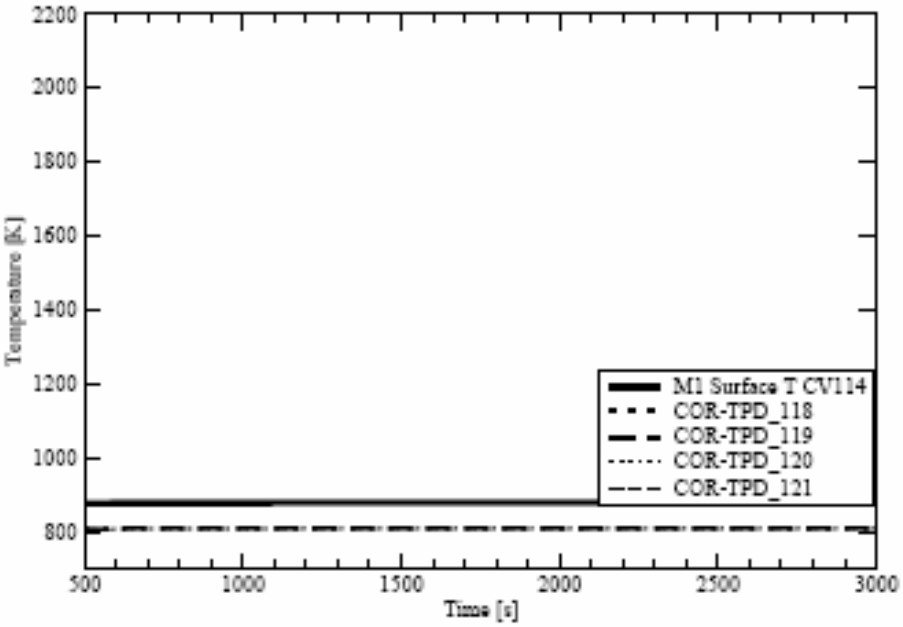

Figure 2-14. Pebble surface temperature vs. isothermal pebble temperature in CV 114.

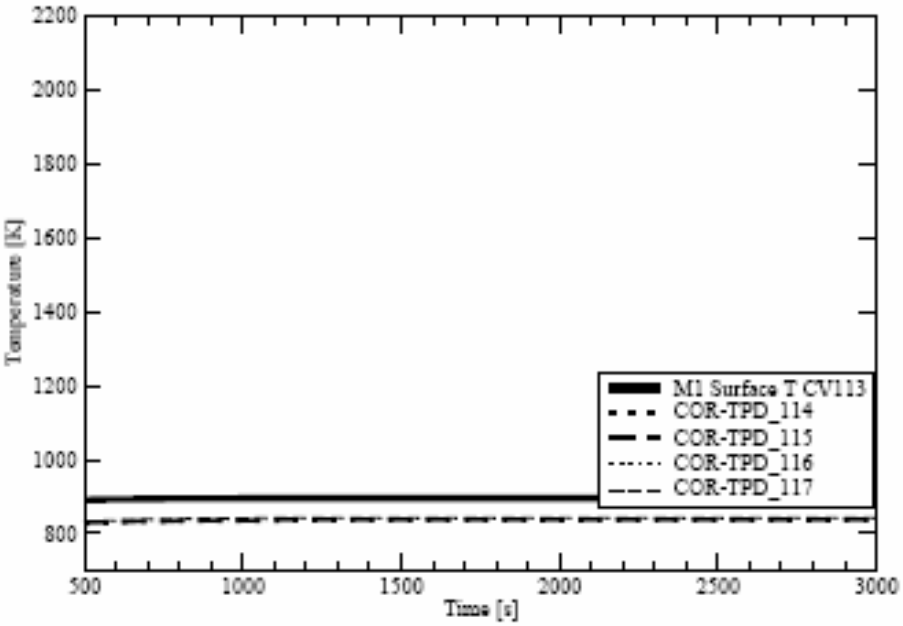

Figure 2-15. Pebble surface temperature vs. isothermal pebble temperature in CV 113.

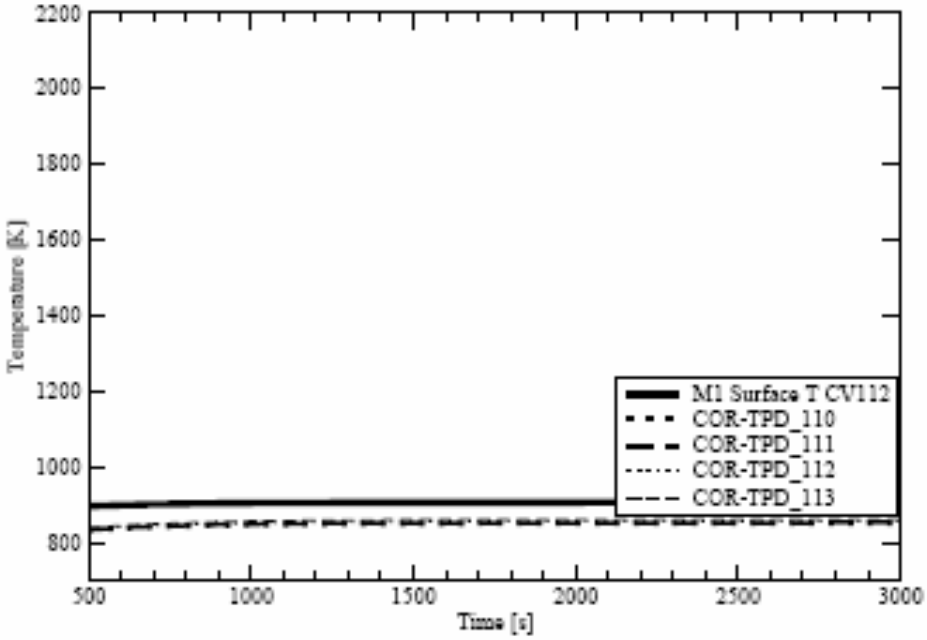

Figure 2-16. Pebble surface temperature vs. isothermal pebble temperature in CV 112.

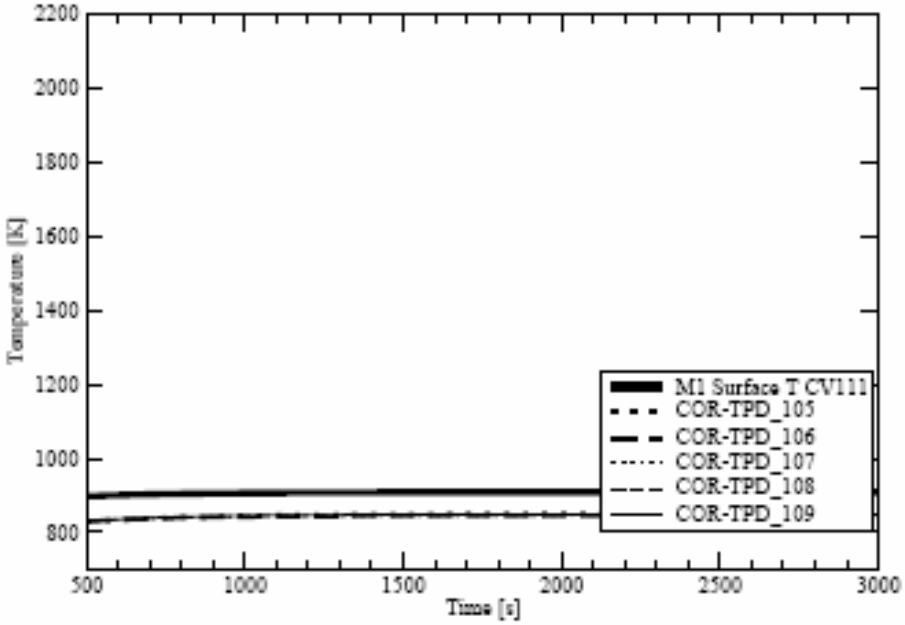

Figure 2-17. Pebble surface temperature vs. isothermal pebble temperature in CV 111.

2.3.1.3 Analysis Method for Transient Radial Temperature Profile

The first method estimates the radial temperature distribution in a sphere at steady state. To estimate the surface temperature of the fuel pebble under transient conditions, a numerical solution for a sphere in convective environment may be used (Incropera and DeWitt, 2002). This time-dependent solution provides the temperature distribution in a sphere that is initially at a uniform temperature and is allowed to cool by convection. The numerical solution gives a better approximation for the fuel pebble temperature as a function of the fluid properties around the sphere.

The MELCOR-calculated energy deposition from the fuel to the coolant and the fluid properties within control volumes are used as input for this methodology. This formulation uses primarily the coolant properties to calculate the temperature distribution of the fuel pebble.

During an initial steady state calculation, arbitrary initial temperatures for the sphere are imposed. Once the coolant properties became steady, the calculated temperature of the sphere will reach a steady state value. The time-dependent response of the fuel temperature to the change in the surrounding environment becomes smaller in time. However, this formulation problem can be overcome by resetting the time once the calculation has reached steady state in terms of coolant temperature properties.

A first term approximation for a series exact solution is presented in Incropera and DeWitt (2002). This solution is valid for $Fo > 0.2$.

$$\theta^* = \theta_\circ^* \frac{1}{\zeta_1 r^*} \sin \zeta_1 r^* \tag{2-15}$$

where θ^* is the dimensionless temperature at distance r^*, and r^* is the dimensionless radial distance outward (r/R).

$$\theta^* = \frac{T_s - T_\infty}{T_{i,s} - T_\infty} \tag{2-16}$$

where T_s is the surface temperature of the sphere. The dimensionless temperature at the sphere center, $\theta_\circ^*$, is defined below.

$$\theta_\circ^* = C_1 \exp -\zeta_1^2 Fo \tag{2-17}$$

ζ_1 and C_1 are tabulated for sphere as a function of the number in standard heat transfer textbooks such as Incropera and DeWitt (2002). T_∞ is the temperature of the coolant around the fuel pebble and $T_{s,i}$ is an initial surface temperature. The Fourier number introduces the time dependency into the dimensionless temperature:

$$Fo = \frac{\alpha t}{r_\circ^2} \tag{2-18}$$

Fluid properties are calculated in the same manner as outlined in the previous section. The numerical solution procedure models and correlations have been implemented in MELCOR-H2 using control functions. Look up tables for the constants ζ and C_1 as a function of the Biot number have also been implemented via Control Functions and Tabular Functions. The models were implemented to calculate coolant properties for each control volume every time step as summarized below.

- Calculate helium viscosity as a function of temperature of the control volume.
- Calculate thermal conductivity for helium as a function of temperature of the control volume.
- Calculate viscosity as a function of density obtained from MELCOR-H2 in the control volume.
- Obtain velocity from MELCOR-H2 calculations and calculate *Re* using viscosity in the previous step.
- Calculate thermal diffusivity, α, and use that to calculate *Pr*.
- Calculate *Nu* using *Re* and *Pr*.
- Calculate heat transfer coefficient using *Nu* and k_{He}.
- Calculate *Fo*.
- Calculate Biot number as function of *Nu* and k_{fuel}.
- Obtain values of C_1 and ζ_1 as a function of the Biot number from tabular functions.
- Calculate dimensionless temperatures $\theta_\circ^*$ and θ^*.
- Calculate surface temperature of the fuel.

In other accident scenarios, where there is a potential for air entering the reactor vessel, some modifications are required to the method. The possibility of air, consisting mostly of nitrogen and oxygen, existing in the reactor requires changes in calculating the properties of the fluid around each sphere.

The changes are to replace the properties of pure helium with those appropriate for the gas mixture. The first step is to calculate viscosity for each gas component in the control volume. The equation to calculate the helium viscosity as a function of temperature, Equation (2-19), can be applied to air as well. However, for air, σ, *M* and Ω_μ will be different values than the ones used for helium. The next step is to calculate the mole fractions X_He and X_{air} in each control volume. This has been done by taking the density of each gas from MELCOR-H2 and dividing by the total density in the control volume. The gas mixture viscosity can be calculated using Chapman-Enskog theory (Bird et al., 1960) using the viscosity of each gas at certain temperature.

$$\mu_{mix} = \sum_{i=1}^{n} \frac{x_i \mu_i}{\sum_{j=1}^{n} x_i \Phi_{ij}} \qquad (2\text{-}19)$$

in which ϕ_{ij} is defined as:

$$\phi_{ij}=\frac{1}{\sqrt{8}}\left(1+\frac{M_i}{M_j}\right)^{-\frac{1}{2}}\left[1+\left(\frac{\mu_i}{\mu_j}\right)^{\frac{1}{2}}\left(\frac{M_j}{M_i}\right)^{\frac{1}{4}}\right]^2 \tag{2-20}$$

where *n* is the number of chemical species in the mixture, x_i and *xj* are mole fractions of species *i* and *j*, and μ_i and μ_j are the viscosities of species *i* and *j* at the control volume temperature. M_i and *Mj* are the corresponding molecular weights of the gases. For the purpose of calculating the Biot number for the gas mixture, thermal conductivity for the gas mixture needs to be calculated. This is accomplished by calculating the thermal conductivity of each gas as a function of temperature using Equation (2-20) from Chapman-Enskog theory (Bird et al., 1960).

$$k=1.9891\text{-}2\frac{\sqrt{T/M}}{\sigma^2\Omega_k} \tag{2-21}$$

where k is $\frac{cal}{s\quad m\quad K}$, σ in Å and $\Omega_k = \Omega_\mu$.

The thermal conductivity for gas mixtures can be approximated in a similar fashion to as for the viscosity of mixtures (Bird et al., 1960).

$$k_{mix}=\sum_{i=1}^{n}\frac{x_i k_i}{\sum_{j=1}^{n} x_i \Phi_{ij}} \tag{2-22}$$

where ϕ_{ij} is obtained from Equation (2-20).

The kinematic viscosity for the mixture can then be calculated using μ_{mix}.

$$\nu=\frac{\mu_{mix}}{\rho} \tag{2-23}$$

Unlike viscosity and thermal conductivity, specific heat of a gas mixture can be weighted proportionally to the mole fraction of each gas component according to Equation (2-24).

$$C_{p_{mix}}=\sum_{i=1}^{n} Cp_i x_i \tag{2-24}$$

Thermal diffusivity of the gas mixture can be calculated using the mixture thermal conductivity and the mixture specific heat:

$$\alpha = \frac{k_{mix}}{\rho C_{p_{mix}}} \tag{2-25}$$

The *Pr*, *Nu*, and *Re* numbers are calculated in the same manner explained in the previous section with the new gas mixture properties that are calculated in this section.

Another change that is required for transient calculation is the implementation of a free convection formulation to calculate *Nu*. This change is currently not implemented in the control function routines made for this calculation. The difference in the above calculation would be use of *Gr* instead of *Re* to calculate the *Nu* (Gauntt, 2005). For free convection, *Nu* will be calculated as in Equation (2-26).

$$Nu = 2.0 + 0.6 Re^{1/2} Gr^{1/3} \tag{2-26}$$

The Grashof Number, *Gr*, for a sphere is defined below.

$$Gr = \frac{g\beta\left(T_s - T_\infty\right)D^3}{\nu} \tag{2-27}$$

β is the thermal expansion coefficient and can be obtained for ideal gases using Equation (2-28) from Incropera and DeWitt (2002).

$$\beta = -\frac{1}{\rho}\left(\frac{\partial \rho}{\partial T}\right) = -\frac{1}{\rho}\frac{P}{RT^2} = \frac{1}{T} \tag{2-28}$$

Flow conditions around fuel pebbles changes dramatically at the beginning of an accident event. One of the important accident scenarios is a depressurized loss of forced cooling (DLOFC). In this event, primary coolant is lost due to a break. This is coupled with a quick depressurization of the system. The Biot number for this transient is less than the 0.1 limit (Figure 2-18).

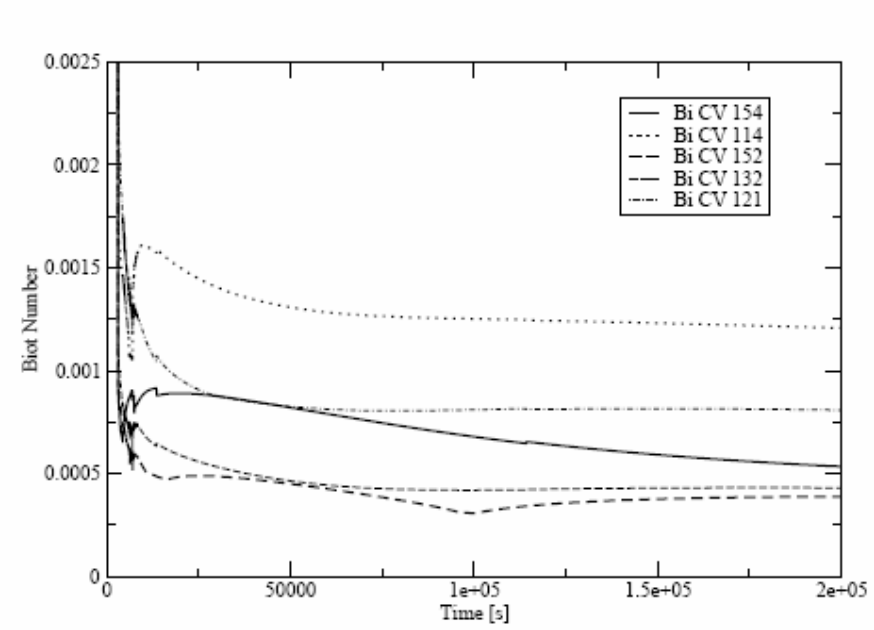

Figure 2-18. Biot number during DLOFC.

Particulate debris temperatures during the transient from MELCOR's calculation are in very good agreement overall with the fuel temperatures obtained from this numerical method. For temperatures that MELCOR-H2 is believed to have overpredicted during the normal operation, MELCOR's temperatures decreased rapidly at the transient onset and matched later on with the calculated temperatures. Figure 2-19 shows the fuel temperature comparison during DLOFC.

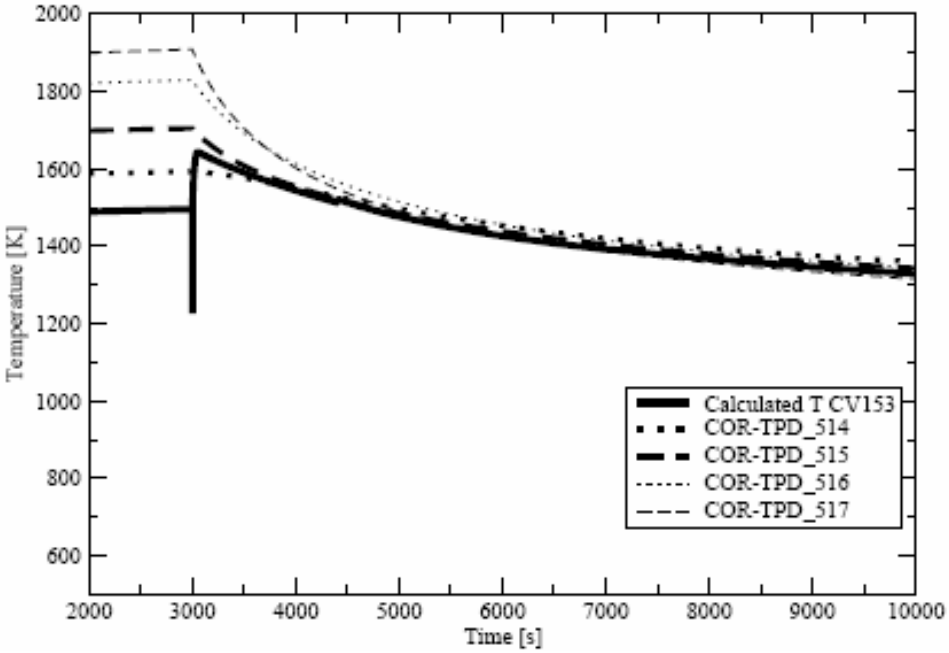

Figure 2-19. Core cell temperatures in CV 153 during DLOFC accident.

2.3.1.4 Recommendations for Radial Fuel Temperature Calculations

The necessity of extending MELCOR-H2 capabilities to include the radial pebble temperature distribution was demonstrated. Two methods for predicting the fuel pebble temperature distribution were developed and implemented via Control Functions. While both methods were largely successful in achieving their goals, implementation of a radial temperature distribution model into the MELCOR-H2 source code is recommended.

Since there are 20 control volumes in the core region, the Control Function methods had to be input 20 times, resulting in an excessive amount of input. Direct code implementation will also allow the related heat transfer subroutines to call upon the pebble center point and surface temperatures for more accurate simulations.

The first solution method, which evaluates pebble temperatures under steady state conditions, shows appropriate behavior with some overprediction of the fuel temperatures in a few control volumes. Limitations particular to this model are:

- Radiative heat transfer is not evaluated.
- Contact between the pebbles is not considered. Heat removal is by convection and not by conduction among pebbles.
- The thermal conductivity is assumed to be constant throughout a sphere.
- The model is not valid at the exact center point location. A radial location very close to the center point must be chosen.
- Heat generation in a fueled pebble is assumed to be generated uniformly throughout the pebble. However, there are no fuel microspheres in the outer coatings of the pebbles.

The second method is based on an approximate numerical solution for the heat equation in spherical coordinates under transient conditions. The model is able to accommodate any mixture of coolant gases. The numerical solution procedure showed better temperature prediction and overall behavior with no temperatures reported beyond the failure limit during steady state operation.

- A heat generation term has not been added to this model.
- Radiative heat transfer is not evaluated.
- Testing is needed on the model to confirm whether it can accommodate scenarios in which the pebbles are submitted to sudden changes in conditions in short time periods.

The methods acquire information from MELCOR-H2 about the fluid conditions in each control volume around the pebbles. This limits the calculation to one radial temperature distribution per control volume. As a result, all pebbles in each control volume will be assumed to have identical temperature distributions.

Limitations imposed by MELCOR-H2 include:

- All pebbles are assumed to generate the same amount of power (Equation (2-4)).
- The power distribution imposed on the core region cannot change with time.

2.3.2 Investigation of Fuel Temperature Overprediction

Other issues were investigated as continuation of the PBMR deck submitted in September 2006. PBMR calculations in FY06 had been showing an overprediction of fueled pebble temperatures.

The first cause for the overprediction was a lack of conservation of energy. The calculations with a large roundoff error had been run with a single-precision (32-bit) version of MELCOR 1.8.5. This problem was eliminated by the use of a MELCOR 1.8.5 executable with double-precision (64-bit) accuracy.

A sampling of the FY06 particulate debris temperature distributions from a steady state calculation with the double-precision executable are shown in Figures 2-20 through 2-24. Temperatures in the rings occupied by fuel spheres consistently have higher particulate debris temperatures than those full or partially full of graphite spheres. The temperature distribution in fueled rings varies far more broadly than the distributions in partially fuel-filled or graphite-filled rings. The maximum temperatures predicted appear in the second axial level and third radial ring, with the highest maximum temperature of the sample group located in cell COR311.

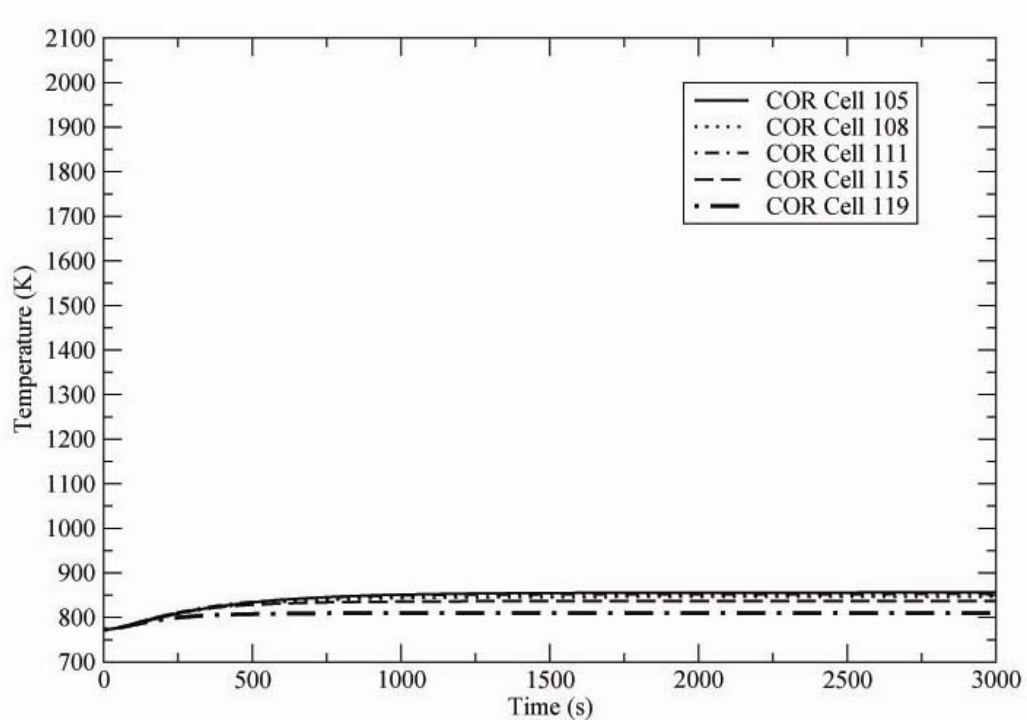

Figure 2-20. Particulate Debris Temperatures in Ring 1.

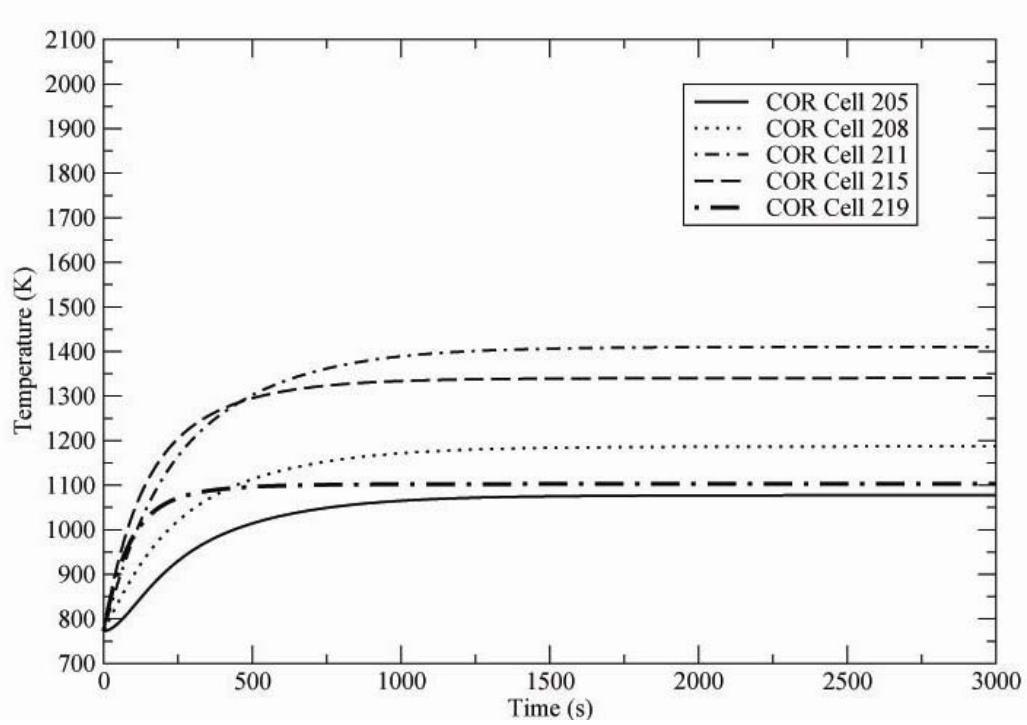

Figure 2-21. Particulate debris temperatures in Ring 2.

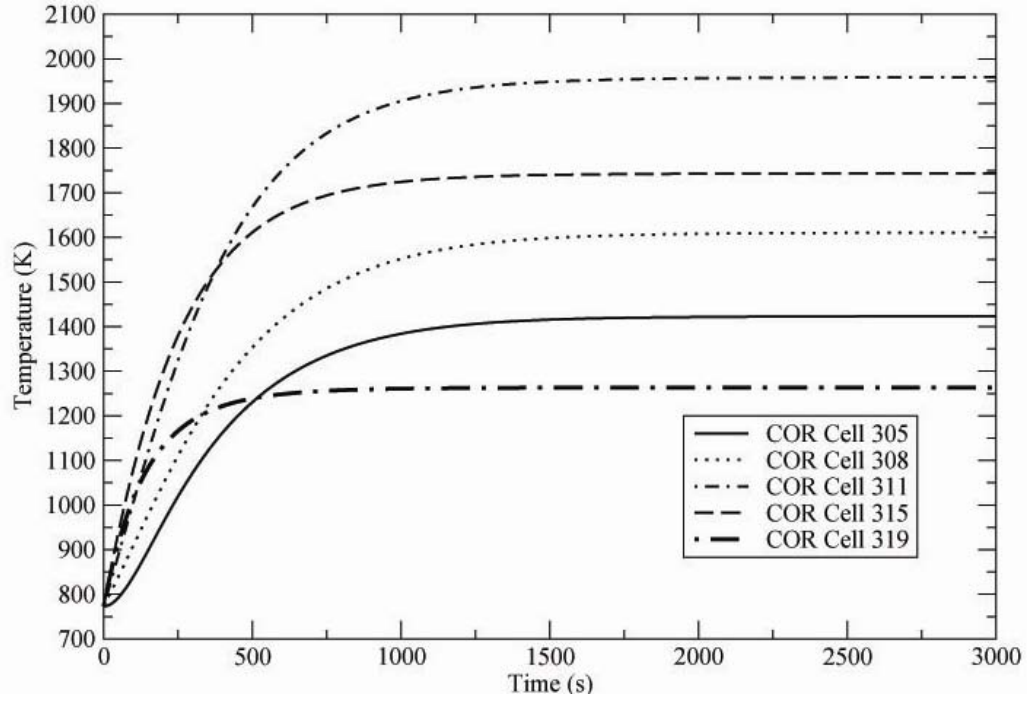

Figure 2-22. Particulate debris temperatures in Ring 3.

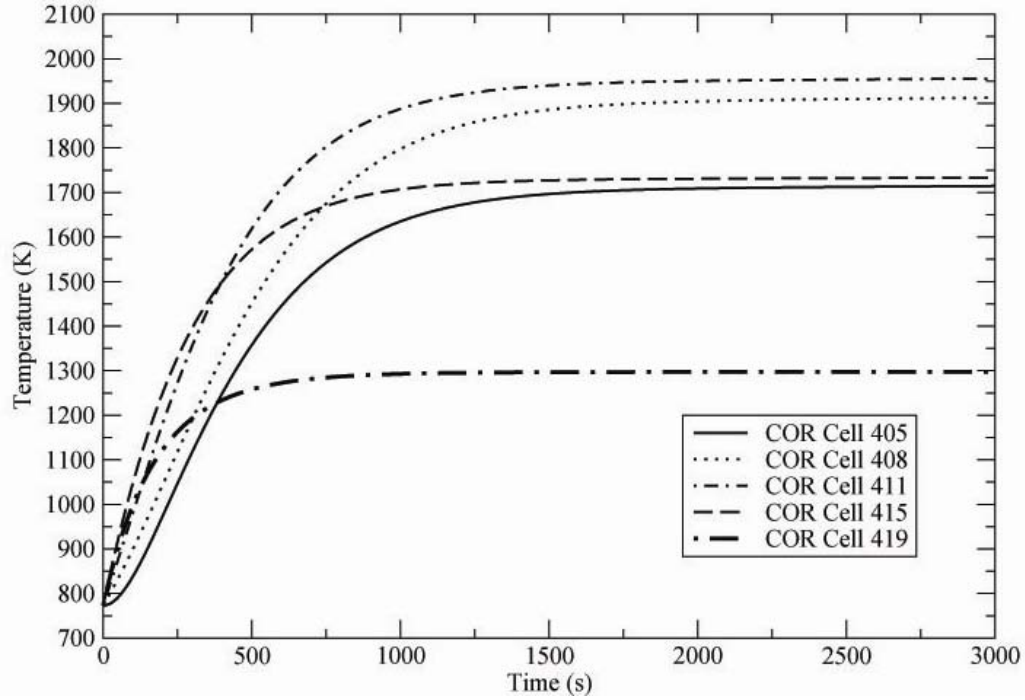

Figure 2-23. Particulate debris temperatures in Ring 4.

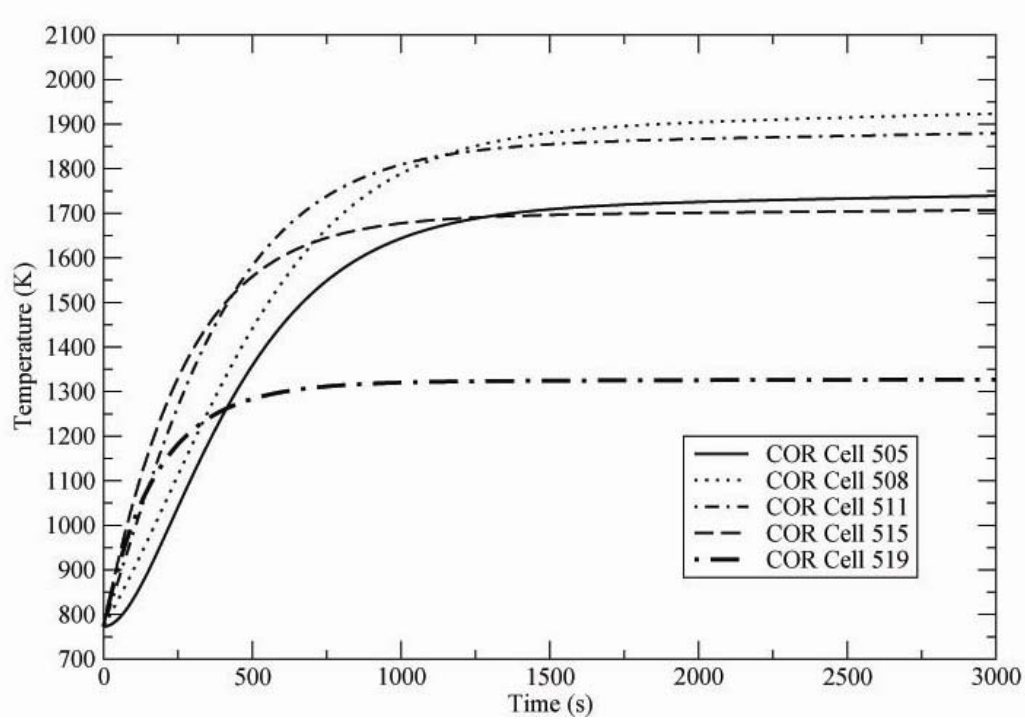

Figure 2-24. Particulate debris temperatures in Ring 5.

The maximum temperatures of the particulate debris predicted by MELCOR-H2 are higher than those predicted by Reitsma (2004), sometimes exceeding the predicted temperature values for a depressurized loss of forced convection without SCRAM by over 50 K. Reitsma's analysis showed that the maximum fuel temperature is about 1900 K. The MELCOR-H2 temperatures should be lower because the MELCOR-H2 analysis was for steady state conditions at full power. Further, the maximum allowable peak fuel temperature must be below 1600 °C to prevent TRISO fuel damage.

The second cause for overprediction of fuel pebble temperatures may be due to the current heat transfer modeling from the pebbles. The conclusion from FY06 was that the discrepancy is most likely caused by uncertainty in the properties of the particulate debris, particularly the enthalpy, and by a less-than-expected heat removal rate from the COR package to the CVH or HS packages. The local heat generation, as well as the temperature difference between the particulate debris and the coolant in the attached CVH cell, dictates the temperature of the fuel pebbles. Hogan (2006) discusses the actual coolant flow paths as helium passes through a packed bed and the potential for non-uniform heat removal rates within control volumes. With the addition to MELCOR-H2 of the FY07 radial temperature distribution models, the predicted pebble surface temperatures in Rings 3, 4, and 5 will be lower and this discrepancy is expected to increase. Computational fluid dynamics (CFD) analysis may prove useful in examining the local flow paths and heat transfer rates.

Another source of possible error to be further pursued is the radiative heat transfer modeling. The reactor has been designed to lose heat passively in the outward direction from the core. A radiative heat transfer model has not yet been developed for MELCOR. Further attempts to develop such a model may focus on a more detailed nodalization of rings surrounding the core and a radiative heat transfer model that would preferentially transfer heat from the outer pebbles of Ring 5 which are "in view of" the surrounding structures. Finer division of the rings with fueled pebbles is not desired because the control volume shapes would become very tall and thin and computational time would increase.

No studies of the radiation heat transfer have been found in the literature survey to support model development or provide validation data.

2.3.3 Conversion of PBMR Deck to 1.8.6 Format

This task included conversion of the PBMR input deck to a double-precision version of MELCOR 1.8.6 that includes the MCH and IHX software. The PBMR input deck supplied by the contractor to SNL in September 2006 was updated by SNL. For the experience, attempts were made by the contractor to update the deck from 1.8.5 to 1.8.6 for use in other parts of this task.

The input deck was converted with MELCOR-H2 Input Deck Converter.xls version 1.01.02. During the conversion process, the lower head was assumed to be hemispherical and no downcomer was assumed. The molten pool model was turned off. The silver release model was left off, as is the default. The control volumes were recalculated by the program. An R*I*F statement for the new input file was added to the MELGEN file. The CORTST01 card was added to the MELCOR-H2 file. Execution was attempted with MELCOR-YP-186.exe.

The deck after it had been run through the Input Deck Converter and the diagnostic errors are included in this report.

2.3.4 Investigation of Radially Inward Flows in 1.8.5 Model

The radial coolant velocities for an FY06 steady state calculation without core power are shown for core Levels 1 and 4 in Figures 2-25 and 2-26. Levels 2 and 3 show zero velocities for the cross flows and are not plotted. The figures show nonzero cross flows present radially outward for Level 1 and radially inward for Level 4. Cases with the nominal 268 MWth power reveal larger cross flows inward due to coolant heating and expansion in the outer rings.

This flow is caused by the differing boundary conditions and geometries imposed at the top and bottom of the core. The circulation pattern that develops in the calculation with the powered core causes increases in radial flow due to the nonuniform power profile present in the core input model.

The radially inward flow issue was not resolved. The same conclusion was reached as in the previous year, namely that the small radial flow patterns observed with and without a heated core have a nodalization dependency. Such flow patterns are not an issue for the prismatic gas-cooled reactor modeling because the coolant flow within the core is restricted to one-dimensional flow through vertical coolant channels.

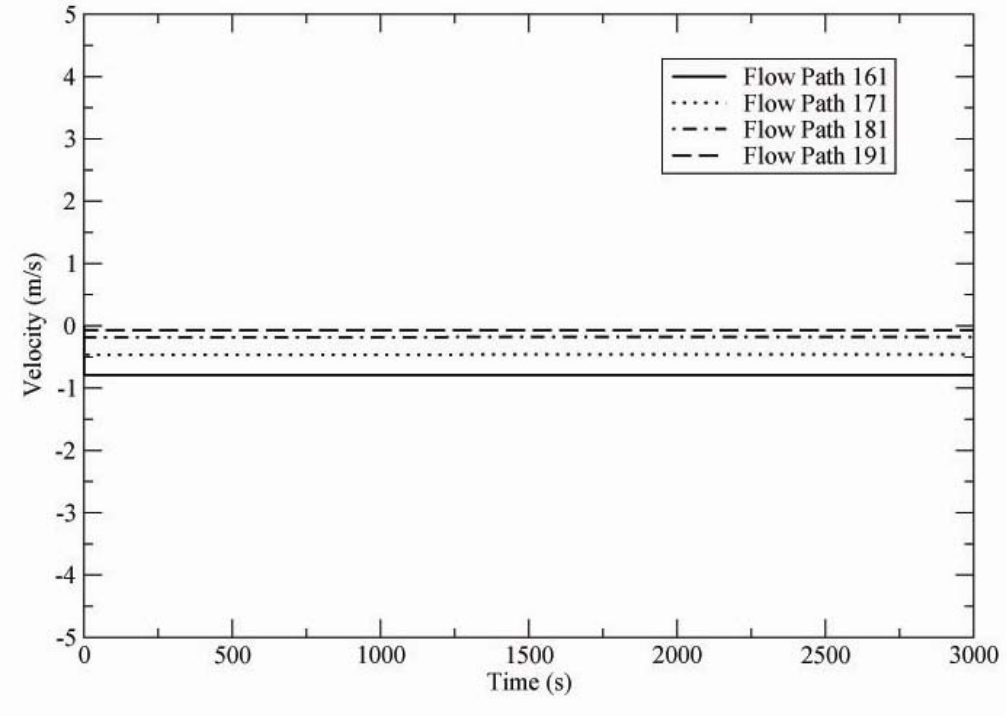

Figure 2-25. Radial coolant velocities of Level 1, no core power.

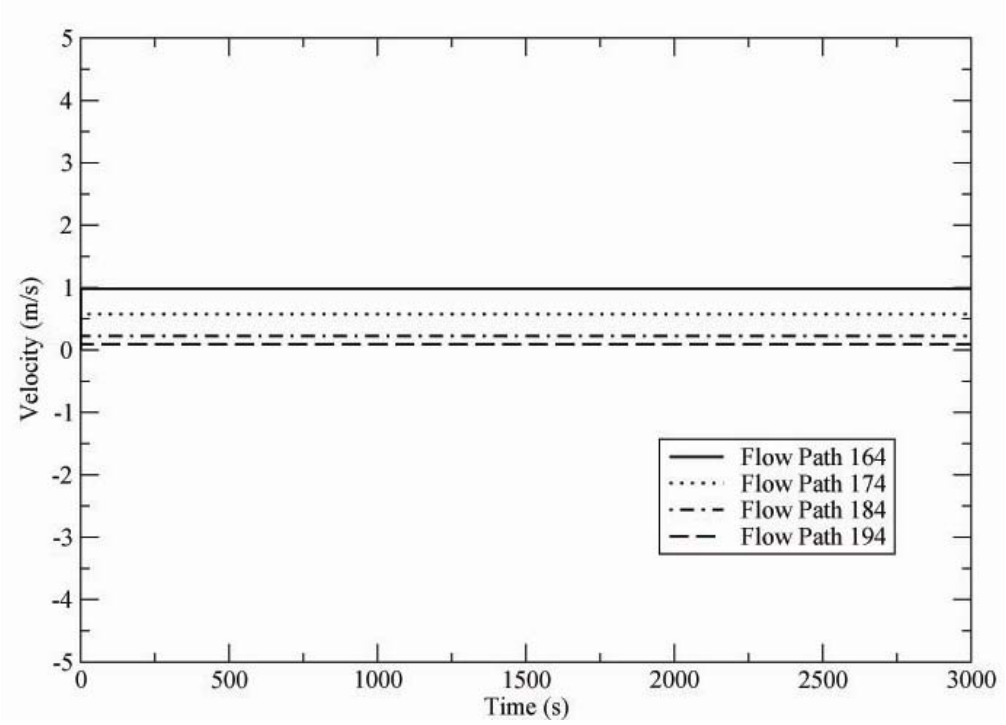

Figure 2-26. Radial coolant velocities of Level 4, no core power.

2.3.5 Radiative Heat Transfer Modeling for the Pebble Bed Reactor

Methods for modeling the radiation heat transfer were considered. Discussions concluded that the view factors for radiative heat transfer are dependent on the control volume and core cell sizes and the local pebble packing fraction. A finer radial division of the heated rings and additional rings outside of the core may be necessary to obtain the correct radiative heat transfer rates. Data for comparison against estimated view factors were not obtained in a literature search.

2.4 Task 2: High-temperature Prismatic Reactor Input Deck Development

2.4.1 Literature Review on Prismatic Reactors

A literature survey was performed to obtain data for development of a MELCOR-H2 input deck for a prismatic reactor. Because the NGNP based on the General Atomics GT-MHR design was chosen as the reference design for the MELCOR-H2 input deck (see next subsection), the most useful references for the GT-MHR and NGNP designs are highlighted below.

A document with general information on the INL "point reactor design" was obtained from a web search. The INL point design document states that the NGNP VHTR design is based on the General Atomics GT-MHR design. The point design report gives credit to General Atomics for providing design information and lists the original General Atomics reports, several of which are not available to the subcontractor. Therefore, much of the data in the MELCOR-H2 input deck

is General Atomics data that has been reported by INL in the Point Design Report (INEEL, 2003).

Most data for the GT-MHR are from designs with a lower outlet gas temperature than the VHTR, about 850 °C, implying that some design modifications may be necessary. Per the technical monitor's suggestion, a VHTR is being modeled with a coolant outlet temperature of 850 °C and 600 MWth.

For data that are missing from the Point Design Report, values from the 450 MWth GT-MHR design are being used or values are estimated with engineering judgment. The literature survey has provided data on the 450 MWth design in sufficient detail to develop much of a MELCOR-H2 input deck (ABB/Combustion Engineering et al., 1994). The current power rating of modular prismatic reactors appears to be around 600 MWth; however, minimal geometric data are available. The only data from the two designs available for comparison are the reactor vessel dimensions, which are fairly similar. The core design was apparently modified to provide for higher power densities. Another key issue to investigate is the ability to provide passive cooling with the higher power rating.

The 450 MWth design is noted to have a lower coolant outlet temperature (850 °C) than is desirable for a high-efficiency VHTR. Two methods for raising the coolant outlet temperature are reduction of the bypass coolant flow from 20% to 10% and inlet orificing for better control of the inlet coolant flow distribution (page 25 of the INEEL Point Design Report). The MELCOR-H2 input deck considers the reduction of bypass flow to achieve higher temperatures. Information on the inlet orificing was not found in public documents.

A reference from SNL provides a brief description of a Very High Temperature Gas Cooled Reactor that represents an "advanced, next generation GT-MHR" (Parma et al., 2003). The exit temperature is 1100 °C. This design may serve as a starting point for the modeling, although detailed data are not provided.

Additional data searches have led to General Atomics documents, such as NERI reports, which describe more of the overall plant concept for electricity generation and lack sufficient data for MELCOR-H2 input deck development. International Atomic Energy Agency (IAEA) documents provide more details on gas-cooled reactor designs, but the designs are generally of lower temperature reactors (coolant outlet temperature is less than 900 °C).

Data on the design of prismatic fuel blocks were referenced from Del Cul et al. (2002).

Regarding modeling techniques, a RELAP5-3D/ATHENA input model description for the VHTR was presented by Bayless (2003). This model employs a much simpler nodalization has been used by MELCOR-H2 for the PBMR (Figure 2-27). The code calculations were benchmarked against calculations of the GT-MHR by General Atomics for high- and low-pressure conduction cooldown and loss of flow scenarios. The comparisons were said to be reasonable. If details of these calculations can be obtained, they may serve as benchmarking data for the current MELCOR-H2 development.

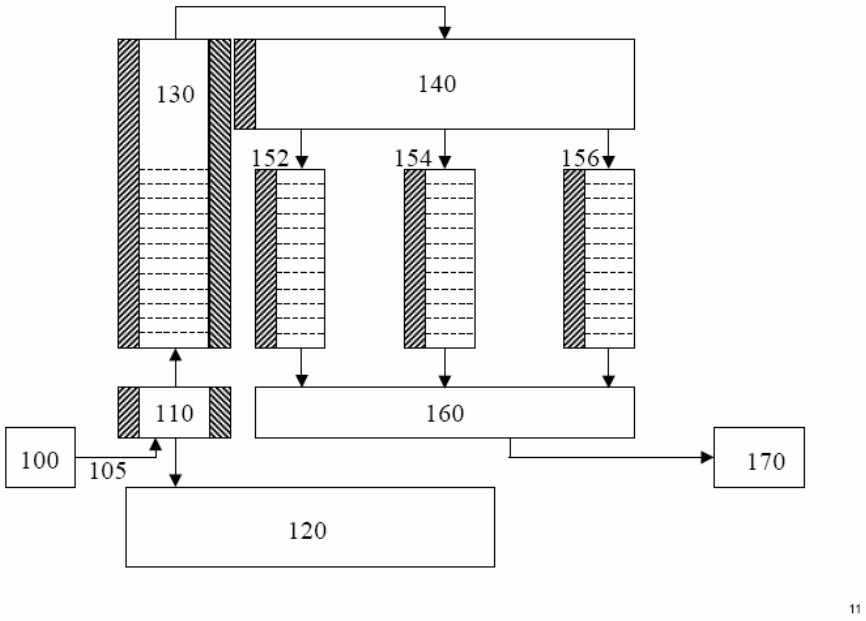

Figure 2-27. RELAP5-3D/ATHENA nodalization of the VHTR vessel.

Modeling techniques for conduction cool-down accident analyses with RELAP5-3D/ATHENA are documented in Section 4.2 of the INEEL Point Design Report. These techniques are providing a frame of reference for the current modeling effort, although the MELCOR-H2 model will be more detailed. Further, data are provided for model benchmarking and will be used when MELCOR-H2 analysis of the VHTR commences. GT-MHR reported data used to benchmark the RELAP5-3D/ATHENA model consisted of:

- RCCS power,
- RCCS flow rate,
- RCCS air outlet temperature,
- Reactor vessel outside temperature,
- Peak RCCS structure temperature, and
- Peak containment concrete temperature.

Additional references that were not used in input deck development but provided general information are listed below.

- Cocheme, 2004
- Davis et al., 2005
- Davis et al., 2004
- Davis et al., 2003
- Gelbard, 2002.
- Haque et al., 2004.
- INEEL, 2004b
- INEEL, 2004a
- Kunitomi et al., 2004.

- LaBar et al., 2003.
- Lee, et al., 2007.
- Morris et al., 2004.
- Oh, 2004.
- Oh, 2005.
- Wu and Yu, 2007.

2.4.2 Selection of Reference Gen IV Reactor Design

The NGNP to be designed and constructed by INL will most likely be for hydrogen generation and will be of a VHTR design. These reactors are intended to supply gas at an outlet temperature as high as 1000 °C (DOE, 2004). Both prismatic core designs and pebble bed designs are candidates for the NGNP, although recent momentum appears to be in favor of the prismatic design.

The NGNP prismatic design published by INL (INL, 2003) was chosen as the reference design for this input deck development, to complement the pebble bed input deck modeled in FY05 and FY06. The gas-cooled reactor is planned to be constructed on the INL site.

2.4.3 Description of the Prismatic Reactor Design

As a candidate design for the U.S. NGNP, a variation of the General Atomics GT-MHR is the referenced high-temperature gas-cooled reactor (HTGR) for the current work. The distinguishing feature between the GT-MHR and other HTGR designs is the use of a prismatic block core instead of a pebble bed core. The same TRISO fuel as for the pebble bed reactors will be made into pellets and stacked vertically in fuel channels.

The main differences between the GT-MHR and the NGNP prismatic reactor will be in the materials needed for higher temperatures and in the details of the thermal hydraulics and core neutronics. Figure 2-28 from the INL Point Design Report illustrates the reactor system (INL, 2003) and Table 2-1 lists the primary operating parameters.

The prismatic NGNP core will be an annular design with an inner and an outer neutron reflector. Approximately one third of the hexagonal blocks will be arranged in an annular core and the other two thirds will comprise the inner and outer reflectors. The target outlet temperature for the coolant is 1000 °C. To increase the power level from the General Atomics GT-MHR design without increasing peak fuel temperatures, the bypass flow fraction is reduced from 20% to 10% and the inlet flow distribution is controlled.

Passive safety is accomplished by conducting heat radially outward through the core and pressure vessel and removing heat by radiative heat transfer to air-cooled panels in the reactor cavity cooling system.

The core description in Figure 2-29 and Table 2-2 is identical to that of the General Atomics GT-MHR. Axial and column-averaged power profiles assumed for the point design analysis and herein are shown in Figures 2-30 and 2-31, respectively. The column-averaged power factures were used to approximate the ring-average radial power distribution for MELCOR-H2 analysis.

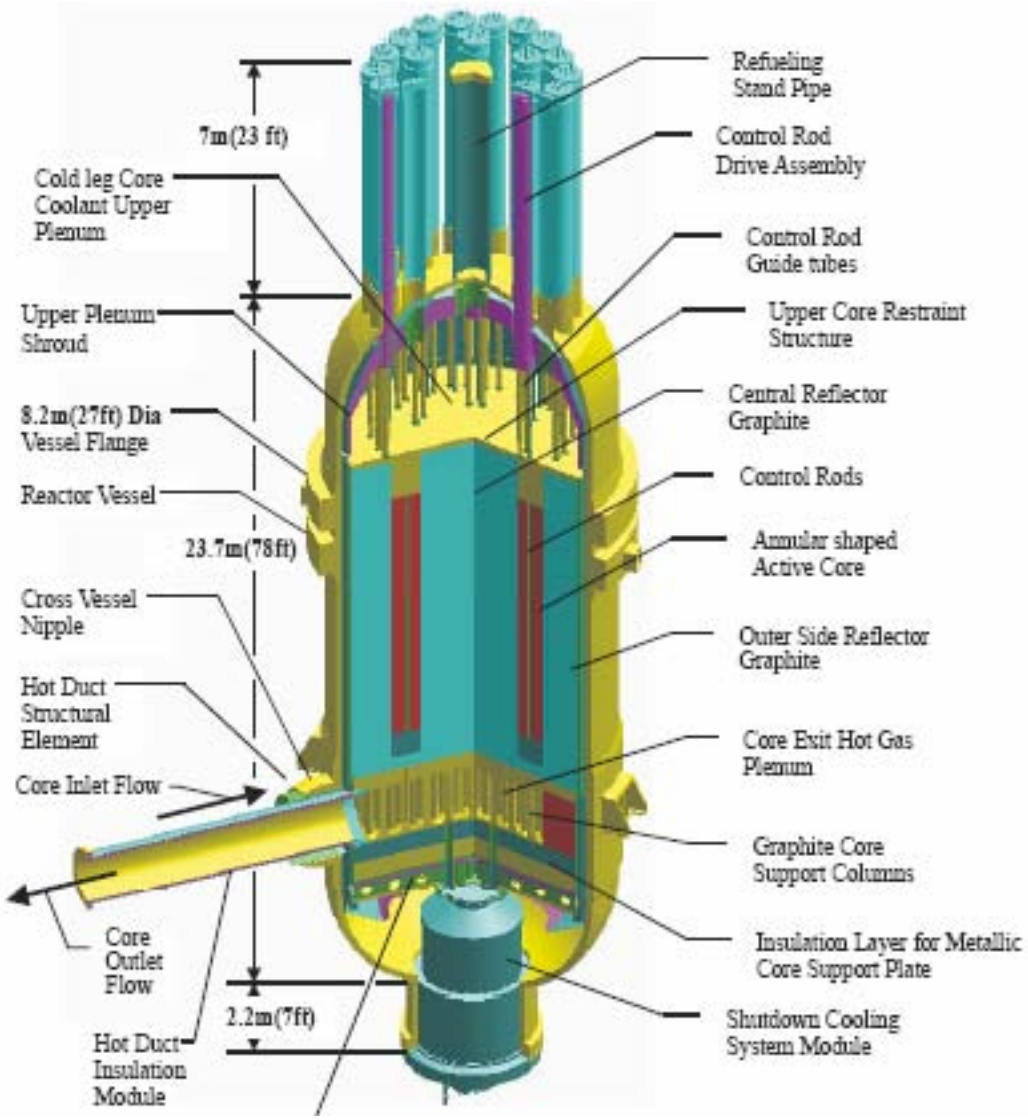

Figure 2-28. NGNP prismatic reactor system illustration.

Table 2-1. Primary Operating Parameters (INL, 2003)

Condition or Feature	Fort St. Vrain HTGR	GT-MHR	NGNP
Power Output [MW(t)]	841	600	600 to 800 (depends on core height)
Average power density (w/cm^3)	6.3	6.5	6.5
Coolant @ Pressure (MPa / psia)	Helium @ 4.83 / 700	Helium @ 7.12 / 1032	Helium @ 7.12 / 1032
Moderator	Graphite	Graphite	Graphite
Core Geometry	Cylindrical	Annular	Annular
Safety Design Philosophy	Active Safety Sys	Passive	Passive
Plant Design Life (Years)	30	60	60
Core outlet temperature (°C)	785	850	1000
Core inlet temperature (°C)	406	488	490
Fuel – Coated Particle	HEU-PyC/SiC Th/ ^{235}U (93% enriched)	LEU-PyC/SiC	a) LEU-PyC/SiC b) LEU-PyC/ZrC
Fuel Max Temp – Normal Operation (°C)	1260	1250	a) ~1250 (SiC coated) b) ~ 1400 (ZrC coated)
Fuel Max Temp – Emergency Conditions (°C)	Active safety system cools fuel.	1600	a) 1600 b) TBD
Fuel Element Design	Particles disbursed in carbon rods 0.5 in. dia x 1.95 in. long placed inside large graphite blocks.	Particles disbursed in carbon rods 0.5 in. dia x 1.95 in. long placed inside large graphite blocks.	Modified GT-MHR design to reduce fuel rod linear heat rate.
Control Rods	Inconel structure containing B_4C compacts.	Carbon-carbon/ Graphite Structure containing B_4C Compacts.	Carbon-carbon/ Graphite Structure containing B_4C Compacts.
Backup Reactivity Control System	B_4C pellets dropped in core	SiC coated B_4C balls dropped in core	SiC coated B_4C balls dropped in core.
Core Inlet Gas Plenum	-Metallic upper core support. -Metallic control rod guide tubes. -Ceramic fiber/metallic plate insulation. -Boronated graphite shielding.	-Carbon-carbon composite upper core support. -High-temp metallic control rod guide tubes. -Ceramic fiber/high-temp metallic plate insulation. -Boronated graphite shielding.	Modified GT-MHR design: -Carbon-carbon composite upper core support. -Carbon-carbon composite control rod guide tubes. -Ceramic fiber/hi-temp metallic plate insulation. -Boronated graphite shielding.
Core Outlet Gas Collector Plenum	Graphite structures with metal covered ceramic fiber and ceramic block insulation. Water-cooled pressure vessel liner.	Graphite structures with graphite and C/C composite insulation.	Requires some modification of the GT-MHR system with possibly more insulation.
Hot Gas Duct	Inconel plates over ceramic fiber insulation mats.	High-temp steel structure with nickel-base alloy sheets containing ceramic fiber mats.	Requires some modification of the GT-MHR system. Specifically, the cover plates may need to be a C/C composite material.
Reactor Internals structures	Medium-temp steel plate rolled into cylinder	High-temp steel sheets & plates fabricated into cylinders and plate.	The upper plenum and some of the other internals insulation material may need to be changed.
SCS heat exchanger entrance structures and tubes	Inconel plates over ceramic fiber insulation mats.	Nickel base alloy sheets containing ceramic fiber mats. High-temp steel tubes.	Requires high temperature insulation.

Table 2-1. Primary Operating Parameters (INL, 2003) (Continued)

Condition or Feature	Fort St. Vrain HTGR	GT-MHR	NGNP
Primary Coolant Gas Circulator	Axial flow-Steam turbine drive: -9550 RPM -Press Rise = 0.097 Mpa/ 14 psi -Inlet temp = 395 °C/ 742 °F	Single shaft Axial flow Gas Turbine with 2 stage axial flow inter-cooled compressor: -Press Rise = 4.69 MPa/ 680 psi -Inlet temp = 26 °C/ 79 °F -Outlet temp = 110 °C/ 230 °F	Extend GT-MHR turbo-machine to 1000 °C turbine inlet temperature or, for hydrogen production, a motor driven axial flow circulator at core inlet conditions (in the vessel with the IHX)
Reactor Vessel	Pre-stressed Concrete Reactor Vessel Designed to ASME Code Div 2 for gas reactors.	2 ¼ CrMo, ASME Code Section III, Div 1 -Normal op Temp: 440 °C -Accident max temp: 500 °C for 400 hr, 540 °C for 50 hr	9Cr MoVNb or 2 ¼ CrMo, ASME Code Section III, Div 1, -Normal op Temp: 490 °C -Accident max temp: 560 °C for 400 hr (initial approximations).
Cross Vessel	NA	2 ¼ CrMo, ASME Code Section III, Div 1, (alternate material: 9CrMoVNb), -Normal op temp: 440 °C -Accident max temp: 440 °C	9CrMoVNb or 2 ¼ CrMo, ASME Code Section III, Div 1 -Normal op temp: 490 °C -Accident max temp: 500 °C (Initial approximations)
Power Conversion System Vessel	NA	2 ¼ CrMo, ASME Code Section III, Div 1, -Normal op temp: 150 °C -Accident max temp: 250 °C	9CrMoVNb or 2 ¼ CrMo, ASME Code Section III, Div 1, -Normal op Temp: 150 °C -Accident max temp: 300 °C

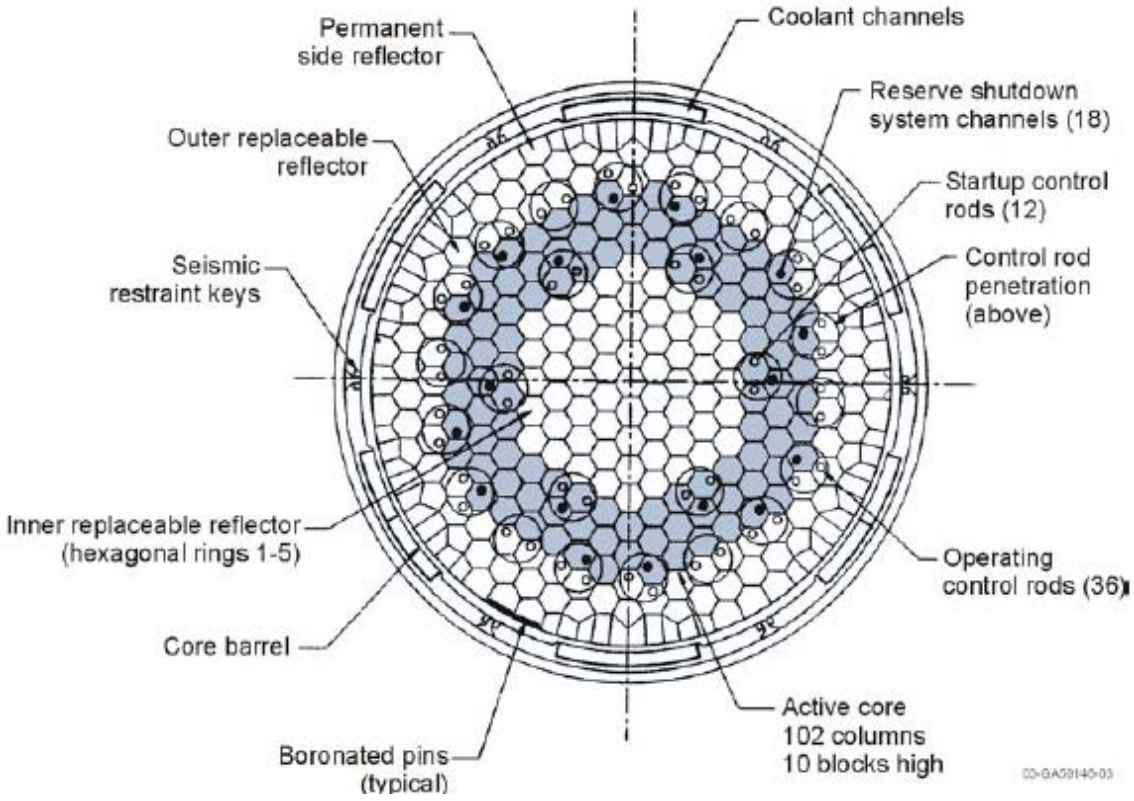

Figure 2-29. NGNP and GT-MHR cores.

Table 2-2. NGNP and GT-MHR Core Characteristics

	GT-MHR	NGNP
Power ($MW_{(th)}$)	550-600	600-800
Average Power Density (W/cc)	6.5	6.5
Inlet Temp (°C)	488	490
Outlet Temp (°C)	850	1,000
Temp Differential (°C)	362	510
Coolant Flow Direction	Downward	Downward
Core Geometry	Annular	Annular
Inner Reflector Eff. Radius (m)	1.48	1.48
Active Core Eff. Radius (m)	2.41	2.41
Outer Reflector Eff. Radius (m)	3.33	3.33
Number of Fuel Columns	102	102
Number of Fuel Blocks per column	10	10 (600 MWt version)
Active Core Volume (m^3)	90.767	90.767 (600 MWt version)
Active Core Height (m)	7.93	7.93 (600 MWt version)
Fuel Element Geometry	Fort St. Vrain	Fort St. Vrain
Fuel Particle(s)	Fissile and Fertile	Fissile only
Enrichment	19.9 wt% U-235 0.711 wt% U-235	10.36 wt% U-235 (initial core) 15.5 wt% U-235 (re-load cores)
Capacity Factor	84%	>90%
Power Cycle Length	14-15.7 months	18-24 months

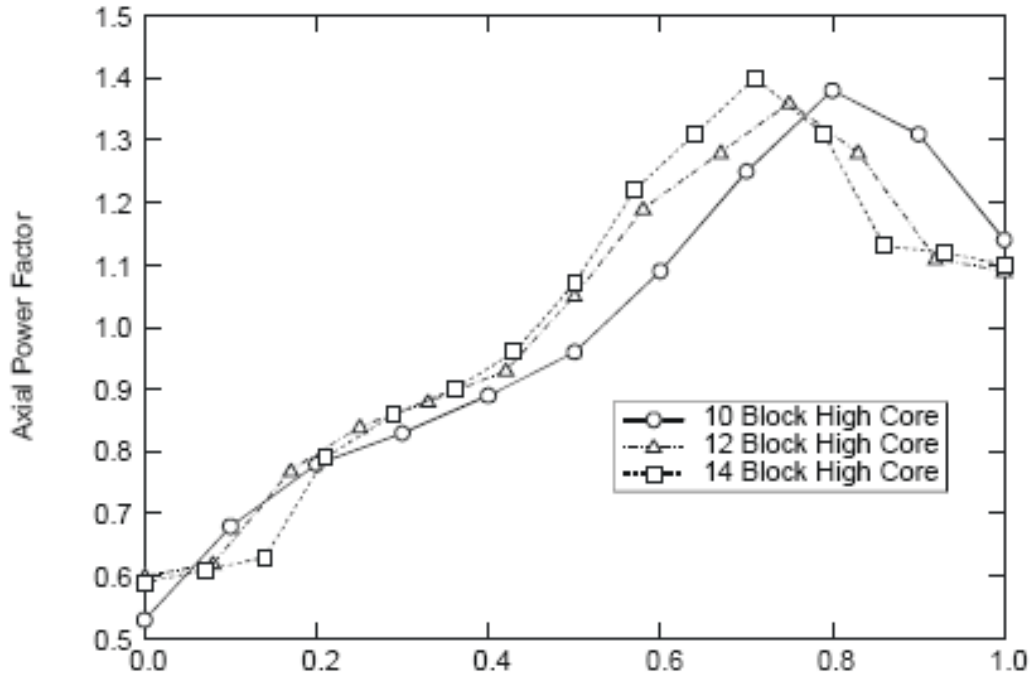

Figure 2-30. Axial power factors.

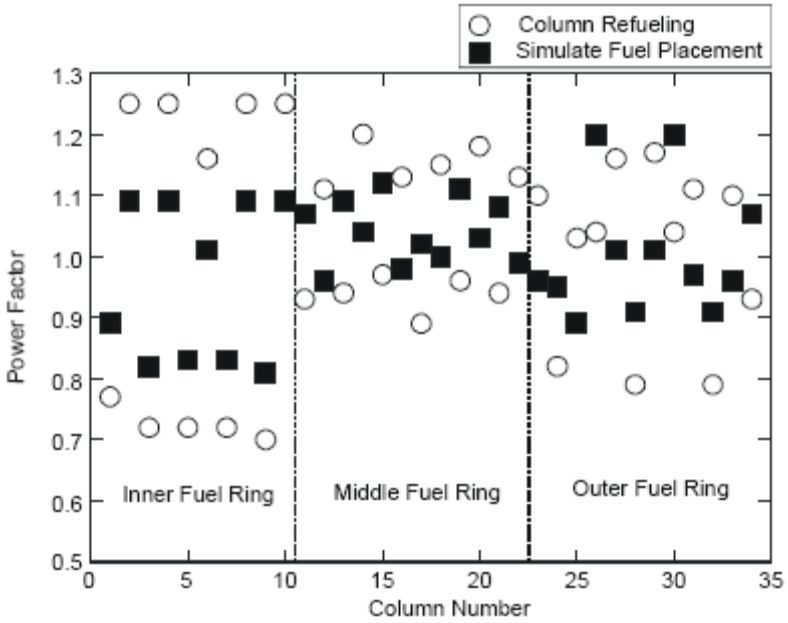

Figure 2-31. Column-averaged power factors.

2.4.4 Modeling Challenges for Current Analysis Tools

Tools for modeling of HTGRs have been undergoing development for over 25 years. The GRSAC code (Ball, 2002) boasts the longest history among gas-cooled reactor codes in the United States, having been developed at Oak Ridge National Laboratories for evaluation of the earlier generation HTGRs. While the GRSAC experience is extensive, the numerical architecture of the code has not been modernized. It is currently not capable of evaluating rapid reactor transients and does not model the balance of plant. Due to these and other code limitations, discussions at the NRC meetings in 2002 on PBMR analysis led to the suggestion of using GRSAC in combination with a light water reactor (LWR) code such as MELCOR-H2 that would be modified for HTGR analysis. Because Exelon withdrew its interest in submitting the PBMR design to the NRC for design certification, the NRC effort to prepare for a design certification review was discontinued.

Interest in developing more sophisticated tools for PBMR analysis has been kindled recently by the possibility that the NGNP will be a VHTR for hydrogen production. As described in the FY06 annual progress report, several efforts worldwide are ongoing to develop new codes or to extend the capabilities of LWR codes for HTGR analysis. A review revealed that the codes are all in the developmental stage and have not been validated.

Code development effort could be reduced by taking advantage of the basic modeling features and numerical architectures in the current fleet of light water reactor safety codes. Several efforts are at the beginning stages to modify LWR codes for HTGR analysis. Particular challenges that are raised for LWR codes include the following:

a. Redefinition of the core materials or adding to the available core materials (graphite, etc.)
b. Geometry of graphite blocks (hexagonal)

c. Material properties and thermodynamic properties at higher operating temperatures
d. Radiative heat transfer within the core and to the passive reactor cavity cooling system
e. Capturing local fluid dynamics and heat transfer such as thermal “hot streaks” in the lower plenum and hot duct exit
f. Temporally varying power distribution
g. Severe accident models for phenomena peculiar to HTGRs (graphite oxidation, containment gas diffusion in pressure vessel)
h. Events relevant to HTGRs (loss of forced circulation for helium, air ingression)

2.4.5 Input Description for Simplified Model

The initial MELCOR-H2 deck was built as a simplified model of the coolant through an annular core region and the inner and outer graphite reflectors. The purpose of this deck was to demonstrate MELCOR’s ability to model passive cooling by thermal conduction through the graphite reflectors.

Control volumes were set up for the gas coolant flow and the reflectors were modeled by heat structures, as seen in Figure 2-32. “CV” and “HS” designate control volumes and heat structures, respectively. Helium enters the system via a mass and enthalpy source at CV 160. The flow is upward to an upper plenum volume, and then downward across an upper plenum plate, where it is distributed to three axial fuel rings divided into seven axial levels. Among these seven axial levels, the top most is an upper reflector, and the bottom most is a lower reflector. The five in between are active fuel zones. Flow exiting the core flows into a core exit plenum (CV 054), and out of the system through a mass and enthalpy sink at CV 200.

The core region is composed of three radial regions: an inner reflector region, an active core, and an outer reflector region. These correspond to heat structure HS32, Rings 1-3 and HS33, respectively. This deck does not contain COR package input.

The upper reflector is located above the active core and the outer reflector, and the lower reflector is below them. Since the MELCOR-H2 code does not allow the modeling of an HS adjacent to another HS, the upper reflector region that is located above the active core and the lower reflector region that is located beneath the active core are modeled as control volumes. The upper reflector region that is located above the side reflector and the lower reflector region that is located beneath the side reflector are modeled as heat structures.

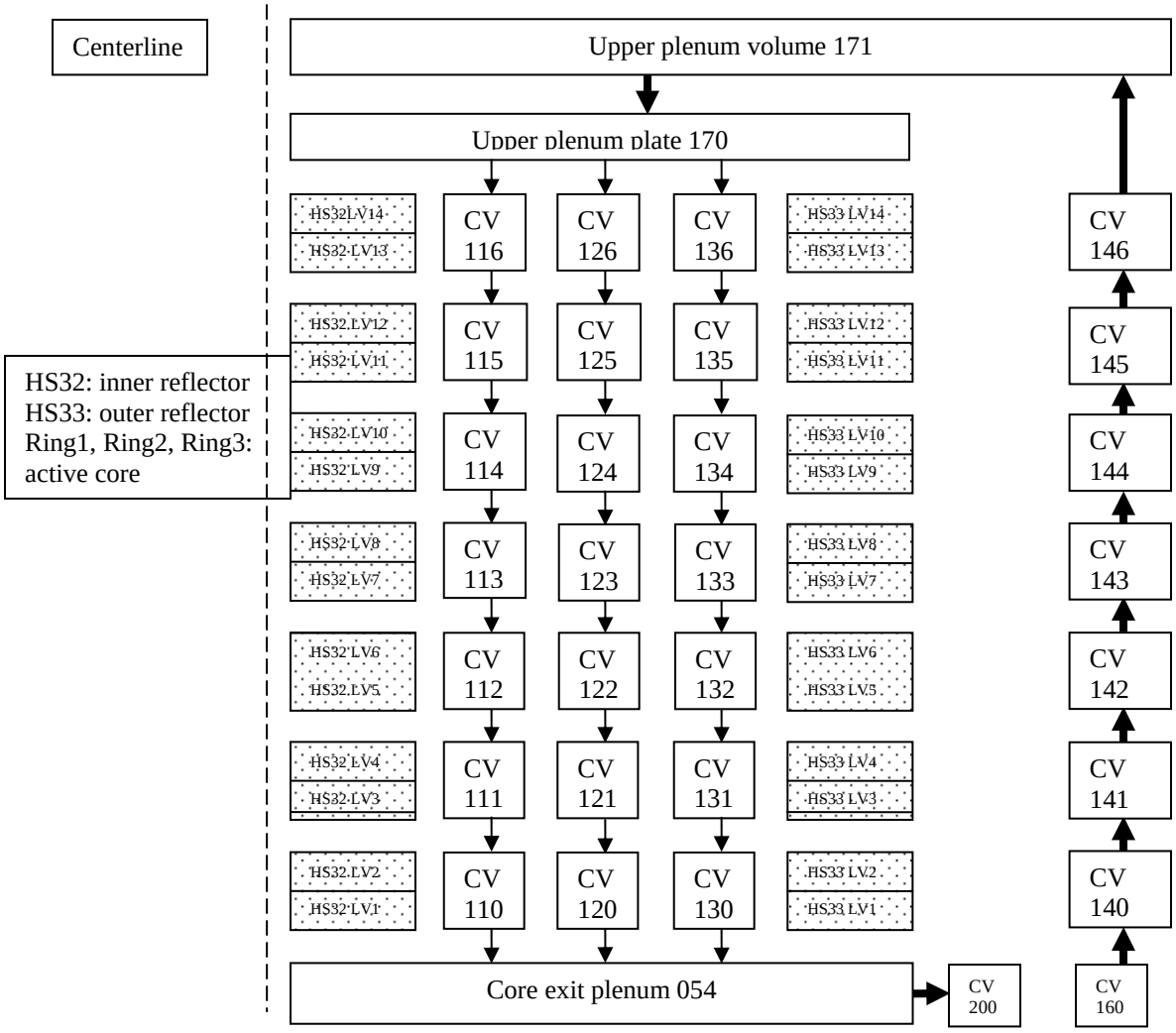

Figure 2-32. Nodalization of simplified MELCOR-H2 prismatic NGNP model.

2.4.6 Heat Removal through Graphite Reflector Heat Structures

Demonstration calculations showed that heat flowed from the hotter core region into the inner graphite reflector and towards the reactor boundary through the outer reflector. The heat from the core region is calculated to transfer through the heat structures by conduction heat transfer, as evidenced by the temperature transients throughout the inner and outer reflectors. The pressure drop in the active core and mass flow rate correspond well with the NGNP design data provided by the Point Reactor Design Report.

The initial temperature in the reflector region is 764 K while the initial temperature of the coolant is 1200 K (Figure 2-33). The square data points represent the temperature profile of the innermost temperature node of the reflector region, which is located next to the active core, while the dashes show the temperature profile of the outermost temperature node of the reflector adjacent to the core barrel. There are altogether four temperature nodes evenly located along the radius of the outer reflector region. This figure shows the passive heat removal feature of the outer reflectors.

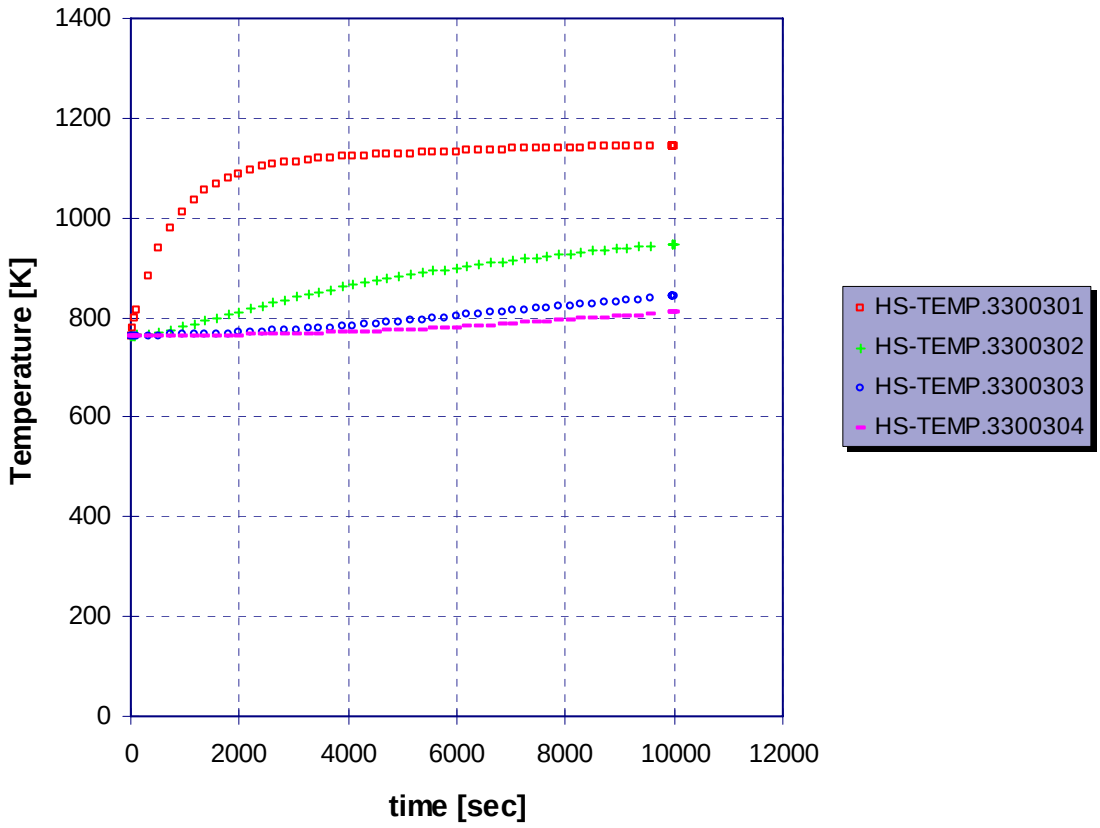

Figure 2-33. Conduction heat transfer in the outer reflector.

2.4.7 Input Description for Detailed Model

In discussion with the developers, the subcontractor found that the simplified deck could not be used to faithfully model the core and various components in and around the core region. The modeling strategy was modified to represent the graphite fuel elements and reflectors with core cells. The hexagonal graphite blocks are modeled as "clad." The reactor type was declared a PWR. The upper and lower reflectors also presented difficulties for the original model and had to be rewritten.

A second input deck was developed for the new modeling strategy. The control volume and heat structure input was debugged; however, difficulties were encountered with debugging of the lower head. The subcontractor's current knowledge of the 1.8.6 lower head is insufficient,

particularly with regard to modeling the bypass flows and null cells in the lower head. The debugging effort is ongoing with the focus on devising techniques to properly associate radial rings in the lower plenum of the prismatic reactor with components above the bottom of active fuel.

The nodalization for the detailed model is discussed in Table 2-3. The number of rings has been expanded to five, and additional rings may be required to accommodate the 1.8.6 lower head modeling.

Table 2-3. MELCOR-H2 Nodalization Summary

Input Component	Region Modeled
Ring 1	Inner reflector
Ring 2, 3, 4	Active core
Ring 5	Outer reflector
Ring 6	Bypass
Ring 7	Helium inlet
Core levels 1-5	Lower head hemisphere for MELCOR
Core levels 6-10	Core exit plenum
Core levels 11-12	Core plate for MELCOR
Core levels 12-15	Inner reflector in Ring 1, Lower reflector in Rings 2, 3, 4 Outer reflector in Ring 5
Core levels 16-35	Inner reflector in Ring 1, Active core in Rings 2, 3, 4 Outer reflector in Ring 5
Core levels 36-38	Inner reflector in ring 1, Upper reflector in Rings 2, 3, 4 Outer reflector in Ring 5

The core contains columns of graphite blocks stacked ten-high. Each control volume in the core is associated with two layers of graphite blocks. The control volumes are 0.793 m × 2 = 1.586 m in height. Each core cell represents one-half of a graphite block layer. The core cells are 0.793/2 – 0.392 m in height.

In order to include graphite properties as a core material, the Zircaloy material properties have been replaced with graphite properties. The graphite is modeled as "clad."

Four types of control rods are present at different steady state insertions. The mass of each type of control rod is input proportional to its insertion. Reserve shutdown control rods are fully out; therefore, their mass is not included. The startup control rods and operating control rods are all half inserted; therefore, half of their total masses is specified. The Burnable control rods are fully inserted; therefore, their total mass is specified.

The current model is set up to simulate the reactor at full power and steady state.

Many dimensions are not available for the 600 MWe GT-MHR or the NGNP, particularly for the inlet and outlet plenum geometries. In these instances, data were taken from the 450 MWe GT-MHR design or estimated from drawings.

The current main issues with respect to the detailed input model are as follows.

- The lower head has not been successfully accommodated to the entire model. More experience with the 1.8.6 lower head is needed.
- There are questions as to when null core cells can be defined. They have not yet been successfully defined on card CORijj01.
- There is uncertainty as to the best approach for modeling the core barrel. Should it be modeled with Heat Structures or Control Volumes?
- Difficulties with the bypass control volumes are being encountered. These control volumes are required for MELCOR-H2 to run. Since there is no identical bypass flow in the prismatic reactor, fixes such as very low flow rates are being tried to include the PWR bypass flow and enable a successful run.

A description of a RELAP5 input model for the passive heat removal system, the reactor cavity cooling system, was found in the literature survey. Design data for the passive cooling system is scarce, with a particular deficiency of data needed for the radiative heat transfer modeling. For a future work task, a simplified model will be developed as a place holder.

2.5 Conclusions and Recommendations

2.5.1 Task 1: Improvement of PBMR Modeling

The necessity of extending MELCOR-H2 capabilities to include the radial pebble temperature distribution in the PBMR model was demonstrated. Two methods for predicting the fuel pebble temperature distribution were developed and implemented via Control Functions. While both methods were largely successful in achieving their goals, implementation of a radial temperature distribution model into the MELCOR-H2 source code would provide a more accurate and efficient scheme for estimating fuel temperatures.

Two solution methods were tested. The first evaluates pebble temperatures under steady state conditions with internal heat generation. The second is based on an approximate numerical solution for the heat equation in spherical coordinates under transient conditions and is able to accommodate any mixture of coolant gases. Recommendations for extending the models are detailed in the main text.

Regarding the overprediction of fuel pebble temperatures, possible causes are uncertainty in the properties of the particulate debris, particularly the enthalpy, and a less-than-expected heat removal rate from the COR package to the CVH or HS packages. For the latter cause, CFD analysis may prove useful in examining the local flow paths and heat transfer rates. Another source of possible error to be further pursued is the radiative heat transfer modeling. A more detailed study on radiation heat transfer models applicable for MELCOR-H2 implementation is suggested.

2.5.2 Task 2: High-temperature Prismatic Reactor Input Deck Development

A literature survey was conducted for design data of the prismatic NGNP reactor. The most valuable sources are an NGNP point design report by INL and two design reports on the General Atomics GT-MHR with 450 MWth and 600 MWth ratings. Many engineering assumptions were required to fill in gaps of missing information and some scaling up from the 450 MWth reactor data to higher output data was also necessary.

A simplified prismatic deck was developed to verify MELCOR's ability to perform a passive heat removal analysis of decay heat cooling through the outer reflector. This deck consisted of control volumes and heat structures, with no core model. The heat source was hot coolant and heat was shown to conduct at an acceptable rate through the outer graphite reflector.

This simplified model was not able to provide a detailed representation of the core due to conflicts with heat structure locations and insufficient radial nodalization. A new model has been developed. The control volume and heat structure input was debugged, but the core input is currently presenting difficulties. Points of difficulty are listed in the report. The debugging process is continuing and a running deck will be provided as soon as possible. No MELCOR-H2 deficiencies have been encountered with respect to prismatic reactor modeling.

2.6 Chapter 2 References

ABB/Combustion Engineering, Inc., Bechtel National Inc., Gas-Cooled Reactor Associates, General Atomics, Massachusetts Institute of Technology, Oak Ridge National Laboratory, and Stone & Webster Engineering Corp., 1994, *Evaluation of the Gas Turbine Modular Helium Reactor*, DOE-GT-MHT-100002, ESEERCO Project 91-19, Issued by Gas-Cooled Reactor Associates.

Ball, S., 2002, MHTGR Accident Analysis, presentation at the 2002 ANS MHTGR Course, ANS 2002 Winter Meeting, Washington, DC, November 2002.

Bayless, P. D., 2003, Prismatic Core VHTR Analysis using RELAP5-3D/ATHENA, *Proceedings of 2003 RELAP5 International Users Seminar*, West Yellowstone Meeting, West Yellowstone, MT, August 28, 2003.

Bird, R. B., W. E. Stewart, and E. N. Lightfoot, 1960, *Transport Phenomena*, John Wiley and Sons, first edition, 2004.

Cocheme, F. G., 2004, *Assessment of Passive Decay Heat Removal in the General Atomic Modular Helium Reactor*. MS Thesis, Texas A&M University, December 2004.
*** This report provides information on a General Atomics design of a VHTR. ***

Davis, C. B., L. J. Siefken, and C. H. Oh, 2005, Assessment of RELAP5-3D for Analysis of Very High Temperature Gas-Cooled Reactors, *Proceedings of NURETH-11*, paper 422, Avignon, France, October 2005.

Davis, C. B., L. J. Siefken, and C. H. Oh, 2004, Assessment of a Molecular Diffusion Model in RELAP5-3D, *Proceedings of ANS Winter Meeting*, Washington, DC, pp. 193-194, November 2004.

Davis, C. B., and C. H. Oh, 2003, The Addition of Noncondensable Gases into RELAP5-3D for Analysis of High Temperature Gas-Cooled Reactors, *Proceedings of 10th Intl. Topical Mtg. on Nuclear Reactor Thermal Hydraulics (NURETH-10)*, Seoul, Korea, October 5-9, 2003.

DelCul, G. D., B. B. Spencer, C. W. Forsberg, E. D. Collins, and W. S. Rickman, 2004, *TRISO-Coated Fuel Processing to Support High-Temperature Gas-Cooled Reactors*, prepared by Oak Ridge National Laboratory for the U.S. Deptartment of Energy, contract DE-AC05-00OR22725, ORNL/TM-2002/156, September 2002.

Deptartment of Energy, 2004, *Appendix I: Very High Temperature Reactor*, February 19, 2004.

Futterer, M. A., H. Lohner, R. Conrad, K. Bakker, S. de Groot, and C. M. Sciolla, 2004, Irradiation of High Temperature Reactor Fuel Pebbles at VHTR Conditions in the HFR Petten, *Proceedings of 2nd Intl. Top. Mtg. on High Temperature Reactor Technology*, Beijing, China, 2004.

Gauntt, R. O., et al., 2005, *MELCOR-H2 Computer Code Manuals, Vol. 2: Reference Manuals, Version 1.8.6*, Prepared by Sandia National Laboratories for the U.S. Nuclear Regulatory Commission, Office of Nuclear Regulatory Research, NUREG/CR-6119, Vol. 2, Rev. 3, SAND 2005-5713, September 2005.

Gelbard, F., 2002, *Graphite Oxidation Modeling for Application in MELCOR*, draft report for review received from R. Gauntt, May 2002.

Gieseke, J. A., et al., 1986, *Source Term Code Package A User's Guide*, NUREG/CR-4587, BMI-2138, prepared for the US NRC by Battelle Memorial Inst.

Haque, Hamidul, Wolfgang Feltes, and Gerd Brinkmann, 2004, Thermal Response of a High Temperature Reactor during Passive Cooldown under Pressurized and Depressurized Conditions, *Proceedings of the Conference on High Temperature Reactors*, Beijing, China, September, 22-24, 2004.
Also, *Nuclear Engineering and Design*, Vol. 236, Issues 5-6, pp. 475-484.
*** THERMIX modeling of prismatic fuel ***

Hogan, K.J., 2006, Pebble Bed Modular Reactor Analysis with MELCOR. M.S. Thesis, Purdue University, 2006.

Idaho National Engineering and Environmental Laboratory, 2003, *NGNP Point Design – Results of the Initial Neutronics and Thermal-hydraulic Assessments During FY-03*, INEEL/EXT-03-00870, Rev. 1, prepared for the US DOE Office of Nuclear Science and Technology, September 2003. http://www.inl.gov/technicalpublications/Documents/2699872.pdf

Idaho National Engineering and Environmental Laboratory, Independent Technology Review Group, 2004a, *Design Features and Technology Uncertainties for the Next Generation*

Nuclear Plant Design Features and Technology Uncertainties for the Next Generation Nuclear Plant, prepared for the US DOE Office of Nuclear Science and Technology, June 30, 2004.

Idaho National Engineering and Environmental Laboratory, 2004b, *Initial Scaling Studies and Conceptual Thermal Fluids Experiments for the Prismatic NGNP Point Design*, INEEL/EXT-04-02367, prepared for the US DOE Office of Nuclear Science and Technology, September 2004. http://www.inl.gov/technicalpublications/Documents/2906952.pdf

Incropera, F. P., and D. P.DeWitt, 2002, *Fundamentals of Heat and Mass Transfer*, 5th edition, Wiley, New York, March 2002.

Kunitomi, K., S. Katanishi, S. Takada, X. Yan, and N. Tsuji, 2004, Reactor Core Design of Gas Turbine High Temperature Reactor 300, *Nuclear Engineering and Design*, Vol. 230, pp. 349-366, 2004.
*** design data for VHTR core ***

LaBar, M. P., A. S. Shenoy, W. A. Simon, and E. M. Campbell, 2003, The Gas Turbine-Modular Helium Reactor, *Nuclear News*, pp. 28-37, November 2003.

Lee, J. I., P. Hejzlar, P. Saha, and M. S. Kazimi, 2007, Studies of the deteriorated turbulent heat transfer regime for the gas-cooled fast reactor decay heat removal system, *Nuclear Engineering and Design*, Vol. 237, Issue 10, pp. 1033-1045, 2007.

Morris, R. N., D. A. Petti, D. A. Powers, and B. E. Boyack, 2004, *TRISO-Coated Particle Fuel Phenomenon Identification and Ranking Tables (PIRTS) for Fission Product Transport Due to Manufacturing , Operations and Accidents – Appendix G*, NUREG/CR-6844, Vol. 3, July 2004. (on NRC website as ML042300649)
MELCOR-H2 air ingress study

Nichols, D., 2001, The Pebble Bed Modular Reactor, *Nuclear News*, Vol. 44, No. 10, pp. 35-40, 2001.

No, H. C., 2001, *PBR System Simulation Code for Depressurization Accident Analysis in a Modular Pebble Bed*, technical report, Massachusetts Institute of Technology.

Oh, C. H., 2004, *Development of Safety Analysis Codes and Experimental Validation for a Very-High-Temperature Gas-Cooled Reactor*, International Nuclear Engineering Research Initiative 2003 Annual Report, published by Deptartmentof Energy, pp. 61-63.

Oh, C. H., 2005, *Development of Safety Analysis Codes and Experimental Validation for a Very High Temperature Gas-Cooled Reactor*, INERI US-ROK Annual Review Meeting, Washington, DC, January 26, 2005.

Parma, E. J., P. S. Pickard, and A. J. Suo-Antilla, 21003, *Very High Efficiency Reactor (VHER) Concepts for Electrical Power Generation and Hydrogen Production*, SAND2003-1755, Sandia National Laboratories, June 2003.

Reitsma, F., T. J. Downar, et al., 2004, The PBMR Steady State and Coupled Kinetics Core Thermal-Hydraulics Benchmark Test Problems, HTR-2004, The Second Topical Meeting on High Temperature Reactor 2004, Beijing, China, September 22-24, 2004.

Wu, Z., and S. Yu, 2007, HTGR Projects in China, *Nuclear Engineering and Technology*, Vol. 39, No. 2, pp. 103-110, 2007.

3. SULFUR IODINE AND HYBRID SULFUR DYNAMIC MODELING

3.1 Chapter 3 Highlights

A sustainable hydrogen economy requires a variety of hydrogen generation methods. The most common current method of hydrogen production is steam reforming using methane gas. This process inherently retains a reliance on fossil fuels, specifically natural gas. The emission of CO_2 and other greenhouse gases leads one to question the efficacy of steam reformation as a long-term hydrogen production solution.

Various thermo-chemical water-splitting cycles, electrolysis, and hybrid processes have been proposed to address hydrogen production on a large scale. Most of these cycles utilize a high-temperature heat source to provide energy. The sulfur iodine (SI) water splitting cycle and the hybrid sulfur (HyS) cycle are two examples. In the SI cycle, the decomposition of water is attained via three main chemical reactions. In the HyS cycle, one thermo-chemical reaction step and one electrolysis step are combined to produce hydrogen.

As a high-temperature heat source, nuclear energy is a leading candidate for clean and economic large-scale hydrogen production. In the nuclear-chemical coupled plant, system performance and safety analyses are required for any operating conditions including normal operation, plant startup, plant shutdown, and anticipated transients.

For the coupled system analysis, a comprehensive reaction chamber model is developed. Governing equations applicable for a control volume (reaction chamber) are derived. A simplified SI model where all chemical processes are connected with an appropriate simplification was developed and is shown in Sections 3.2 and 3.3. For the simplified HyS model, a mathematical model for the electrolysis process was developed in Section 3.4. To conduct system-level analysis on the coupled nuclear-chemical plant, the coupling between the developed simplified model and the MELCOR-H2 was performed.

In addition, this chapter discusses the model upgrades for the ongoing experiments conducted at SNL in relation to the decomposition of the sulfuric acid component of the SI cycle chemistry. The MELCOR-H2 Version 1 code is used to provide the model for the experiments, primarily the ½-scale experiment, which is analyzed only in the ambient pressure condition. In this experiment, the bayonet section's volume and the expected material flow and thermal conditions are modeled.

Section 3.5 provides the gross energy balance for the bayonet section of the SNL sulfuric acid decomposition experiments. Section 3.6 presents the dimensional calculations for the bayonet section. Section 3.7 discusses the implementation of the models into MELCOR-H2 that are associated with this experiment. To retain upward compatibility, different options were considered for modeling this experiment.

Appendix A is a report on MELCOR-H2 Benchmarking of the SNL transient sulfuric acid decomposition experiments.

3.2 Sulfur Iodine Chemistry Cycle

The SI cycle consists of three sets of chemical reactions expressed by the following equations:

$$I_2+SO_2+2H_2O \rightarrow 2HI+H_2SO_4 \text{ (Bunsen reaction)} \quad (3\text{-}1)$$

$$H_2SO_4 \rightarrow H_2O+SO_2+1/2O_2 \text{ (sulfuric acid decomposition)} \quad (3\text{-}2)$$

$$2HI \rightarrow H_2+I_2 \text{ (hydrogen iodide decomposition)} \quad (3\text{-}3)$$

Figure 3-1 presents the concept of the SI cycle. Equation (3-1) is called Bunsen reaction and proceeds in liquid phase. This reaction produces two kinds of acid, sulfuric acid (H_2SO_4) and hydriodic acid (hydrogen iodide (HI) in water) from sulfur dioxide (SO_2), iodine (I_2), and water (H_2O). The mixed acid separates into two types of acid of its own accord (liquid–liquid separation). The acid, which is rich in HI, is HI_x phase (HI_x solution), while the acid, which is rich in sulfuric acid phase. After separation of the acids, they are purified, concentrated and decomposed in the other two reactions. Equation (3-2) is the sulfuric acid decomposition reaction that produces oxygen, sulfur dioxide, and water. Equation (3-3) is the HI decomposition reaction that produces hydrogen and iodine. With the exception of hydrogen and oxygen, the other products in Equations (3-2) and (3-3) can be reused in the Bunsen reaction step as the reactant material. The endothermic H_2SO_4 decomposition reaction can be operated at about 800-1000 °C. The decomposition of hydriodic acid involves an endothermic reaction around 400-500 °C. The Bunsen reaction occurs exothermically at temperatures of about 100 °C. Heat source of two endothermic acid decomposition reactions in the SI cycle can be provided by the nuclear heat.

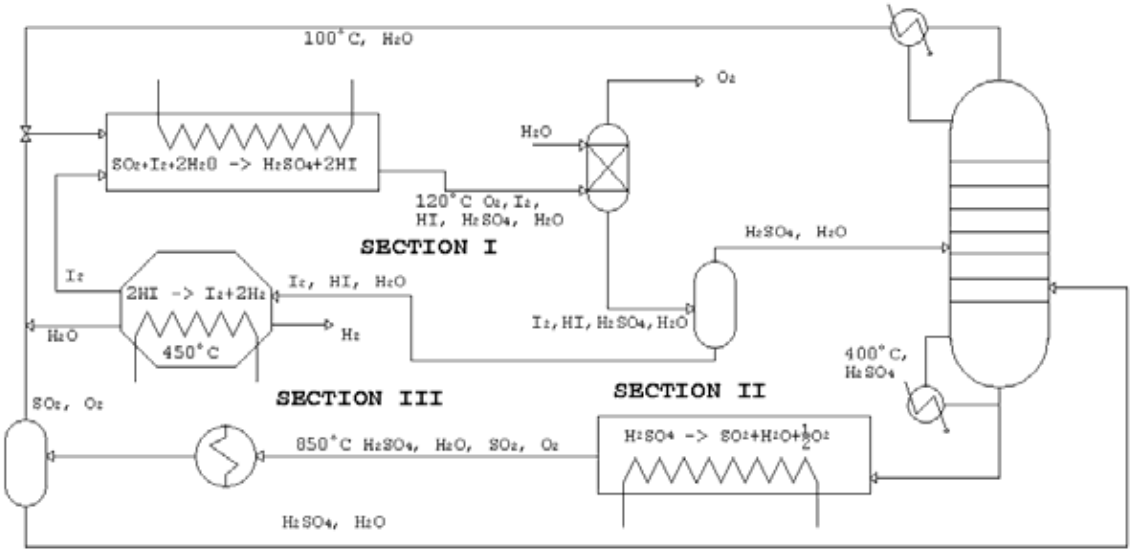

Figure 3-1. Schematic diagram of sulfur-iodine cycle.

The net reaction of the SI cycle is the water splitting into hydrogen and oxygen expressed as the following equations.

$$H_2O \rightarrow H_2 + ½O_2 \text{ (net reaction)} \quad (3\text{-}4)$$

In the SI cycle, all process fluids are recycled and no greenhouse gases are emitted. Also, the SI cycle has been fully flow sheeted and operated at the bench scale in the United States and Japan. This cycle has the highest efficiency (~52%) of any process that has been fully flow sheeted. Since the hydrogen is produced at high pressure, it eliminates the necessity of compressing the hydrogen for pipeline transmission or other downstream processing. One of the most challenging issues regarding the SI cycle is the material issue, which comes from the high process temperature (800–1000 ºC), and the corrosive reactants such as the sulfuric acid and hydrogen iodide.

3.3 Simplified SI Model Development

Regardless of any specific process, such as SI cycle or HyS cycle, the chemical reaction process plants for the hydrogen generation is quite a complicated system in terms of system analysis. Worldwide strong efforts on the development of the efficient process flowsheet have been conducted.

If the chemical process is connected to the nuclear power plant, the problem is much more complex. Reliable and safe operations for any nuclear plant conditions such as normal operation, plant startup, plant shutdown, and any anticipated operational transients must be demonstrated. For this purpose a comprehensive system model is necessary for the coupled nuclear-chemical plant. The model can be used to optimize hydrogen production as a function of key parameters such as reactor outlet temperature, core geometry, heat exchanger efficiency, and mass flow rates.

3.3.1 Reaction Chamber Model

In this chapter, a comprehensive reaction chamber model is developed. Governing equations applicable for a control volume of reaction chamber with inlet and outlet flow will be suitably derived. This reaction chamber model is so general that it could be used for any kind of reactor. The model is used to analyze the reaction chamber of H_2SO_4 and HI decomposition reactor in the SI cycle. Transients initiated from the high-temperature helium side such as helium inlet temperature or helium inlet flow rate changes are simulated.

3.3.1.1 Extent of Reaction

The general chemical reaction can be written as

$$|\nu_1|A_1 + |\nu_2|A_2 + \cdots = |\nu_3|A_3 + |\nu_4|A_4 + \cdots \tag{3-5}$$

where the $|\nu_i|$ are stoichiometric coefficients and the A_i stand for chemical species. The left side and right side of the equation are reactants and products, respectively. The ν_i are called stoichiometric numbers, which are positive for products and negative for reactants. For example, the hydrogen iodide decomposition reaction can be written as $2_{HI} = H_2 + I_2$ then $\nu_{HI} = -2$, $\nu_{H_2} = 1$, $\nu_{I_2} = 1$. Equation (3-6) can be rearranged as

$$\sum_i \nu_i A_i = 0 \tag{3-6}$$

For the reaction represented by Equation (3-6), the changes in the numbers of moles of the species are directly proportional to the stoichiometric numbers.

$$\frac{dM_1}{\nu_1} = \frac{dM_2}{\nu_2} = \cdots = \frac{dM_i}{\nu_i}$$

where the M_i are the numbers of moles of the species. Each term is related to an amount of reaction. Since all terms are equal, they can be represented by a single quantity dX.

$$dX = \frac{dM_1}{\nu_1} = \frac{dM_2}{\nu_2} = \cdots = \frac{dM_i}{\nu_i} \tag{3-7}$$

The variable, X, called the reaction coordinate or the molar extent of reaction, characterizes the extent or degree to which a reaction has taken place. The general relation between a differential change $dM_{i,RXN}$ in the number of moles of a reacting species and dX is

$$dM_{i,RXN} = \nu_i dX \tag{3-8}$$

The sum of the changes in the number of moles for all species is then

$$dM_{RXN} = \sum_i dM_{i,RXN} = \left(\sum_i \nu_i\right) dX = (\Delta\nu) dX \tag{3-9}$$

3.3.1.2 Balance Equation in a Reaction Chamber

A schematic diagram of a reaction chamber is shown in Figure 3-2.

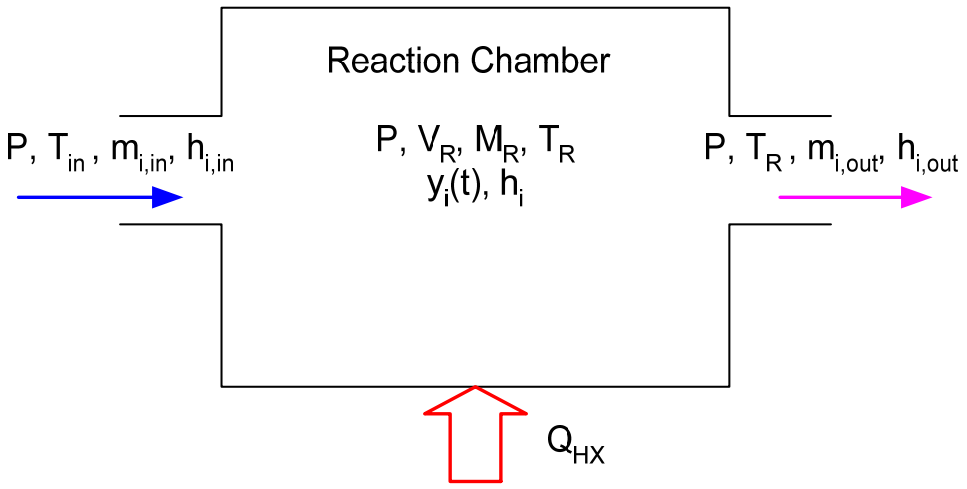

Figure 3-2. Schematic diagram of a reaction chamber.

The Molar Balance

The molar balance for each species in the reaction chamber can be written as

$$\frac{dM_{i,R}}{dt} = m_{i,in} - m_{i,out} + \frac{dM_{i,RXN}}{dt} \tag{3-10}$$

where

$M_{i,R}$ = the number of moles of species i in the reaction chamber,

$m_{i,in}$ = the molar flow rate of species i into the reaction chamber,

$m_{i,out}$ = the molar flow rate of species i out of the reaction chamber.

The total number of moles in reaction chamber and the total molar flow rate into and out of the chamber can be written as

$$M_R = \sum_i M_{i,R} \tag{3-11}$$

$$m_{in} = \sum_i m_{i,in} \tag{3-12}$$

$$m_{out} = \sum_i m_{i,out} \tag{3-13}$$

The molar fraction of each species in the reaction chamber is defined as

$$y_i = \frac{M_{i,R}}{M_R} \tag{3-14}$$

The mole fraction of the outlet stream can be assumed to be same as one of the reaction chamber, i.e.,

$$y_i = m_{i,out} / m_{out} . \tag{3-15}$$

Combining Equations (3-8), (3-10), (3-13) and (3-15),

$$\frac{dy_i M_R}{dt} = m_{i,in} - m_{i,out} + \nu_i \frac{dX}{dt} \tag{3-16}$$

where $\frac{dX}{dt}$ is the molar extent of reaction rate of change in the reaction chamber. This is the molar continuity equation for a species, *i*. For the HI decomposition reaction, the molar balance equation for each species can be written as

$$\frac{dM_{HI,R}}{dt} = m_{HI,in} - m_{HI,out} - 2\frac{dX}{dt}$$

$$\frac{dM_{H_2,R}}{dt} = m_{H_2,in} - m_{H_2,out} + \frac{dX}{dt}$$

$$\frac{dM_{I_2,R}}{dt} = m_{I_2,in} - m_{I_2,out} + \frac{dX}{dt}$$

By summing the molar balance equation for species *i* in Equation (3-16), global molar balance equation can be obtained as

$$\frac{dM_R}{dt} = m_{in} - m_{out} + \Delta\nu\frac{dX}{dt} \tag{3-17}$$

The left side of Equation (3-16) can be expanded as

$$M_R\frac{dy_i}{dt} + y_i\frac{dM_R}{dt} = m_{i,in} - m_{i,out} + \nu_i\frac{dX}{dt}.$$

Using Equation (3-17), the above equation can be written as

$$M_R\frac{dy_i}{dt} + y_i\left(m_{in} + \Delta\nu\frac{dX}{dt}\right) = m_{i,in} + \nu_i\frac{dX}{dt} \tag{3-18}$$

The above equation is a final form of molar balance equation for species *i*. Equations (3-17) and (3-18) form an expression of the global and species molar balance equation.

The Energy Balance

From the first law of the thermodynamics for the open system with negligible kinetic and potential energy, the energy balance equation for the entire reaction chamber can be expressed as

$$\frac{dU}{dt} = \sum_i\left(m_{i,in}h_{i,in}\right) - \sum_i\left(m_{i,out}h_{i,out}\right) + \dot{Q}_{HX} \tag{3-19}$$

where

U = total internal energy in the reaction chamber,

$h_{i,in}$ = the enthalpy of each reactant species entering the reaction chamber,

$h_{i,out}$ = the enthalpy of each reactant species exiting the reaction chamber,

$\dot{Q}_{HX}$ = the energy input from the heat exchanger.

Using the definition of enthalpy, Equation (3-19) can be written as

$$\frac{dH}{dt} = \sum_i \left(m_{i,in} h_{i,in}\right) - \sum_i \left(m_{i,out} h_{i,out}\right) + \dot{Q}_{HX} + V_R \frac{dP}{dt} \tag{3-20}$$

where $H = U + PV$ = total enthalpy in the reaction chamber,

P = pressure in the reaction chamber,

V_R = the reaction chamber volume remaining constant during transient.

For simplicity, the ideal gas mixture assumption is used in this model. If M moles of an ideal-gas mixture occupy a total volume V_R at temperature T_R, the pressure is

$$PV_R = M_R \cdot R \cdot T_R \tag{3-21}$$

If $M_{i,R}$ moles of species i in this mixture occupy the same total volume alone at the same temperature, the pressure is

$$p_i \cdot V_R = M_{i,R} \cdot R \cdot T_R \tag{3-22}$$

Dividing the latter equation by the former gives

$$\frac{p_i}{P} = \frac{M_{i,R}}{M_R} = y_i \text{ or } p_i = y_i P$$

where y_i is the mole fraction of species i in the gas mixture, and p_i is known as the partial pressure of species i. The sum of the partial pressures equals to the total pressure.

An ideal gas is a model gas comprised of imaginary molecules of zero volume that do not interact. Each chemical species in an ideal gas mixture therefore has its own private properties, uninfluenced by the presence of other species. This is the basis of *Gibbs's theorem*:

A total thermodynamic property (U, H, Cp, S, A, or G) of an ideal-gas mixture is the sum of the total properties of the individual species, each evaluated at the mixture temperature but at its own partial pressure.

This is expressed mathematically for the enthalpy *H* by the equation

$$H = M \cdot \overline{h^{ig}}(T,P) = \sum M_i h_i^{ig}(T, p_i) \text{ or } \overline{h^{ig}}(T,P) = \sum y_i h_i^{ig}(T, p_i)$$

where the superscript *ig* denotes an ideal gas property. Since the molar enthalpy of an ideal gas is independent of pressure,

$$\overline{h^{ig}}(T) = \sum y_i h_i^{ig}(T) \tag{3-23}$$

The superscript *ig* will be dropped for simplicity hereafter.

The total enthalpy of the system can be related to the molar enthalpy using the ideal gas mixture relations.

$$H = M_R \cdot \bar{h} = \sum_i M_{i,R} \cdot h_i = M_R \sum_i y_i \cdot h_i \tag{3-24}$$

where

$\bar{h}$ = the mixture molar enthalpy in the reaction chamber,

h_i = the molar enthalpy of each species *i* in the reaction chamber.

The expression for the change in the total enthalpy can be expanded as

$$dH = \sum_i (y_i h_i) dM_R + M_R \sum_i (h_i dy_i) + M_R \sum_i (y_i dh_i) \tag{3-25}$$

By substituting Equation (3-25) into Equation (3-20), we can reduce the energy balance equation to dependence on more computationally relevant quantities.

$$\sum_i \left(y_i h_i \frac{dM_R}{dt} + M_R h_i \frac{dy_i}{dt} + M_R y_i \frac{dh_i}{dt} \right) = \sum_i \left(m_{i,in} h_{i,in} \right) - \sum_i \left(m_{i,out} h_{i,out} \right) + \dot{Q}_{HX} + V_R \frac{dP}{dt}$$

This expression may be further reduced via the substitution of Equation (3-17) and (3-18):

$$\sum_i \begin{pmatrix} y_i h_i \left(m_{in} - m_{out} + \nu_i \frac{dX}{dt} \right) + \\ h_i \left(- y_i m_{in} - y_i \nu_i \frac{dX}{dt} + m_{i,in} + \nu_i \frac{dX}{dt} \right) + M_R y_i \frac{dh_i}{dt} \end{pmatrix} =$$

$$\sum_i \left(m_{i,in} h_{i,in} \right) - \sum_i \left(m_{i,out} h_{i,out} \right) + \dot{Q}_{HX} + V_R \frac{dP}{dt}$$

The change in molar enthalpy of each species in the reaction chamber is then

$$dh_i = c_{P,i} dT_R \tag{3-26}$$

where

$c_{P,i}$ = the molar specific heat at constant pressure,

dT_R = the temperature change in the reaction chamber.

The molar enthalpy of the outlet stream is assumed as one in the reaction chamber, $h_{i,out} = h$. Then, the energy equation is further simplified as

$$M_R \sum_i y_i c_{P,i} \frac{dT_R}{dt} = \sum_i m_{i,in} \left(h_{i,in} - h_i \right) - \frac{dX}{dt} \sum_i \nu_i h_i + \dot{Q}_{HX} + V_R \frac{dP}{dt}.$$

The heat of reaction and mixture specific heat are defined as

$$\Delta h_{RXN} = \sum_i \nu_i h_i \tag{3-27}$$

$$\overline{c_P} = \sum_i y_i c_{P,i} \tag{3-28}$$

Finally, the energy balance equation can be written as

$$M_R \overline{c_P} \frac{dT_R}{dt} = \sum_i m_{i,in} (h_{i,in} - h_i) - \Delta h_{RXN} \frac{dX}{dt} + \dot{Q}_{HX} + V_R \frac{dP}{dt} \tag{3-29}$$

To summarize, the continuity equation for the reaction chamber is

$$\frac{dM_R}{dt} = m_{in} - m_{out} + \Delta \nu \frac{dX}{dt} \tag{3-17}$$

$$M_R \frac{dy_i}{dt} + y_i \left(m_{in} + \Delta \nu \frac{dX}{dt} \right) = m_{i,in} + \nu_i \frac{dX}{dt} \quad i = 1,2,\ldots,\text{n} \tag{3-18}$$

As an equation of state, ideal gas law is used.

$$PV_R = M_R R T_R \text{ or } P = C_R R T_R \tag{3-21}$$

where $C_R = M_R/V_R$ the molar concentration in the reaction chamber.

The energy equation for the reaction chamber is

$$M_R \overline{c_P} \frac{dT_R}{dt} = \sum_i m_{i,in} (h_{i,in} - h_i) - \Delta h_{RXN} \frac{dX}{dt} + \dot{Q}_{HX} + V_R \frac{dP}{dt} \tag{3-29}$$

The extent of reaction, X, can be related to the reaction temperature, T_R, as well as the species concentration, $C_i = y_i C_R$. Thus,

$$X = X(T_R, C_i) \tag{3-30}$$

The energy balance through heat exchanger is

$$\dot{Q}_{HX} = U \cdot A \cdot \Delta T = m_{He}(h_{He,in} - h_{He,out}) \tag{3-31}$$

where

U = overall heat transfer coefficient of heat exchanger,

A = heat transfer surface area,

ΔT = mean temperature difference in heat exchanger,

m_{He} = molar flow rate of helium stream,

$h_{He,in}$ = molar enthalpy of helium stream at inlet with T_{h1},

$h_{He,out}$ = molar enthalpy of helium stream at outlet with T_{h2}

The unknowns in Equations (3-17), (3-18), (3-21), (3-29), (3-30) and (3-31) are M_R, X, y_i (i=1,2,…,n), m_{out}, P, T_R and T_{h2}. We have (n+6) unknowns but only have (n+5) equations. We need one more equation to close the problem. One missing equation is a momentum balance equation through the reaction chamber. We can construct the momentum balance for the reaction chamber with an appropriate consideration of pressure forces, viscous forces, and gravitational forces. A realistic set up of the momentum balance is related with specific process system design and control logics (piping configuration, pump performance and control logic, valve characteristics and control logic, etc.). Such information is not available now and it is not appropriate for the purpose of this a simplified model. Instead of solving the momentum balance, a few possible model assumptions could be used for the present simplified model:

1. The pressure in the reaction chamber is constant (i.e., $\frac{dP}{dt} = 0$),
2. The total mole number in the chamber is constant (i.e., $\frac{dM_R}{dt} = 0$), or
3. The outlet molar flow rate is constant (i.e., $\frac{dm_{out}}{dt} = 0$).

A reasonable assumption seems to be that, during a transient, the pressure in the reaction chamber does not change. We can expect that the actual process system would have such a pressure control logic in each reaction chamber. Therefore, the constant pressure in the reaction chamber is assumed in the present analysis.

$$\frac{dP}{dt} = 0 \text{ or } P = \text{constant} \tag{3-32}$$

3.3.1.3 Chemical Reactions in the SI Cycle

To close the governing equations derived in the previous section, the extent of reaction in Equation (3-30) should be specified for each reaction. The main chemical reaction in the SI cycle is modeled with an appropriate simplification and the other chemical processes for the separation, concentration, and recycling are neglected or simplified. For Section 1, the depletion rate of sulfur dioxide can be expressed as (Brown et al., 2003),

$$-\frac{d[SO_2]}{dt} = k_1 \cdot [I_2] \cdot [H_2O] \cdot [SO_2] \tag{3-33}$$

Thus, the depletion rate of sulfur dioxide is dependent on the reaction rate, as well as the concentration of each of the constituents.

For Section 2, the analysis of the sulfuric acid decomposition is carried out in two steps. First, sulfuric acid is assumed to be decomposed into water and sulfur trioxide. Second, oxygen and sulfur dioxide are produced by the decomposition of sulfur trioxide (Huang and T-Raissi, 2005). These steps are

1. $H_2SO_4 \longrightarrow H_2O + SO_3$

2. $SO_3 \longrightarrow SO_2 + \frac{1}{2}O_2$

From the chemical equilibrium calculation, the sulfuric acid decomposition (first reaction) is close to 100% at above 700 ^{o}C (Huang and T-Raissi, 2005). Therefore, 100% conversion is assumed in this model. Then, the chemical kinetics for Section 2 is expressed as

$$-\frac{d[H_2SO_4]}{dt} = -\frac{d[SO_3]}{dt} = k_2 \cdot [SO_3] \tag{3-34}$$

Because the reverse reaction rate of Section 3 is substantial, the definition of the hydrogen iodide depletion rate is significantly more complex. The reaction $2HI \underset{k_{-3}}{\overset{k_3}{\Leftrightarrow}} H_2 + I_2$ can be quantified via three coupled differential equations for the production of hydrogen and iodine and the depletion of hydrogen iodide. These expressions are

$$\frac{d[H_2]}{dt} = k_3 \cdot [HI]^2 - k_{-3} \cdot [H_2] \cdot [I_2]$$

$$\frac{d[H_2]}{dt} = \frac{d[I_2]}{dt} \tag{3-35}$$

$$\frac{1}{2}\frac{d[HI]}{dt} = -k_3 \cdot [HI]^2 + k_{-3} \cdot [H_2] \cdot [I_2]$$

These coupled equations for Section 3 are solved using the Runge-Kutta method. Assuming each reaction is elementary; these reaction rate constants can be calculated using the following relationships:

$$k_1 = A_1 \exp\left(-\frac{E_1}{R} \left\{ \frac{1}{T_1} - \frac{1}{T_0} \right\} \right)$$

$$k_2 = A_2 \exp\left(-\frac{E_2}{RT_2} \right) \qquad (3\text{-}36)$$

$$k_3 = A_3 \exp\left(-\frac{E_3}{RT_3} \right),\ k_{-3} = A_{-3} \exp\left(-\frac{E_{-3}}{RT_3} \right)$$

Table 3-1 summarizes each parameter in Equation (3-36). Thus, a simple chemical model of the steady state and transient behavior of each reaction chamber has been described. This chemical reaction chamber model, when coupled to a relevant thermal model, constitutes a fully coupled simplified model of the SI cycle.

Table 3-1. Reaction Rate Parameters

Section 1: Bunsen reaction (Liquid Phase, 120 °C)	
Pre-Exponential Factor (A1)	3e-6 $L^2/(mol^2\ s)$
Activation Energy (E1)	4.187 kJ/mol
Section 2: H_2SO_4 decomposition (Gas Phase, 850 °C)	
Pre-Exponential Factor (A2)	6.8e4 s^{-1}
Activation Energy (E2)	73.1 kJ/mol
Section 3: HI decomposition (Gas Phase, 450 °C)	
Reverse Reaction	
Pre-Exponential Factor (A-3)	1.596e7 L/(mol s)
Activation Energy (E-3)	108 kJ/mol
Forward Reaction	
Pre-Exponential Factor (A3)	1e11 L/(mol s)
Activation Energy (E3)	184 kJ/mol

3.3.1.4 Model Implementation

To implement the transient model, a comprehensive steady state calculation must first be performed. The steady state analysis involves calculating a steady state hydrogen production rate based on reactor coolant and reactant flow rates and temperatures. After the initial steady state calculation, one of the relevant quantities, such as reactor coolant temperature, can be perturbed, and the resultant transient can be observed.

The initial steady state condition can be obtained by fixing all but one of the relevant quantities. For example, a desired hydrogen production rate should be fixed, and the required coolant flow rate should be calculated. Alternatively the coolant flow rate would be fixed and the heat exchanger transfer area required could be calculated. Thus, there are a variety of potential steady state solutions that could be reached.

Once a steady state solution has been attained, a quantity, such as the reactor coolant flow rate or the reactor coolant temperature, should be perturbed. Then, using the time-dependent energy balance, continuity balance, reaction rates, and momentum assumption, the transient response of the SI-cycle system should be observed.

Some of the most important transients are those such as a partial loss-of-coolant accident, where some percentage of the reactor coolant is removed from the coolant stream. This is a potentially severe reactor accident. Understanding the transient behavior of the chemical plant in such an event is an important nuclear safety question. Thus, a sudden change in flow rate is an important perturbation in transient analysis. Occasionally, to prevent an out-of-control nuclear reaction, an emergency insertion of negative reactivity is necessitated. As a result of the reactivity removal, the outlet temperature of the reactor coolant will quickly drop. The change in chemical plant reaction rates and hydrogen production rate would be important to understand in such an event. In the following section, perturbations for helium inlet temperature and helium inlet flow rate are simulated as transient analyses.

3.4 Hydrogen Sulfur Model

The Westinghouse HyS cycle has two reactions. From the two reactions electrolysis produces sulfuric acid and hydrogen from water and sulfur dioxide at low temperature. The thermodynamic properties of the chemical species are well known. The HyS cycle was the highest-ranked cycle from the preliminary screening process in previous Nuclear Energy Research Initiative (NERI) project. The two reactions can be written as

(I) $H_2SO_4(aq) \rightarrow H_2O+SO_2(g)+½O_2(g)$ - thermochemical (800 °C min.)

(II) $2H_2O(aq)+SO_2(g) \rightarrow H_2SO_4(aq) + H_2$ - electrolysis (80 °C).

The first reaction, sulfuric acid decomposition reaction, is the same reaction in the SI cycle. Therefore, the model developed for the SI cycle can be used directly for this reaction with appropriate modification of recycling flows. Figure 3-3 presents a schematic diagram for the simplified HyS model.

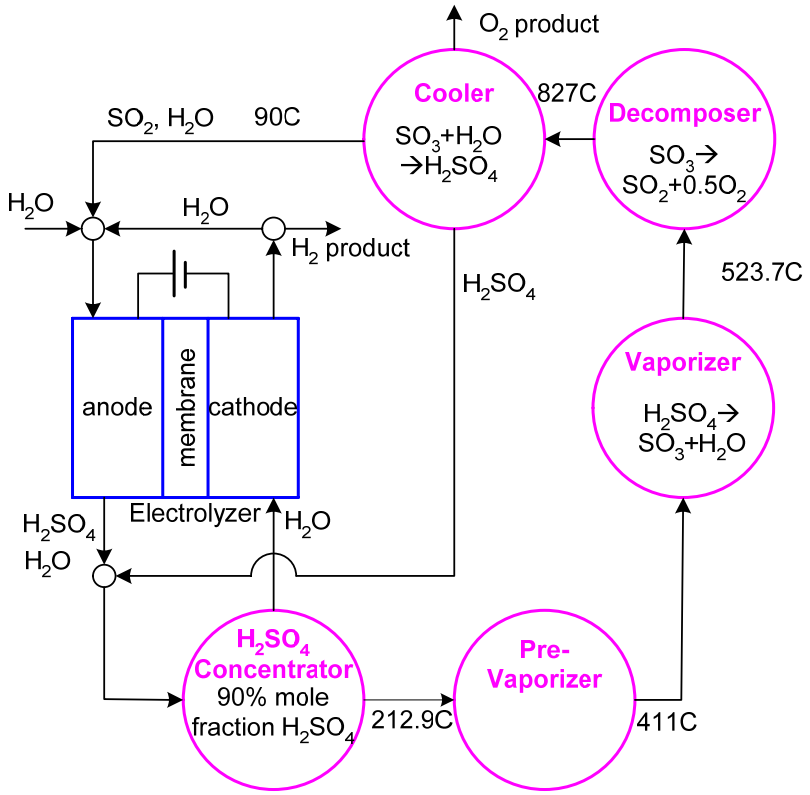

Figure 3-3. Schematic diagram for the simplified HyS model.

The challenge in modeling the HyS cycle is the modeling of the water and sulfur-dioxide electrolyzer. Electrolysis is a process where a current is applied to two electrodes in an ionic solution, causing charge to concentrate on both electrodes. A thermodynamic analysis of electrolysis provides some insight into modeling electrolyzer behavior.

Using thermodynamics, the electrical work that a spontaneous chemical reaction is capable of producing is directly related to the change in Gibbs free energy, ΔG, of the reaction (II). The change in Gibbs free energy for an electrochemical cell is expressed as

$$\Delta G = \Delta E + P\Delta V - T\Delta S \tag{3-37}$$

Where ΔE is the sum of the thermal and electrical work done to the system, $P\Delta V$ is the pressure volume work done to the system and $T\Delta S$ is the increase in entropy of the system. For a reversible process, the Gibbs free energy expression is simplified as

$$\Delta G = w_{elec} + q - T\Delta S = w_{elec} + T\Delta S - T\Delta S \tag{3-38}$$

Thus, the Gibbs free energy is be written as

$$\Delta G = w_{elec} \tag{3-39}$$

Simplifying, the electrical work required for a given electrolysis process is given by

$$E_0 = -\frac{\Delta G}{nF} \tag{3-40}$$

where *n* is the number of charges exchanged in the electrolysis reaction and *F* is the Faraday constant, i.e., the charge of 1 mol of electrons (Oxtoby and Nachtrieb, 1986).

For the HyS cycle, the relevant electrolysis reaction is

$$SO_2\,(aq) + 2H_2O\,(l) \leftrightarrow H_2SO_4\,(aq) + H_2\,(g) \quad (80\text{-}120)\ ^\circ C \tag{3-41}$$

This is not an elementary reaction; rather it is composed of at least two component reactions. These reactions are (Jeong et al., 2005),

$$2H^+\,(aq) + 2e^- \rightarrow H_2\,(g) \quad \textit{Cathode} \tag{3-42}$$

$$2H_2O\,(l) + SO_2\,(g) \rightarrow H_2SO_4\,(aq) + 2H^+\,(aq) + 2e^- \quad \textit{Anode} \tag{3-43}$$

The concentration dependent cell energy required is given by the Nernst equation,

$$E = E_0 - \frac{RT}{nF}\ln Q \tag{3-44}$$

Here, Q is the reaction quotient. Jeong et al. (2005) gives the expressions for the potential at the cathode, anode, and the entire cell as

$$E_{cathode} = -\frac{RT}{nF}\ln\frac{[H_2]}{[H^+]^2} \tag{3-45}$$

$$E_{anode} = E_0 - \frac{RT}{nF}\ln\frac{[H_2SO_4][H^+]^2}{[H_2O]^2[SO_2]} \tag{3-46}$$

$$E = E_{cathode} + E_{anode} = E^0_{anode} - \frac{RT}{nF}\ln\frac{[H_2SO_4][H_2]}{[H_2O]^2[SO_2]} \tag{3-47}$$

In these equations, the concentrations of each of the constituents are in brackets. Several values are presented in literature for the open circuit potential of the anode. Jeong et al. (2005) gives -0.17 Volts and Forsberg et al. (2004) gives -0.29 Volts. This open circuit voltage may be calculated from thermodynamic tables of Gibbs free energy. Thus, the value of this potential may vary slightly depending on the thermodynamic data used. In reality, the electrode potential is higher than the theoretical value. The actual voltage of the electrolyzer is composed of a theoretical open circuit voltage and three losses: activation losses, ohmic losses, and concentration losses. Activation losses occur because of the slowness of the chemical reaction taking place. The loss becomes quite large at low current densities, but levels out quickly. Ohmic losses are caused by internal resistance to current flow. This resistance is very difficult to model analytically, as it is dependent on many factors. Generally, an empirical formula is used.

In the cathode hydrogen is generated. The molar rate of hydrogen generation is directly related to the amount of current supplied by Faraday's law of electrolysis (Larminie 2003), which states

$$\dot{n}_{H_2,rxn} = \frac{NI}{nF} \tag{3-48}$$

where N is the number of electrolyzer and I is the total current applied.

If we could control the total current in the electrolyzer as a constant, a constant hydrogen generation can be achievable theoretically as long as the water is supplied to the process and the sulfuric acid is recycled continuously. Water flowing across membrane of the electrolyzer is usually not a concern since the electrolyzer operates with a flooded membrane.

The mass balance in the anode and cathode can be established by the same way in the Equation (3-10).

$$\frac{dM_{i,R}}{dt} = m_{i,in} - m_{i,out} + \dot{n}_{i,rxn} \tag{3-49}$$

where

$M_{i,R}$ = the number of moles of species i in the anode or cathode,

$m_{i,in}$ = the molar flow rate of species i into the anode or cathode,

$m_{i,out}$ = the molar flow rate of species i out of the anode or cathode,

$\dot{n}_{i,rxn}$ = the molar generation rate of species i in the anode or cathode.

For a detailed energy balance, we need a specific design data of the electrolyzer such as the volume, surface area, solid heat capacity, etc. For the present, we can assume an isothermal condition in the electrolyzer.

Total energy supplied through the electrolyzer can be calculated by

$$P = N\ E\ I \tag{3-50}$$

3.5 Gross Energy Balance for the Bayonet Section

Let T_{inlet} (30 °C) be the acid solution inlet temperature and T_{react} (850 °C, maximum) be the acid reaction temperature. The boiling temperature of the solution is well below T_{react}; therefore, we need to account for the sensible heat of the vapor phase.

$\dot{M}_{inlet}$ is the solution flow rate at mol/s with f_1, the mole fraction of acid.

1. From T_{inlet} to T_{react}, it is assumed to include the decomposition of SO_3 to $SO_2 + \frac{1}{2}O_2$. t_1 is the corresponding time (s) from T_{inlet} to T_{react}.

   a. H_2O (l+g):

   $$\Delta E^{(1)}_{H_2O,\,sensible}(t) = (1 - f_1)\cdot \dot{M}_{inlet}\cdot t_1 \cdot \left[\int_{T_{inlet}}^{T_{boil}} Cp_{H_2O(l)}(T)\,dT + H_{fg,\,H_2O} + \int_{T_{boil}}^{T_{react}} Cp_{H_2O(g)}(T)\,dT\right]$$

   b. H_2SO_4 (l+g):

   $$\Delta E^{(1)}_{acid,\,sensible}(t) = f_1\cdot \dot{M}_{inlet}\cdot t_1 \cdot \left[\int_{T_{inlet}}^{T_{boil}} Cp_{acid(l)}(T)\,dT + H_{fg,\,acid} + \int_{T_{boil}}^{T_{react}} Cp_{acid(g)}(T)\,dT\right]$$

2. At T_{react}, $H_2SO_4 \xrightarrow{K_1} SO_3 + H_2O$, $SO_3 \xrightarrow{K_2} SO_2 + \frac{1}{2}O_2$:

   Let ΔH_{RX} in J/mole be the reaction energy taken to convert H_2SO_4 to SO_2, O_2, and H_2O. $K = K_1 + K_2$, which accounts for concentration, catalyst bed dimension, and reaction temperature K (C, L, T_{react}).

   Let $M_{acid,\,r} = \text{number of mole of } H_2SO_4 \text{ actually decomposed}$.

   a. $M_{SO_2} = M_{acid,\,r}\cdot 1$

   b. $M_{O_2} = M_{acid,\,r}\cdot 0.5$

   c. $M_{H_2O} = M_{acid,\,r}\cdot 1$

   Thus, for each mole of H_2SO_4 decomposed, 2½ moles of products are created.

   d. Conversion efficiency. $\eta_{acid} = \dfrac{M_{acid,\,r}}{f_1\cdot \dot{M}_{inlet}\cdot t_1}$

3. From T_{react} *to* T_{outlet}, assume that unreacted SO_3 will combine with H_2O and form H_2SO_4. η_{acid} takes into account t_2 = time from T_{react} to T_{outlet}. Fred indicates that T_{outlet} is 180 °C, which means that the solution may be still in the vapor form.

   Review the inlet condition again:

   a. $\dot{M}_{H_2O} = \dot{M}_{inlet}(1 - f_1)$

   b. $\dot{M}_{acid} = \dot{M}_{inlet}\cdot f_1$

Outlet condition:

c. $\dot{M}_{acid,unreacted} = \dot{M}_{acid} \cdot (1-\eta_{acid})$

d. $\dot{M}_{SO_2} = \dot{M}_{acid} \cdot \eta_{acid}$

e. $\dot{M}_{O_2} = \dot{M}_{acid} \cdot \eta_{acid} \cdot \frac{1}{2}$

f. $\dot{M}^{(2)}_{H_2O} = \dot{M}_{inlet}(1-f_1) + \dot{M}_{acid} \cdot \eta_{acid}$

g.
$$\begin{aligned}\dot{M}_{outlet} &= \dot{M}_{acid,unreacted} + \dot{M}_{SO_2} + \dot{M}_{O_2} + \dot{M}^{(2)}_{H_2O} \\ &= \dot{M}_{inlet}(1-f_1) + \dot{M}_{acid}\left(1-\eta_{acid}+\eta_{acid}+\frac{1}{2}\eta_{acid}+\eta_{acid}\right)(1+1.5\eta_{acid}) \\ &= \dot{M}_{inlet}(1-f_1) + \dot{M}_{inlet} \cdot f_1 \cdot (1+1.5\eta_{acid}) \\ &= \dot{M}_{inlet}(1+1.5\ f_1\ \eta_{acid})\end{aligned}$$

h. $\dot{M}_{SO_2} = \dot{M}_{inlet} \cdot \left(\frac{f_1\ \eta_{acid}}{1+1.5\ f_1\ \eta_{acid}}\right)$

i. $\dot{M}_{O_2} = \dot{M}_{inlet} \cdot \frac{1}{2}\left(\frac{f_1\ \eta_{acid}}{1+1.5\ f_1\ \eta_{acid}}\right)$

j. $\dot{M}^{(2)}{}_{acid} = \dot{M}_{inlet} \cdot \frac{f_1(1-\eta_{acid})}{1+1.5\ f_1\ \eta_{acid}}$

k. $\dot{M}^{(2)}{}_{H_2O} = \dot{M}_{inlet} \cdot \left(\frac{1-f_1+f_1\ \eta_{acid}}{1+1.5\ f_1\ \eta_{acid}}\right)$

H_2O (g):

l. $\Delta E^{(2)}_{H_2O,sensible}(t) = \dot{M}_{inlet}\left(\frac{1-f_1+f_1\ \eta_{acid}}{1+1.5\ f_1\ \eta_{acid}}\right) \cdot t_2 \cdot \left[\int_{T_{react}}^{T_{outlet}} Cp_{H_2O}(T)\,dT\right]$

SO_2 (g):

m. $\Delta E^{(2)}_{SO_2,sensible}(t) = \dot{M}_{inlet}\left(\frac{f_1\ \eta_{acid}}{1+1.5\ f_1\ \eta_{acid}}\right) \cdot t_2 \cdot \int_{T_{react}}^{T_{outlet}} Cp_{SO_2}(T)\,dT$

O_2:

n. $\Delta E^{(2)}_{O_2,\,sensible}(t) = \dot{M}_{inlet} \cdot \frac{1}{2}\left(\frac{f_1\,\eta_{acid}}{1+1.5\,f_1\,\eta_{acid}} \right) \cdot t_2 \cdot \int_{T_{react}}^{T_{outlet}} Cp_{O_2}(T)\,dT$

H_2SO_4:

o. $\Delta E^{(2)}_{acid,\,sensible}(t) = \dot{M}_{inlet} \left\{ \frac{f_1(1-\eta_{acid})}{1+1.5\,f_1\,\eta_{acid}} \right\} \cdot t_2 \cdot \left[\int_{T_{react}}^{T_{outlet}} Cp_{acid}(T)\,dT - H_{fg,\,H_2SO_4} \right]$

4. Using the definition of η_{acid}:

a. $\eta_{acid} = \frac{M_{acid,\,r}}{f_1 \dot{M}_{inlet} \cdot t_1}$

b. $M_{acid,\,r} = f_1 \dot{M}_{inlet} \cdot t_1 \cdot \eta_{acid}$ Both η_{acid} and $f_1 \dot{M}_{inlet}$ are experimental values.

The unknown is t_1.

Since $\dot{M}_{inlet}$ and f_1 are given, t_1 can be solved based on the length of the Bayonet and the cross-section flow area of the outer annulus.

The liquid density of the acid solution is given as from Howard Stone's dissertation. It is assumed to be valid up to its boiling temperature (T_{soln}(f), f=mole fraction of the acid). Table 3-2 shows the tabular value of boiling temperature as a function of % acid.

c. $\rho_{solution}(f_1) = 1 + 3.528 \cdot f_1 - 6.83 \cdot f_1^{\,2} + 6.402 \cdot f_1^{\,3} - 2.26 \cdot f_1^{\,4}$ (g/cc)

Table 3-2. Boiling Temperature of Sulfuric Acid Solution at Percent of Acid

% Acid	Boiling Temp (°C)	% Acid	Boiling Temp (°C)
0	100	70	170
10	100	80	220
20	102	90	275
30	106	93.3	338
40	115	100	290
50	124		
60	140		

Using the data provided in Table 3-2, the following correlation of the boiling temperature ($T_{fg}(f)$ in °C), where f is the mole fraction of the acid, of the acid solution is given by:

For $0 < f \leq 0.933$,

d. $T_{fg}(f) = 2193.3 \times f^5 - 4106.8 \times f^4 + 2923.8 \times f^3 - 749.12 \times f^2 + 73.102 \times f + 99.369$

For $0.933 < f < 1.0$,

e. $T_{fg}(f) = 290 - (290 - 338) \times \dfrac{1-f}{1-0.933}$

Mass rate of H_2O:

f. $\dot{m}_{H_2O} = \dot{M}_{inlet} \cdot (1 - f_1) \cdot MW_{H_2O}$

Mass rate of acid:

g. $\dot{m}_{acid} = \dot{M}_{inlet} \cdot f_1 \cdot MW_{acid}$

Thus,

h.
$$\begin{aligned} \dot{m}_{inlet} &= \dot{m}_{H_2O} + \dot{m}_{acid} \\ &= \dot{M}_{inlet} \left\{ (1 - f_1) \cdot MW_{H_2O} + f_1 MW_{acid} \right\} \end{aligned}$$

$\therefore$ Volumetric flow rate (cc/s) is:

i.
$$\begin{aligned} \dot{V}_{inlet} &= \frac{\dot{m}_{inlet}}{\rho_{solution}(f_1)} \\ &= \frac{\dot{M}_{inlet} \left\{ (1 - f_1) \cdot MW_{H_2O} + f_1 MW_{acid} \right\}}{\rho_{solution}(f_1)} \end{aligned}$$

Let V_{upflow} be the upflow volume inside the Bayonet, which includes the outer flow annulus and the catalyst bed flow. Note that the computation of time may be overestimated if we assume that the fluid in the upflow direction is 100% liquid, as opposed to two phase flow (liquid and gas). This is not known *a priori*, so we calculate t_l as:

j. $\therefore \quad t_1 = \dfrac{V_{upflow}}{\dot{V}_{inlet}}$

Similarly, t_2 can be solved by assuming that $V_{downflow}$ is the down flow volume inside the Bayonet, which includes the inner flow annulus and the flow volume between the catalyst bed.

The outlet flow consists of all gases, according to the T_{outlet} given to be 180 °C.

k. $\dot{M}_{outlet} = \dot{M}_{inlet}(1+1.5 f_1 \eta_{acid})$

Assume $\overline{V}_{gas}$ = mole/cc at outlet temperature (22.4 liters/mole of gas per standard test and pressure (STP) condition, and ideal gas).

l. $\dot{V}_{outlet} = \frac{\dot{M}_{inlet}(1+1.5 f_1 \eta_{acid})}{\overline{V}_{gas}(T_{outlet})}$

Thus,

m. $\therefore \quad t_2 = \frac{V_{downflow}}{\dot{V}_{outlet}}$

5. Once t_1 and t_2 are determined, all the energy terms can be solved for a given $\dot{M}_{acid}$, f_1, and η_{acid}.

   It is assumed that the reacted acid rate constant is given in 1/s, so it is not dependent on concentration.

   a. $\therefore \quad m_{acid,r} = f_1 \dot{M}_{inlet} \cdot t_1 \cdot \left(1 - e^{-kt_1}\right)$

   t is given above, and *k* is the reaction constant.

   Note that the current SI model applies the above-defined *k* term, which can be changed, and

   b. $m_{acid,r} = f_1 \dot{M}_{inlet} \cdot t_1 \cdot \eta_{acid}$

   Thus,

   c. $\eta_{acid} = 1 - e^{-kt_1}$

   $\therefore$ *k* can be correlated with η_{acid}

6. To benchmark the Bayonet, we could simulate the experiment by:

   a. Matching the data points on the attached graph from the experiment.

   b. Modifying the existing H2C module–SI coding to allow flow rate input for reactions.

   c. Using the existing reaction constant for the decomposition of the sulfuric acid, and predicting the gas product rate for a given mole fraction of acid, and acid inlet flow rate.

d. Adjusting the reaction constant to permit the match of the gas production rate, and efficiency. Then simulate other data points in the graph.

e. Assumption is that $T_{inlet} = 30°C$, $T_{react} = 850°C$, and $T_{outlet} = 180°C$.

3.6 Computation of Bayonet Dimensions

The dimension of the Bayonet Section of Fred Gelbard's ½-scale experiment is computed based on the dimensions shown in Figure 3-4. The schematic of this section is shown in Figure 3-5.

1. Outer Flow Annulus

$$\frac{\pi}{4}\left(D_2{}^2 - D_3{}^2\right) = \frac{\pi}{4}\left(25.4\,\text{mm}^2 - 20\,\text{mm}^2\right)$$
$$= 192.5482\,\text{mm}^2 = 1.9255\,\text{cm}^2$$

2. Inner Flow Annulus

$$\frac{\pi}{4}\left(D_4{}^2 - D_5{}^2\right) = \frac{\pi}{4}\left(17\,\text{mm}^2 - 15.875\,\text{mm}^2\right)$$
$$= 29\,\text{mm}^2 = 0.2905\,\text{cm}^2$$

3. Length of Bayonet is 27 inches (68.58 cm) = *x*

$$\text{Height before bed} = \frac{2}{3}x = \frac{2}{3}(68.58\,\text{cm}) = 45.72\,\text{cm}$$

$$\text{Inner flow volume} = 0.2905\,\text{cm}^2 \cdot 45.72\,\text{cm} = \underline{\underline{13.2817\,\text{cm}^3}}$$

$$\text{Outer flow volume} = 1.9255\,\text{cm}^2 \cdot 45.72\,\text{cm} = \underline{\underline{88.0339\,\text{cm}^3}}$$

Bed volume is based on ⅓ of length *x*. $\left(68.58\,\text{cm} \times \frac{1}{3}\right) = 22.86\,\text{cm}$

Assume the same thickness of the baffle (3 mm)

$$\text{Inner bed flow volume} = \frac{\pi\left(13\,\text{mm}^2\right)}{4 \cdot 10^2} \cdot 22.86\,\text{cm} = \underline{\underline{30.3426\,\text{cm}^3}}$$

Account for the bed porosity of 50%, then

$$\text{Outer bed flow volume} = 0.5 \cdot \frac{\pi\left\{D_2{}^2 - (13\,\text{mm} + 3\,\text{mm})^2\right\}}{4 \cdot 10^2} \cdot 22.86\,\text{cm}$$

$$= \underline{\underline{34.9353\,\text{cm}^3}}$$

$$\text{Total flow volume} = 13.2817 + 88.0339 + 30.3426 + 34.9353$$

$$= 166.5935\,\text{cc or } 1.6659 \times 10^{-4}\ \text{m}^3$$

$$\text{Up Flow volume} = 88.0339 + 34.9353 = 122.9692\,\text{cc}$$

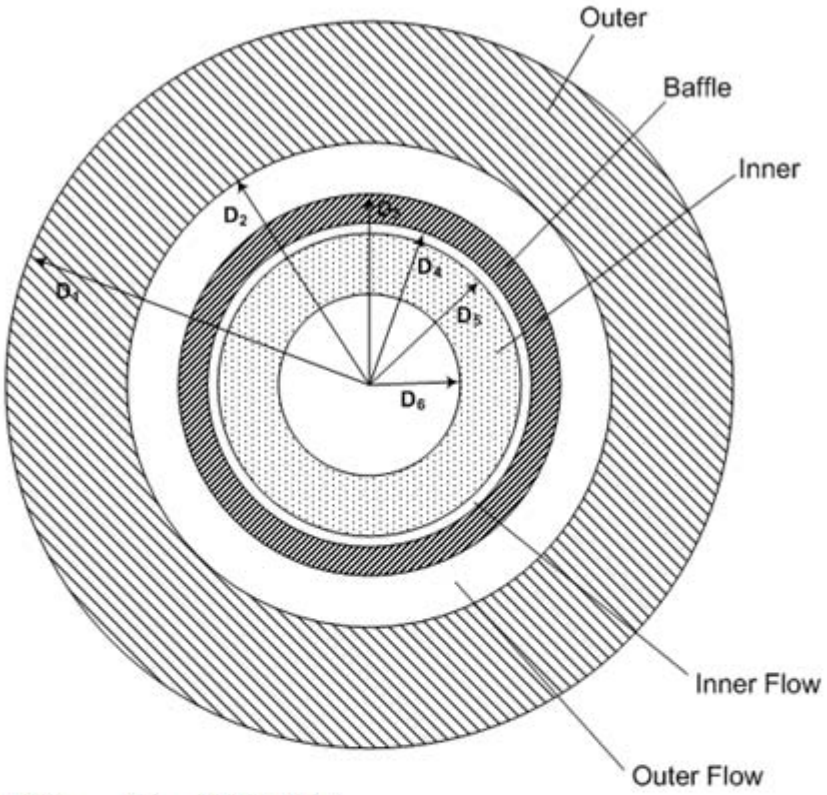

Outer:	OD	38.1 mm (D_1)
	ID	25.4 mm (D_2)
Baffle:	OD	20 mm (D_3)
	ID	17 mm (D_4)
Inner:	OD	15.875 mm (D_5)
	ID	9.525 mm (D_6)

Outer Flow Annulus	$D_{o1} = D_2$
	$D_{i1} = D_3$
Inner Flow Annulus	$D_{o2} = D_4$
	$D_{i2} = D_5$

Figure 3-4. Dimension of the bayonet section.

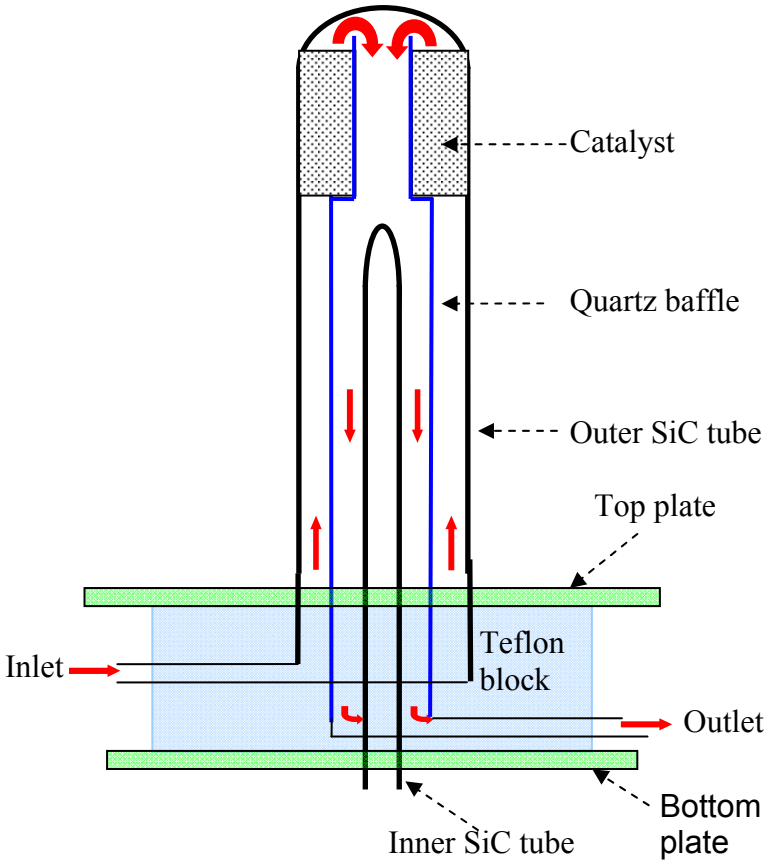

Figure 3-5. Schematic of the bayonet section.

3.7 Implementation in MELCOR-H2

A. OPTION—"IFLOW"

This option is used to simulate Fred Gelbard's ½-scale experiment on the decomposition of the sulfuric acid. Much of the existing mass (mole) and energy balance model in the H2C package will remain the same. Only the programming associated with IFLOW will be implemented according to the following description. See Figure 3-6.

1. Following is the optional input when Option "IFLOW" = 1 is input:

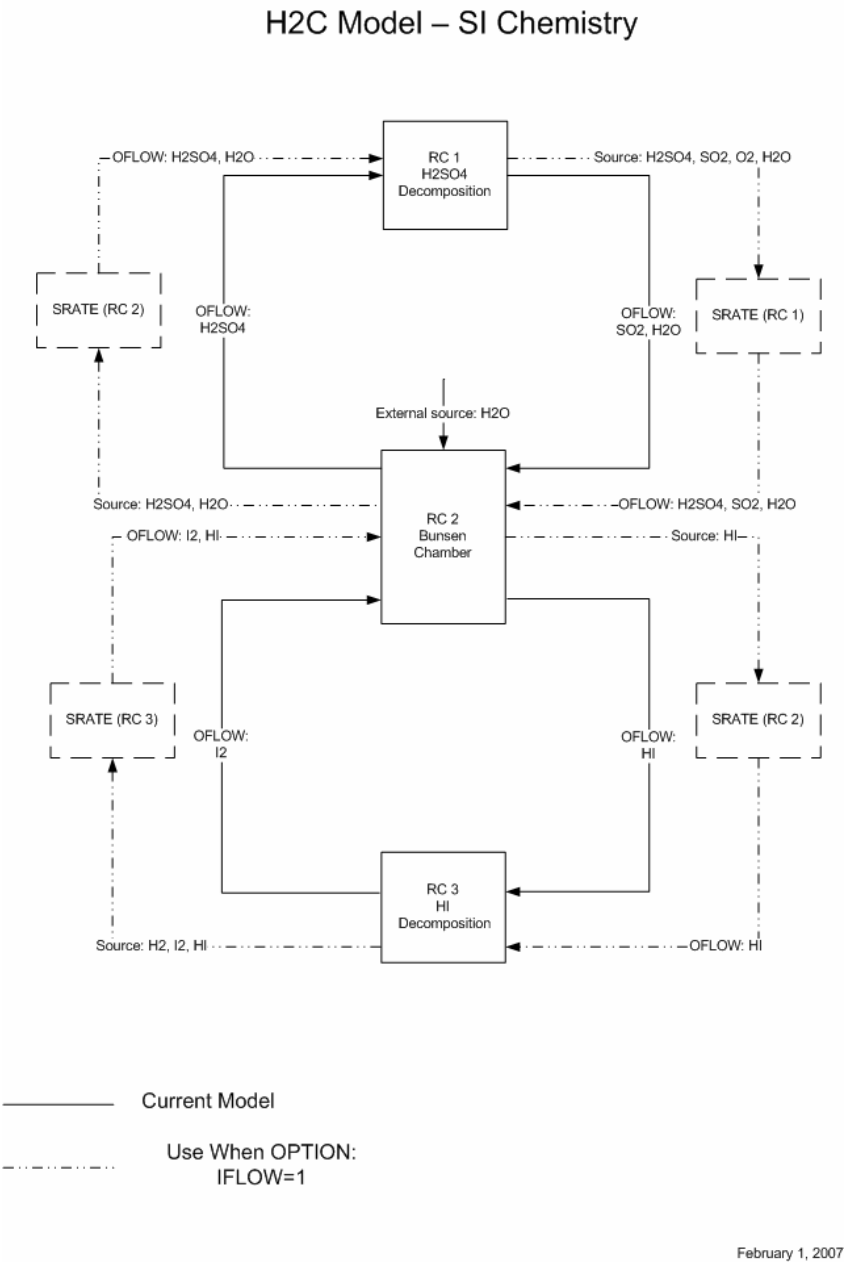

Figure 3-6. Flow diagram for the current and the proposed flow models in H2C package.

2. Species tracked when IFLOW=1:

   <u>RC 1:</u> $H_2SO_4 \rightarrow \quad SO_2 + 0.5\ O_2 + H_2O$

   $H_2O \rightarrow \quad H_2O$

   $V_{RC1} = V_{upflow} + V_{downflown}$ (as input)

   Add: H_2O inlet stream to the existing model

H_2SO_4 outlet stream to the existing model

No material will remain in the RC 1 chamber

3. ALL in and out-flow species:

RC 1: (inflow)

H_2SO_4, H_2O which depend on f, mole fraction of the acid solution as input. (temperature of the inflow is taken as $T_{RC2,\ source}$)

(outflow)

SO_2, $_O2$, H_2O, H_2SO_4 (unreacted) will be sourced out of chamber, calculated source rate with no material remained in the chamber

Only SO_2, H_2O, H_2SO_4 are permitted to outflow to RC 2 (Bunsen chamber)

$T_{RC1,\ react}$ (as input, 850 °C maximum)

$T_{RC1,\ source}$ (as input, 180 °C)

RC 2: (inflow)

H_2O (sourced in as fresh water)

SO_2, H_2O, H_2SO_4 (unreacted) [from RC 1]

I2, HI (unreacted) [from RC 3]

(outflow)

H_2SO_4, H_2O to RC 1, as sourced out of the chamber

HI to RC 3, as sourced out of the chamber

$T_{RC2,\ react} = T_{RC2,\ source}$ (as input, 30 °C)

RC 3: (inflow)

HI [from RC 2]

(outflow)

H2, I2, HI (unreacted) as sourced out of the chamber, calculated source rate with no material remained in the chamber

$T_{RC3,\ react} = T_{RC3,\ source}$ (as input, 450 °C)

Heat transfer is assumed the following, and no heat involved in RC2:

$$RC2 \xrightarrow[Srate:H2SO4,H2O]{} Source2 \xrightarrow[Oflow:H2SO4,H2O]{} RC1$$

$$T_{RC2} \xrightarrow[Srate:H2SO4,H2O]{} T_{RC2,Source} \xrightarrow[Oflow:H2SO4,H2O]{} T_{RC1}$$

$$RC2 \xleftarrow[Oflow:H2SO4,SO2,H2O]{} Source1 \xleftarrow[Srate:H2SO4,SO2,O2,H2O]{} RC1$$

$$T_{RC2} \xleftarrow[Oflow:H2SO4,SO2,H2O]{} T_{RC1,Source} \xleftarrow[Srate:H2SO4,SO2,O2,H2O]{} T_{RC1}$$

$$RC2 \xrightarrow[Srate:HI]{} Source2 \xrightarrow[Oflow:HI]{} RC3$$

$$T_{RC2} \xrightarrow[Srate:HI]{} T_{RC2,Source} \xrightarrow[Oflow:HI]{} T_{RC3}$$

$$RC2 \xleftarrow[Oflow:I2,HI]{} Source3 \xleftarrow[Srate:H2,I2,HI]{} RC3$$

$$T_{RC2} \xleftarrow[Oflow:I2,HI]{} T_{RC3,Source} \xleftarrow[Srate:H2,I2,HI]{} T_{RC3}$$

Note: Oflow will take place if sufficient Srate for that species is available according to the direction of flow. Thus $Srate_i \geq Oflow_i$, where i= species ID.

4. Simulate Fred's ½-scale experiment on the decomposition of sulfuric acid:

   a. Invoke IFLOW = 1

      [1] $T_{RC2,\ react} = T_{inlet}$ of Fred Experiment (30 °C)

      [2] $T_{RC2,\ source} = T_{inlet}$ of Fred Experiment (30 °C)

      [3] $T_{RC1,\ react} = T_{maximum}$ of Fred Experiment (850 °C)

      [4] $T_{RC1,\ source} = T_{outlet}$ of Fred Experiment (180 °C)

      [5] $T_{RC3,\ react} = T_{inlet}$ of Fred Experiment (30 °C)

      [6] $T_{RC3,\ source} = T_{inlet}$ of Fred Experiment (30 °C)

   b. Source and Outflow data

      [1] SRATE & OFLOW (H_2SO_4, H_2O) for RC 2—match data from Fred Experiment (acid solution inlet flow rate with f).

      [2] SRATE (H_2SO_4, SO_2, O_2, H_2O) for RC 1—rate computed as what in the chamber, so that no material remained in the chamber.

      [3] OFLOW (H_2SO_4, SO_2, H_2O) for RC 1—set to zero in order to simulate the experiment, because the temperatures in A.[1] and A.[4] above are very different—to properly account for the energy balance in Fred's experiment.

      [4] SRATE & OFLOW (HI) for RC 2—set to zero

[5] SRATE & OFLOW (I2, H2) for RC 3—set to zero

c. Chamber volume data:

[1] Volume for RC 1 = V_{upflow} + $V_{downflow}$ of Fred Experiment (1.6659×10^{-4} m^3)

[2] Volumes for RC 2 and RC 3 = 1 m^3

d. T_{fg} (in ºC) for H2SO4 with f, mole fraction of the acid, using equations in 4.d and 4.e in Section I.

B. INPUT DESCRIPTION

H2C00000 (activate H2 chemistry model flag) Contain (optional) keywords to activate the specific chemistry model

OPTION – Hydrogen generation chemistry model flag (CHARACTER)

='SULFUR_IODINE'	Sulfur Iodine (default)
='WESTING_SULFUR'	Westinghouse Sulfur (not implemented)
='CALCIUM_BR'	Ca Br (not implemented)
='USER_DEFINED'	User Defined (not implement)

TSTART – Time starts for turning on the chemistry model, after the reactor side goes through some iterations or establishes some steady flow. For SI, the decomposition of H_2SO_4 and HI are affected by this input. The formation of H_2SO_4 progresses at time zero.

ICHX – Number of heat exchanger(s) connected to the chemistry node. It is only used by the User Defined option above. All other models have this value hardwired (integer). (Not implemented)

IFLOW – Optional keyword to turn on and off the FLOW feature of the model. This is used to simulate Fred Gelbard's decomposition of the sulfuric acid experiment. On – 1, and Off – 0. (Default: 0)

H2Cnn001 (Specific chemistry model information for each reaction chamber). For example, SI contains three chambers. RC-1 models the formation of sulfuric acid and HI, RC-2 models the decomposition of sulfuric acid, and RC-3 models the decomposition of HI.nn is the chamber number for which the REQUIRED input is designated.

NAME= Characters (size=24)

IREACT= 1 for Decomposition of Sulfuric acid
2 for Formation of Sulfuric acid and HI
3 for Decomposition of HI

Note MELCOR will check if all three values have been assigned to an H2CnnRC1 card. It is a required input.

RCVOL= Corresponding volume for RCnn (m^3). This volume should be sufficient for the production of hydrogen for an 8-hour operation. Default=MELCOR will calculate the appropriate volume for an 8-hour operation based on the stoichiometric composition of the constituent in each chamber.

For IREACT=2, minimum volume = 1m3
For IREACT=1, RCVOL=1

RTEMP= Design reaction temperature for RCxx (K). Although MELCOR would calculate this temperature based on the heat transfer between the reactor side and chemistry side of the heat exchange (CHX), this value is used to set the maximum temperature of the chamber. Ideally, the following reaction temperature is recommended:

RTEMP (IREACT=1) = 1123.15 ºK,
RTEMP (IREACT=2) = 393.15 ºK, and
RTEMP (IREACT=3) = 723.15 ºK.

H2Cnn002 (Specific chemistry model information for each reaction chamber), nn is the chamber number for which the optional input is designated. Fresh water flow is needed for generating continually hydrogen. In addition, the plant should also need to know how fast oxygen and hydrogen removed from the plant. One mole of fresh water in, there should be half mole of oxygen and 1 mole of hydrogen produced. Although the input is optional, it suggests that the user should select an appropriate flow rate based on the volume(s) of the chamber(s) selected. REQUIRED input, enter all zero, if want to use default. *Note that if IFLOW = 1 is invoked, additional SRATE entries are expected. All SRATE entries must be entered, following by a single STEMP input for each chamber*.

SRATE – Source or sink rate (mol/s). Positive is the constant rate. Negative is the control function number for which rate versus time is expected.

When IFLOW = 0, the following entries are expected:

For SI model, If IREACT=2, it is the water flow in rate (default= 1 mol/s). If IREACT=1, it is the oxygen flow out rate (default = 0.0 mol/s). This permits MELCOR to calculate the flow out rate based on the amount reacted. If IREACT=3, it is the hydrogen flow out rate (default = 0.0 mol/s). This permits MELCOR to calculate the flow out rate based on the amount reacted.

When IFLOW = 1, the following entries are expected for each source in the chamber:

For SI model, If IREACT=2, in addition to the water flow in rate (default = 1 mol/s), MELCOR requires additional sourced out flow rates of the sulfuric acid solution to RC1, and HI to RC3. Thus the order of entries is: H_2O, H_2SO_4, and HI (default: all at 0.0 mole/s) [4 entries are expected]. If IREACT=1,

in addition to the oxygen flow out rate, MECLOR requires additional sourced out flow rates of the un-reacted sulfuric acid solution, and sulfuric dioxide to RC2. Thus, the order of entries is H_2SO_4, SO_2, and H_2O (default: all at 0.0 mole/s) [4 entries are expected]. If IREACT=3, in addition to the hydrogen flow out rate, MELCOR requires additional sourced out flow rates for both iodine and un-reacted HI. The order of entries is I_2 and HI (default: all at 0.0 mole/s). [3 entries are expected] Note that the sourced out rate is a designed value, MELCOR will calculate the sourced out rate based on the amount reacted, and un-reacted. Of course, the MELCOR rate will not exceed the designed rate entered here.

STEMP – Corresponding temperature for SRATE above (K). (Default = 393.15 K). Only one entry per chamber, it is the last value to be entered for this card.

H2Cnn003 is the designated species inventory card for RCnn. Species y concentration input entry is according to each IREACT value. For those species that are not entered, MELCOR would calculate the corresponding species concentration according to stoichiometric composition of the reaction in the chamber. y for CONC entry below for RCnn (integer). For IREACT=1, value should be 1 to 5 and up to 5 entries are expected for input. The order is based on the table entry in Table RC-1.1. For IREACT=2, use Table RC-2.1, and For IREACT=3, use Table RC-3.1. MELCOR will check against IREACT value, and valid species y index. It is suggested to only enter the initial amount of H_2O, SO_2, and I_2 in RC-2 as a start and let MELCOR to compute the concentration of the other species in RC-1 and RC-3.

CONC = Corresponding Initial species concentration for y above (mol/m^3).

H2CnnCF1 is designated as the design flow between reaction chambers. Outflow entries are expected. For IREACT=1, 2 values are expected for the sulfuric acid solution (H_2O, SO_2) to RC1. For IREACT=2, 2 values are expected for the sulfuric acid to RC1, and HI to RC3. For IREACT=3, 1 value is expected for the I_2 to RC2. For IFLOW=1, additional entries are required. See below.

When IFLOW = 0, required entries are explained above:

OFLOW = Corresponding molar flow rate out of RCnn (mol/s). For IREACT=2, the corresponding OFLOW of H_2SO_4 (currently no H_2O is assumed).

When IFLOW = 1 required entries are followed:

OFLOW = Corresponding molar flow rate out of RCnn (mol/s).

For IREACT = 1, 3 entries are required in the order for (H_2SO4, SO_2, H_20) to RC2 (default: None).

For IREACT = 2, 3 entries are required in the order for (H_2O, H_2SO_4) to RC1 (default: None), and HI to RC3 (default: None).

For IREACT = 3, 2 entries are required in the order for (HI, I_2) to RC1 (default: None).

Heat exchanger information card entries (Required). CHX module is a modification of the IHX module developed by Randy C., and is only permitted flow through the reactor side and no flow is modeled in the chemistry node. Each reaction chamber (RC) requires a CHX. Note: the model assumes no heat from the chemistry side to dump back into the reactor side. It is assumed that heat is required from the reactor side of CHX to carry out hydrogen production, for which one is for the decomposition of H_2SO_4 and the other is for decomposition of HI. Note that RC-2 does not require any heat from the heat exchanger. All its sensible heat for the inflow and outflow from and to other chambers are accounted for in the other chambers. The following is recommended:

H2CnnHX0 Name Type IFL

Name – character string for name of the heat exchanger

IFL1 – Flow path associated with this heat exchanger

H2CnnHX1 Area Data

Area – Heat transfer area (m^2)

Data – Heat transfer coefficient data. If REAL is entered it is the value of heat transfer coefficient, and if INTEGER is entered it is the CONTROL FUNCTION NUMBER, and it will require CF card entries. J/m^2-K

Chemistry dependence information card entries (Required). This card is intended for the user to supply the chemistry dependence information, such as the reaction rate constant, k, in the Arrhenius form ($k = A \cdot e^{\frac{-E}{R \cdot T}}$, where A is a pre-exponential or frequency factor, which has unit dependent on the reaction type (i.e., s^{-1} for the decomposition of H_2SO_4, E is the activation energy (J/mole), R is the gas constant (8.314 J/mole-K), and T is the reaction temperature (K)). In addition, because the reaction such as when the flow feature is turned on (IFLOW=1), then a residence time may be entered to match the time taken for the reaction. Note currently k is ONLY applied to the FORWARD reaction. Future card for the REVERSE reaction will be developed.

H2CnnCH1 ACOEF EACT RTIME

ACOEF – Pre-exponential or frequency factor, if zero is entered, default value will be used (default is for that IREACT)

EACT – Activation Energy (J/mole), if zero is entered, default value will be used (default is for that IREACT)

RTIME – Residence time (s), if zero is entered, MELCOR timestep will be used (default is for that IREACT). Note that RTIME is applied only for IFLOW=1. If IFLOW=0, this input is not used. Also, for the HI decomposition, this time is not used.

Default Parameters

IREACT=1, ACOEF= 6.8e4 s^{-1}, EACT=73.1e3 J/mol

IREACT=2, ACOEF= 3.0e-12 m^2/mol^2-s, EACT=4.187e3 J/mol

IREACT=3, ACOEF= 1.0e8 m/mol-s, EACT=108e3 J/mol

Available Plot Variables and Control Function Variables

FL-H2C-TOUT –Primary side outlet temperature (Heat Exchanger) for RC (K)
FL-H2C-TRIN –Secondary side inlet temperature (Heat Exchanger) for RC (K)
FL-H2C-TROUT –Secondary side outlet (reaction) temperature for RC (K)
FL-H2C-HCOEFF –Heat transfer coefficient for heat exchanger in RC (J/m^2-K)
FL-H2C-Qhx –Power for heat exchanger in RC (W)
FL-H2C-SP-1 –chamber inventory for species 1 (mole/m3)
FL-H2C-SP-2 –chamber inventory for species 2(mole/m3)
FL-H2C-SP-3 –chamber inventory for species 3(mole/m3)
FL-H2C-SP-4 –chamber inventory for species 4(mole/m3)
FL-H2C-SP-5 –chamber inventory for species 5(mole/m3)
FL-H2C-OF-1 -outflow rate for species 1 (mol/s)
FL-H2C-OF-2 -outflow rate for species 2 (mol/s)
FL-H2C-OF-3 -outflow rate for species 3(mol/s)
FL-H2C-OF-4 -outflow rate for species 4(mol/s)
FL-H2C-OF-5 -outflow rate for species 5(mol/s)
FL-H2C-OF-6 -outflow rate for species 6(mol/s)
FL-H2C-OF-7 -outflow rate for species 7(mol/s)
FL-H2C-OF-8 -outflow rate for species 8(mol/s)
FL-H2C-SR-1 -source rate for species 1 (mol/s)
FL-H2C-SR-2 -source rate for species 2 (mol/s)
FL-H2C-SR-3 -source rate for species 3 (mol/s)
FL-H2C-SR-4 -source rate for species 4 (mol/s)
FL-H2C-OINV-1 -outflow inventory for species 1 (moles) for IFLOW=1
FL-H2C-OINV-2 -outflow inventory for species 2 (moles) for IFLOW=1
FL-H2C-OINV-3 -outflow inventory for species 3 (moles) for IFLOW=1
FL-H2C-OINV-4 -outflow inventory for species 4 (moles) for IFLOW=1
FL-H2C-OINV-5- outflow inventory for species 5 (moles) for IFLOW=1
FL-H2C-OINV-6- outflow inventory for species 6 (moles) for IFLOW=1
FL-H2C-OINV-7- outflow inventory for species 7 (moles) for IFLOW=1
FL-H2C-OINV-8- outflow inventory for species 8 (moles) for IFLOW=1
FL-H2C-SINV-1- source out inventory for species 1 (moles) for IFLOW=1
FL-H2C-SINV-2- source out inventory for species 2 (moles) for IFLOW=1
FL-H2C-SINV-3- source out inventory for species 3 (moles) for IFLOW=1
FL-H2C-SINV-4- source out inventory for species 4 (moles) for IFLOW=1

3.8 Chapter 3 References

Brown, L. C., G. E. Besenbruch, R. D. Lentsch, et al., 2003, *High Efficiency Generation of Hydrogen Fuels Using Nuclear Power*, General Atomics, GA-A24285, Rev. 1, December 2003.

Forsberg, C., L. Trowbridge, B. Bischoff, and L. K. Mansur, 2004, Sulfur Thermochemical Processes with Inorganic Membranes to Produce Hydrogen, *3rd Topical Conference on Fuel Cell Technology (Embedded Topical), 2004 American Institute of Chemical Engineers Spring National Meeting*, New Orleans, Louisiana.

Huang, C. and A. T-Raissi, 2005, Analysis of Sulfur-Iodine Thermochemical Cycle for Solar Hydrogen Production. Part I: Decomposition of Sulfuric Acid, *Solar Energy 2005*, 78:632-646.

Jeong, Y. H., M. S. Kazimi, K. J. Hohnholt, and B. Yildiz, 2005, *Optimization of the hybrid sulfur cycle for hydrogen generation.* MIT Report MIT-NES-TR-004.

Larminie, J., and A. Dicks, 2003, *Fuel Cell Systems Explaines*, 2nd Ed., Wiley, New York.

Oxtoby, D. W., and N. H. Nachtrieb, 1986, *Principles of modern chemistry*, Saunders College Publishing.

4. SECONDARY COMPONENT MODELING

4.1 Chapter 4 Highlights

We are currently extending the capabilities of the MELCOR-H2 code (Gauntt et al., 2000) to analyze large-scale hydrogen production plants with a VHTR and cogeneration of electricity. Sophisticated but fast-running mean-line analysis flow models of axial-flow, multistage turbine and compressor units, and a transient, multi-node model of a generic heat exchanger were developed for a VHTR-Closed Brayton Cycle (CBC) nuclear power plant. Also, FORTRAN source codes were developed for incorporation into MELCOR-H2. The developed models, written in FORTRAN 95 standard language, were compiled and tested using Compaq Visual FORTRAN Professional Edition 6.5.0 (2000), which provides a superset of the FORTRAN 95 standard with other extensions for compatibility with previous FORTRAN languages and platforms. Nonetheless, the present models do not use any of the advanced capabilities of the FORTRAN 95 language, and are therefore backward compatible with FORTRAN 77.

The constituent equations for the present models of the turbine and compressor units and generic heat exchanger have been previously documented in Report No. UNM-ISNPS-2-2006, entitled *Models of turbine and Compressor Units for MELCOR Secondary System Modules* (Tournier and El-Genk, 2006). These equations are included in Appendices B and C; however, the reader is encouraged to acquire a copy of this earlier document for more details. This document also highlights the changes made to the models. These changes are necessary in order to predict the operation of the turbine and compressor units at off-design (and extremely off-design) conditions, which are encountered during startup and shut-down of the CBC. Furthermore, an effective numerical solution of the flow conservation equations was developed, which is more stable and significantly reduces the number of internal iterations and the amount of CPU time, compared to the numerical technique suggested in Tournier and El-Genk (2006).

Due to the complexity of the geometry and the large number of parameters necessary to define the blade cascades of the axial-flow, multistage turbine and compressor units, input files are provided which emulate the design of the Japanese GTHTR300 turbo-machinery (Takizuka et al., 2004). Model results were compared successfully with the performance of the Japanese GTHTR300 6-stage turbine rated 530 MW, and that of the GTHTR300 20-stage compressor rated 251 MW. The present performance results using helium gas properties (which behave essentially like a perfect gas) predict compressor exit temperature and pressure of 408.8 K and 7.10 MPa, compared to the reported values of 410 K and 7.11 MPa by Takizuka et al. (2004). The calculated shaft work to the compressor is 251.3 MW, compared to 251 MW (Takizuka et al., 2004). For the turbine unit, the calculated shaft work is 531.5 MW, compared to 530 MW. The present calculations also predict turbine exit temperature and pressure of 891.5 K and 3.64 MPa, compared to 891 K and 3.68 MPa reported by Takizuka et al. (2004). Furthermore, operation maps of these two rotating units are developed, which exhibit expected trends. These maps are included in this Manual for benchmarking purposes.

The new changes made to the turbine and compressor models over those described in Tournier and El-Genk (2006) and the present numerical solution technique are presented in Sections 4.3 and 4.4, respectively. The turbine and compressor input files and the model subroutines are described in detail in Sections 4.5 and 4.6, and guidelines for implementing them into

MELCOR-H2 are presented. The operation maps of the Japanese GTHTR300 turbine and compressor were developed using the present models, and presented in Sections 4.7 and 4.8. The constituent equations of the turbine and compressor loss models are summarized in Appendices B and C with complete nomenclature of the symbols used in the equations. The FORTRAN code of the subroutines is collected in the subsequent Appendices D through R.

A transient model of a multi-node, generic heat exchanger was also developed (Chapter 4-7). The model assumes that the primary and secondary coolants are single phase (gas or liquid), and can handle either parallel-flow or counter-current flow arrangement. An extremely efficient, iterative segregated solution technique based on the SIMPLE-Consistent algorithm was developed for solving the coupled transient and compressible energy, momentum, and mass balance equations of the heat exchanger. The subroutines of the models and the input and output files parameters are described in Section 4.10, and guidelines are given to properly implement the model in MELCOR-H2 and to extend the thermophysical property subroutines to other working fluids and heat exchanger structural materials. Finally, transient and performance results of a helium/water pre-cooler and a helium/helium recuperator operating at the inlet flow conditions encountered in the Japanese GTHTR300 CBC plant are presented in Sections 4.11 and 4.12. These results are provided for benchmark purposes and to verify the proper implementation of the heat exchanger model into MELCOR-H2.

4.2 Chapter 4 Nomenclature

A	Cross–sectional flow area (m^2)
c	Gas sonic velocity (m/s), $c = \sqrt{\gamma RT}$
C	Actual chord length of blade (m)
C_L	Blades lift coefficient based on mean vector velocity
C_p	Specific heat at constant pressure (J / kg.K)
CR	Convergence ratio, $CR = \cos\phi_1 / \cos\phi_2$
C_v	Heat capacity at constant volume (J/kg.K), $C_v = C_p - R$
C_x	Axial chord length of blade (m), $C_x = C \times \cos\Phi$
D	Diameter (m)
D_{eq}	Equivalent diffusion ratio (suction surface peak velocity / outlet velocity)
D_{eq}	Equivalent hydraulic diameter (m)
D_{hub}	Hub diameter of rotor wheel (m)
e	Internal energy per unit mass (J/kg)
f	Darcy friction factor
F_t	Tangential loading parameter
h	Enthalpy per unit mass, $h = e + P/\rho$ (J / kg)
$\hat{h}$	Stagnation (or total) enthalpy per unit mass, $\hat{h} = h + 0.5\overline{\alpha}_3 V^2$ (J / kg)
H	Height of blades (m)
h^{CV}	Convective heat transfer coefficient ($W / m^2.K$), $h^{CV} = Nu\ \lambda / D_{eq}$
H_{TE}	Boundary-layer shape factor, $H_{TE} = \delta^*_{TE} / \theta_{TE}$
i	Blade incidence angle at leading edge (^{o})
i_C	Negative stall incidence angle of blades cascade (^{o})

i_o	Blade incidence angle for zero camber (^{o})
i_S	Positive stall incidence angle of blades cascade (^{o})
i_{SR}	Reference stalling incidence angle for turbine cascade with $S / C = 0.75$ (^{o})
i^*	Optimum design incidence angle at leading edge of compressor blades (^{o})
K_{inc}	Off-design incidence correction factor
k	Boltzmann constant, $k = 1.3804 \times 10^{-23}$ J/K
L	Length of flow channel (m)
L_{fin}	Length of heat transfer fins (m)
$\dot{m}$	Mass flow rate of working fluid (kg / s)
M	Molecular weight (kg/mole)
Ma	Gas Mach number, $\text{Ma} = \overline{V} / c$
N	Shaft angular speed in rotations per minute (rpm)
N_{a}	Avogadro number, $N_{\text{a}} = 6.0225 \times 10^{23}$ molecules/mole
N_{rot}	Number of rotor blades
N_{sta}	Number of stator blades
Nu	Coolant Nusselt number
O	Throat width between blades in cascade (m)
P	Pressure (Pa)
$\hat{P}$	Stagnation (or total) pressure, $\hat{P} = P + 0.5\overline{\alpha}_3 \rho V^2$ (Pa)
Pe	Peclet number, Pe = Re x Pr
Pr	Coolant Prandtl number, $\text{Pr} = \mu C_{\text{p}} / \lambda$
r	Average radius of blade (m), $r = 0.5 \times (r_{hub} + r_{tip})$
R	Gas constant, $R = R_g / M$ (J / kg.K)
R	Radius (m)
Re	Flow Reynolds number, $\text{Re} = \rho \overline{V} D^{eq} / \mu$
S	Pitch or distance between blades in cascade (m)
S_{fin}	Finned heat transfer surface area (m^2)
S_{un}	Unfinned heat transfer surface area (m^2)
R_g	Universal gas constant, $R_g = kN_{\text{a}} = 8.3143$ J/mole.K
t	Time (s)
t_{max}	Maximum blade thickness (m)
t_{TE}	Thickness of blades trailing edge (m)
T	Temperature (K)
U	Rotor tangential velocity (m / s), $U = R\omega$
$\vec{\mathbf{V}}$	Gas absolute velocity vector (m / s)
V_r	Gas radial velocity component (m / s)
V_x	Gas meridional velocity component (m / s)
V_θ	Gas tangential velocity component (m / s)
$\overline{V}$	Average flow velocity in channel (m / s)
$\vec{W}$	Gas relative velocity vector with respect to rotor wheel (m/s), $\vec{W} = \vec{V} - \vec{U}$

$\dot{W}$	Rate of mechanical work done by working fluid on surrounding (W)
Y	Pressure loss coefficient of a blades cascade
Z	Gas compressibility factor
Z/C	Relative position of maximum camber, measured from leading edge
Z_{TE}	Spanwise penetration depth between primary and secondary loss regions (m)

Greek

α	Angle between gas absolute velocity vector and meridional plane (degrees)
$\overline{\alpha}_n$	Coefficient which accounts for the non–uniformity of velocity profile
$\overline{\alpha}_2$	Velocity profile correction factor, $\overline{\alpha}_2$ = 1.020 for turbulent flow
$\overline{\alpha}_3$	Velocity profile correction factor, $\overline{\alpha}_3$ = 1.056 for turbulent flow
β	Blade angle relative to meridional plane (degrees)
γ	Ratio of specific heat capacities, $\gamma = C_p / C_v$
$\Gamma*$	Blade circulation parameter (dimensionless)
δ	Boundary layer thickness (m)
$\delta*$	Boundary layer displacement thickness (m)
δ_{fin}	Thickness of heat transfer fins (m)
δ_M	Mach number correction to incidence angle (^{o})
Δi_S	Stalling incidence angle correction for other S / C values (degrees)
ΔP	Total pressure loss (Pa)
$\Delta\Phi$	Kinetic energy loss coefficient
ζ	Camber angle of compressor blades (^{o}), $\zeta = \lvert\beta_1 - \beta_2\rvert$
η	Efficiency, dimensionless
θ	Boundary layer momentum thickness (m)
λ	Thermal conductivity (W / m.K)
μ	Coolant dynamic viscosity (kg / m.s)
ρ	Density (kg / m^3)
σ	Blade cascade solidity, $\sigma = C / S$
τ	Blades clearance gap (m)
ϕ	Angle between gas relative velocity vector and meridional plane (degrees)
Φ	Blades stagger angle measured from axial direction (degrees)
ω	Shaft angular speed (radians / s)

Subscript/Superscript

θ	Tangential or “whirl” component
AM	Loss model of Ainley and Mathieson (1951)
b	Coolant bulk
C	Compressor
cas	Casing of turbo-machinery
disk	Disk friction losses degraded to gas enthalpy increase
fin	Heat transfer fins
hub	Hub of impeller
LE	Leading edge of blades

n	Iteration number
o	Value for constant properties case
p	Profile losses
r	Radial component
s	Secondary losses
T	Turbine
TC	Tip clearance losses
TE	Trailing edge of blades
tip	Tip of impeller
w	Wall surface
wind	Windage mechanical losses
x, z	Axial component
0	Inlet of contraction/expansion zone (previous blade trailing edge)
1	Inlet of blades cascade (leading edge)
2	Outlet of blades cascade (trailing edge)
(*n*)	Best estimate at present iteration
(*n*+1)	New value at completion of iteration

4.3 Off-Design Performance Model of Turbine Unit

This section describes the changes made to the turbine performance model described previously by Tournier and El-Genk (2006). These changes were necessary in order to predict the operation of the turbine unit at off-design (and extremely off-design) conditions, which are encountered during startup and shutdown of the CBC. Furthermore, a new numerical solution of the flow conservation equations is developed, which exhibits much stronger stability and significantly reduces the number of internal iterations and the amount of CPU time, compared to the numerical technique suggested previously (Tournier and El-Genk, 2006). What follows is a quick description of the design and operation principle of a multi-stage, axial-flow turbine.

4.3.1 Turbine Design and Operation Principle

Figure 4-1 illustrates the basic configuration of an axial-flow turbine with three stages. Each stage consists of a cascade of stationary blades (Inlet Guide Vanes, IGV, or Stator, S), which increases the swirl (tangential) velocity of the gas in the direction of rotation, followed by a cascade of rotating blades (Rotor, R), which absorbs the gas swirl velocity and converts it to rotor mechanical (or kinetic) energy. Both processes in the turbine operate at the expense of gas static pressure, so that the gas pressure decreases as the gas flows through each blades cascade. It is a common practice in axial-flow turbomachines to design a multistage turbine for nearly constant axial flow velocity throughout. As a result, the annular flow area must increase from inlet to outlet since the gas pressure and density decrease as the gas flows through the turbine. Typically, an exit guide vanes cascade (EGV) follows the last turbine stage to remove any residual swirl velocity and convert that kinetic energy to an increase in static pressure (Figure 4-1). Although not shown on the figure, a diffuser will follow the exit guide vanes to recover as much kinetic energy as possible, as well as to direct the flow to its intended destination. Similarly, an inlet flow passage will precede the inlet guide vanes. This can range from a smooth axial bell-mouth inlet to a complex side inlet, depending on the application.

The construction of velocity diagrams (or triangles) is a fundamental tool for all turbomachinery aerodynamic design and analysis. Since successive blade cascades alternate between stator and rotor, it is necessary to be able to view the velocity vectors in both stationary and rotating coordinate systems at any location. Typical velocity triangles at the leading and trailing edges of a turbine rotor cascade are shown in Figure 4-2. An orthogonal coordinate system (x , θ) is used where the meridional coordinate, x, is identical to the axial coordinate (axis of the turbomachinery), and θ is the polar angle of a cylindrical coordinate system. Subscript 1 refers to the cascade inlet station, and subscript 2 refers to the cascade exit station. The velocity in the stationary coordinate system (absolute velocity) is designated by V, and the velocity in the rotating coordinate system (relative velocity) is designated as W (Figure 4-2). Finally, U is the tangential velocity of the rotating blades ($U = U_\theta$), and α and ϕ designate the absolute and relative velocity angles, respectively (Figure 4-2).

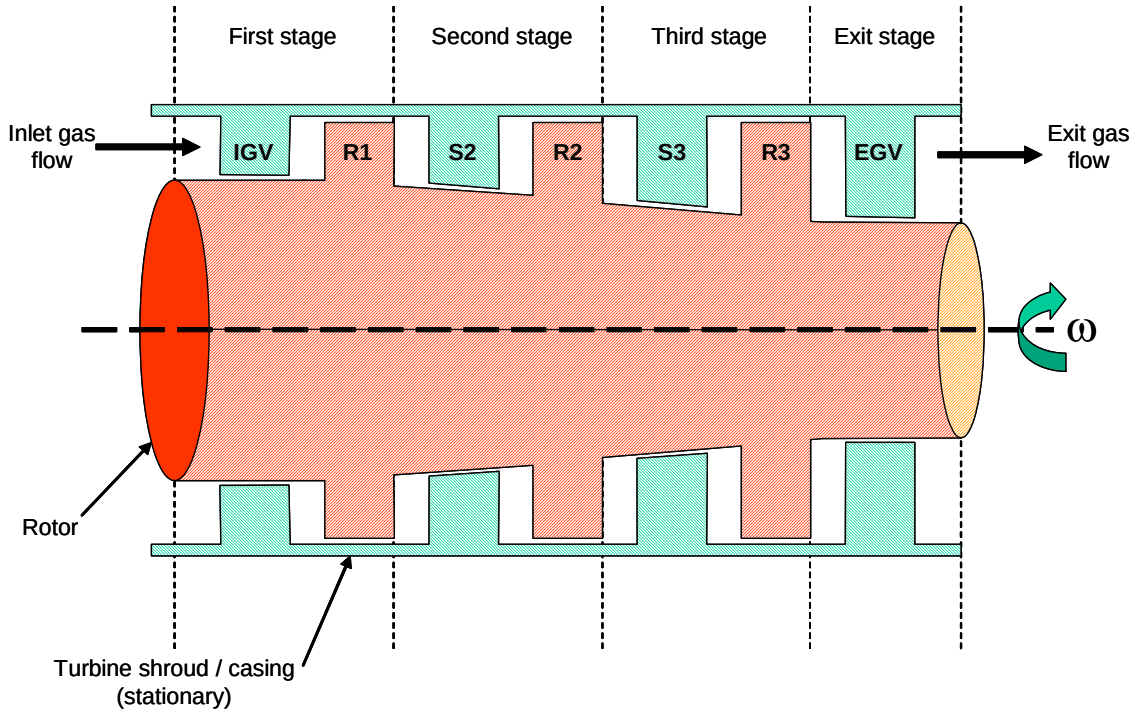

Figure 4-1. Schematic of a multistage axial-flow turbine.

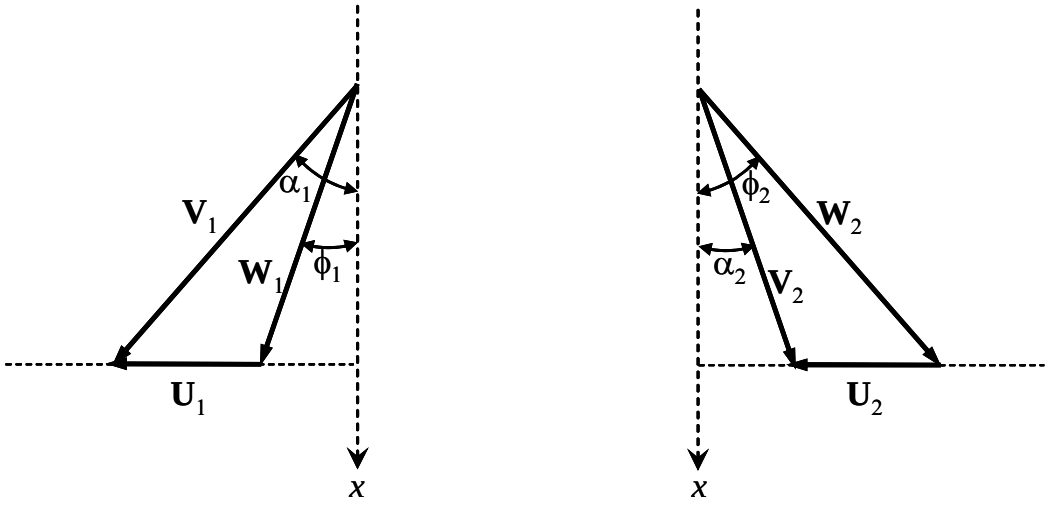

(a) Leading edge (b) Trailing edge

Figure 4-2. Velocity triangles of turbine rotor blades.

4.3.2 Incidence Losses for Off-Design Conditions

According to the loss scheme of Benner et al. (2006a and 2006b), the total pressure loss coefficient of a turbine blades cascade at optimum design conditions is the sum of the coefficients for profile losses, secondary losses, trailing edge losses and tip clearance (leakage) losses (see Appendix B):

$$Y = (1 - Z_{TE} / H) \times Y'_p + Y'_s + Y_{TE} + Y_{TC} \,. \tag{4-1}$$

In this equation, Z_{TE} is the spanwise penetration depth of the passage vortex separation line ($Z_{TE} \leq H/2$) at the trailing edge.

Ainley and Mathieson (1951) have introduced an off-design incidence correction factor, K_{inc}, such that Equation (4-1) is rewritten more generally:

$$Y = K_{inc} \times (1 - Z_{TE} / H) \times Y'_p + Y'_s + Y_{TE} + Y_{TC} \,. \tag{4-2}$$

Figure 4-3 shows K_{inc} as a function of the ratio of the incidence angle, $i = \phi_1 - \beta_1$, to the stalling incidence angle, i_S, based on a correlation proposed by Aungier (2006) from fitting the experimental data of Ainley and Mathieson (1951):

$$\text{When} \quad i < 0, \qquad K_{inc} = 1 + 0.52 \times \left| i / i_S \right|^{1.7} \;; \tag{4-3a}$$

$$\text{When} \quad i \geq 0, \qquad K_{inc} = 1 + \left| i / i_S \right|^{2.3 + 0.5 \times i / i_S} \;. \tag{4-3b}$$

An upper limit of K_{inc} = 20 is required in the model. The stalling incidence angle, i_S, is a function of ϕ_2, $\xi = \beta_1 / \phi_2$ and S / C, the ratio of blades pitch to chord length. It is calculated as the sum of a reference value $i_{SR}(\phi_2, \xi)$ corresponding to a blades cascade with S / C = 0.75, and a correction term, $\Delta i_S(\phi_2, S/C)$ to adjust for other values of pitch-to-chord ratio:

$$i_S(\phi_2, \xi, S/C) = i_{SR}(\phi_2, \xi) + \Delta i_S(\phi_2, S/C) \ . \tag{4-4}$$

Figure 4-4 shows the stalling incidence angle for S / C = 0.75, as a function of ξ and ϕ_2, based on a correlation proposed by Aungier (2006) from fitting the experimental data of Ainley and Mathieson (1951):

$$\text{When } \phi_2 \geq 50^o, \qquad i_{SR}(\phi_2, \xi) = i_{So} + A - B\xi^2 + D\xi^3 + E\xi^4, \quad \text{where} \tag{4-5a}$$

$$i_{So} = 20 - (\xi + 1)/0.11 \ , \tag{4-5b}$$

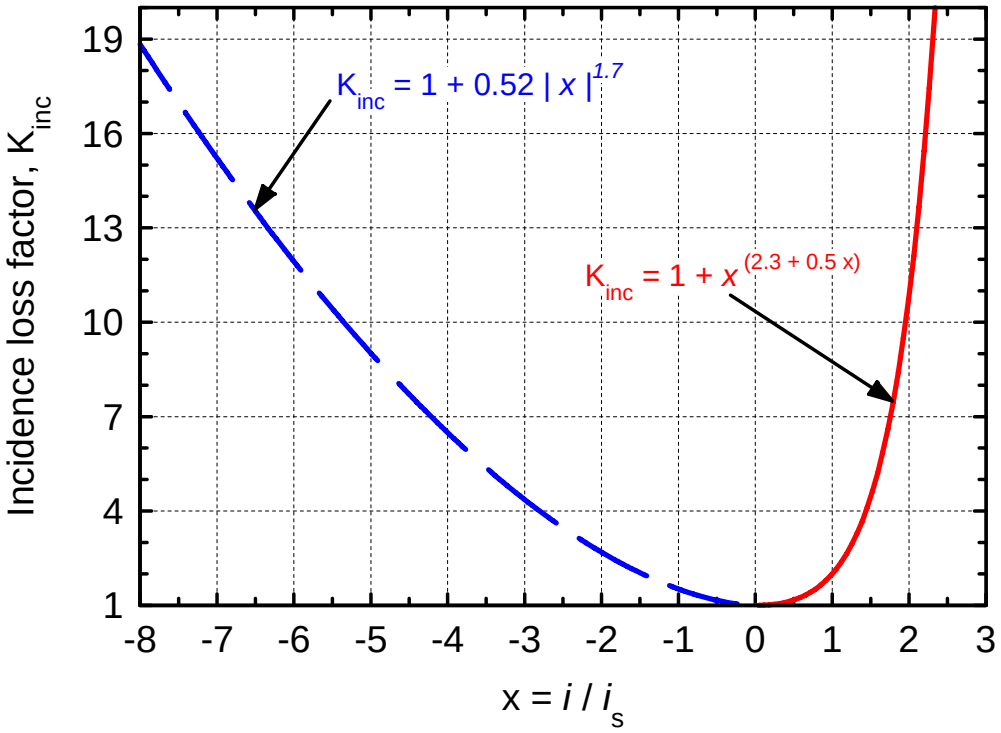

Figure 4-3. Off-design incidence correction factor for turbine blades (Aungier, 2006).

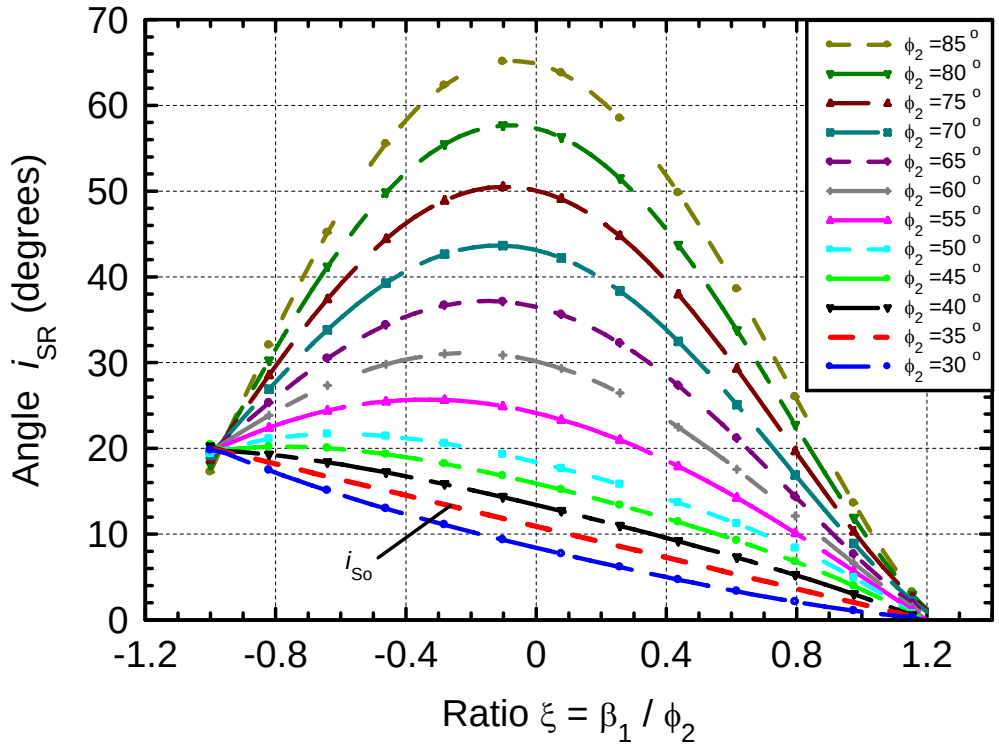

Figure 4-4. Stalling incidence angle for *S* / *C* = 0.75 (Aungier, 2006).

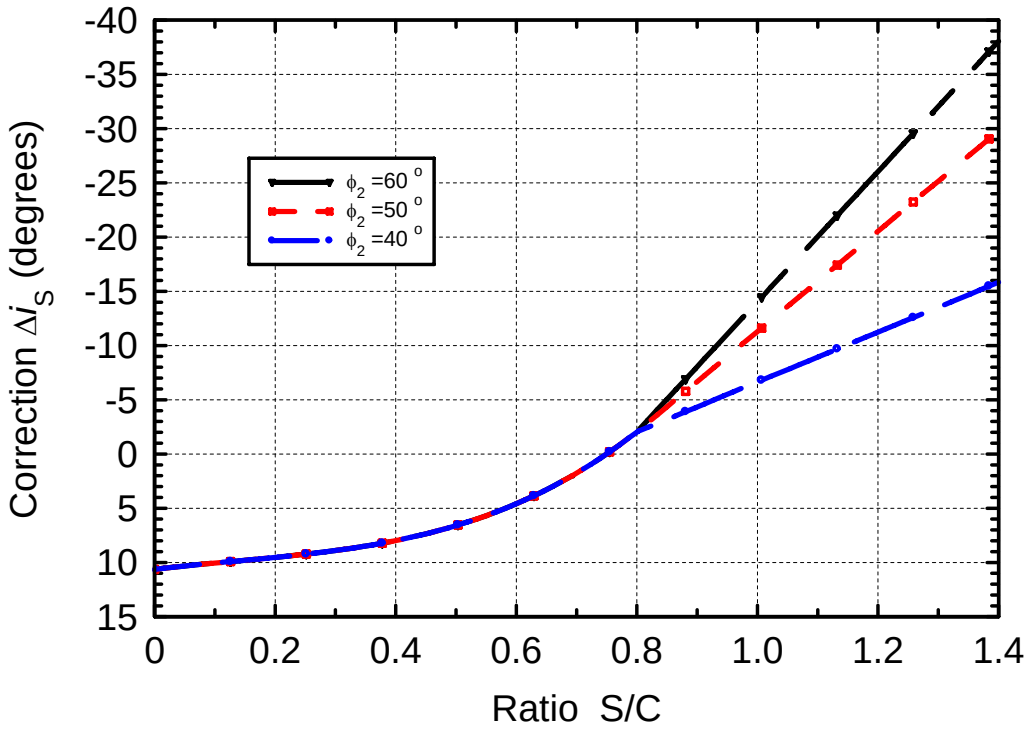

Figure 4-5. Stalling incidence correction factor (Aungier, 2006).

$$A = 61.8 - (90^o - \phi_2) \times \left[1.6 - (90^o - \phi_2)/165\right] \quad , \tag{4-5c}$$

$$B = 71.9 - (90^o - \phi_2) \times 1.69 \quad , \tag{4-5d}$$

$$D = \ 7.8 - (90^o - \phi_2) \times \left[0.28 - (90^o - \phi_2)/320\right] \quad , \tag{4-5e}$$

$$E = 14.2 - (90^o - \phi_2) \times \left[0.16 + (90^o - \phi_2)/160\right] \quad . \tag{4-5f}$$

When $\phi_2 < 50^o$, $\quad i_{SR}(\phi_2, \xi) = i_{So} + \left| i_{SR}(50^o, \xi) - i_{So} \right| \times \dfrac{(55 - 90 + \phi_2)}{15}$. (4-5g)

Note that the last term in parentheses on the right -side must be allowed to change sign, unlike the Equation 4-52 reported in Aungier (2006).

Finally, Figure 4-5 shows the correction term, $\Delta i_S(\phi_2, S/C)$, using the correlation developed by Aungier (2006):

When $S/C < 0.8$, $\quad \Delta i_S = -38X - 53.5X^2 - 29X^3$, where $\quad X = S/C - 0.75$. (4-6a)

When $S/C \geq 0.8$, $\quad \Delta i_S = -2.0374 - (S/C - 0.8) \times \left[69.58 - \left| \dfrac{90^o - \phi_2}{14.48} \right|^{3.1} \right]$. (4-6b)

Note that the first constant (– 2.0374) must be negative, unlike the Equation (4-55) reported in Aungier (2006). Note that all angles are expressed in degrees in these equations.

4.3.3 Solution of Flow Conservation Equations in Turbine Blades Cascade

The numerical solution of a multistage turbo-machinery component proceeds in the direction of the flow; that is, when conditions are known at the entrance of a section, the outlet conditions are calculated as a function of inlet conditions, from section to section and stage to stage, moving downstream. Each stage consists of a stator half-stage, followed by a rotor half-stage (except the exit guide vanes, which are followed by a diffuser). A half-stage consists of an isentropic expansion section {0 – 1} between two cascades, followed by a blades section {1 – 2} that exhibits pressure losses. For the sake of discussion, we assume that all flow conditions at station {0} are known, and we proceed to calculating those at stations {1} and {2}. The relative gas flow angle, ϕ_2 at the trailing edge of the blades is a function of the blades angle and the deviation angle, δ:

$$\phi_2 = \beta_2 + \delta \, . \tag{4-7a}$$

The deviation angle at the trailing edge of a turbine blade cascade is calculated using a recent correlation developed by Zhu and Sjolander (2005), as:

$$\delta = 17.3\frac{(S/C)^{0.05}\times(\phi_1+\beta_2)^{0.63}\times\cos^2(\Phi)\times(t_{\max}/C)^{0.29}}{(30+0.01\beta_1^{2.07})\times\tanh(\mathrm{Re}_{2C}/200{,}000.)}, \tag{4-7b}$$

where all angles are expressed in degrees. The Reynolds number at the trailing edge is based on the relative gas velocity and the actual blade chord: $\mathrm{Re}_{2C} = (\rho_2 W_2 C)/\mu_2$.

Because the deviation angle does not change very quickly, a solution technique that performs iterations based on the convergence of δ and/or ϕ_2 converges much more quickly than one based on finding the absolute gas flow angle of the rotor. The off-design model assumes that the flow does not turn in the expansion zone (Ainley and Mathieson, 1951), i.e.,

$$\alpha_1 = \alpha_o . \tag{4-8}$$

This means that the trailing edge of the upstream cascade controls the direction of the flow as it impinges onto the leading edge of the next cascade. If the angle of attack is correct, that is if the incidence angle $i_1 = \phi_1 - \beta_1$ is small, the blades cascade operates near optimum design conditions. A large angle of attack, however, will result in large off-design incidence losses, which are then calculated using the model described in Section 4.4.2.

To illustrate the new solution technique, we take the example of a turbine stator cascade, {1 – 2}. We know all flow conditions at station {1}, and the absolute gas flow angle at the trailing edge, $\alpha_2^{(n)} = \phi_2^{(n)}$ is known from Equation (4-7). The technique is extended for any real gas by linearizing the state equations as follows:

$$h_2^{(n+1)} = h_2^{(n)} + C_{p2}^{(n)} \times \left(T_2^{(n+1)} - T_2^{(n)}\right), \tag{4-9}$$

$$P_2^{(n+1)} = \rho_2^{(n+1)} R Z_2^{(n)} T_2^{(n+1)}, \tag{4-10}$$

where the subscript (n) refers to values calculated at the previous iteration, and (n+1) refers to the new iteration values. The conservation of mass, energy, and momentum can then be written:

$$\dot{m} = \rho_2^{(n+1)} V_2^{(n+1)} A_2 \cos\alpha_2^{(n)}, \tag{4-11}$$

$$\dot{m}\,\hat{h}_1 = \dot{m}\left(h_2^{(n+1)} + \frac{\overline{\alpha}_3}{2}\left(V_2^{(n+1)}\right)^2\right) + Q_{loss} - \dot{W}_T^{disk}, \tag{4-12}$$

$$\hat{P}_1 - P_2^{(n+1)} = (1+Y)\times\frac{\overline{\alpha}_3}{2}\rho_2^{(n+1)}\left(V_2^{(n+1)}\right)^2 . \tag{4-13}$$

As before, the five Equations (4-9) – (4-13) are solved explicitly for the five unknowns V_2, ρ_2, P_2, T_2, and h_2 at iteration (n+1), using simple substitution. Expressing all quantities in terms of V_2, the momentum conservation Equation (4-13) reduces to a second-order polynomial for the trailing edge velocity:

$$a(V_2)^2 + b(V_2) + c = 0\,, \tag{4-14}$$

where

$$a = \frac{\overline{\alpha}_3}{2}\left(\frac{\dot{m}}{A_2 \cos\alpha_2^{(n)}}\right)\times\left(1 + Y - \frac{RZ_2^{(n)}}{C_{p2}^{(n)}}\right), \tag{4-14b}$$

$$b = -\hat{P}_1\,, \tag{4-14c}$$

$$c = \left(\frac{\dot{m}}{A_2 \cos\alpha_2^{(n)}}\right)\times RZ_2^{(n)} \times T_{ref}\,, \tag{4-14d}$$

$$C_{p2}^{(n)}T_{ref} = C_{p2}^{(n)}T_2^{(n)} + \hat{h}_1 - h_2^{(n)} - \frac{Q_{loss} - \dot{W}_T^{disk}}{\dot{m}}\,. \tag{4-14e}$$

The solution of this polynomial equation is simply:

$$V_2^{(n+1)} = \frac{-b - \sqrt{b^2 - 4ac}}{2a}\,. \tag{4-14f}$$

In practice, numerical iterations are required, since the end-disk windage losses, $\dot{W}_T^{disk}$, heat losses, Q_{loss}, pressure loss coefficient, Y, and gas properties are also functions of the flow conditions at the trailing edge, which are not known a priori.

The same technique applies to the stator and rotor leading edges, where subscripts {1} and {2} are replaced with subscripts {0} and {1}, and the loss coefficient $Y = 0$ in the isentropic expansion zones. For the rotor leading edge {1}, the relative flow velocities and the incidence angle are easily calculated using the velocity triangle (Figure 4-2a) once the absolute gas flow velocity V_1 is obtained, as:

$$W_{1x} = V_{1x} = V_1 \cos\alpha_1 \tag{4-15a}$$

$$W_{1\theta} = V_{1\theta} - U_1 = V_1 \sin\alpha_1 - U_1 \tag{4-15b}$$

$$W_1^2 = W_{1x}^2 + W_{1\theta}^2\,, \tag{4-15c}$$

$$\tan\phi_1 = \frac{W_{1\theta}}{W_{1x}} \quad , \qquad \text{and} \tag{4-15d}$$

$$i_1 = \phi_1 - \beta_1 \quad . \tag{4-15e}$$

The sign convention for tangential velocity is positive in the direction of the impeller velocity (Figure 4-2).

The technique for the rotor cascade {1 – 2} is somewhat different, due to the interdependence between mechanical work, losses, absolute gas flow angle and velocity triangle. Again, we assume that all flow conditions at station {1} are known, and the relative gas flow angle at the trailing edge, $\phi_2^{(n)} = \beta_2 + \delta_2^{(n)}$ is known from Equation (4-7). The technique is again extended for any real gas by linearizing the state equations using Equations (4-9) and (4-10). We found that it was most efficient to write all quantities in terms of the unknown relative velocity $W_2^{(n+1)}$, and find its proper value which satisfies the momentum balance equation by a simple dichotomic research. For a given trial value W_2, the absolute gas velocity at the trailing edge is obtained from the velocity triangle (Figure 4-2b) as:

$$V_2 = \left(W_2^2 - 2U_2 W_2 \sin\phi_2 + U_2^2\right)^{1/2}, \tag{4-16}$$

and the absolute gas flow angle at the trailing edge is calculated as:

$$\tan\alpha_2 = \frac{\sin\phi_2 - U_2 / W_2}{\cos\phi_2} . \tag{4-17}$$

The gas density is obtained from the conservation of mass, as:

$$\rho_2 = \frac{\dot{m}}{A_2 V_2 \cos\alpha_2}, \tag{4-18}$$

And the cascade shaft work is given by Euler's equation:

$$\dot{W}_T = \dot{m} \times (U_1 V_{1\theta} + U_2 V_2 \sin\alpha_2) \quad . \tag{4-19}$$

The gas temperature is obtained from the energy balance equation as:

$$T_2 = T_{ref} - \left(\frac{\overline{\alpha}_3}{2} V_2^2 + \frac{\dot{W}_T}{\dot{m}} \right) / C_{p2}^{(n)} , \text{ where} \tag{4-20}$$

$$T_{ref} = T_2^{(n)} + \left(\hat{h}_1 - h_2^{(n)} - \frac{Q_{loss} - \dot{W}_T^{disk}}{\dot{m}} \right) / C_{p2}^{(n)} . \tag{4-21}$$

The gas pressure is calculated using the state Equation (4-10), as:

$$P_2 = \rho_2 R Z_2^{(n)} T_2 \ . \tag{4-22}$$

Finally, the function $F_2^T(\phi_2, W_2)$ is calculated, using the momentum balance equation with the proper definition of the pressure loss factor for a rotor cascade (Horlock, 1960; Fielding, 2000):

$$F_2^T(\phi_2, W_2) = P_2 + \frac{\overline{\alpha}_3}{2} \rho_2 \times (1+Y) W_2^2 - P_1 - \frac{\overline{\alpha}_3}{2} \rho_1 \times W_1^2 \ . \tag{4-23}$$

The function F_2^T is a monotonically decreasing function of W_2, and is equal to zero when the momentum balance equation is satisfied. The solution technique then simply consists in finding the zero of this function by performing a dichotomic research on W_2. Once the zero of F_2^T has been found, the conservation Equations (4-18), (4-20) through (4-23), Euler Equation (4-19), and velocity triangle Relations 4-16 and 4-17 are all satisfied. Internal iterations are then performed to resolve the dependences of pressure loss factor Y, deviation angle δ_2, heat losses Q_{loss}, and real gas enthalpy h_2 and compressibility factor Z_2.

4.4 Off-Design Performance Model of Compressor Unit

This section describes the changes made to the compressor performance model described previously by Tournier and El-Genk (2006). The philosophy used in the turbine model and solution technique, described in the previous sections, is also applied to the model of the compressor unit, but using the proper incidence loss model correlations and velocity triangle relationships. What follows is a quick description of the design and operation principle of a multistage axial-flow compressor.

4.4.1 Compressor Design and Operation Principle

Figure 4-6 illustrates the basic configuration of an axial-flow compressor with three stages. Each stage consists of a cascade of stationary blades (Inlet Guide Vanes, IGV, or Stator, S), which decreases the swirl (tangential) velocity of the gas in the direction of rotation, followed by a cascade of rotating blades (Rotor, R), which imparts mechanical (or kinetic) energy to the gas by increasing the swirl velocity. The next stator row removes the swirl developed by the rotor cascade to convert kinetic energy into static pressure and to establish the proper swirl velocity for the flow to enter the next rotor stage. Both processes in the compressor contribute to increasing the gas static pressure. It is a common practice in axial-flow turbomachines to design a multistage compressor for nearly constant axial flow velocity throughout. As a result, the annular flow area must decrease from inlet to outlet since the gas pressure and density increase as the gas flows through the compressor. Typically, an exit guide vanes cascade (EGV) follows the last compressor stage to remove any residual swirl velocity and convert that kinetic energy to an increase in static pressure (Figure 4-6). Although not shown on the figure, a diffuser will follow the exit guide vanes to recover as much kinetic energy as possible, as well as to direct the flow to its intended destination. Similarly, an inlet flow passage will precede the inlet guide vanes. This can range from a smooth axial bell-mouth inlet to a complex side inlet, depending on the application.

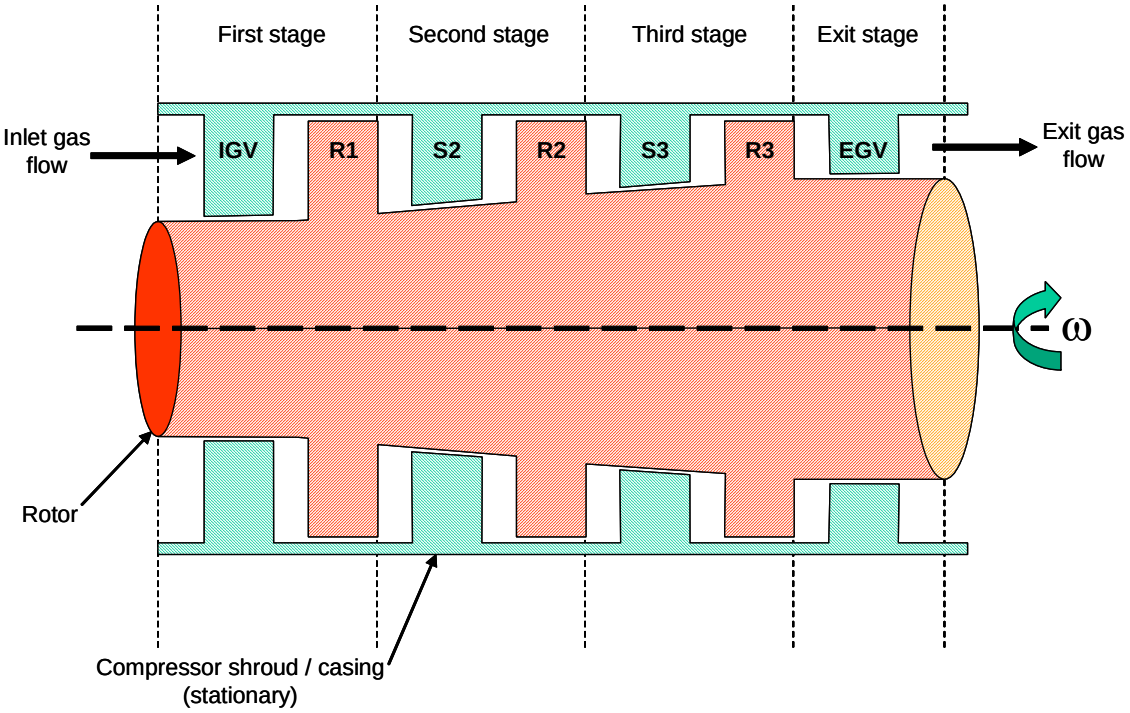

Figure 4-6. Schematic of a multistage axial-flow compressor.

Typical velocity triangles at the leading and trailing edges of a compressor rotor cascade are shown in Figure 4-7. An orthogonal coordinate system (x, θ) is used where the meridional coordinate, x, is identical to the axial coordinate (axis of the turbomachinery), and θ is the polar angle of a cylindrical coordinate system. Subscript 1 refers to the cascade inlet station, and subscript 2 refers to the cascade exit station. The velocity in the stationary coordinate system (absolute velocity) is designated as V, and the velocity in the rotating coordinate system (relative velocity) is designated as W (Figure 4-7). Finally, U is the tangential velocity of the rotating blades ($U = U_\theta$), and α and ϕ designate the absolute and relative velocity angles, respectively (Figure 4-7).

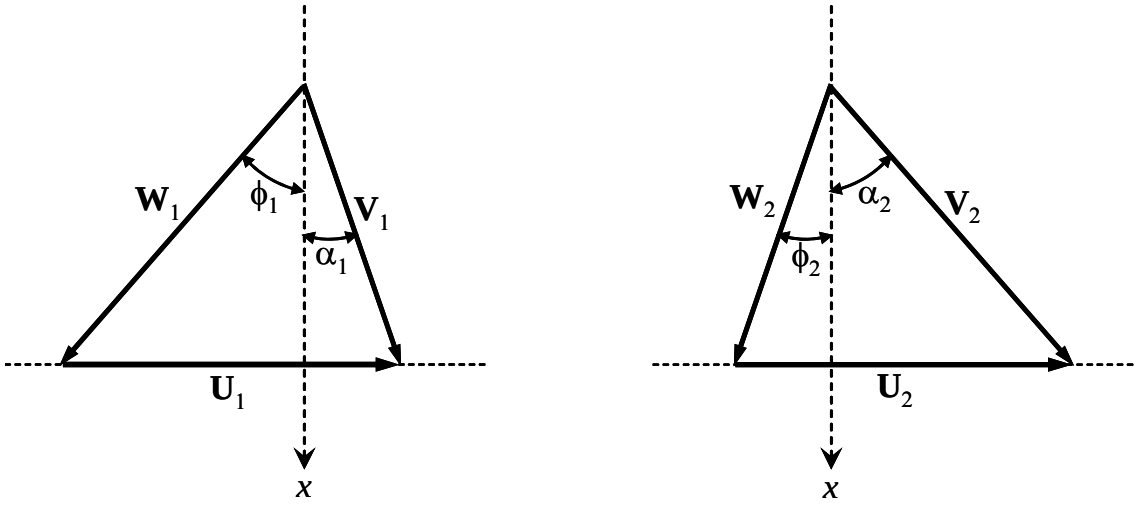

(a) Leading edge (b) Trailing edge

Figure 4-7. Velocity triangles of compressor rotor blades.

4.4.2 Incidence Losses for Off-Design Conditions

According to the loss scheme of Koch and Smith (1976), an improvement of the model of Lieblein (1959), the total pressure loss coefficient of a compressor blades cascade at optimum design conditions is the sum of the coefficients for profile losses and tip clearance (leakage) losses (Appendix C):

$$Y = Y_p + Y_{TC} \ . \tag{4-24}$$

Aungier (2003) has introduced an off-design incidence correction factor, K_{inc}, such that Equation (4-24) is rewritten more generally:

$$Y = K_{inc} \times (Y_p + Y_{TC}) \ . \tag{4-25}$$

Figure 4-8 shows K_{inc} as a function of a normalized incidence angle parameter, ξ, based on a correlation proposed by Aungier (2003):

$$\text{When} \quad \xi < -2, \qquad K_{inc} = -4\xi - 3 \ ; \tag{4-26a}$$

$$\text{When} \quad -2 \le \xi \le 1, \qquad K_{inc} = 1 + \xi^2 \ ; \tag{4-26b}$$

$$\text{When} \quad 1 < \xi \ , \qquad K_{inc} = 2\xi \ . \tag{4-26c}$$

An upper limit of $K_{inc} = 20$ is required in the model. The parameter ξ is a function of the incidence angle, $i = \phi_1 - \beta_1$, optimum angle of attack i^*, and positive (i_S) and negative (i_C) stall incidence angles, as:

$$\text{When} \quad i \geq i^*, \qquad \xi = \frac{i - i^*}{i_S - i^*} \geq 0 \; ; \tag{4-27a}$$

$$\text{When} \quad i < i^*, \qquad \xi = \frac{i - i^*}{i^* - i_C} < 0 \; . \tag{4-27b}$$

As shown in Figure 4-8, the positive and negative stall incidence angles are defined as usual, such that the cascade losses are twice those at optimum design conditions, i.e., $K_{inc} = 2.0$.

The optimum design angle of attack, i^*, is a function of the blades and cascade geometry (Aungier, 2003):

$$i^* = \Phi - \beta_1 + \left[3.6 K_t + 0.3532\, \zeta \times \left(\frac{Z}{C} \right)^{0.25} \right] \times \left(\frac{C}{S} \right)^{0.65 - 0.002\zeta} \tag{4-28}$$

where Φ is the blades stagger angle (^{o}) and $\zeta = |\beta_1 - \beta_2|$ is the absolute camber angle (^{o}). The maximum blade thickness correction factor is given by:

$$K_t = \left(10 \frac{t_{max}}{C} \right)^{\frac{0.28}{0.1 + (t_{max}/C)^{0.3}}} . \tag{4-29}$$

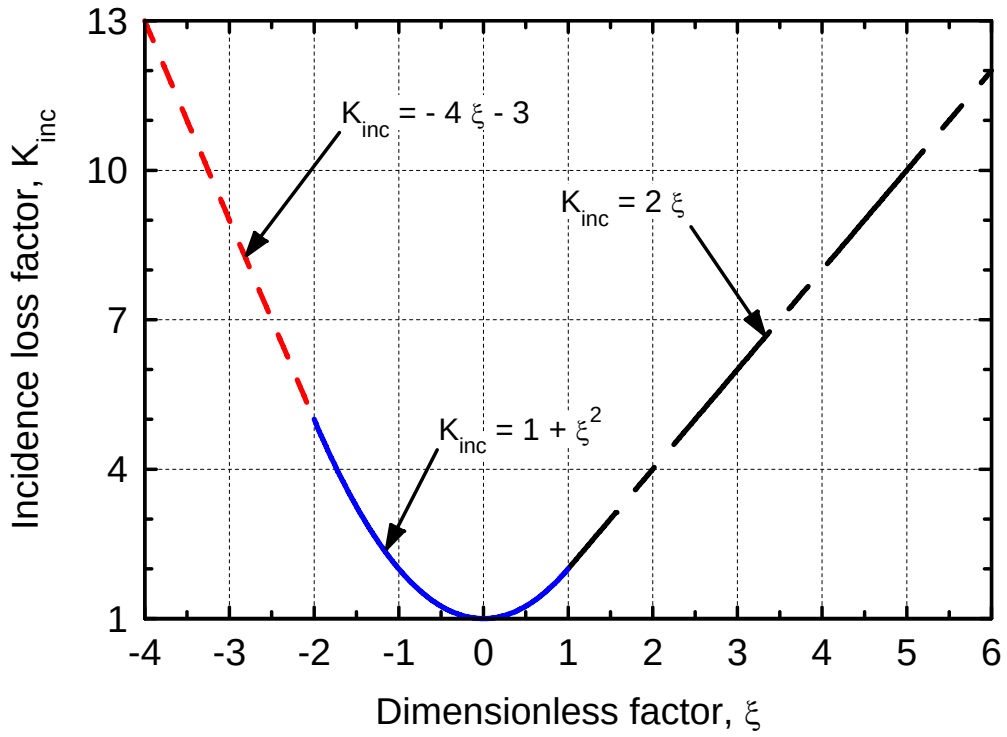

Figure 4-8. Off-design incidence correction factor for compressor blades (Aungier, 2003).

The incidence angle for positive stall, i_S, is calculated using a correlation developed by Aungier (2003), as:

$$i_S = i^* + 10.3 + \left(2.92 - \frac{\phi_1}{15.6}\right) \times \frac{\zeta}{8.2} \quad > \; i^* , \tag{4-30}$$

and the incidence angle for negative stall, i_C, is given by (Aungier, 2003):

$$i_C = i^* - 9.0 + \left[1.0 - \left(\frac{30}{\phi_1}\right)^{0.48}\right] \times \frac{\zeta}{4.176} \quad < \; i^* . \tag{4-31}$$

A minimum value of $\phi_1 = 10^o$ is used in Equation (4-31) to avoid the singularity in extremely off-design conditions. Note that all angles are expressed in degrees in these equations.

4.4.3 Solution of Flow Conservation Equations in Compressor Blades Cascade

As for the turbine model, a compressor half-stage consists of an isentropic contraction section {0 – 1} between two cascades, followed by a blades section {1 – 2} which exhibits pressure losses. For the sake of discussion, we assume that all flow conditions at station {0} are known, and we proceed to calculating those at stations {1} and {2}. The relative gas flow angle, ϕ_2 at the trailing edge of the blades is a function of the blades angle and the deviation angle, δ:

$$\phi_2 = \beta_2 + \delta \ . \tag{4-32a}$$

The deviation angle at the trailing edge of a compressor blade is calculated using a recent correlation developed by Zhu and Sjolander (2005), and adapted for a compressor blade as:

$$\delta = 17.3 \frac{(S/C)^{0.05} \times \left|\phi_1 - \beta_2\right|^{0.63} \times \cos^2(\Phi) \times (t_{\max}/C)^{0.29}}{(30 + 0.01\beta_1^{2.07}) \times \tanh(\mathrm{Re}_{2C}/200{,}000.)} \ . \tag{4-32b}$$

All angles in this equation are expressed in degrees, and the Reynolds number at the trailing edge is based on the relative gas velocity and the actual blade chord: $\mathrm{Re}_{2C} = (\rho_2 W_2 C)/\mu_2$.

The off-design model assumes that the flow does not turn in the expansion zone (Ainley and Mathieson, 1951), i.e.,

$$\alpha_1 = \alpha_o \ . \tag{4-33}$$

This means that the trailing edge of the upstream cascade controls the direction of the flow as it impinges onto the leading edge of the next cascade. If the angle of attack is correct, that is if the incidence angle $i_1 = \phi_1 - \beta_1 = i^*$, the blades cascade operates near optimum design conditions. An off-design angle of attack, however, will result in large incidence losses, which are then calculated using the model described in Section 4.4.2.

To illustrate the new solution technique, we take the example of a compressor stator cascade, {1 – 2}. We know all flow conditions at station {1}, and the absolute gas flow angle at the trailing edge, $\alpha_2^{(n)} = \phi_2^{(n)}$ is known from Equation (4-32). Again, the technique is extended for any real gas by linearizing the state equations as follows:

$$h_2^{(n+1)} = h_2^{(n)} + C_{p2}^{(n)} \times \left(T_2^{(n+1)} - T_2^{(n)} \right), \tag{4-34}$$

$$P_2^{(n+1)} = \rho_2^{(n+1)} R Z_2^{(n)} T_2^{(n+1)} . \tag{4-35}$$

The conservation of mass, energy and momentum can then be written:

$$\dot{m} = \rho_2^{(n+1)} V_2^{(n+1)} A_2 \cos \alpha_2^{(n)} , \tag{4-36}$$

$$\dot{m}\, \hat{h}_1 = \dot{m} \left(h_2^{(n+1)} + \frac{\overline{\alpha}_3}{2} \left(V_2^{(n+1)} \right)^2 \right) + Q_{loss} - \dot{W}_C^{disk} , \tag{4-37}$$

$$\hat{P}_1 = P_2^{(n+1)} + \frac{\overline{\alpha}_3}{2} \rho_2^{(n+1)} \left(V_2^{(n+1)} \right)^2 + \Delta \hat{P}_{loss} , \tag{4-38}$$

where the pressure losses are given by:

$$\Delta \hat{P}_{loss} = Y \times \frac{\overline{\alpha}_3}{2} \rho_1^{(n)} \left(V_1^{(n)} \right)^2 . \tag{4-38b}$$

The five Equations (4-34) through (4-38) are solved <u>explicitly</u> for the five unknowns V_2, ρ_2, P_2, T_2, and h_2 at iteration (n+1), using simple substitution. Expressing all quantities in terms of V_2, the momentum conservation Equation (4-38a) reduces to a second-order polynomial for the trailing edge velocity:

$$a (V_2)^2 + b (V_2) + c = 0 , \tag{4-39a}$$

where

$$a = \frac{\overline{\alpha}_3}{2} \left(\frac{\dot{m}}{A_2 \cos \alpha_2^{(n)}} \right) \times \left(1 - \frac{R Z_2^{(n)}}{C_{p2}^{(n)}} \right), \tag{4-39b}$$

$$b = -\hat{P}_2 = \Delta \hat{P}_{loss} - \hat{P}_1 , \tag{4-39c}$$

$$c = \left(\frac{\dot{m}}{A_2 \cos \alpha_2^{(n)}} \right) \times R Z_2^{(n)} \times T_{ref} , \tag{4-39d}$$

$$C_{p2}^{(n)} T_{ref} = C_{p2}^{(n)} T_2^{(n)} + \hat{h}_1 - h_2^{(n)} - \frac{Q_{loss} - \dot{W}_C^{disk}}{\dot{m}} \quad . \tag{4-39e}$$

The solution of this polynomial equation is simply:

$$V_2^{(n+1)} = \frac{-b - \sqrt{b^2 - 4ac}}{2a} . \tag{4-39f}$$

In practice, numerical iterations are required, since the heat losses, Q_{loss}, pressure loss coefficient, Y, and gas properties are also functions of the flow conditions at the trailing edge, which are not known a priori.

The same technique applies to the stator and rotor leading edges, where subscripts {1} and {2} are replaced with subscripts (0) and {1}, and the loss coefficient $Y = 0$ in the isentropic contraction zones. For the rotor leading edge {1}, the relative flow velocities and the incidence angle are easily calculated using the velocity triangle (Figure 4-7a) once the absolute gas flow velocity V_1 is obtained, as:

$$W_{1x} = V_{1x} = V_1 \cos \alpha_1 \tag{4-40a}$$

$$W_{1\theta} = V_{1\theta} - U_1 = V_1 \sin \alpha_1 - U_1 \tag{4-40b}$$

$$W_1^2 = W_{1x}^2 + W_{1\theta}^2 , \tag{4-40c}$$

$$\tan \phi_1 = - \frac{W_{1\theta}}{W_{1x}} , \text{ and} \tag{4-40d}$$

$$i_1 = \phi_1 - \beta_1 . \tag{4-40e}$$

The sign convention for tangential velocity is positive in the direction of the impeller velocity (Figure 4-7).

The technique for the rotor cascade {1 – 2} is somewhat different, due to the interdependence between mechanical work, losses, absolute gas flow angle and velocity triangle. Again, we assume that all flow conditions at station {1} are known, and the relative gas flow angle at the trailing edge, $\phi_2^{(n)} = \beta_2 + \delta_2^{(n)}$, is known. The technique is again extended for any real gas by linearizing the state equations using Equations (4-34) and (4-35). We found that it was most efficient to write all quantities in terms of the unknown relative velocity $W_2^{(n+1)}$, and find its proper value, which satisfies the momentum balance equation by a simple dichotomic research. For a given trial value W_2, the absolute gas velocity at the trailing edge is obtained from the velocity triangle (Figure 4-7b) as:

$$V_2 = \left(W_2^2 - 2U_2 W_2 \sin \phi_2 + U_2^2 \right)^{1/2} , \tag{4-41}$$

and the absolute gas flow angle at the trailing edge is calculated as:

$$\tan\alpha_2 = \frac{U_2 / W_2 - \sin\phi_2}{\cos\phi_2}\,. \tag{4-42}$$

The gas density is obtained from the conservation of mass, as:

$$\rho_2 = \frac{\dot{m}}{A_2 V_2 \cos\alpha_2}, \tag{4-43}$$

And the cascade shaft work is given by Euler's equation:

$$\dot{W}_C = \dot{m} \times (U_1 V_{1\theta} - U_2 V_2 \sin\alpha_2) \; < \; 0\,. \tag{4-44}$$

The gas temperature is obtained from the energy balance equation as:

$$T_2 = T_{ref} - \left(\frac{\overline{\alpha}_3}{2} V_2^2 + \frac{\dot{W}_C}{\dot{m}} \right) / C_{p2}^{(n)}\,, \text{ where} \tag{4-45}$$

$$T_{ref} = T_2^{(n)} + \left(\hat{h}_1 - h_2^{(n)} - \frac{Q_{loss} - \dot{W}_C^{disk}}{\dot{m}} \right) / C_{p2}^{(n)}\,. \tag{4-46}$$

The gas pressure is calculated using the state Equation (4-35), as:

$$P_2 = \rho_2 R Z_2^{(n)} T_2\,. \tag{4-47}$$

Finally, the function $F_2^C(\phi_2, W_2)$ is calculated, using the momentum balance equation with the proper definition of the pressure loss factor for a rotor cascade (Horlock, 1960; Fielding, 2000):

$$F_2^C(\phi_2, W_2) = P_2 + \frac{\overline{\alpha}_3}{2} \rho_2 \times W_2^2 - P_1 + \frac{\overline{\alpha}_3}{2} \rho_1 \times (Y - 1) \times W_1^2\,. \tag{4-48}$$

The function F_2^C is a monotonically decreasing function of W_2, and is equal to zero when the momentum balance equation is satisfied. The solution technique then simply consists in finding the zero of this function by performing a dichotomic research on W_2. Once the zero of F_2^C has been found, the conservation Equations (4-43), (4-45) – (4-48), Euler Equation (4-34), and velocity triangle Relations (4-41) and (4-42) are all satisfied. Internal iterations are then performed to resolve the dependences of pressure loss factor Y, deviation angle δ_2, heat losses Q_{loss}, real gas enthalpy, h_2 and compressibility factor, Z_2.

4.5 Operation Maps of 6-Stage GTHTR300 Turbine

Due to the complexity of the geometry and the large number of parameters necessary to define the blade cascades of the axial-flow, multistage turbine, and compressor units, input files are provided that emulate, to the best of the authors' knowledge, the design of the Japanese GTHTR300 turbo-machinery (Takizuka et al., 2004). Model results were compared successfully with the performance of the Japanese 6-stage turbine rated 530 MW, and of the 20-stage compressor rated 251 MW. Furthermore, operation maps of these two rotating units are developed, which exhibit expected trends. These maps are included in this section and the following for benchmarking purposes.

The GTHTR300 turbine has casing and hub diameters of 2.156 m and 1.844 m at the inlet, and casing and hub diameters of 2.25 m and 1.75 m at the exit, corresponding to annular flow areas of A_{in} = 0.9802 m^2 and A_{ex} = 1.5708 m^2, respectively (Takizuka et al., 2004). In the present model, the hub and casing radii are assumed to vary linearly between the entrance and exit. The clearance at the blades tip is τ = 1 mm, and the stator and rotor blade cascades use N = 82 and 80 blades each, respectively (Takizuka et al., 2004). The model then assumes that all the blades have a chord, C = 7 cm, and a trailing edge thickness, t_{TE} = 5 mm. Because of the flexibility in designing a turbine for given operating conditions, due to the choices of different degrees of reaction and flow coefficient, a commonly made assumption was used: the rotor and stator blades were assumed to have identical shape and mirror orientation: the blades trailing edge angle, which controls the mechanical work output, was taken equal to $\beta_2 = 70.5^o$, while the blades' leading edge angle, which controls the incidence and pressure losses, was chosen equal to $\beta_1 = 3^o$ to minimize the losses. The other blade parameters were calculated by the model using the empirical relationships available in subroutine TURBINE_INPUT. The nominal operating conditions of the GTHTR300 turbine are:

(a) an inlet mass flow rate of 441.8 kg/s;
(b) an inlet gas temperature of 1123 K (850 ^{o}C);
(c) an inlet gas pressure of 6.88 MPa; and
(d) a rotational speed of 3600 rpm (Takizuka et al., 2004).

The operation map of the Japanese GTHTR300 6-stage axial-flow turbine was developed using the following input flow conditions reported by Takizuka et al. (2004): an inlet helium gas temperature of 1123 K, and an inlet helium gas pressure of 6.88 MPa. The map is developed by selecting a rotational shaft speed $\omega = 2\pi N / 60$, then varying the inlet gas mass flow rate between 0 and 500 kg/s. Values of N = 600, 1200, 1800, 2400, 3000, and 3600 rpm were selected.

The maps obtained using the present axial-flow turbine model are shown in Figures 4-9 through 4-14. The present simulation results using helium gas properties (which behaves essentially like a perfect gas) predict turbine exit temperature and pressure of 891.5 K (Figure 4-12) and 3.64 MPa (Figure 4-13), compared to the reported values of 891 K and 3.68 MPa by Takizuka et al. (2004). The predicted turbine work to the shaft is 531.5 MW (Figure 4-11), compared to 530 MW. The calculated pressure ratio is 1.89 (Figure 4-9), compared to 1.87. The predicted polytropic efficiency, η_T = 91.7% (Figure 4-10), is slightly lower than the reported value of 92.8%, since the calculated pressure losses are greater by 0.4 bar. The total pressure losses calculated by the model amount to 3.8 bars (Figure 4-14).

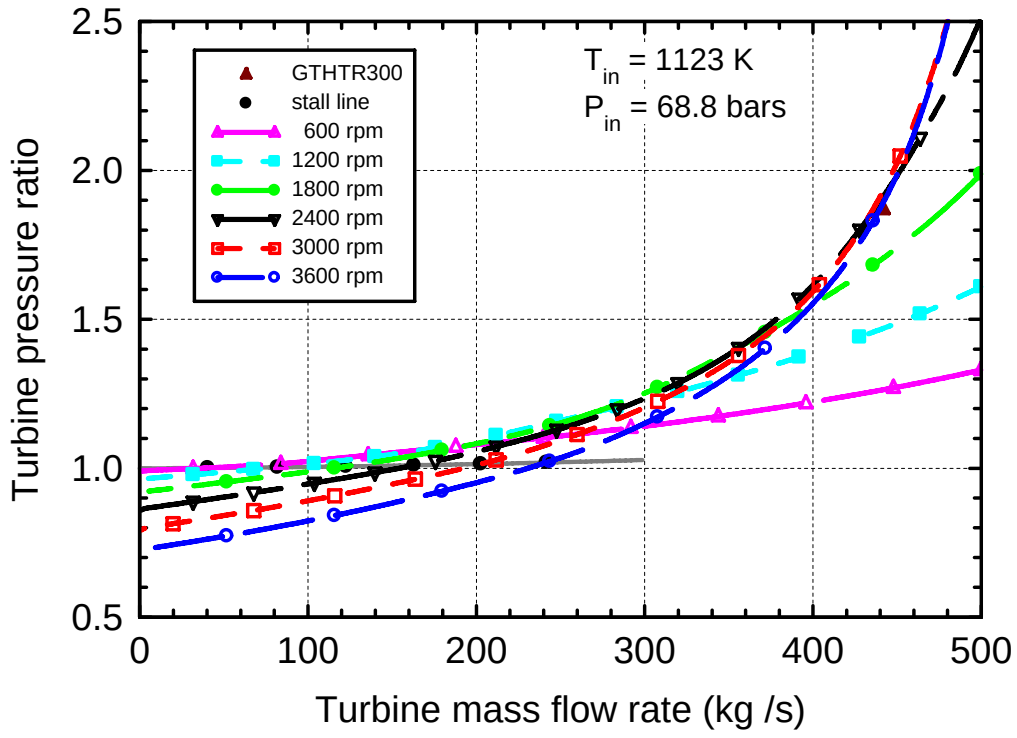

Figure 4-9. Predicted pressure ratio of GTHTR300 turbine.

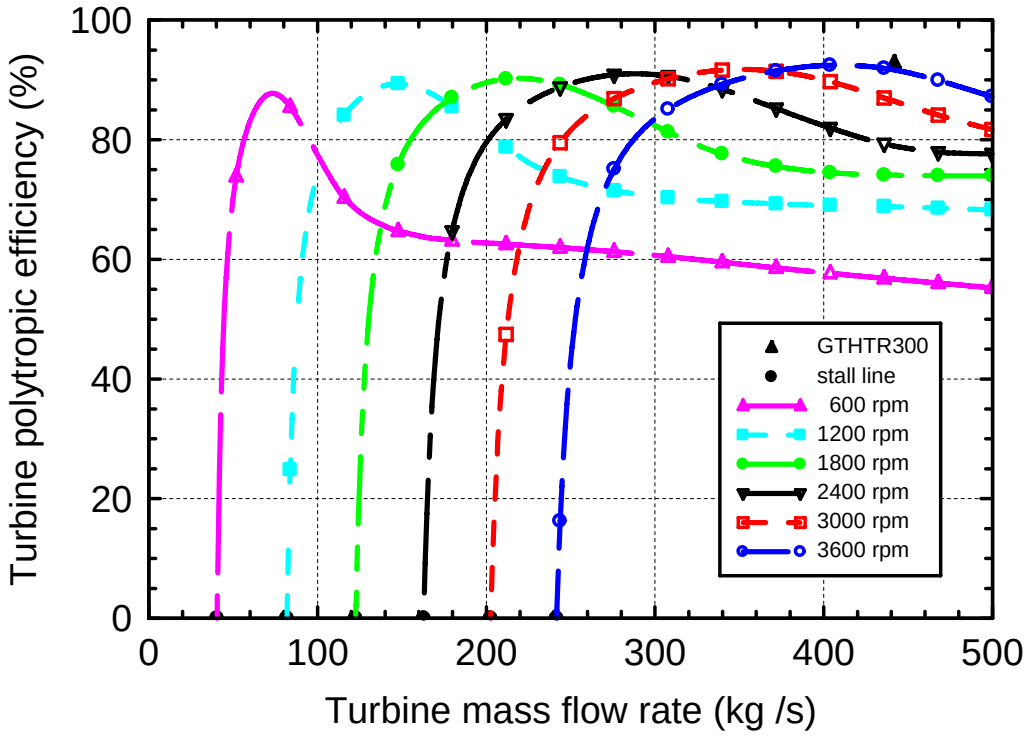

Figure 4-10. Predicted polytropic efficiency of GTHTR300 turbine.

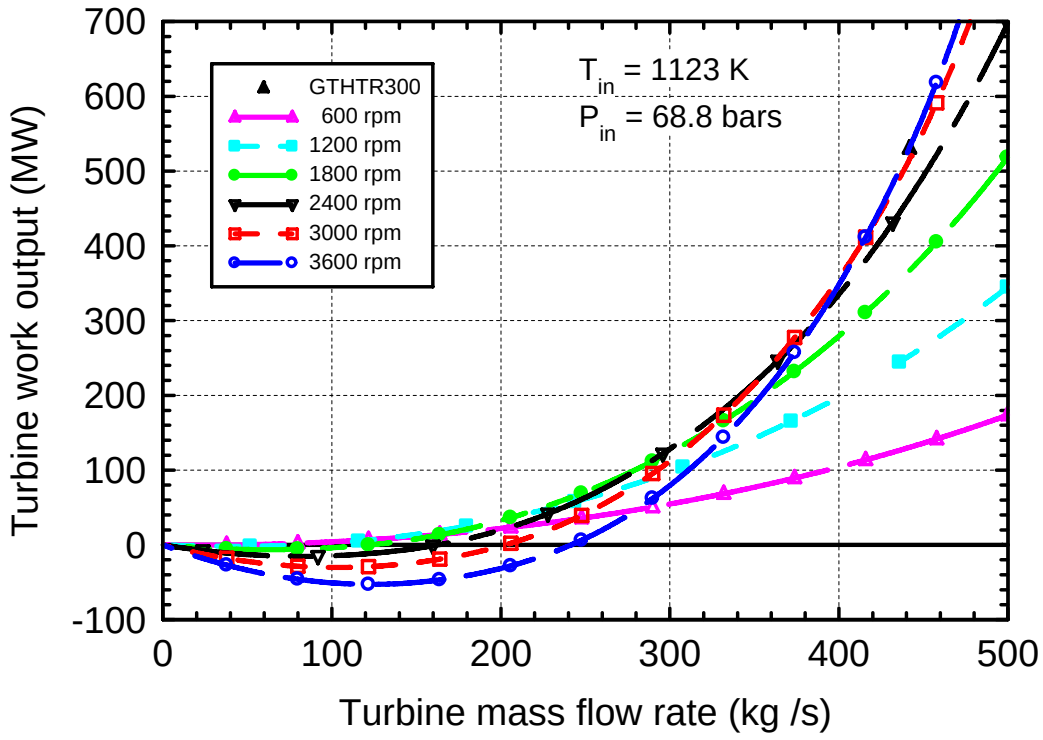

Figure 4-11. Predicted shaft work output of GTHTR300 turbine.

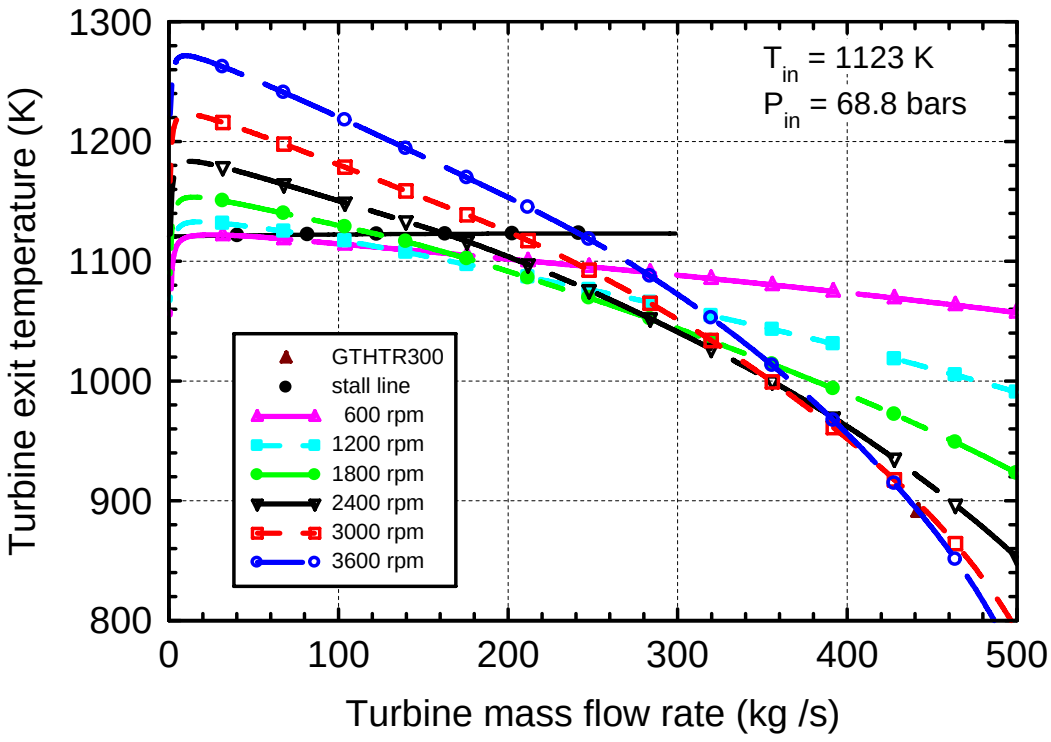

Figure 4-12. Predicted exit temperature of GTHTR300 turbine.

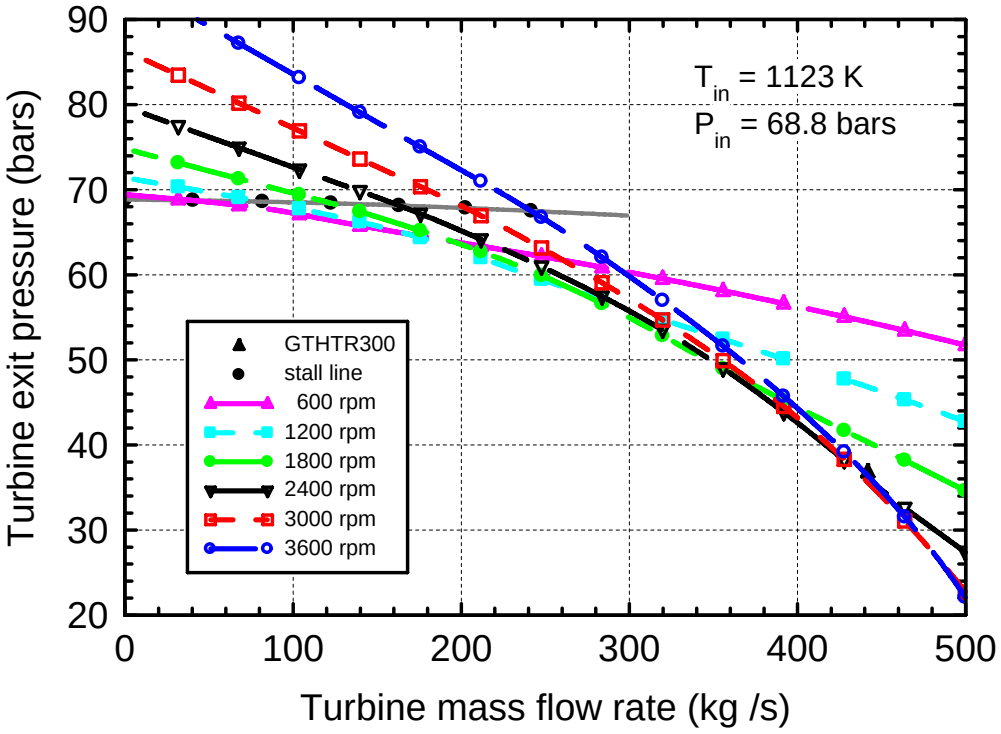

Figure 4-13. Predicted exit pressure of GTHTR300 turbine.

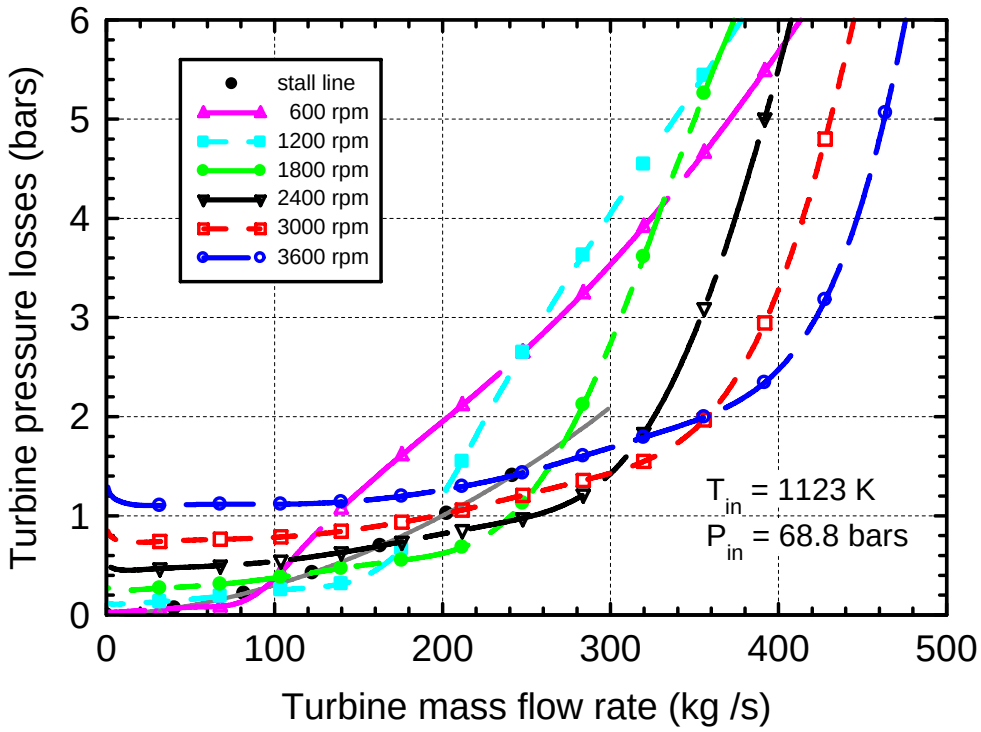

Figure 4-14. Predicted pressure losses in GTHTR300 turbine.

Figures 4-9 through 4-11 show that when operating at constant shaft speed, inlet temperature and pressure, the work output and pressure ratio decrease with decreasing mass flow rate. As the pressure ratio drops towards 1, the polytropic efficiency starts dropping very quickly (Figure 4-10), eventually reaching zero when the turbine work to the shaft vanishes (Figure 4-11). This condition, called stalling, occurs because the rear stages of the multistage turbine now consume mechanical energy and dissipates it into heat, resulting in excessive temperature and entropy rise (windmilling, see Figures 4-10 and 4-12) (Shobeiri and Abouelkheir, 1992). Turbine stalling occurs at a pressure ratio slightly greater than 1, due to the pressure losses (Figure 4-11).

Decreasing the mass flow rate below that at the stall line causes the entropy of the gas to increase further, since the pressure losses are maintained nearly constant (Figure 4-14); the gas exit pressure increases above its inlet value (Figure 4-13), and the net work output of the turbine becomes negative (Figure 4-11); that is, mechanical energy must be provided to the turbine shaft in order to maintain its rotational speed.

Note that the sharp decrease in temperature as the mass flow rate goes to zero (Figure 4-12) is simply caused by the heat losses to ambient air through the turbine casing. These losses are taken out of the gas enthalpy, and a low mass flow rate results in a large temperature drop. This sharp temperature drop would not occur if the turbine casing were perfectly insulated.

The present operation maps of the 6-stage axial-flow turbine show that the model can operate in a stable manner, and provide results of reasonable trend, even in extremely off-design conditions that would be encountered during startup and shutdown of the CBC.

4.6 Operation Maps of 20-Stage GTHTR300 Compressor

The GTHTR300 compressor has casing and hub diameters of 1.704 m and 1.5 m at the inlet, and casing and hub diameters of 1.645 m and 1.5 m at the exit, corresponding to annular flow areas of A_{in} = 0.5133 m^2 and A_{ex} = 0.3582 m^2, respectively (Takizuka et al., 2004). This compressor geometry is modeled in the present model using a constant casing radius of R_{cas} = 0.837 m, and inlet and exit hub radii R_{hub}^{in} = 0.7329 m and R_{hub}^{ex} = 0.7649 m to match the reported annular flow areas. The hub radius is assumed to vary linearly between the entrance and exit. The clearance at the blades tip is τ = 1 mm, and the stator and rotor blade cascades use N = 94 and 72 blades each, respectively (Takizuka et al., 2004). The stator blades have a chord, C = 6 cm, and the rotor blades have C = 7.8 cm. The model assumes a location of maximum camber, Z/C = 0.4, and a trailing edge thickness, t_{TE} = 4 mm, for all blades. The rotor blade cascades were assumed to be identical in all 20 stages. Similarly, the stator blade cascades were all identical. The blades' trailing edge angles β_2, which control the mechanical work input, were chosen equal to 48^o and 10^o for the stator and rotor cascades, respectively. The blades' leading edge angles β_1, which control the incidence and pressure losses, were chosen equal to 58° and 42° for the stator and rotor cascades, respectively, to minimize these losses. The other blade geometrical parameters were then calculated using the empirical relationships available in subroutine COMPRESSOR_INPUT. The nominal operating conditions of the GTHTR300 compressor are:

(a) an inlet mass flow rate of 449.7 kg/s;
(b) an inlet gas temperature of 301 K (28 ^{o}C);

(c) an inlet gas pressure of 3.52 MPa; and
(d) a rotational speed of 3600 rpm (Takizuka et al., 2004).

The operation maps of the Japanese GTHTR300, 20-stage axial-flow compressor were developed using the following input flow conditions: an inlet helium gas temperature of 301 K, and an inlet helium gas pressure of 3.52 MPa. The maps are developed by selecting a rotational shaft speed $\omega = 2\pi N/60$, then varying the inlet gas mass flow rate between 0 and 500 kg/s. Values of N = 600, 1200, 1800, 2400, 3000, and 3600 rpm were selected.

The maps obtained using the present axial-flow compressor model are shown in Figures 4-15 through 4-20. The present simulation results using helium gas properties predict compressor exit temperature and pressure of 408.8 K (Figure 4-18) and 7.104 MPa (Figure 4-19), compared to the reported values of 410 K and 7.11 MPa by Takizuka et al. (2004). The predicted compressor work from the shaft is 251.3 MW (Figure 4-17), compared to 251 MW. The calculated pressure ratio is 2.01 (Figure 4-15), compared to 2.02. The predicted polytropic efficiency, η_T = 90.7% (Figure 4-16), is very close to the reported value of 90.5%. As shown in Figure 4-20, the rotor and stator blades leading edge angles were chosen properly, such that at the nominal operating conditions ($\dot{m}$ = 449.7 kg/s and N = 3600 rpm), the incidence losses were nearly minimum, and the polytropic efficiency of the compressor, near its peak value (Figure 4-16).

Decreasing the gas mass flow rate below its design value causes the pressure losses through the compressor to increase rapidly (Figure 4-20), due to the strong off-design incidence conditions developing at the blades' leading edges. As a result of the viscous dissipation, the gas temperature at the exit of the compressor increases with decreasing mass flow rate (Figure 4-18), and the compressor polytropic efficiency decreases steadily from its peak value (Figure 4-16).

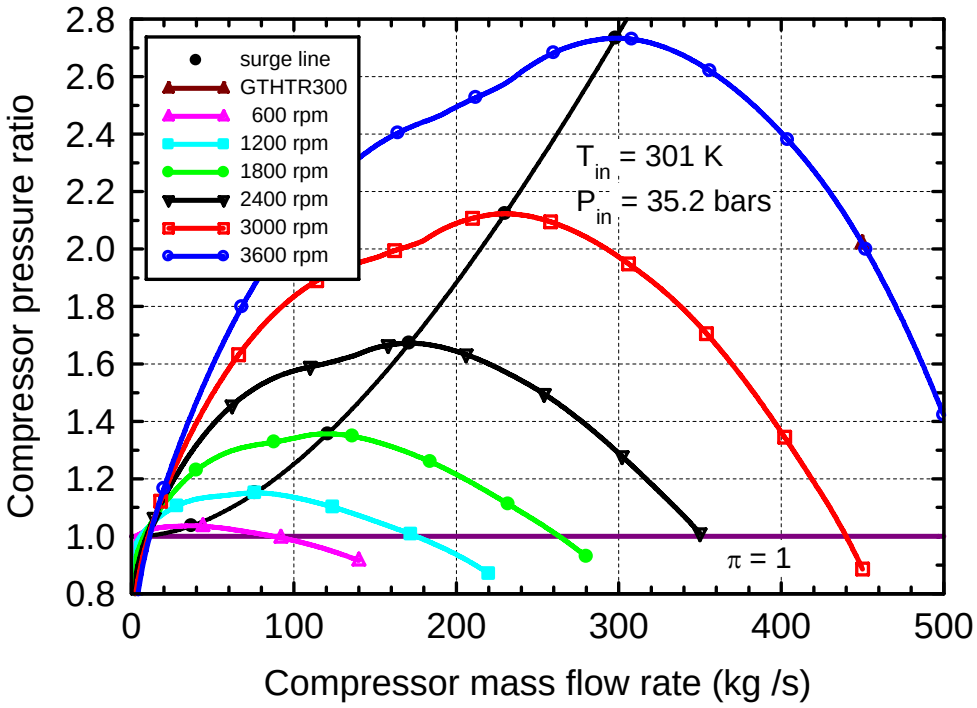

Figure 4-15. Predicted pressure ratio of GTHTR300 compressor.

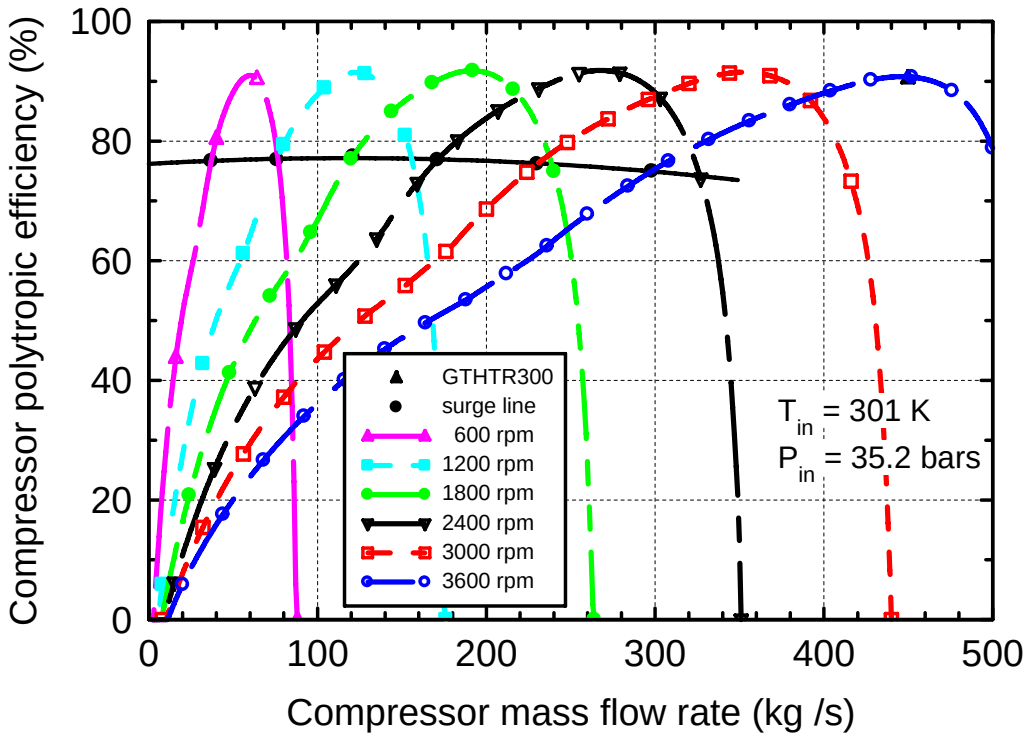

Figure 4-16. Predicted polytropic efficiency of GTHTR300 compressor.

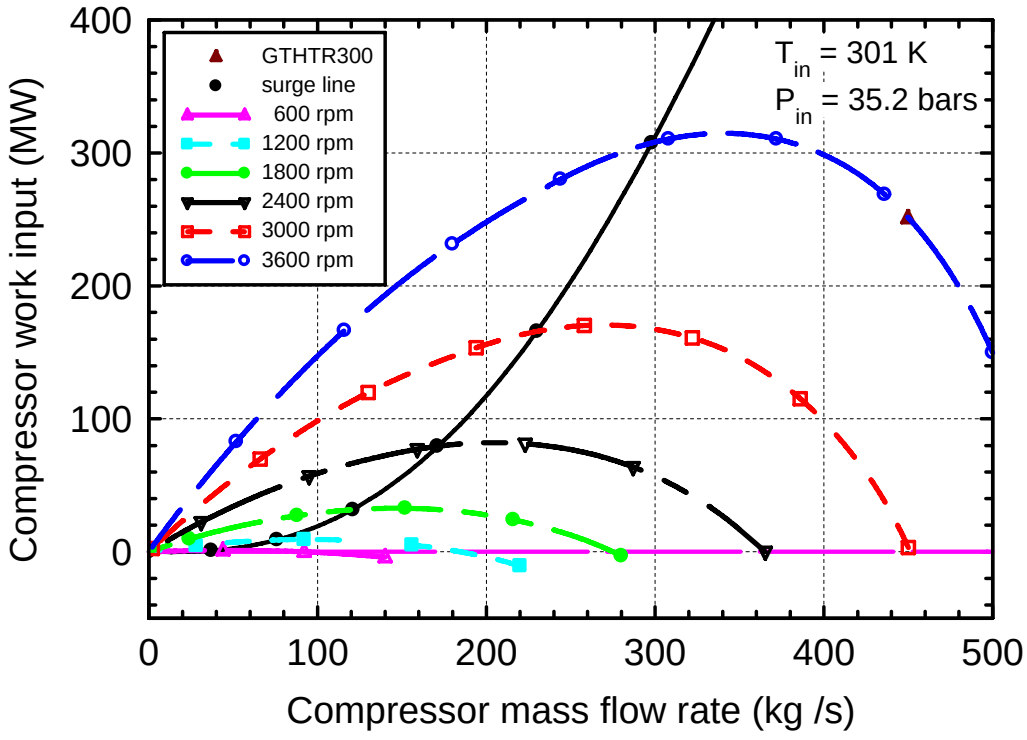

Figure 4-17. Predicted shaft work output of GTHTR300 compressor.

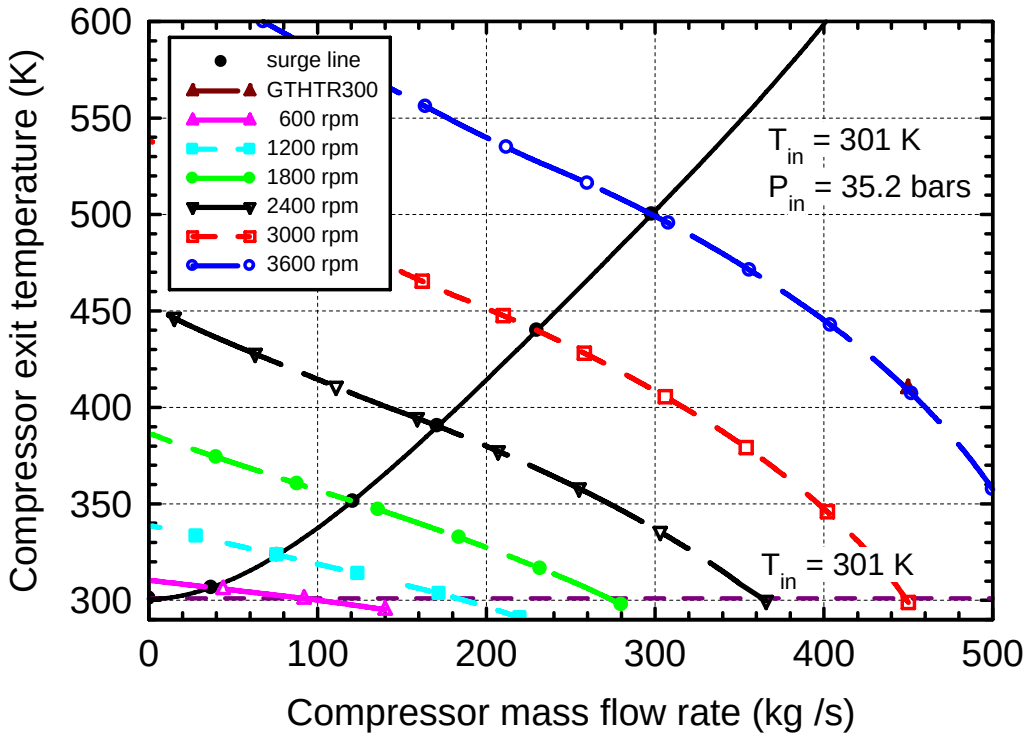

Figure 4-18. Predicted exit temperature of GTHTR300 compressor.

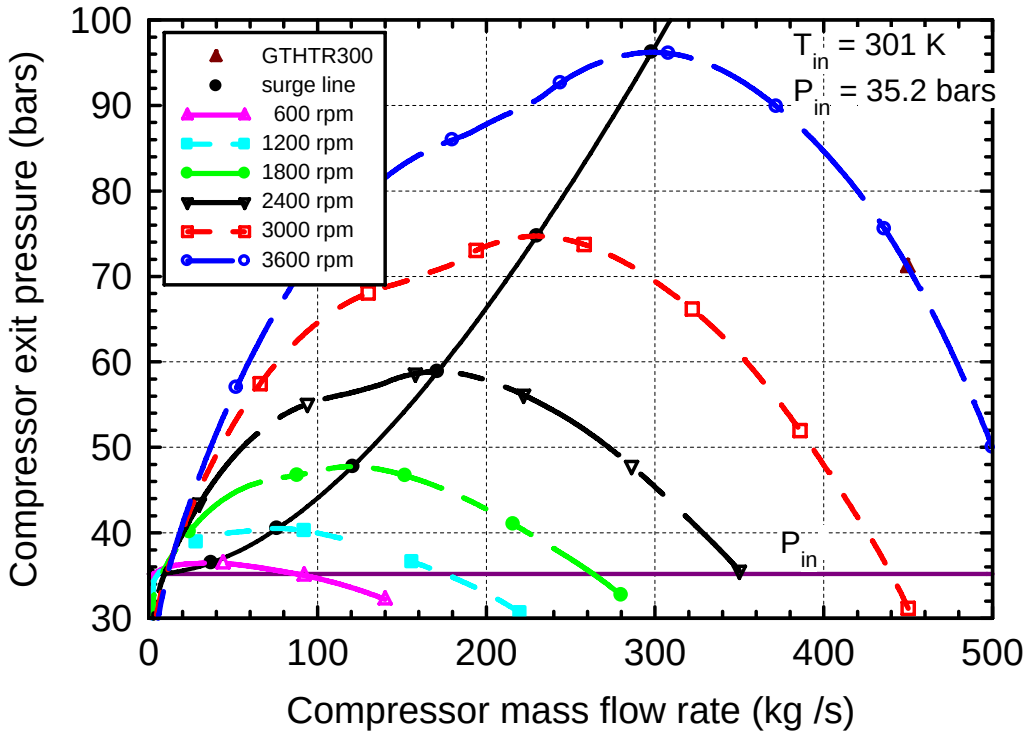

Figure 4-19. Predicted exit pressure of GTHTR300 compressor.

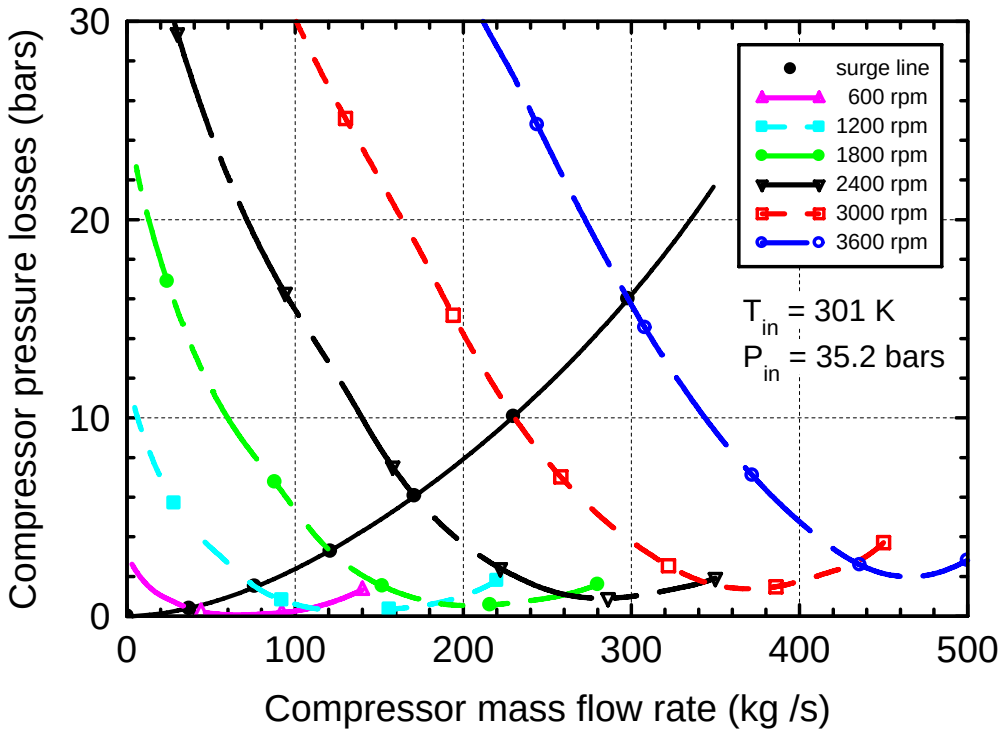

Figure 4-20. Predicted pressure losses in GTHTR300 compressor.

Nonetheless, the mechanical power required to maintain the compressor's shaft speed increases with decreasing mass flow rate (Figure 4-17), and the gas exit pressure and compressor pressure ratio increase (Figures 4-15 and 4-19). As the mass flow rate is decreased further, the compressor exit pressure (or the pressure ratio) eventually reaches its peak value, which defines the surging limit of the compressor. This hydrodynamic instability is characterized by a pressure wave bouncing back and forth through the compressor stages. Such operation is extremely detrimental to the compressor, and may destroy it. Therefore, during startup and shutdown of the CBC in the power plant, care must be taken never to operate the compressor to the left of the surge line (Figures 4-15 through 4-20).

The present operation maps of the 20-stage axial-flow compressor show that the model can operate in a stable manner in the normal operation domain of the compressor, and provide results of reasonable trend, even in extremely off-design conditions that would be encountered during startup and shutdown of the CBC. These maps are provided as benchmark test cases to the MELCOR-H2 team to verify the proper implementation of the FORTRAN subroutines into MELCOR-H2.

4.7 Input and Output Files of Turbine Model

FORTRAN subroutines of the present turbine and compressor models were developed and tested using Compaq Visual FORTRAN Professional Edition 6.5.0 (2000), which provides a superset of the FORTRAN 95 standard with other extensions for compatibility with previous FORTRAN languages and platforms. Nonetheless, all the coding instructions used in the present model are compatible with Standard FORTRAN 77.

The axial-flow multistage turbine model consists of three major components:

- an input file TURBINE.INP (Appendix D), which defines all geometrical parameters of the turbine unit and blades cascade;

- a subroutine TURBINE_INPUT (Appendix E), which reads the input file "TURBINE.INP." and writes a verification file "TURBINE.VRF" to verify the formatting of all numerical values; this subroutine then calculates additional cascade geometrical parameters, and populates the COMMON /GEOMETRY_T/ and COMMON /CASCADES_T/;

- a subroutine AXIAL_TURBINE (Appendix F), which, given input flow conditions, calculates the flow conditions at all intermediate stations and at the exit of the turbine; this subroutine accesses the geometrical parameters stored in the COMMON /GEOMETRY_T/ and COMMON /CASCADES_T/; this subroutine also populates a number of output text files:

  – "TURBINE.OUT" collects information pertaining to the convergence of the main iterations;

  – "TURBINE_ITERATIONS.OUT" gives detailed information on the convergence of all internal iterations for each half-stage;

  – "TURBINE_SUMMARY.OUT" summarizes the calculated flow conditions for each half-stage of the turbine, and the overall performance of the turbine;

  – "TURBINE_LOSSES.OUT" collects information on the pressure loss coefficient parameters calculated by the model; and finally,

  – "TURBINE_DICHO.OUT" monitors the dichotomic research iterations for the solution technique of the rotor blade cascades; this file also collects the dichotomic research iterations used to calculate the exit enthalpy for an isentropic evolution; this value is used to calculate the polytropic efficiency of the turbine.

Due to the complexity of the geometry and the large number of parameters necessary to define the blade cascades of the axial-flow multistage turbine unit, an input file "TURBINE.INP" is provided in Appendix D that emulates, to the best of the authors' knowledge, the design of the Japanese GTHTR300, 6-stage turbine (Takizuka et al., 2004). The FORTRAN codes of the subroutines TURBINE_INPUT and AXIAL_TURBINE are given in Appendices E and F. The subroutine that calculates the properties of the He-Xe binary gas mixture, HE_XE, is shown in Appendix J. The main subroutine AXIAL_TURBINE uses other subroutines and functions, such as TURBINE_STATOR, TURBINE_ROTOR, COMPRESSOR_STATOR, and DIFFUSER. The input file and all subroutines and functions are available on the CD-ROM included with this manual. The next subsections describe the input and output parameters of the subroutines TURBINE_INPUT and AXIAL_TURBINE.

4.7.1 Input File "TURBINE.INP"

This section describes in detail the variables of the input file "TURBINE.INP." For clarity, all variable names used in the program are typed in BOLD in this manual. The model uses the International System Units throughout.

The second line of the text file "TURBINE.INP" is a text description of the turbine design and case run, and is read as the text variable TITLE by the subroutine TURBINE_INPUT. This text line is used as headers in all output files to identify the case.

The first block of parameters defines the geometry of the axial-flow turbine:

Nstages Number of rotor stages of axial-flow turbine
Rcas_in Inner radius of turbine casing at inlet (m)
Rcas_ex Inner radius of turbine casing at outlet (m)
Rhub_in Hub radius at turbine inlet (m)
Rhub_ex Hub radius at turbine outlet (m)
XLturbine Axial length of turbine stages (m)
THICKcas Thickness of metallic casing (m)
EMISScas Radiative emissivity of metallic casing
Tair Ambient air temperature (K)
deltaDisk Clearance between housing and end-disks (m)

The model assumes that the casing and hub diameters vary linearly along the turbomachinery. The next block of parameters defines the geometry of the stator cascades (Figure 4-21), including the exit guide vanes. For example, a turbine with 6 stages (Nstages = 6) consists of a total of 7 stator sections (the first one is the inlet guide vanes, the last one the exit guide vanes), and 6 rotor sections.

beta1(i) Stator blades angle at Leading Edge (degrees)
beta2(i) Stator blades angle at Trailing Edge (degrees)
C(i) True chord length of stator blades (m)
N(i) Number of stator blades in cascade
Stagger Stagger angle of stator blades (degrees)
Z(i) Location of maximum camber (m)
O(i) Throat opening of stator cascade (m)

Model Parameters

- Blade angle at LE, β_1 (º)
- Blade angle at TE, β_2 (º)
- Chord length, *C* (m)
- Blades spacing / pitch, *S* (m)
- Blade stagger angle, Φ (º)
- Location of maximum camber, *Z* (m)
- Throat opening, *O* (m)
- Blade maximum thickness, t_{max} (m)
- Blade thickness at TE, t_{TE} (m)
- Blade tip clearance, τ (m)

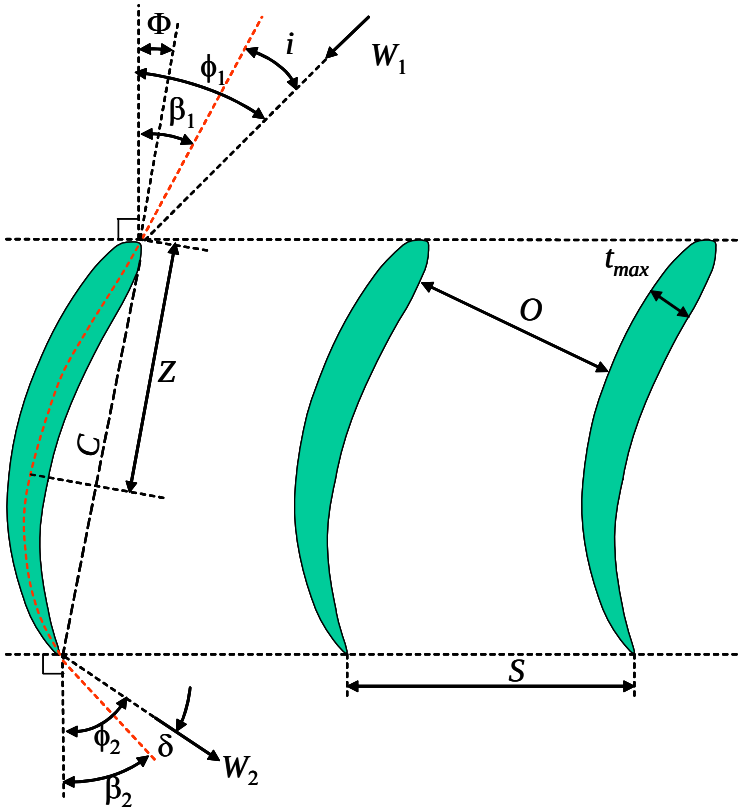

Figure 4-21. Geometry and nomenclature of turbine blades cascade.

tmax(i)	Maximum thickness of stator blades (m)
tTE(i)	Blade thickness at trailing edge (m)
tau(i)	Blade tip clearance to shroud (m)

In practice, many of these parameters are not reported in the literature and are not known. To simplify the work of the designer, the model is capable of calculating the parameters **Stagger**, **Z**, **O**, and tmax in terms of the other known parameters of the cascade, using empirical relations developed in Section 6 of the previous report (Tournier and El-Genk, 2006). In such case, the user must enter negative values of the parameters in the input file.

The last block of parameters in the input file "TURBINE.INP" defines the geometry of the rotor cascades, and is identical to that for the stator sections:

beta1(i)	Stator blades angle at Leading Edge (degrees)
beta2(i)	Stator blades angle at Trailing Edge (degrees)
C(i)	True chord length of stator blades (m)
N(i)	Number of stator blades in cascade
Stagger	Stagger angle of stator blades (degrees)
Z(i)	Location of maximum camber (m)
O(i)	Throat opening of stator cascade (m)
tmax(i)	Maximum thickness of stator blades (m)

tTE(i) Blade thickness at trailing edge (m)
tau(i) Blade tip clearance to shroud (m)

Again, the model will calculate the parameters **Stagger**, **Z**, **O**, and **tmax** in terms of the other known parameters of the cascade, if negative values are entered. A sample of an input file is given in Appendix D. Note that proper design of the turbine cascade blades requires that for a turbine cascade, **beta1 + beta2** $\leq 90°$.

4.7.2 Subroutine TURBINE_INPUT

The subroutine TURBINE_INPUT (see Appendix E) reads the input file "TURBINE.INP." and writes a verification file "TURBINE.VRF" to verify the proper formatting of all input values. This subroutine then calculates additional cascade geometrical parameters, and populates the COMMON /GEOMETRY_T/ and COMMON /CASCADES_T/.

The input parameters passed to the subroutine TURBINE_INPUT through the argument list are:

IO0 Unit number of input file "TURBINE.INP"
IO1 Unit number of output file "TURBINE.VRF" for verification

These files must be opened by the main program unit before calling the subroutine TURBINE_INPUT. For example:

IO0 = 20
OPEN(UNIT=**IO0**, FILE='TURBINE.inp', STATUS='OLD')
IO1 = 21
OPEN(UNIT=**IO1**, FILE='TURBINE.vrf', STATUS='NEW')

The output parameters returned by the subroutine TURBINE_INPUT through the argument list are:

STARLINE Text line of star characters ("*") for printout
TITLE Text title to identify turbine design in output files (second text line of input file"TURBINE.INP")

The subroutine TURBINE_INPUT also populates the COMMON /GEOMETRY_T/ and COMMON /CASCADES_T/, which collect all necessary geometrical parameters of the turbomachinery for use by the subroutine AXIAL_TURBINE.

The PARAMETER (NT = 20) defines the maximum number of half-stages of blade cascades, and may have to be increased for a different design. For example, a turbine with 6 rotor stages requires a total of 13 half-stages (6 stators, 6 rotors and another stator corresponding to the exit guide vanes). The parameters of the COMMON /GEOMETRY_T/ are:

Nstages Number of rotor stages of axial-flow turbine
Rcas_in Inner radius of turbine casing at inlet (m)
Rcas_ex Inner radius of turbine casing at outlet (m)
Rhub_in Hub radius at turbine inlet (m)

Rhub_ex Hub radius at turbine outlet (m)
THICKcas Thickness of metallic casing (m)
EMISScas Radiative emissivity of metallic casing
Tair Ambient air temperature (K)
XLturbine Axial length of turbine stages (m)
XLzone Axial length of each zone (quarter stage) (m)
deltaDisk Clearance between housing and end-disks (m)

In addition, the following arrays are populated, where the subscript (*i*) represents the half-stage number. Each half-stage of the turbine consists of an isentropic expansion to the blades leading edge {0 – 1}, followed by a blades cascade {1 – 2}. In the following:

Subscript {0} denotes station {0}: Half-stage entrance;
Subscript {1} denotes station {1}: Leading edge of blades;
Subscript {2} denotes station {2}: Trailing edge of blades.
Subscript {01} denotes: Expansion zone between entrance and blades leading edge;
Subscript {12} denotes: blades cascade zone.

Rhub0(*i*) Hub radius at Station {0} (m)
Rcas0(*i*) Inner radius of turbine casing at Station {0} (m)
A0(*i*) Axial gas flow area at Station {0} (m^2)
Rhub1(*i*) Hub radius at Station {1} (m)
Rcas1(*i*) Inner radius of turbine casing at Station {1} (m)
A1(*i*) Axial gas flow area at Station {1} (m^2)
Rhub2(*i*) Hub radius at Station {2} (m)
Rcas2(*i*) Inner radius of turbine casing at Station {2} (m)
A2(*i*) Axial gas flow area at Station {2} (m^2)
Rhub01(*i*) Average hub radius in zone {01} (m)
Rcas01(*i*) Average inner casing radius in zone {01} (m)
Hb01(*i*) Average width of flow annulus in zone {01} (m)
Rhub12(*i*) Average hub radius in zone {12} (m)
Rcas12(*i*) Average inner casing radius in zone {12} (m)
Hb12(*i*) Average width of flow annulus in zone {12} (m)
Dcas01(*i*) Average outer casing diameter in zone {01} (m)
Acas01(*i*) Casing outer surface area in zone {01} (m^2)
C_Nu01(*i*), e_Nu01(*i*)
Coefficients to calculate Nusselt number for Taylor-Couette gas flow
Dcas12(*i*) Average outer casing diameter in zone {12} (m)
Acas12(*i*) Casing outer surface area in zone {12} (m^2)
C_Nu12(*i*), e_Nu12(*i*)
Coefficients to calculate Nusselt number for Taylor-Couette gas flow

Finally, the subroutine TURBINE_INPUT populates the COMMON/CASCADES_T/, again arranged by half-stage number:

beta1(*i*) Blades angle at Leading Edge (degrees)
beta2(*i*) Blades angle at Trailing Edge (degrees)

C(*i*) True chord length of blades (m)
N(*i*) Number of blades in cascade
Cx(*i*) Axial chord length of blades (m)
S(*i*) Blades spacing/pitch in cascade (m)
Z(*i*) Location of maximum camber (m)
O(*i*) Throat opening (m)
tmax(*i*) Maximum thickness of blades (m)
tTE(*i*) Blade thickness at Trailing Edge (m)
tau(*i*) Blade tip clearance to shroud (m)
theta(*i*) Blade camber angle (degrees)
sigma(*i*) Blade solidity
chi1(*i*) Leading edge blade angle with respect to the chord line (degrees)
chi2(*i*) Trailing edge blade angle with respect to the chord line (degrees)
stagger(*i*) Stagger angle of blades (degrees)
Hb1(*i*) Blades height at leading edge (m)
Hb2(*i*) Blades height at trailing edge (m)
Hb(*i*) Average height of blades (m)
r1m(*i*) Average blade radius at leading edge (m)
r2m(*i*) Average blade radius at trailing edge (m)
rm(*i*) Average blade radius (m)
At(*i*) Estimate of annular throat area (m^2)

4.7.3 Subroutine AXIAL_TURBINE

The subroutine AXIAL_TURBINE (see Appendix F), given input flow conditions, calculates the flow conditions at all intermediate stations and at the exit of the turbine. This subroutine accesses the geometrical parameters stored in the COMMON/GEOMETRY_T/ and COMMON /CASCADES_T/; this subroutine also populates a number of output text files:

- "TURBINE.OUT" collects information pertaining to the convergence of the main iterations;
- "TURBINE_ITERATIONS.OUT" gives detailed information on the convergence of all internal iterations for each half-stage;
- "TURBINE_SUMMARY.OUT" summarizes the calculated flow conditions for each half-stage of the turbine, and the overall performance of the turbine;
- "TURBINE_LOSSES.OUT" collects information on the pressure loss coefficient parameters calculated by the model; and finally,
- "TURBINE_DICHO.OUT" monitors the dichotomic research iterations for the solution technique of the rotor blades cascades; this file also collects the dichotomic research iterations used to calculate the exit enthalpy for an isentropic evolution; this value is used to calculate the polytropic efficiency of the turbine.

These files must be opened by the main program unit before calling the subroutine AXIAL_TURBINE. For example:

IO2T = 22
OPEN(UNIT=**IO2**T,FILE='TURBINE.OUT',STATUS='NEW')
WRITE(**IO2T**,'(A)') **STARLINE**
WRITE(**IO2T**,'(A)') **TITLE**
WRITE(**IO2T**,'(A)') **STARLINE**
WRITE(**IO2T**,'(A)') ' '

C +++ OUTPUT FILE TO MONITOR ALL INTERNAL ITERATIONS PER HALF-STAGE:
IO3T = 23
OPEN(UNIT=**IO3T**,FILE='TURBINE_ITERATIONS.OUT',STATUS='NEW')
WRITE(**IO3T**,'(A)') **STARLINE**
WRITE(**IO3T**,'(A)') **TITLE**
WRITE(**IO3T**,'(A)') **STARLINE**
WRITE(**IO3T**,'(A)') ' '

C +++ OUTPUT FILE WHICH SUMMARIZES PERFORMANCE OF TURBINE:
IO4T = 24
OPEN(UNIT=**IO4T**,FILE='TURBINE_SUMMARY.OUT',STATUS='NEW')
WRITE(**IO4T**,'(A)') **STARLINE**
WRITE(**IO4T**,'(A)') **TITLE**
WRITE(**IO4T**,'(A)') **STARLINE**
WRITE(**IO4T**,'(A)') ' '

C +++ OUTPUT FILE TO CHECK PRESSURE LOSS COEFFICIENT MODEL:
IO5T = 25
OPEN(UNIT=**IO5T**,FILE='TURBINE_LOSSES.OUT',STATUS='NEW')
WRITE(**IO5T**,'(A)') **STARLINE**
WRITE(**IO5T**,'(A)') **TITLE**
WRITE(**IO5T**,'(A)') **STARLINE**
WRITE(**IO5T**,'(A)') ' '

C +++ OUTPUT FILE TO MONITOR SEARCH FOR ZERO OF FUNCTION FDICHO_W2T:
IO6T = 26
OPEN(UNIT=**IO6T**,FILE='TURBINE_DICHO.OUT',STATUS='NEW')
WRITE(**IO6T**,'(A)') **STARLINE**
WRITE(**IO6T**,'(A)') **TITLE**
WRITE(**IO6T**,'(A)') **STARLINE**
WRITE(**IO6T**,'(A)') ' '

The input parameters passed to the subroutine AXIAL_TURBINE through the argument list are:

IO1T	Unit number of output file for convergence of main iterations
IO2T	Unit number of output file to monitor all internal iterations per half-stage
IO3T	Unit number of output file which summarizes performance of multistage turbine

IO4T Unit number of output file to check pressure loss coefficient model
IO5T Unit number of output file to monitor search for zero of function FDICHO_W2T

iINIT0 Flag for initialization of variables in internal iterations
iINIT0 = 1: initialize internal iterations variables with first initial guess
iINIT0 <>1: use previous converged values of internal iterations variables
iSTEP Iteration or time step number (used for outputs in conjunction with **Nprintout**)
Nprintout Store transient values in output files every **Nprintout** time steps

x_He Molar fraction of helium in He-Xe gas mixture
TinT Gas temperature at inlet of turbine (K)
PinT Gas pressure at inlet of turbine (Pa)
FLRATET Gas mass flow rate through turbine (kg/s)
omega Shaft rotational (angular) speed (rad/s)

The parameter **iINIT0** is important and useful in reducing the number of internal iterations and amount of CPU time. Since typically the subroutine AXIAL_TURBINE will be called in succession, caused by a transient calculation (in which case **iSTEP** is the time step number), or by a performance curve development for which an input parameter is varied smoothly (in this case, **iSTEP** is simply a counter for data points), the parameter **iINIT0** must be set equal to 1 by the main program unit before calling the subroutine for the first time, and then set equal to 0 (any value different than 1) for all subsequent calls of the subroutine. This allows the subroutine to use previously calculated values of the flow conditions in the turbine to be used as initial guesses for the new iteration, thus reducing the amount of CPU time needed to achieve convergence.

The parameter **Nprintout** is set to 1 (during the debugging process, for example) if printout information is required every single time that the subroutine is called. Larger values are used to minimize the size of the output files, depending on the number of time steps used in the calculation.

Finally, the output parameters returned by the subroutine AXIAL_TURBINE through the argument list are:

TexT Gas temperature at exit of turbine (K)
PexT Gas pressure at exit of turbine (Pa)
AexT Gas flow area at exit of turbine (m^2)
VexT Gas velocity at exit of turbine (m/s)
MaexT Gas Mach number at exit of turbine
QlossesT Heat losses to ambient air through turbine casing (W)
WdiskT Sum of end-disk windage losses in turbine (W)
DPlossesT Total pressure losses in turbine (Pa)
WorkT Rate of mechanical work to the shaft (W)
EFFT Polytropic efficiency of turbine
TexTs Turbine exit temperature for isentropic evolution (K)
hexTs Turbine exit enthalpy for isentropic evolution (J/kg)
hin Turbine inlet enthalpy (J/kg)

Note that the end-disk windage losses WdiskT, which appear as a heat source in the gas energy conservation Equation (4-12), are a net power drain on the shaft, and must be included in the kinetic energy balance of the turbine shaft as such.

The subroutine AXIAL_TURBINE itself calls four major subroutines: TURBINE_STATOR, TURBINE_ROTOR, COMPRESSOR_STATOR, and DIFFUSER. The subroutine COMPRESSOR_STATOR is used for the exit guide vanes, while the subroutine DIFFUSER is used to calculate the flow conditions at the exit of the diffuser. These subroutine are included on the CD-ROM accompanying this manual.

4.7.4 Subroutine for Calculating Gas Properties

A subroutine called HE_XE is included with the present turbine and compressor models to calculate the thermodynamic and thermophysical properties of a binary mixture of helium and xenon gases. The model assumes that the gas behaves like a perfect gas, i.e., constant specific heat capacity and a compressibility factor of unity. This is a good assumption for helium gas and He-Xe binary mixtures with a molecular weight < 25 gram/mole. The FORTRAN models, nonetheless, have been written for handling real gases as well. The MELCOR-H2 team should replace the subroutine HE_XE with the properties of a gas of its choosing, given that the input and output parameters of the subroutine are identical to those of the subroutine HE_XE. The input parameters of this subroutine, from the argument list, are:

x_He	Molar fraction of helium in He-Xe gas mixture
T	Temperature of gas mixture (K)
P	Pressure of gas mixture (Pa)

The parameter **x_He**, of course, can be eliminated if binary mixtures are not used. The output parameters are, again from the argument list:

RHO	Density of gas mixture (kg/m^3)
CP	Specific heat capacity at constant pressure (J / kg.K)
h	Enthalpy (J/kg)
gamma	Specific heat ratio
S	Entropy (J/kg.K)
VISCO	Dynamic viscosity (kg/m.s)
CONDUC	Thermal conductivity (W/m.K)
XMOLW	Molecular weight of gas (kg/mol)
R	Gas constant (J/kg.K)
Z	Compressibility factor

4.8 Input and Output Files of Compressor Model

The axial-flow multistage compressor model consists of three major components:

- an input file COMPRESSOR.INP (Appendix G), which defines all geometrical parameters of the compressor unit and blades cascade;

- a subroutine COMPRESSOR_INPUT (Appendix H), which reads the input file "COMPRESSOR.INP." and writes a verification file "COMPRESSOR.VRF" to verify the formatting of all numerical values; this subroutine then calculates additional cascade geometrical parameters, and populates the COMMON/GEOMETRY_C/ and COMMON /CASCADES_C/;

- a subroutine AXIAL_COMPRESSOR (Appendix I), which, given input flow conditions, calculates the flow conditions at all intermediate stations and at the exit of the compressor; this subroutine accesses the geometrical parameters stored in the COMMON /GEOMETRY_C/ and COMMON /CASCADES_C/; this subroutine also populates a number of output text files:

  – "COMPRESSOR.OUT" collects information pertaining to the convergence of the main iterations;

  – "COMPRESSOR_ITERATIONS.OUT" gives detailed information on the convergence of all internal iterations for each half-stage;

  – "COMPRESSOR_SUMMARY.OUT" summarizes the calculated flow conditions for each half-stage of the compressor, and the overall performance of the compressor;

  – "COMPRESSOR_LOSSES.OUT" collects information on the pressure loss coefficient parameters calculated by the model; and finally,

  – "COMPRESSOR_DICHO.OUT" monitors the dichotomic research iterations for the solution technique of the rotor blades cascades; this file also collects the dichotomic research iterations used to calculate the exit enthalpy for an isentropic evolution; this value is used to calculate the polytropic efficiency of the compressor.

Due to the complexity of the geometry and the large number of parameters necessary to define the blade cascades of the axial-flow multistage compressor unit, an input file "COMPRESSOR.INP" is provided in Appendix G that emulates, to the best of the authors' knowledge, the design of the Japanese GTHTR300 20-stage compressor (Takizuka et al., 2004). The FORTRAN codes of the subroutines COMPRESSOR_INPUT and AXIAL_COMPRESSOR are given in Appendices H and I. The main subroutine AXIAL_COMPRESSOR uses other subroutines and functions, such as COMPRESSOR_STATOR, COMPRESSOR_ROTOR, and DIFFUSER. The input file and all subroutines and functions are available on the CD-ROM included with this manual. The next subsections describe the input and output parameters of the subroutines COMPRESSOR_INPUT and AXIAL_COMPRESSOR.

4.8.1 Input File "COMPRESSOR.INP"

This section describes in details the variables of the input file "COMPRESSOR.INP." The second line of the text file "COMPRESSOR.INP" is a text description of the compressor design and case run, and is read as the text variable TITLE by the subroutine COMPRESSOR_INPUT. This text line is used as headers in all output files to identify the case.

The first block of parameters defines the geometry of the axial-flow compressor:

Nstages	Number of rotor stages of axial-flow compressor
Rcas_in	Inner radius of compressor casing at inlet (m)
Rcas_ex	Inner radius of compressor casing at outlet (m)
Rhub_in	Hub radius at compressor inlet (m)
Rhub_ex	Hub radius at compressor outlet (m)
XLcompres	Axial length of compressor stages (m)
THICKcas	Thickness of metallic casing (m)
EMISScas	Radiative emissivity of metallic casing
Tair	Ambient air temperature (K)
deltaDisk	Clearance between housing and end-disks (m)

The model assumes that the casing and hub diameters vary linearly along the turbomachinery. The next block of parameters defines the geometry of the stator cascades (Figure 4-22), including the exit guide vanes. For example, a turbine with 20 stages (Nstages = 20) consists of a total of 21 stator sections (the first one is the inlet guide vanes, the last one the exit guide vanes), and 20 rotor sections.

beta1(i)	Stator blades angle at Leading Edge (degrees)
beta2(i)	Stator blades angle at Trailing Edge (degrees)
C(i)	True chord length of stator blades (m)
N(i)	Number of stator blades in cascade
Stagger	Stagger angle of stator blades (degrees)
Z(i)	Location of maximum camber (m)
O(i)	Throat opening of stator cascade (m)
tmax(i)	Maximum thickness of stator blades (m)
tTE(i)	Blade thickness at trailing edge (m)
tau(i)	Blade tip clearance to shroud (m)

In practice, many of these parameters are not reported in the literature and are not known. To simplify the work of the designer, the model is capable of calculating the parameters **Stagger**, **Z**, **O**, and **tmax** in terms of the other known parameters of the cascade, using empirical relations developed in Section 6 of the previous report (Tournier and El-Genk, 2006). In such case, the user must enter negative values of the parameters in the input file.

Model Parameters

- Blade angle at LE, β_1 (º)
- Blade angle at TE, β_2 (º)
- Chord length, *C* (m)
- Blades spacing / pitch, *S* (m)
- Blade stagger angle, Φ (º)
- Location of maximum camber, *Z* (m)
- Throat opening, *O* (m)
- Blade maximum thickness, t_{max} (m)
- Blade thickness at TE, t_{TE} (m)
- Blade tip clearance, τ (m)

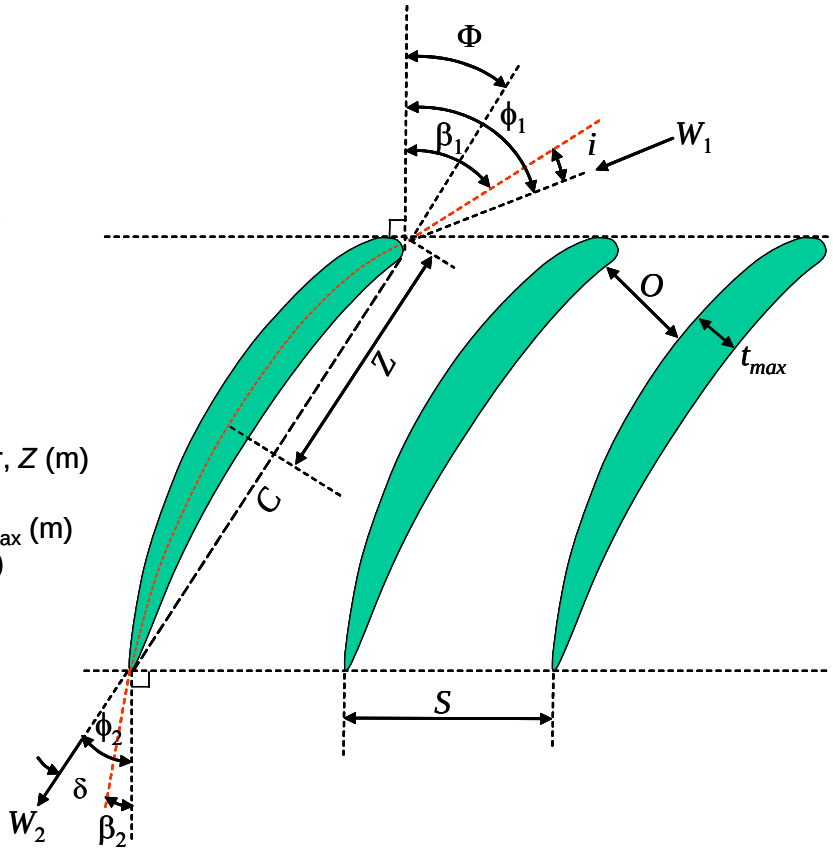

Figure 4-22. Geometry and nomenclature of compressor blades cascade.

The last block of parameters in the input file "COMPRESSOR.INP" defines the geometry of the rotor cascades, and is identical to that for the stator sections:

beta1(i)	Stator blades angle at Leading Edge (degrees)
beta2(i)	Stator blades angle at Trailing Edge (degrees)
C(i)	True chord length of stator blades (m)
N(i)	Number of stator blades in cascade
Stagger	Stagger angle of stator blades (degrees)
Z(i)	Location of maximum camber (m)
O(i)	Throat opening of stator cascade (m)
tmax(i)	Maximum thickness of stator blades (m)
tTE(i)	Blade thickness at trailing edge (m)
tau(i)	Blade tip clearance to shroud (m)

Again, the model will calculate the parameters **Stagger**, **Z**, **O**, and **tmax** in terms of the other known parameters of the cascade, if negative values are entered. A sample of an input file is given in Appendix G. Note that proper design of the compressor cascade blades requires that for a compressor cascade, $|\mathbf{beta1} - \mathbf{beta2}| \leq 90^o$, which is always satisfied in practice since the gas turning angle must be small in compressor blades to avoid detachment of the boundary layer in a positive pressure gradient field.

4.8.2 Subroutine COMPRESSOR_INPUT

The subroutine COMPRESSOR_INPUT (see Appendix H) reads the input file "COMPRESSOR.INP." and writes a verification file "COMPRESSOR.VRF" to verify the proper formatting of all input values. This subroutine then calculates additional cascade geometrical parameters, and populates the COMMON/GEOMETRY_C/ and COMMON /CASCADES_C/.

The input parameters passed to the subroutine COMPRESSOR_INPUT through the argument list are:

IO0 Unit number of input file "COMPRESSOR.INP"
IO1 Unit number of output file "COMPRESSOR.VRF" for verification

These files must be opened by the main program unit before calling the subroutine COMPRESSOR_INPUT. For example:

IO0 = 10
OPEN(UNIT=**IO0**, FILE= 'COMPRESSOR.inp', STATUS='OLD')
IO1 = 11
OPEN(UNIT=**IO1**, FILE= 'COMPRESSOR.vrf', STATUS='NEW')

The output parameters returned by the subroutine COMPRESSOR_INPUT through the argument list are:

STARLINE Text line of star characters ("*") for printout
TITLE Text title to identify compressor design in output files (second text line of input file "COMPRESSOR.INP")

The subroutine COMPRESSOR_INPUT also populates the COMMON /GEOMETRY_C/ and COMMON /CASCADES_C/, which collect all necessary geometrical parameters of the turbomachinery for use by the subroutine AXIAL_COMPRESSOR.

The PARAMETER (NC = 70) defines the maximum number of half-stages of blade cascades, and may have to be increased for a different design. For example, a compressor with 20 rotor stages requires a total of 41 half-stages (20 stators, 20 rotors and another stator corresponding to the exit guide vanes). The parameters of the COMMON /GEOMETRY_C/ are:

Nstages Number of rotor stages of axial-flow compressor
Rcas_in Inner radius of compressor casing at inlet (m)
Rcas_ex Inner radius of compressor casing at outlet (m)
Rhub_in Hub radius at compressor inlet (m)
Rhub_ex Hub radius at compressor outlet (m)
THICKcas Thickness of metallic casing (m)
EMISScas Radiative emissivity of metallic casing
Tair Ambient air temperature (K)
XLcompres Axial length of compressor stages (m)
XLzone Axial length of each zone (quarter stage) (m)

deltaDisk Clearance between housing and end-disks (m)

In addition, the following arrays are populated, where the subscript (*i*) represents the half-stage number. Each half-stage of the compressor consists of an isentropic contraction to the blades leading edge {0 – 1}, followed by a blades cascade {1 – 2}. In the following:

Subscript {0} denotes station {0}: Half-stage entrance;
Subscript {1} denotes station {1}: Leading edge of blades;
Subscript {2} denotes station {2}: Trailing edge of blades.
Subscript {01} denotes: Contraction zone between entrance and blades leading edge;
Subscript {12} denotes: blades cascade zone.

Rhub0(*i*) Hub radius at Station {0} (m)
Rcas0(*i*) Inner radius of compressor casing at Station {0} (m)
A0(*i*) Axial gas flow area at Station {0} (m^2)
Rhub1(*i*) Hub radius at Station {1} (m)
Rcas1(*i*) Inner radius of compressor casing at Station {1} (m)
A1(*i*) Axial gas flow area at Station {1} (m^2)
Rhub2(*i*) Hub radius at Station {2} (m)
Rcas2(*i*) Inner radius of compressor casing at Station {2} (m)
A2(*i*) Axial gas flow area at Station {2} (m^2)
Rhub01(*i*) Average hub radius in zone {01} (m)
Rcas01(*i*) Average inner casing radius in zone {01} (m)
Hb01(*i*) Average width of flow annulus in zone {01} (m)
Rhub12(*i*) Average hub radius in zone {12} (m)
Rcas12(*i*) Average inner casing radius in zone {12} (m)
Hb12(*i*) Average width of flow annulus in zone {12} (m)
Dcas01(*i*) Average outer casing diameter in zone {01} (m)
Acas01(*i*) Casing outer surface area in zone {01} (m^2)
C_Nu01(*i*), e_Nu01(*i*)
Coefficients to calculate Nusselt number for Taylor-Couette gas flow
Dcas12(*i*) Average outer casing diameter in zone {12} (m)
Acas12(*i*) Casing outer surface area in zone {12} (m2)
C_Nu12(*i*), e_Nu12(*i*)
Coefficients to calculate Nusselt number for Taylor-Couette gas flow

Finally, the subroutine COMPRESSOR_INPUT populates the COMMON /CASCADES_C/, again arranged by half-stage number:

beta1(*i*) Blades angle at Leading Edge (degrees)
beta2(*i*) Blades angle at Trailing Edge (degrees)
C(*i*) True chord length of blades (m)
N(*i*) Number of blades in cascade
Cx(*i*) Axial chord length of blades (m)
S(*i*) Blades spacing / pitch in cascade (m)
Z(*i*) Location of maximum camber (m)
O(*i*) Throat opening (m)

tmax(*i*) Maximum thickness of blades (m)
tTE(*i*) Blade thickness at Trailing Edge (m)
tau(*i*) Blade tip clearance to shroud (m)
theta(*i*) Blade camber angle (degrees)
sigma(*i*) Blade solidity
chi1(*i*) Leading edge blade angle with respect to the chord line (degrees)
chi2(*i*) Trailing edge blade angle with respect to the chord line (degrees)
stagger(*i*) Stagger angle of blades (degrees)
Hb1(*i*) Blades height at leading edge (m)
Hb2(*i*) Blades height at trailing edge (m)
Hb(*i*) Average height of blades (m)
r1m(*i*) Average blade radius at leading edge (m)
r2m(*i*) Average blade radius at trailing edge (m)
rm(*i*) Average blade radius (m)
At(*i*) Estimate of annular throat area (m^2)

4.8.3 Subroutine AXIAL_COMPRESSOR

The subroutine AXIAL_COMPRESSOR (see Appendix I), given input flow conditions, calculates the flow conditions at all intermediate stations and at the exit of the compressor. This subroutine accesses the geometrical parameters stored in the COMMON/GEOMETRY_C/ and COMMON /CASCADES_C/; this subroutine also populates a number of output text files:

- "COMPRESSOR.OUT" collects information pertaining to the convergence of the main iterations;
- "COMPRESSOR_ITERATIONS.OUT" gives detailed information on the convergence of all internal iterations for each half-stage;
- "COMPRESSOR_SUMMARY.OUT" summarizes the calculated flow conditions for each half-stage of the compressor, and the overall performance of the compressor;
- "COMPRESSOR_LOSSES.OUT" collects information on the pressure loss coefficient parameters calculated by the model; and finally,
- "COMPRESSOR_DICHO.OUT" monitors the dichotomic research iterations for the solution technique of the rotor blades cascades; this file also collects the dichotomic research iterations used to calculate the exit enthalpy for an isentropic evolution; this value is used to calculate the polytropic efficiency of the compressor.

These files must be opened by the main program unit before calling the subroutine AXIAL_COMPRESSOR. For example:

IO2 = 12
OPEN(UNIT=**IO2**,FILE= 'COMPRESSOR.OUT',STATUS='NEW')
WRITE(**IO2**,'(A)') **STARLINE**
WRITE(**IO2**,'(A)') **TITLE**

WRITE(**IO2**,'(A)') **STARLINE**
WRITE(**IO2**,'(A)') ' '

C +++ OUTPUT FILE TO MONITOR ALL INTERNAL ITERATIONS PER HALF-STAGE:
IO3 = 13
OPEN(UNIT=**IO3**,FILE= 'COMPRESSOR_ITERATIONS.OUT',STATUS='NEW')
WRITE(**IO3**,'(A)') **STARLINE**
WRITE(**IO3**,'(A)') **TITLE**
WRITE(**IO3**,'(A)') **STARLINE**
WRITE(**IO3**,'(A)') ' '

C +++ OUTPUT FILE WHICH SUMMARIZES PERFORMANCE OF COMPRESSOR:
IO4 = 14
OPEN(UNIT=**IO4**,FILE= 'COMPRESSOR_SUMMARY.OUT',STATUS='NEW')
WRITE(**IO4**,'(A)') **STARLINE**
WRITE(**IO4**,'(A)') **TITLE**
WRITE(**IO4**,'(A)') **STARLINE**
WRITE(**IO4**,'(A)') ' '

C +++ OUTPUT FILE TO CHECK PRESSURE LOSS COEFFICIENT MODEL:
IO5 = 15
OPEN(UNIT=**IO5**,FILE= 'COMPRESSOR_LOSSES.OUT',STATUS='NEW')
WRITE(**IO5**,'(A)') **STARLINE**
WRITE(**IO5**,'(A)') **TITLE**
WRITE(**IO5**,'(A)') **STARLINE**
WRITE(**IO5**,'(A)') ' '

C +++ OUTPUT FILE TO MONITOR SEARCH FOR ZERO OF FUNCTION FDICHO_W2C:
IO6 = 16
OPEN(UNIT=**IO6**,FILE= 'COMPRESSOR_DICHO.OUT',STATUS='NEW')
WRITE(**IO6**,'(A)') **STARLINE**
WRITE(**IO6**,'(A)') **TITLE**
WRITE(**IO6**,'(A)') **STARLINE**
WRITE(**IO6**,'(A)') ' '

The input parameters passed to the subroutine AXIAL_COMPRESSOR through the argument list are:

IO1	Unit number of output file for convergence of main iterations
IO2	Unit number of output file to monitor all internal iterations per half-stage
IO3	Unit number of output file which summarizes performance of multi-stage unit
IO4	Unit number of output file to check pressure loss coefficient model
IO5	Unit number of output file to monitor search for zero of function FDICHO_W2C

iINIT0 Flag for initialization of variables in internal iterations
iINIT0 = 1: initialize internal iterations variables with first initial guess
iINIT0 <>1: use previous converged values of internal iterations variables

iSTEP	Iteration or time step number (used for outputs in conjunction with **Nprintout**)
Nprintout	Store transient values in output files every **Nprintout** time steps

x_He	Molar fraction of helium in He-Xe gas mixture
TinC	Gas temperature at inlet of compressor (K)
PinC	Gas pressure at inlet of compressor (Pa)
FLRATEC	Gas mass flow rate through compressor (kg/s)
omega	Shaft rotational (angular) speed (rad/s)

The parameter **iINIT0** is important and useful in reducing the number of internal iterations and amount of CPU time. Since typically the subroutine AXIAL_COMPRESSOR will be called in succession, caused by a transient calculation (in which case **iSTEP** is the time step number), or by a performance curve development for which an input parameter is varied smoothly (in this case, **iSTEP** is simply a counter for data points), the parameter **iINIT0** must be set equal to 1 by the main program unit before calling the subroutine for the first time, and then set equal to 0 (any value different than 1) for all subsequent calls of the subroutine. This allows the subroutine to use previously calculated values of the flow conditions in the compressor to be used as initial guesses for the new iteration, thus reducing the amount of work needed to achieve convergence.

The parameter **Nprintout** is set to 1 (during the debugging process, for example) if printout information is required every single time that the subroutine is called. Larger values are used to minimize the size of the output files, depending on the number of time steps used in the calculation.

Finally, the output parameters returned by the subroutine AXIAL_COMPRESSOR through the argument list are:

TexC	Gas temperature at exit of compressor (K)
PexC	Gas pressure at exit of compressor (Pa)
AexC	Gas flow area at exit of compressor (m^2)
VexC	Gas velocity at exit of compressor (m/s)
MaexC	Gas Mach number at exit of compressor
QlossesC	Heat losses to ambient air through compressor casing (W)
WdiskC	Sum of end-disk windage losses in compressor (W)
DPlossesC	Total pressure losses in compressor (Pa)
WorkC	Rate of mechanical work to the shaft (W)
EFFC	Polytropic efficiency of compressor
TexCs	Compressor exit temperature for isentropic evolution (K)
hexCs	Compressor exit enthalpy for isentropic evolution (J/kg)
hin	Compressor inlet enthalpy (J/kg)

Note that the end-disk windage losses WdiskC, which appear as a heat source in the gas energy conservation Equation (4-37), are a net power drain on the shaft, and must be included in the kinetic energy balance of the compressor shaft as such.

The subroutine AXIAL_COMPRESSOR itself calls three major subroutines: COMPRESSOR_STATOR, COMPRESSOR_ROTOR, and DIFFUSER. The subroutine

COMPRESSOR_STATOR is used for the stator cascades and exit guide vanes, while the subroutine DIFFUSER is used to calculate the flow conditions at the exit of the diffuser. These subroutine are included on the CD-ROM accompanying this manual.

4.8.4 Subroutine for Calculating Gas Properties

The reader is directed to the discussion in Section 4.7.4, which also applies here to the axial-flow compressor models.

4.9 Transient Model of Generic Heat Exchanger

MELCOR-H2 requires the development and implementation of a number of heat exchanger models, i.e., gas/gas intermediate heat exchangers (IHX), gas/gas recuperator, and gas/liquid pre-cooler and inter-coolers. These heat exchangers may have different configurations and geometries, such as shell-and-tube heat exchangers, gasketed-plate heat exchangers, Lamella (or Ramen) heat exchangers, and extended-surface heat exchangers such as plate-fin and tubular-fin heat exchangers (Kakaç and Liu, 1998). The selection of each heat exchanger design, beyond the scope of the present work, is driven by many considerations, such as type of primary and secondary working fluids, fluid pressures and differential pressure losses, temperatures, accommodation of the differential thermal expansion, ease of cleaning, required heat transfer surface area and component size, and the cost of construction and maintenance.

To accommodate the different heat exchanger configurations of interest, a generic, transient and multi-node heat exchanger model is developed to simulate single-phase, parallel and/or counter-current flow arrangements. This generic model is applied to the particular heat exchanger configuration selected using appropriate flow path length, cross-sectional flow areas, equivalent diameters and heat transfer areas of the cold- and hot-leg channels. The transient generic heat exchanger model developed in this work for incorporation into MELCOR-H2 is described briefly next. More details on the constitutive governing equations of the problem and the numerical technique used to solve them can be found in Chapter 7 of the previous report (Tournier and El-Genk, 2006). The present heat exchanger model currently incorporates two different working fluids, helium gas and liquid water, and one structural material, stainless steel 304/316. Additional working fluids and structural materials can easily be incorporated by the MELCOR-H2 team, by following the guidelines given in subsequent sections of this manual. Since the model uses partial derivatives of the density and internal energy with respect to temperature and pressure, it can handle non-perfect gases and other highly compressible fluids as well.

4.9.1 Definition of Domain, Geometry and Boundary Conditions

The developed generic model of the heat exchanger is shown in Figure 4-23. The governing equations and boundary conditions are discretized on a staggered grid using the control volume integration approach. The coolant in the hot leg, represented by a string of cells (i = 2), is separated from the coolant in the cold leg (string i = 4) by a solid, heat transfer wall (string i = 3). The model uses two additional strings of solid cells (i = 1 and i = 5), thermally insulated on the far side, to appropriately account for the thermal mass of the structure of the heat exchanger. The physical domain is divided into a two-dimensional grid of 5 by Nz cells, on a staggered grid. In the axial direction, each flow channel is divided into Nz numerical cells of identical size ΔZ,

and extends from (j = 1) to (j = Nz). The surface areas of the sides of cell (i,j) are $A_r^{i,j}$, $A_r^{i-1,j}$, and A_z^i in the transverse and axial directions, respectively (Figure 4-23). The volume of the mass cell (i,j) is $VOL^{i,j}$. The denomination "cell" refers to the mass balance cell. On the staggered grid, the fluid density, ρ, pressure, P, temperature, T, and the internal energy, e, are defined at the center of the mass balance cells, while the velocity, V_z, and mass flux, G_z, are defined at the center of the faces of these cells (Figure 4-23).

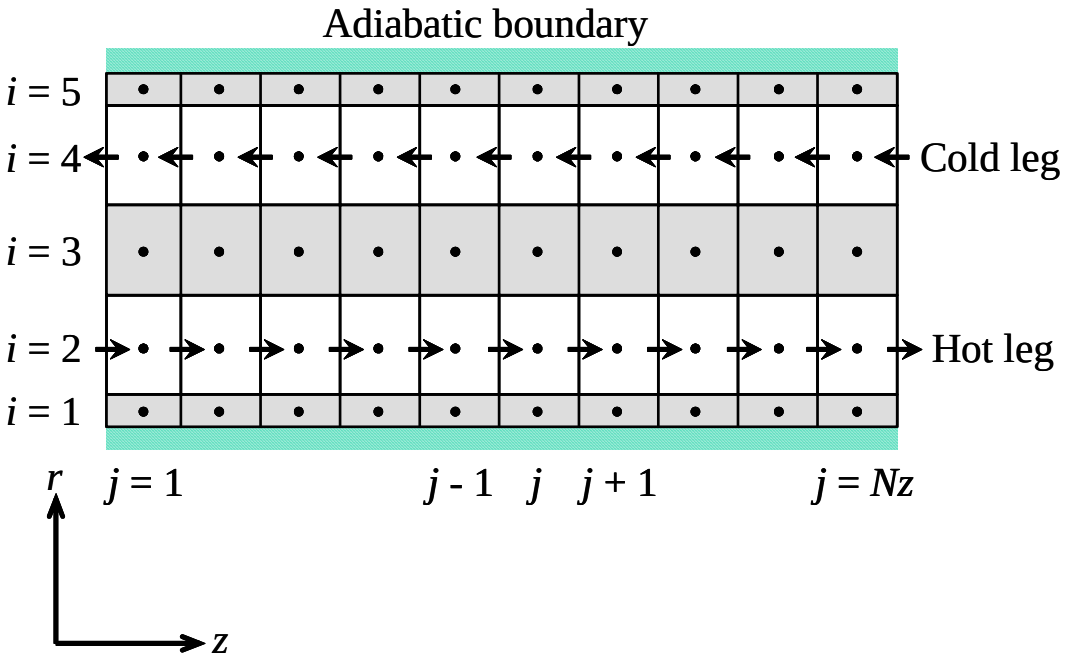

Figure 4-23. Numerical grid layout for heat exchanger.

The coolant in the hot leg (i = 2) enters the heat exchanger at interface (j = 0), and exits at interface (j = Nz). Therefore, the velocities, V_z(2,j), and mass fluxes, G_z(2,j), are positive. In the case of a parallel flow arrangement, the coolant in the cold leg (i = 4) also enters the heat exchanger at interface (j = 0), and exits at interface (j = Nz). For a counter-current flow arrangement, the coolant in the cold leg (i = 4) enters the heat exchanger at interface (j = Nz), and exits at interface (j = 0). In this case, the velocities, V_z(4,j), and mass fluxes, G_z(4,j), are negative.

At time zero (initial conditions), the model assumes a uniform temperature distribution; that is, all coolant and structural nodal temperatures are initialized at the same value. Furthermore, the pressure and mass flow rate in each coolant leg are assumed uniform at time zero. However, different values of the initial pressure and flow rate can be used for the primary and secondary sides of the heat exchanger.

The following boundary conditions are used in the model. The hot and cold side walls of the heat exchanger are assumed adiabatic (thermally insulated). Finally, the coolant temperature, pressure, and mass flow rate at the entrance of both the hot and cold legs are known, and specified by MELCOR-H2 at all time steps. Using these initial and boundary conditions, the

present model calculates all nodal temperatures, pressures, and mass fluxes in the heat exchanger as function of times. In particular, the model returns to MELCOR-H2 the coolant temperatures, pressures, and mass flow rates at the exit of the hot and cold legs.

4.9.2 Numerical Solution Algorithm

The numerical approach selected to solve the present non-linear governing equations in the secondary and primary sides and structural walls of the heat exchanger combines the power of the most advanced numerical methods to date and the advantage of algorithmic flexibility (Tournier and El-Genk, 2006). The developed technique is a SIMPLEC-type segregated solution technique (van Doormaal and Raithby, 1984), which includes two internal iterative steps to resolve the pressure-velocity and temperature-velocity couplings and reduce the linearization errors of the equations of state. Such a discretization method requires much less computational time and storage than finite-element methods. The final attraction of this integration approach is that it is simple to implement, and the finite-difference forms can be interpreted as integral laws over the control volume cell. The solution obtained using this approach satisfies global conservation, even on a non-uniform grid.

The SIMPLE-Consistent (SIMPLEC) algorithm of van Doormaal and Raithby (1984) uses a consistent simplification of the momentum correction equations and does not require any pressure under-relaxation (the off-diagonal velocity corrections appearing in the diffusion-convection fluxes are equated to the diagonal velocity correction). Any basic iteration of the present numerical technique is made of the following sequential steps:

(a) *energy predictor step:* best estimates of pressures and convective fluxes are used explicitly, and the energy conservation equations are solved for the temperatures, in the coolant channels and structural walls simultaneously.

(b) *properties update:* transport properties (conductivities and viscosities) are updated.

(c) *pressure corrector step:* the simplified (corrected) form of the axial momentum conservation equations is used to implicitly relate the mass fluxes and pressure gradients. The mass fluxes are then eliminated in terms of pressures in the mass balance (continuity) equations, and densities are linearized using the equations of state. The resulting elliptical Poisson equations are solved for the pressure field, which is updated.

(d) *momentum predictor step:* best estimates of the pressure gradients are calculated explicitly, and the axial momentum conservation equations are solved for the velocity field.

(e) *properties update:* the coolant (gas and/or liquid) densities are updated.

(f) iterations to (c) are performed until velocities and pressures converge (that is, until pressure corrections are below a prescribed value).

(g) iterations to (a) are performed until temperatures converge (that is, until temperature corrections are below a prescribed value).

In the pressure corrector step (c), the SIMPLEC procedure is used to eliminate the off-diagonal mass flux corrections. The predictor steps are stabilizing steps for the convection/diffusion terms.

The next section reviews the generic Nusselt number and friction factor correlations used in the present heat exchanger model.

4.9.3 Nusselt Number and Friction Factor Correlations

The Nusselt number for a fully-developed laminar flow in a coolant channel with a constant heat flux boundary condition, and assuming constant fluid properties, is given by (Kakaç and Lui, 1998):

$$\mathbf{Nu}_o = 4.36 \ , \quad \text{when} \quad \mathbf{Pe_b} D_{eq} / L \ < 10 \ , \tag{4-49a}$$

$$\mathbf{Nu}_o = 1.953 \times \left(\frac{\mathbf{Pe_b} D_{eq}}{L} \right)^{1/3} \ , \quad \text{when} \quad \mathbf{Pe_b} D_{eq} / L \ > 100 \ , \tag{4-49b}$$

where the fluid properties are evaluated at the coolant bulk temperature. The superposition of two asymptotes as proposed by Schlunder gives sufficiently good results (Figure 4-24):

$$\mathbf{Nu}_o = \left[(4.36)^3 + (1.953)^3 \times \left(\frac{\mathbf{Pe_b} D_{eq}}{L} \right) \right]^{1/3} \ . \tag{4-50}$$

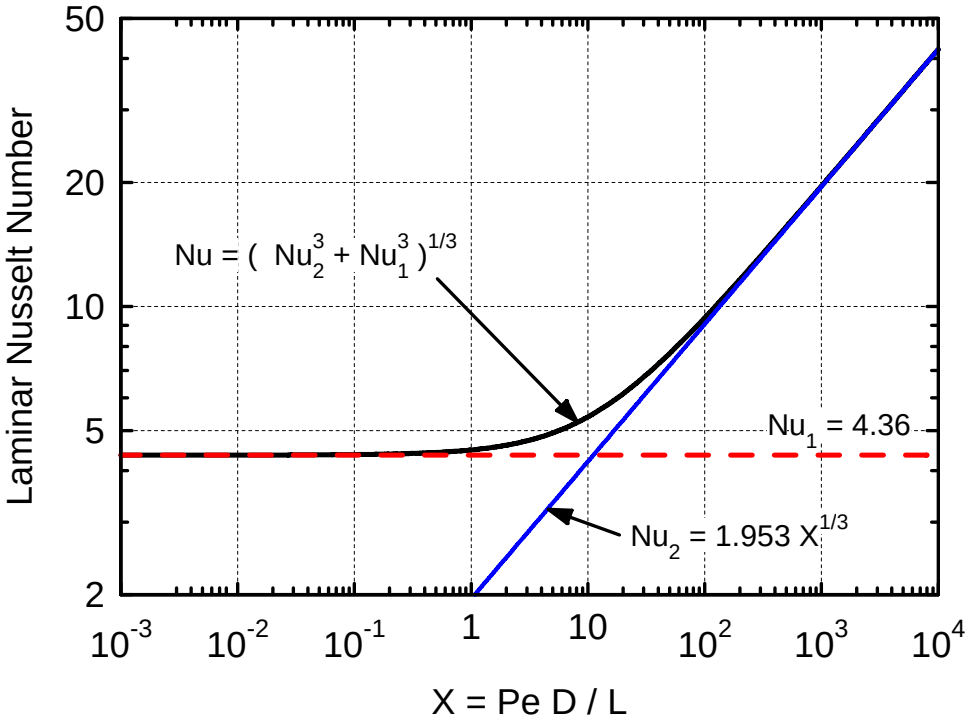

Figure 4-24. Laminar Nusselt number for constant heat flux boundary condition.

When the previous correlation is applied to practical heat transfer cases with large temperature differences between the wall and the coolant, the variation of fluid properties with temperature influences the velocity and temperature profiles through the boundary layer or over the cross-section flow area of the channel. Correction factors are applied to account for such effects. For the laminar flow of liquids, the Nusselt number of Equation (4-50) is corrected as (Kakaç and Lui, 1998):

$$\mathbf{Nu} = \mathbf{Nu}_o \times \left(\frac{\mu_b}{\mu_w} \right)^{0.14} . \tag{4-51}$$

No correction is necessary for the laminar flow of gases.

For the case of turbulent flow in smooth circular tubes, assuming constant properties and a constant heat flux boundary condition, Pethukov and Popov's theoretical calculations based on the three-layer turbulent boundary layer model, with constants adjusted to match a wide variety of experimental data, yielded (Pethukov, 1970; Kakaç and Lui, 1998):

$$\mathbf{Nu}_o = \frac{(f_o/8)\,\mathrm{Re}_b\,\mathrm{Pr}_b}{1.07 + 12.7 \times (f_o/8)^{1/2}(\mathrm{Pr}_b^{2/3} - 1)} , \tag{4-52}$$

where $f_o = (0/79 \times \mathrm{Ln}\,\mathrm{Re}_b - 1.64)^{-2}$ is Flonenko's Darcy friction factor. This correlation predicts the experimental data of gases and liquids with an error < 6% in the ranges $10^4 < \mathrm{Re}_b < 5 \times 10^6$ and $0.6 < \mathrm{Pr}_b < 200$. Gnielinski (1976) further modified Pethukov's correlation so that it covered experimental data in the transition flow region as well, i.e., $2300 < \mathrm{Re}_b < 10^4$:

$$\mathbf{Nu}_o = \frac{(f_o/8)(\mathrm{Re}_b - 1000)\,\mathrm{Pr}_b}{1 + 12.7 \times (f_o/8)^{1/2}(\mathrm{Pr}_b^{2/3} - 1)} . \tag{4-53}$$

Gnielinski's correlation predicted the experimental data of gases (such as air and helium) and liquids (such as water, oil, and glycerin) with an error < 6% in the ranges $2300 < \mathrm{Re}_b < 5 \times 10^6$ and $0.5 < \mathrm{Pr}_b < 200$. This successful and more general correlation is used in the present model of a generic heat exchanger.

The effect of thermal boundary conditions is almost negligible in turbulent forced convection. Therefore, Equation (4-53) can be used for both constant wall temperature and constant wall heat flux boundary conditions. For turbulent flow in non-circular channels, the practice of using the hydraulic diameter of the channel in place of the inner tube diameter leads to predicted Nusselt numbers that are within $\pm$ 10% of the experimental data, except for some sharp-cornered channels (Kakaç and Lui, 1998). This order of accuracy is adequate for the overall heat transfer coefficient (and the pressure drop calculations) in most of the practical heat exchanger designs.

To account for non-constant properties, the turbulent Nusselt number (Equation (4-53) is corrected as follows (Pethukov, 1970; Kakaç and Lui, 1998). For the turbulent flow of liquids:

$$\mathbf{Nu} = \mathbf{Nu}_o \times \left(\frac{\mu_b}{\mu_w} \right)^n \quad . \tag{4-54}$$

The exponent $n = 0.11$ when the liquid is heated ($\mu_w < \mu_b$), and $n = 0.25$ when the liquid is cooled ($\mu_w < \mu_b$). For the turbulent flow of gases:

$$\mathbf{Nu} = \mathbf{Nu}_o \times \left(\frac{T_b}{T_w} \right)^m \quad . \tag{4-55}$$

The exponent $m = 0.47$ when the gas is heated ($T_w < T_b$), and $m = 0.36$ when the gas is cooled ($T_w < T_b$).

The Darcy friction coefficient for smooth channels is shown in Figure 4-25. For a fully developed flow in the turbulent regime, the well-known expression derived by von Kármán, with constants adjusted to best fit Nikuradse's experimental data, is valid in the range $500 < \mathrm{Re}_b < 3 \times 10^6$:

$$\frac{1}{\sqrt{f_o / 4}} = 1.737 \times \ln\left(\frac{\mathrm{Re}_b}{\sqrt{f_o / 4}} \right) - 0.4 \quad . \tag{4-56}$$

This equation, however, is a transcendental function of the friction factor f_o. We use instead the approximation developed by Flonenko with < 2% error (Pethukov, 1970; Kakaç and Lui, 1998) (see Figure 4-25), which gives an explicit expression for f_o:

$$f_o = (0.79 \times \ln \mathrm{Re}_b - 1.64)^{-2} \quad . \tag{4-57}$$

For the case of laminar flow in smooth tubes and channels of triangular and trapezoidal cross-sections, the Darcy friction factor is given by:

$$f_o = \frac{64}{\mathrm{Re}_b} \quad . \tag{4-58}$$

A linear interpolation is used in the transition region, when $2300 < \mathrm{Re}_b < 5000$ (Figure 4-25).

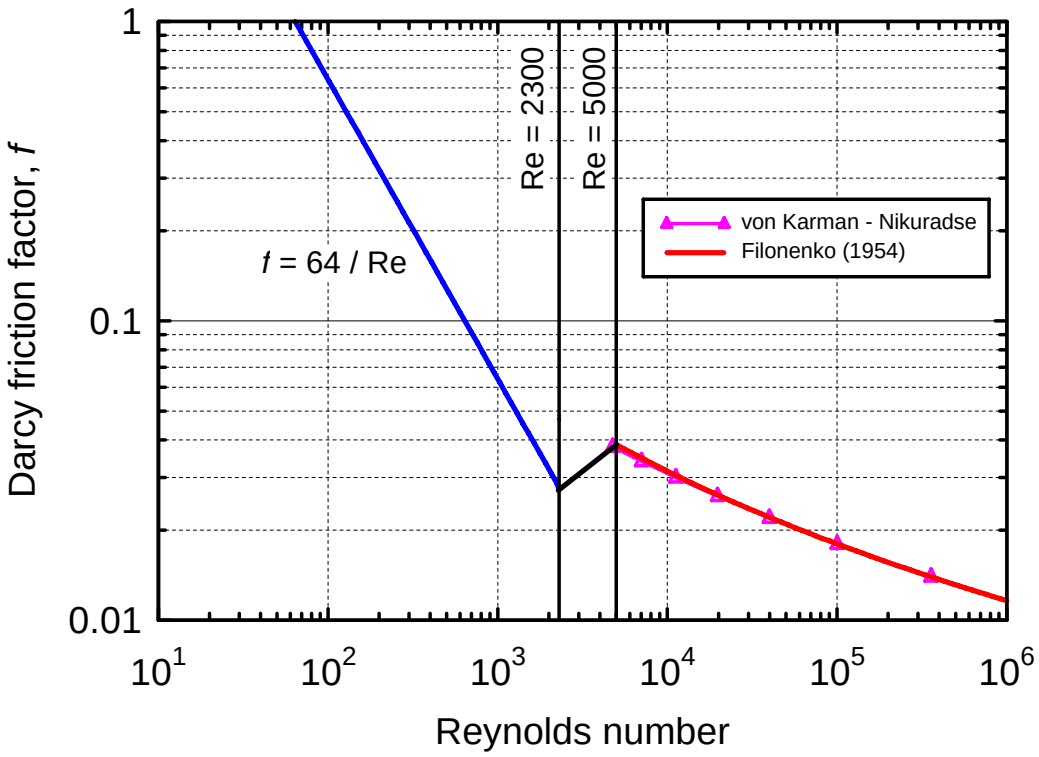

Figure 4-25. Darcy friction factor for smooth surfaces.

To account for non-constant properties, the friction factor (Equation (4-58)) is corrected as follows (Pethukov, 1970; Kakaç and Lui, 1998). For the laminar flow of liquids:

$$f = f_o \times \left(\frac{\mu_b}{\mu_w} \right)^n \quad . \tag{4-59}$$

The exponent $n = -0.58$ when the liquid is heated ($\mu_w < \mu_b$), and $n = -0.50$ when the liquid is cooled ($\mu_w < \mu_b$). For the laminar flow of gases:

$$f = f_o \times \left(\frac{T_b}{T_w} \right)^m \quad . \tag{4-60}$$

The exponent $m = -1.0$ when the gas is heated ($T_w < T_b$), and $m = -0.81$ when the gas is cooled ($T_w < T_b$).

For the turbulent flow of liquids that are heated:

$$f = \frac{f_o}{6} \times \left(7 - \frac{\mu_b}{\mu_w} \right) . \tag{4-61}$$

For the turbulent flow of liquids that are cooled:

$$f = f_o \times \left(\frac{\mu_b}{\mu_w} \right)^{-0.24} . \tag{4-62}$$

For the turbulent flow of gases:

$$f = f_o \times \left(\frac{T_b}{T_w} \right)^{m} . \tag{4-63}$$

The exponent $m = 0.52$ when the gas is heated ($T_w < T_b$), and $m = 0.38$ when the gas is cooled ($T_w < T_b$).

Due to the poor heat transfer characteristics of gases, most heat exchanger designs use extended, i.e., finned heat transfer surface areas, and such designs are allowed in the present, generic model. In each axial Section {j}, the thermal heat flow between the coolant and the wall is given by:

$$Q_j = h_j^{CV} \left(S_{un} + \eta_{fin} S_{fin} \right)_j \times \left(T_b - T_w \right)_j , \tag{4-64}$$

Where S_{un} is the unfinned heat transfer area, S_{fin} is the finned surface area between coolant and wall, and η_{fin} is the fins efficiency (Kakaç and Lui, 1998). The most common fins are rectangular fins of constant thickness δ_{fin}. For the case of symmetric fins, whose ends are both in contact with the wall, encountered in stacked matrices for example, the fin efficiency is given by:

$$\eta_{fin} = \frac{\tanh(\alpha)}{\alpha}, \text{ where } \alpha = L_{fin} \left(\frac{h^{CV}}{2 \lambda_{fin} \delta_{fin}} \right)^{1/2} . \tag{4-65}$$

For the case of fins with an adiabatic tip, as in the case of longitudinal fins attached to the outside wall of a tube, for example, the fin efficiency is given by:

$$\eta_{fin} = \frac{\tanh(\alpha)}{\alpha}, \text{ where } \alpha = L_{fin} \left(\frac{2h^{CV}}{\lambda_{fin} \delta_{fin}} \right)^{1/2} . \tag{4-66}$$

The average fin temperature can then be calculated using:

$$\overline{T}_{fin} = T_b + \eta_{fin} \times (T_w - T_b) . \tag{4-67}$$

4.10 Input and Output Files of Heat Exchanger Model

FORTRAN subroutines of the present heat exchanger model were developed and tested using Compaq Visual FORTRAN Professional Edition 6.5.0 (2000), which provides a superset of the FORTRAN 95 standard with other extensions for compatibility with previous FORTRAN languages and platforms. Nonetheless, all the coding instructions used in the present model are compatible with Standard FORTRAN 77.

The transient, multi-node heat exchanger model consists of four major components:

- an input file "HX.INP" (Appendices K and L), which defines all geometrical parameters of the heat exchanger;

- a subroutine HX_INPUT (Appendix M), which reads the input file "HX.INP." and writes a verification file "HX.VRF" to verify the formatting of all numerical values; this subroutine then calculates additional geometrical parameters, generates the numerical mesh, and populates the COMMON /HX_DATA/, /HX_DATAi/, /MESH/, /SOLUTION/ and /OUTPUT/;

- a subroutine INITIALIZE (Appendix N), which initializes temperatures, pressures, densities and axial mass fluxes at the nodes of the numerical grid, and coefficients for heat transfer boundary conditions;

- a subroutine HEAT_EXCHANGER (Appendix O), which, given input flow conditions for both the hot and cold legs and the time step, calculates the new values, at the end of the time step, of all temperatures, pressures, and axial mass fluxes in the heat exchanger and at the exit of the hot and cold legs; this subroutine accesses the geometrical parameters stored in the COMMON /HX_DATA/, /HX_DATAi/ and /MESH/; this subroutine also populates two output text files:

  – "HX.OUT" collects information showing the succession of subroutine calls and pertaining to the convergence of the main iterations;

  – "RESIDU.OUT" gives detailed information on the convergence of all internal iterations by monitoring the value of the residuals and the changes in the temperature and pressure corrections for each iteration.

Two examples of input files "HX.INP" are provided in Appendices K and L, which emulate a helium/water pre-cooler rated ~ 300 MW (Appendix K) and a He/He plate-fin recuperator with triangular stacked matrices rated ~ 1000 MW (Appendix L), when operating at the inlet conditions encountered in the pre-cooler and recuperator of the Japanese GTHTR300 power plant (Takizuka et al., 2004). The FORTRAN source codes of the subroutines HX_INPUT, INITIALIZE and HEAT_EXCHANGER are given in Appendices M, N, and O. The subroutines that calculate the coolant and wall properties, COOLANT_PROPERTIES and WALL_PROPERTIES, are given in Appendices P and Q. The main subroutine HEAT_EXCHANGER uses other subroutines, such as COOLANT_DENSITY, VELOCITIES, ENERGY, HEAT_FLOW, MOMENTUM, and SPOISSON. The input file and all subroutines

and functions are available on the CD-ROM included with this manual. The next subsections describe the input and output parameters of the subroutines HX_INPUT, INITIALIZE, and HEAT_EXCHANGER.

4.10.1 Input File "HX.INP"

This section describes in details the variables of the input file "HX.INP." For clarity, all variable names used in the program are typed in **BOLD** in this manual. The model uses the International System Units throughout.

The second line of the text file "HX.INP" is a text description of the heat exchanger design and case run, and is read as the text variable **TITLE** by the subroutine HX_INPUT. This text line is used as headers in all output files to identify the case.

IFLAG13 A value of 1 is used for debugging the model; in this case, all printouts are generated in output files "HX.out" and "RESIDU.out." pertaining to the value of the residuals and the convergence of all iterations

iCOOLANT2 Flag for selecting hot-leg coolant (1 = helium)
iCOOLANT4 Flag for selecting cold-leg coolant (1 = helium, 2 = H_2O)
iWALL Flag for structural material (1 = SS-304/316)

The following block of parameters defines the geometry of the heat exchanger.

iCURRENT Type of flow arrangement (1 = counter-current, else = parallel flow)
XL Total length of the flow channels (m)
AFLOW2 Total flow area of hot-leg coolant channels (m^2)
Dequ2 Equivalent diameter of hot-leg coolant channels (m)
AFLOW4 Total flow area of cold-leg coolant channels (m^2)
Dequ4 Equivalent diameter of cold-leg coolant channels (m)

XMASSw1 Total mass of hot-leg outer walls (kg)
XMASSw3 Total mass of heat-exchange walls and fins (kg)
XMASSw5 Total mass of cold-leg outer walls (kg)
DR1 Thickness of hot-leg outer walls (m)
DR3 Thickness of separation walls between coolant legs (m)
DR5 Thickness of cold-leg outer walls (m)

Sun2 Unfinned, total heat-exchange area on hot side (m^2)
Sfin2 Finned, total heat-exchange area on hot side (m^2)
iFIN2 Hot fins type (1 = stacked matrices, 2 = adiabatic tip)
XLfin2 Length of hot-side fins (m)
dFIN2 Thickness of hot-side fins (rectangular fins) (m)

Sun4 Unfinned, total heat-exchange area on cold side (m^2)
Sfin4 Finned, total heat-exchange area on cold side (m^2)
iFIN4 Cold fins type (1 = stacked matrices, 2 = adiabatic tip)

XLfin4 Length of cold-side fins (m)
dFIN4 Thickness of cold-side fins (rectangular fins) (m)

In the absence of fins, use **Sfin2** = 0 (or **Sfin4** = 0), but non-zero values of the fins thickness.

Nz Number of discretization nodes along flow channels (use **Nz** $\geq$ 3 since special treatment is necessary in the entrance and exit cells; also **Nz** $\leq$ 60 presently). To allow larger values, increase the value of the parameter **Mz** in the statement PARAMETER (**Mr**=5, **Mz**=60), wherever it appears in the source code. In practice, 10 to 20 nodes is sufficient for good accuracy.

The following block of the input file "HX.INP" defines the numerical solution parameters.

CWJYZ3 Defines the type of momentum conservation equations approximation (0 = SIMPLE 1 = SIMPLEC approximation)

The use of SIMPLEC is strongly recommended for the present model.

IOKMAX Maximum number of temperature-coupling internal iterations. A value > 20

Ensures good convergence even when using large time steps > 1.0 s.

CVGSIMPL Maximum value of mass balance residual (kg/s) for convergence of SIMPLEC internal iterations. These iterations are usually not limiting; therefore a small value of 10^{-12} kg/s can be used without penalty.

INTERMAX Maximum number of SIMPLEC internal iterations (3 or more is adequate)

CVGenth Maximum value of energy balance residual (W) for convergence of energy internal iterations; for multi-megawatt size exchangers, CVGenth = 100 W is adequate.

ITERhMAX Maximum number of energy internal iterations (3 or more is adequate)

4.10.2 Subroutine HX_INPUT

The subroutine HX_INPUT (see Appendix M) reads the input file "HX.INP." and writes a verification file "HX.VRF" to verify the proper formatting of all input values. This subroutine then calculates additional geometrical parameters, generates the numerical mesh, and populates the COMMON /HX_DATA/, /HX_DATAi/, /MESH/, /SOLUTION/ and /OUTPUT/.

The input parameters passed to the subroutine HX_INPUT through the argument list are:

IO0 Unit number of input file "HX.INP"
IO1 Unit number of output file "HX.VRF" for verification
IO2 Unit number of output file "HX.OUT" to monitor the subroutine calls and iterations

IO3 Unit number of output file "RESIDU.OUT" to monitor the value of the residuals and the convergence of the internal iterations

These files are opened by the subroutine HX_INPUT itself.

The output parameters returned by the subroutine HX_INPUT through the argument list are:

STARLINE Text line of star characters ("*") for printout
TITLE Text title to identify heat exchanger design in output files (second text line of input file "HX.INP")

The subroutine HX_INPUT also generates the numerical mesh and populates the COMMON /HX_DATA/, /HX_DATAi/, /MESH/, /SOLUTION/ and /OUTPUT/; a detailed description of the parameters of these COMMONs is given in the source code, at the beginning of each subroutine which uses them.

This subroutine also calculates the density of the structural material, based on the input parameter iWALL. The subroutine HX_INPUT uses an array ROMATRIX which contains the density values (kg/m^3) of the structural materials. The initialization of this array reads presently:

```
C +++ ===> iWALL = 1: DENSITY OF STAINLESS-STEEL 304/316:
      DOUBLE PRECISION ROMATRIX(1)
      DATA ROMATRIX  /7900.D0/
```

New structural materials can be added by the MELCOR-H2 team by extending the size of this array and of the corresponding DATA statement.

4.10.3 Subroutine INITIALIZE

The subroutine INITIALIZE (see Appendix N) initializes temperatures, pressures, densities, and axial mass fluxes at the nodes of the numerical grid, and coefficients for heat transfer boundary conditions. The input parameters passed to the subroutine INITIALIZE through the argument list are:

IO2 Unit number of output file "HX.OUT"
T_INIT Initial temperature of heat exchanger (K)
P_INIT2 Initial pressure of hot-leg gas coolant (Pa)
P_INIT4 Initial pressure of cold-leg coolant (Pa)
MDOTin2 Initial mass flow rate through hot-leg gas coolant (kg/s)
MDOTin4 Initial mass flow rate through cold-leg coolant (kg/s)

The output parameters passed back to the calling program through the argument list are:

Tex2 Exit temperature of hot-leg gas coolant (K)
Pex2 Exit pressure of hot-leg gas coolant (Pa)
Tex4 Exit temperature of cold-leg coolant (K)
Pex4 Exit pressure of cold-leg coolant (Pa)

This subroutine also initializes temperatures, pressures, densities, and axial mass fluxes at the nodes of the numerical grid, and populates the variables of the COMMON /OLDFIELD/:

RO(i,j)	Previous-time densities in fluid and solid phases (kg/m^3)
P(i,j)	Previous-time pressure field in fluid phases (Pa)
T(i,j)	Previous-time temperature field in fluid and solid phases (K)
Gz(i,j)	Previous-time axial mass fluxes in fluid regions (kg/m^2.s)

The MELCOR-H2 code must therefore include a number of instructions during the initialization period of the heat exchanger model. For example, these could be as follows:

```
C ### ********************************************************************
C +++ *  READING OF THE INPUT FILE "HX.INP" and NUMERICAL MESH DEVELOPMENT
C +++ ********************************************************************
C +++ UNIT NUMBER OF INPUT FILE "HX.INP":
      IO0 = 10
C +++ UNIT NUMBER OF VERIFICATION FILE "HX.VRF":
      IO1 = 11
C +++ UNIT NUMBER OF OUTPUT FILE "HX.OUT" TO MONITOR ITERATIONS:
      IO2 = 12
C +++ UNIT NUMBER OF OUTPUT FILE "RESIDU.OUT" TO MONITOR RESIDUALS:
      IO3 = 13

      CALL HX_INPUT(IO0,IO1,IO2,IO3, STARLINE,TITLE )
C
C +++ ********************************************************************
C +++ * INITIALIZATION OF PRESSURES (P), TEMPERATURES (T), MASS FLUXES (Gz),
C +++ * PROPERTIES IN FLUID AND WALL REGIONS, AND BOUNDARY CONDITIONS      *
C +++ ********************************************************************
C +++ INITIAL TEMPERATURE OF HEAT EXCHANGER (K)
      T_INIT  = 410.00D0
C +++INITIAL PRESSURE OF  HOT-LEG GAS COOLANT (Pa)
      P_INIT2 = 36.70D5
C +++ INITIAL PRESSURE OF COLD-LEG COOLANT (Pa)
      P_INIT4 = 70.50D5
C
C +++ INITIAL MASS FLOW RATE OF HOT-LEG COOLANT (kg/s)
      MDOTin2 =  0.D-6
C +++ INITIAL MASS FLOW RATE OF COLD-LEG COOLANT (kg/s)
      MDOTin4 =  0.D-6
C
      CALL INITIALIZE(IO2,T_INIT,P_INIT2,P_INIT4,MDOTin2,MDOTin4,
     &                           Tex2,Pex2,Tex4,Pex4          )
C
C +++ ********************************************************************
C +++ * END OF THE INITIALIZATION PHASE
C +++ ********************************************************************
C
```

4.10.4 Subroutine HEAT_EXCHANGER

The subroutine HEAT_EXCHANGER (see Appendix O), given input flow conditions for both the hot and cold legs and the time step, calculates the new values, at the end of the time step, of all temperatures, pressures, and axial mass fluxes in the heat exchanger and at the exit of the hot and cold legs; this subroutine accesses the geometrical parameters stored in the COMMON /HX_DATA/, /HX_DATAi/ and /MESH/; this subroutine also populates two output text files:

- "HX.OUT" collects information showing the succession of subroutine calls and pertaining to the convergence of the main iterations;

- "RESIDU.OUT" gives detailed information on the convergence of all internal iterations by monitoring the value of the residuals and the changes in the temperature and pressure corrections for each iteration.

The input parameters passed to the subroutine HEAT_EXCHANGER through the argument list re:

IO2	Unit number of output file "HX.OUT"
IO3	Unit number of output file "RESIDU.OUT"
TIME	Time value at the end of the time step (s)
TAU	Numerical time step used to advance the solution (s)
ITER	Time step number
Tin2	New-time inlet temperature of hot-leg gas coolant (K)
Pin2	New-time inlet pressure of hot-leg gas coolant (Pa)
MDOTin2	New-time inlet mass flow rate of hot-leg gas coolant (kg/s)
Tin4	New-time inlet temperature of cold-leg coolant (K)
Pin4	New-time inlet pressure of cold-leg coolant (Pa)
MDOTin4	New-time inlet mass flow rate of cold-leg coolant (kg/s)

The subroutine HEAT_EXCHANGER also requires as input the values of the temperatures, pressures, and axial mass fluxes at the old time (the previous time step values), which are stored in the COMMON /OLDFIELD/:

P(i,j)	Previous-time pressure field in fluid phases (Pa)
T(i,j)	Previous-time temperature field in fluid and solid phases (K)
Gz(i,j)	Previous-time axial mass fluxes in fluid regions ($kg/m^2.s$)

The subroutine HEAT_EXCHANGER itself calls other subroutines, such as COOLANT_DENSITY, VELOCITIES, ENERGY, HEAT_FLOW, MOMENTUM, and SPOISSON. These subroutine are also included on the CD-ROM accompanying this manual.

The output parameters passed back to the calling program through the argument list are:

Tex2	New-time exit temperature of hot-leg gas coolant (K)
Pex2	New-time exit pressure of hot-leg gas coolant (Pa)
MDOTex2	New-time exit mass flow rate of hot-leg gas coolant (kg/s)
Tex4	New-time exit temperature of cold-leg coolant (K)
Pex4	New-time exit pressure of cold-leg coolant (Pa)
MDOTex4	New-time exit mass flow rate of cold-leg coolant (kg / s)
QWALL1	Heat flow between hot-leg coolant and hot side wall {1} (W)
QHOT2	Heat flow between hot-leg coolant and heat exchanger wall {3} (W)
QCOLD3	Heat flow between heat exchanger wall {3} and cold-leg coolant (W)
QWALL4	Heat flow between cold-leg coolant and cold side wall {5} (W)
Qcoolant2	New-time coolant enthalpy loss in hot-leg (W)
Qcoolant4	New-time coolant enthalpy gain in cold-leg (W)
QHOTin	Convection of internal energy at inlet of hot-leg (W)
QHOTex	Convection of internal energy at exit of hot-leg (W)
QCOLDin	Convection of internal energy at inlet of cold-leg (W)
QCOLDex	Convection of internal energy at exit of cold-leg (W)

In addition to these outputs, the subroutine also stores the new-time values (at the end of the time step) of temperatures, pressures, and axial mass fluxes at the nodes of the heat exchanger numerical grid, in the COMMON /NEWFIELD/:

pNEW(i,j)	New-time pressure field in fluid phases (Pa)
TNEW(i,j)	New-time temperature field in fluid and solid phases (K)
GzNEW(i,j)	New-time axial mass fluxes in fluid regions ($kg/m^2.s$)

The two COMMONS /OLDFIELD/ and /NEWFIELD/ are used to give the time-integration routine of MELCOR-H2 full control over advancing the solution in time or not. For example, MELCOR-H2 may use a tentative time step size TAU and perform the solution through the different components of the power plant. It then may find that one of the convergence criteria for one component is not satisfied to obtain the target accuracy, requiring the same time iteration step to be performed again, but with a smaller time step TAU. In such case, the values of temperatures, pressures, and mass fluxes in the heat exchanger at the old time value are still available in the COMMON /OLDFIELD/. Only after all convergence criteria are satisfied at the new time value can the solution of the transient be advanced, by copying the old-time variables P(i,j), T(i,j) and Gz(i,j) over with the new-time values pNEW(i,j), TNEW(i,j) and GzNEW(i,j) calculated by the subroutine HEAT_EXCHANGER. To illustrate this point, the following code lines show a typical time step iteration performed by MELCOR-H2:

```
C +++ ************************************************************************
C +++ * TIME UPDATING (TIME STEP ITERATION)
C +++ ************************************************************************
C
C +++ CALCULATE NEW-TIME VALUE:
       TIME  = TIME + TAU
C
C +++ ************************************************************************
C +++  NEW-TIME VALUES OF INLET PRESSURES, TEMPERATURES, AND MASS FLOW RATES:
C +++ ************************************************************************
C +++ INLET TEMPERATURE    OF HOT-LEG GAS COOLANT      (K)
      Tin2 = ...
C
C +++ INLET PRESSURE       OF HOT-LEG GAS COOLANT     (Pa)
      Pin2 = ...

C +++ INLET MASS FLOW RATE OF HOT-LEG GAS COOLANT   (kg/s)
      MDOTin2 = ...
C
C +++ INLET TEMPERATURE    OF COLD-LEG    COOLANT      (K)
      Tin4 = ...
C
C +++ INLET PRESSURE       OF COLD-LEG    COOLANT     (Pa)
      Pin4 = ...
C
C +++ INLET MASS FLOW RATE OF COLD-LEG    COOLANT   (kg/s)
      MDOTin4 = ...
C
      CALL HEAT_EXCHANGER(IO2,IO3, TIME,TAU,ITER,
     &                       Tin2, Pin2, MDOTin2, Tin4, Pin4, MDOTin4,
     &                       Tex2, Pex2, MDOTex2, Tex4, Pex4, MDOTex4,
     &                  QWALL1,QHOT2,QCOLD3,QWALL4,Qcoolant2,Qcoolant4,
     &                  QHOTin,QHOTex,QCOLDin,QCOLDex)
C
C
C +++ ************************************************************************
C +++ AT THIS POINT, IF ACCURACY CRITERIA FOR ALL COMPONENTS IN THE POWER
C +++ PLANT ARE SATISFIED, MELCOR-H2 CAN ADVANCE THE TRANSIENT SOLUTION BY
C +++ COPYING THE NEW-TIME FIELDS OVER THE OLD-TIME FIELDS FOR NEXT ITERATION
C +++ ************************************************************************
C
      DO 100 j=1,Nz
C
      DO 101 i=1,Nr
        T(i,j) =  TNEW(i,j)
 101  CONTINUE
C
        P(2,j) =  pNEW(2,j)
        P(4,j) =  pNEW(4,j)
C
 100  CONTINUE
C
      DO 103 j=0,Nz
        Gz(2,j) = GzNEW(2,j)
        Gz(4,j) = GzNEW(4,j)
  103 CONTINUE
C
```

```
C +++ ADVANCE TRANSIENT SOLUTION:
       ITER  = ITER + 1
C
```

Therefore, the main time-iteration subroutine of MELCOR-H2 must be able to access the COMMONS /OLDFIELD/ and /NEWFIELD/, by including the following instructions:

```
C ************************************************************************
C * SPATIAL DISTRIBUTION OF HEAT EXCHANGER FIELDS AT OLD TIME:
C ************************************************************************
      COMMON /OLDFIELD/
     &          RO(Mr,Mz)  , P(Mr,Mz)  ,  T(Mr,Mz)  ,E(Mr,Mz),
     &          Uz(Mr,0:Mz),Gz(Mr,0:Mz),ROz(Mr,0:Mz)
C
C
C ************************************************************************
C * SPATIAL DISTRIBUTION OF HEAT EXCHANGER FIELDS AT TENTATIVE NEW TIME:
C ************************************************************************
      COMMON /NEWFIELD/
     &          RONEW(Mr,Mz)  , pNEW(Mr,Mz)  ,TNEW(Mr,Mz),eNEW(Mr,Mz),
     &          UzNEW(Mr,0:Mz),GzNEW(Mr,0:Mz)
C
```

The following section provides some guidelines for incorporating new working fluids and structural materials in the heat exchanger model.

4.10.5 Subroutines for Calculating Coolant and Wall Properties

The present heat exchanger model currently incorporates two different working fluids, helium gas (iCOOLANT = 1) and liquid water (iCOOLANT = 2), and one structural material, stainless steel 304/316 (iWALL = 1). Additional working fluids and structural materials can easily be incorporated by the MELCOR-H2 team, using the following guidelines. Since the model uses partial derivatives of the density and internal energy with respect to temperature and pressure, it can handle non-perfect gases and other highly compressible fluids as well.

The addition of a new working fluid requires modification of the following subroutines:

- COOLANT_DENSITY, which calculates the mass density of the coolant and its partial derivatives with respect to temperature and pressure, $(\partial\rho/\partial T)_P$ and $(\partial\rho/\partial P)_T$, at the nodes of the cold- or hot-leg channel;

- COOLANT_VISCOSITY, which calculates the dynamic viscosity of the coolant at the wall surface nodes of the cold- or hot-leg channel; this subroutine is used to correct the Darcy friction factor and Nusselt number of liquids at the wall (see Section 4.9.3);

- COOLANT_PROPERTIES, which calculates the coolant dynamic viscosity, thermal conductivity, specific heat capacity at constant volume, mass internal energy, and Prandtl number at the nodes of the cold- or hot-leg channel (see Appendix P);

- TofENERGY, which calculates the coolant temperature as a function of internal energy at the nodes of the cold- or hot-leg channel; this routine is used to calculate the temperatures at the exit of the coolant channels.

These subroutines use a simple numbered GOTO structure to access the property correlations of each working fluid, and the MELCOR-H2 team can include new coolants of its choosing, given that the input and output parameters of the subroutines are identical to those shown in the subroutines provided.

In addition, distinction between liquid and gases must be made in the subroutines FRICTION_FACTOR and NUSSELT_NUMBER, according to the equations of Section 4.9.3, used by the model to calculate the Darcy friction factor and Nusselt number. The IF statements in these two subroutines must be modified, based on the value of the coolant type parameter iCOOLANT, to distinguish between a gas and a liquid. The FORTRAN code of the subroutine NUSSELT_NUMBER is included in this manual, in Appendix R.

The addition of a new structural material requires modification of the following subroutines:

- HX_INPUT calculates the density of the structural material, based on the input parameter iWALL (see Appendix M). The subroutine HX_INPUT uses an array ROMATRIX which contains the density values (kg/m^3) of the structural materials (see Section 4.10.2);

- WALL_PROPERTIES calculates the thermal conductivity and specific heat capacity of the structural material in a row i = 1, 3, or 5 of grid nodes, as a function of temperatures (see Appendix Q); this subroutine also uses a simple numbered GOTO structure to access the property correlations of each material, and is easily modified to include new structural materials.

The next two chapters provide transient result calculations of a helium/water pre-cooler rated ~ 300 MW (whose input file “HX.INP” is given in Appendix K), and a He/He plate-fin recuperator with triangular stacked matrices rated ~ 1000 MW (input file “HX.INP” in Appendix L), when operating at the inlet conditions encountered in the pre-cooler and recuperator of the Japanese GTHTR300 power plant (Takizuka et al., 2004). The results are provided for illustration purpose and as benchmark cases to the MELCOR-H2 team to verify the proper implementation of the present generic heat exchanger model.

4.11 Transient Results of a He/Water Pre-Cooler

The input file "HX.INP" of the helium/water pre-cooler test case is shown in Appendix K. During normal operating conditions, the coolant inlet conditions in the pre-cooler are those in the Japanese GTHTR300 power plant (Takizuka et al., 2004). The results are provided for illustration purpose and as a benchmark case to the MELCOR-H2 team to verify the proper implementation of the present generic heat exchanger model.

Initially (at time zero), the water flow is established at 2758 kg/s, and water enters the pre-cooler at a temperature of 290 K and a pressure of 1.3 bars. All temperatures are initialized at 290 K, and the helium pressure is 3.61 MPa. There is no helium mass flow rate.

During the first 60 seconds of the transient, the water inlet flow conditions are maintained constant, and the helium mass flow rate increases linearly from zero to its nominal value of 445.6 kg/s, while the helium inlet temperature increases linearly from 290 K to 438.5 K. Subsequently, at times > 60 s, the helium and water inlet conditions are maintained constant, until a steady-state condition is reached, after about 4 minutes into the transient. The changes in inlet and outlet temperatures, mass flow rates, thermal heat flows to the walls of the heat exchanger, and heat exchanged between the working fluids are shown in Figures 4-26 through 4-29, respectively.

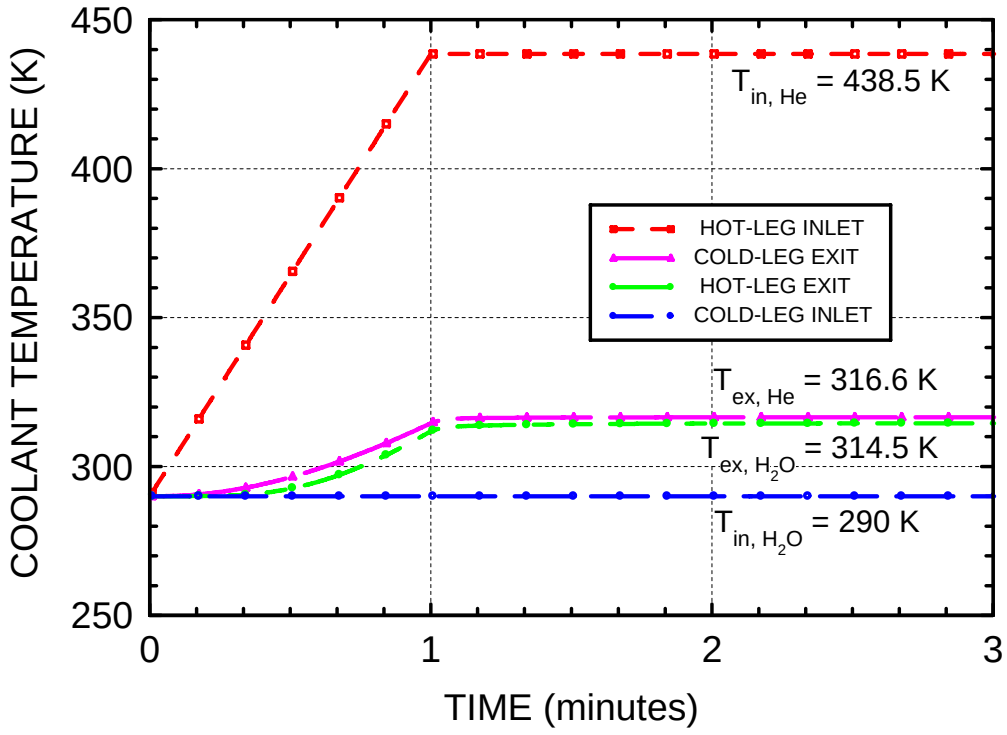

Figure 4-26. Inlet and exit coolant temperatures in the He/H_2O pre-cooler.

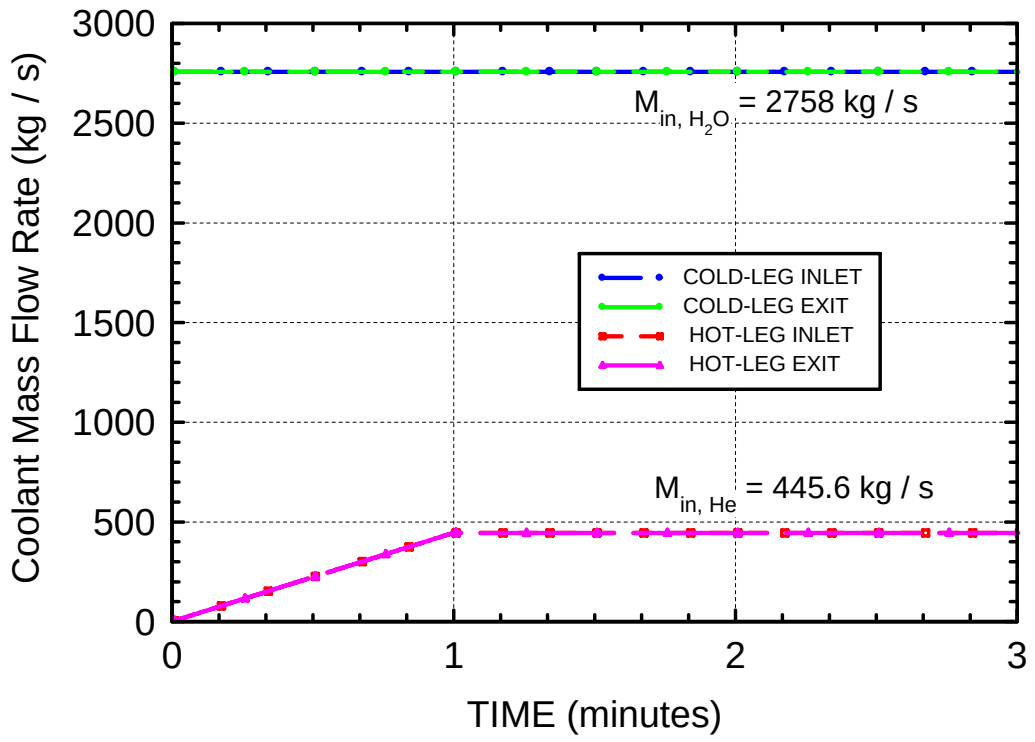

Figure 4-27. Coolant mass flow rates in the He/H_2O pre-cooler.

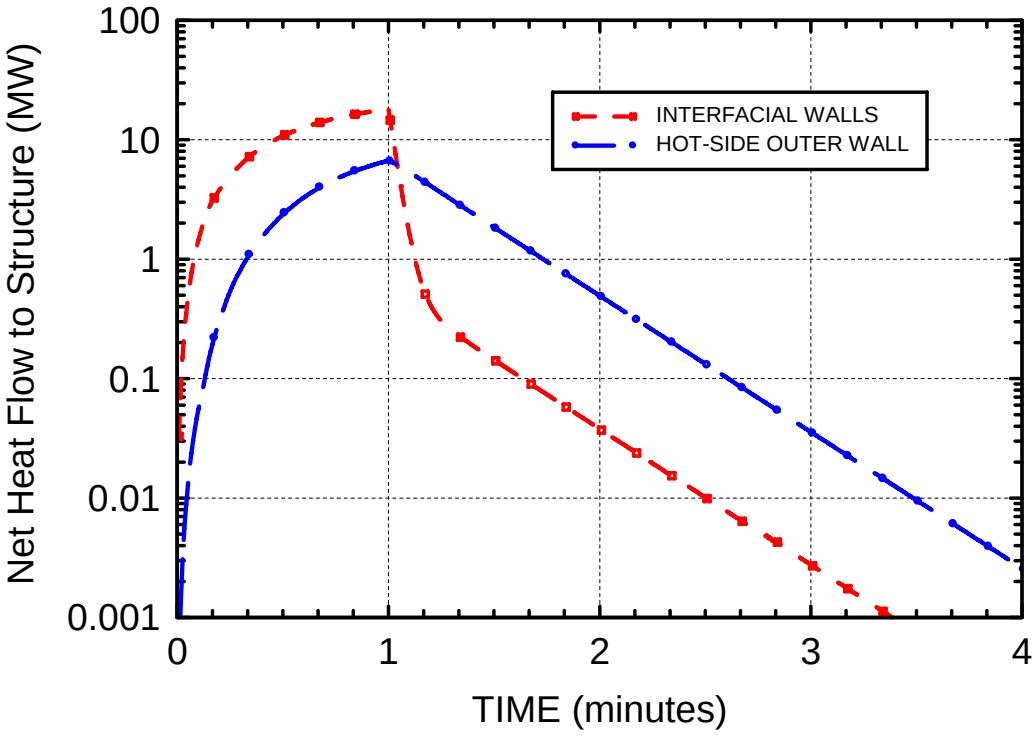

Figure 4-28. Net heat flow to structural walls of the He/H_2O pre-cooler.

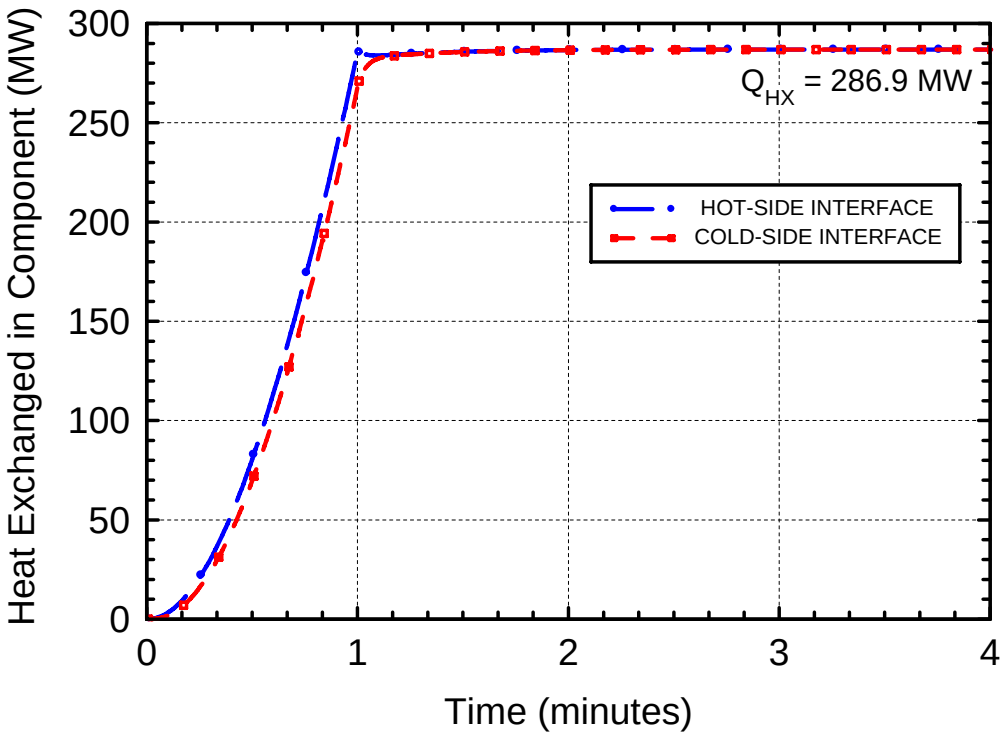

Figure 4-29. Heat exchanged between coolants in the He/H_2O pre-cooler.

After 60 seconds into the transient, the nominal inlet conditions (mass flow rate and temperature) are established in the pre-cooler. The rate of thermal energy storage in the structural walls of the pre-cooler (50,200 kg of stainless steel) then decreases rapidly with time (Figure 4-28), and steady state operating conditions are nearly established in only a few minutes (Figure 4-26). The pre-cooler then exchanges 286.9 MW of thermal energy between the hot helium gas and the water coolant (Figure 4-29).

The temperature and pressure distributions in the pre-cooler at steady state are shown in Figures 4-30 and 4-31. These distributions are typical of those in a pre-cooler with a counter-current flow arrangement. The flow direction is indicated in Figure 4-30. At steady state, the pressure losses in the hot- and cold-leg channels amount to 23 kPa and 34 kPa, respectively (Figure 4-31).

The distributions of the coolant Reynolds numbers, Nusselt numbers and Darcy friction factors at steady-state, calculated using the equations delineated in Section 4.9.3 are also shown in Figures 4-32 through 4-34 for verification purposes.

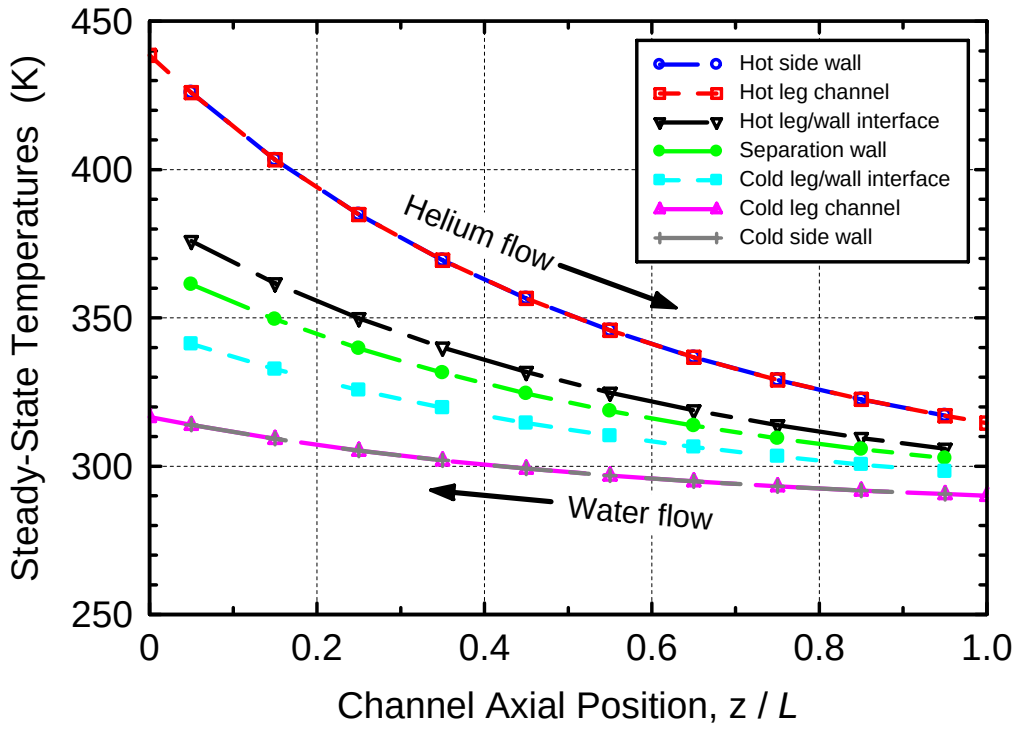

Figure 4-30. Steady state temperature distribution in the He/H_2O pre-cooler.

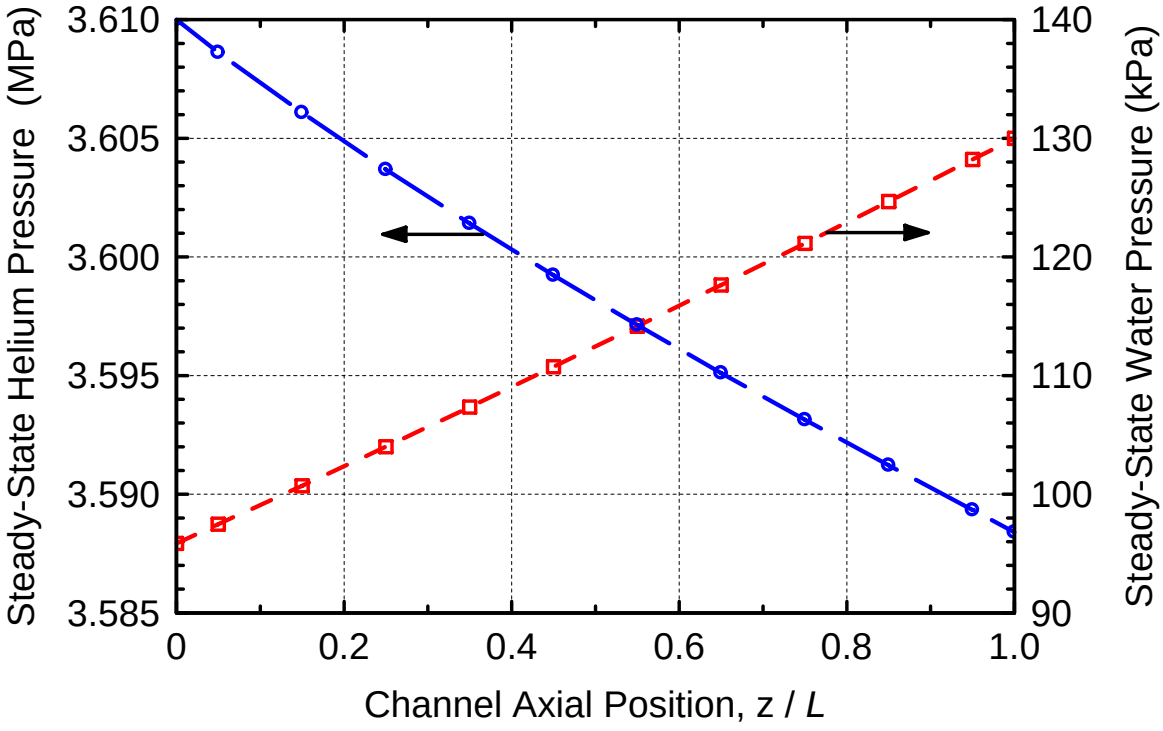

Figure 4-31. Steady state pressure distributions in the He/H_2O pre-cooler.

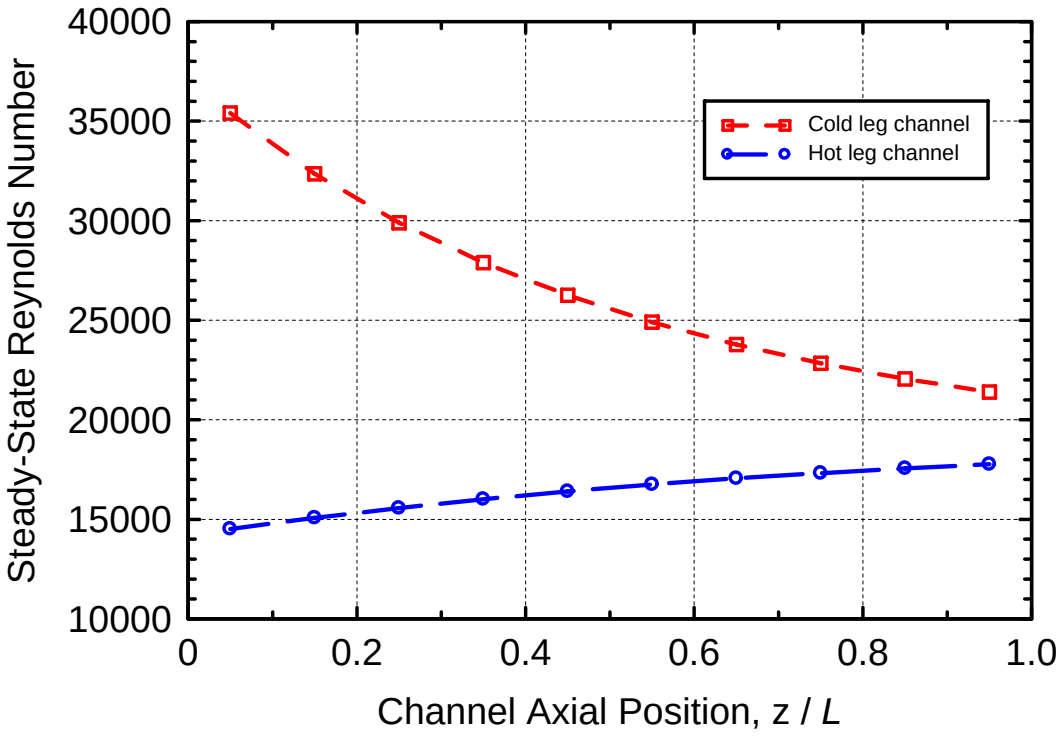

Figure 4-32. Reynolds number in coolant channels of He/H_2O pre-cooler.

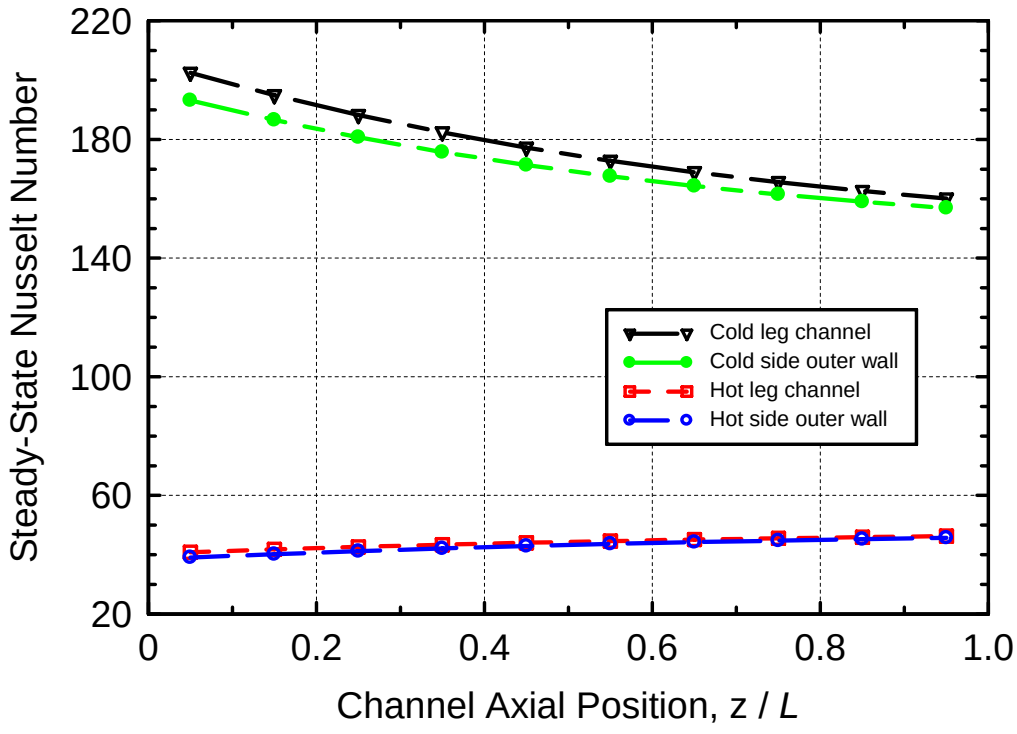

Figure 4-33. Nusselt number in coolant channels of He/H_2O pre-cooler.

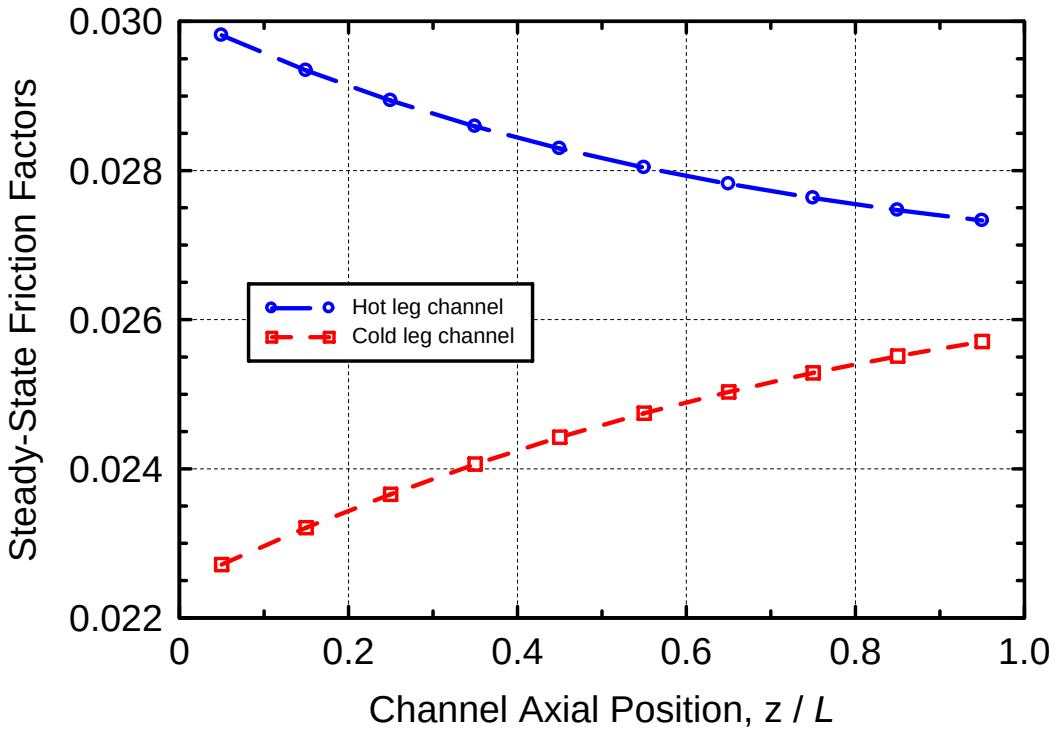

Figure 4-34. Darcy friction factor in coolant channels of He/H_2O pre-cooler.

4.12 Transient Results of a He/He Plate-Fins Recuperator

The input file "HX.INP" of the helium/helium recuperator test case is given in Appendix L. The recuperator is a plate-fin heat exchanger with triangular stacked matrices (Figure 4-35). During normal operating conditions, the coolant inlet conditions in the recuperator are those in the Japanese GTHTR300 power plant (Takizuka et al., 2004). Initially (at time zero), the recuperator is at a uniform temperature of 410 K, the hot- and cold-leg helium pressures are 3.67 MPa and 7.05 MPa, respectively, and the helium flow rates are nil.

During the first 60 seconds of the transient, the cold-leg helium mass flow rate increases linearly from zero to its nominal value of 445.6 kg/s. The inlet temperature of the cold-leg helium is maintained constant at 410 K, while the hot-leg helium inlet temperature increases linearly from 410 K to 886.5 K in 60 seconds. Subsequently, at times > 60 s, the hot- and cold-leg inlet flow conditions are maintained constant, until a steady state condition is reached, after about 10 minutes into the transient. The changes in inlet and outlet temperatures, mass flow rates, thermal heat flows to the walls of the heat exchanger, and heat exchanged between the working fluids are shown in Figures 4-36 through 4-39, respectively.

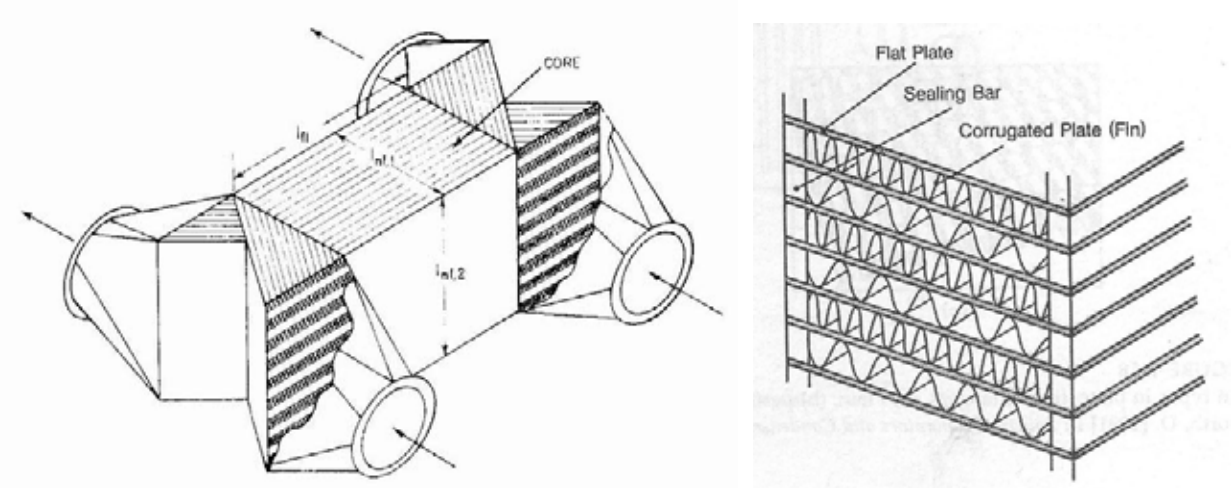

(a) Flow inlet and outlet arrangement (b) Basic construction of core

Figure 4-35. Schematics of counter-current flow, plate-fin heat exchanger (Wilson and Korakianitis, 1998; Kakaç and Liu, 1998).

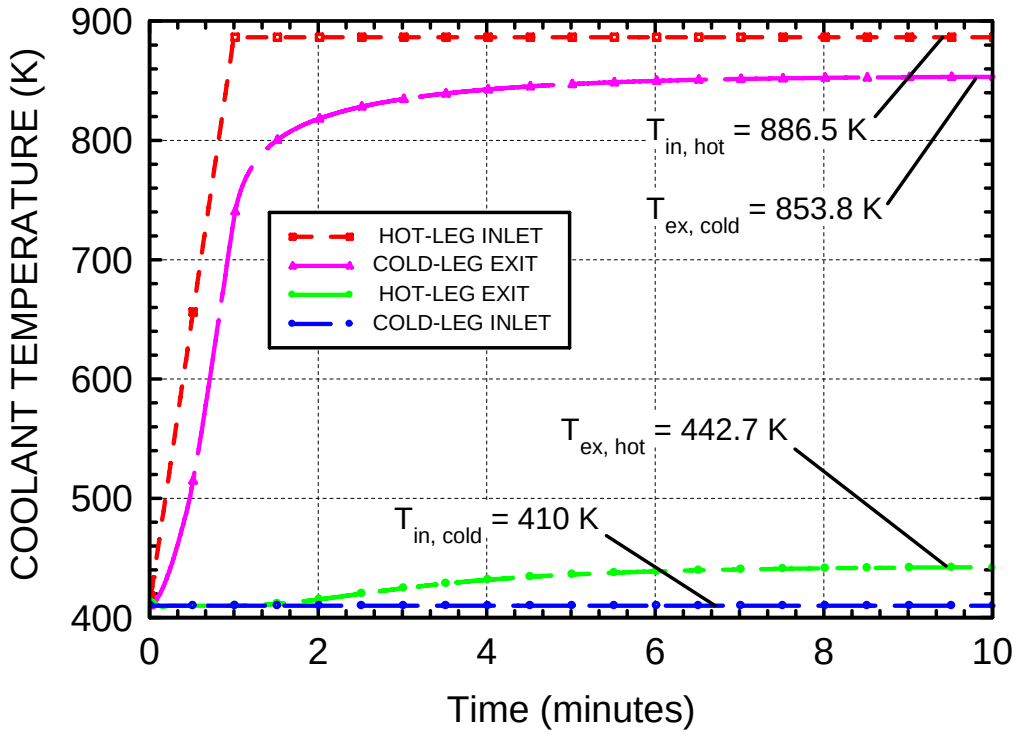

Figure 4-36. Inlet and exit coolant temperatures in the He/He recuperator.

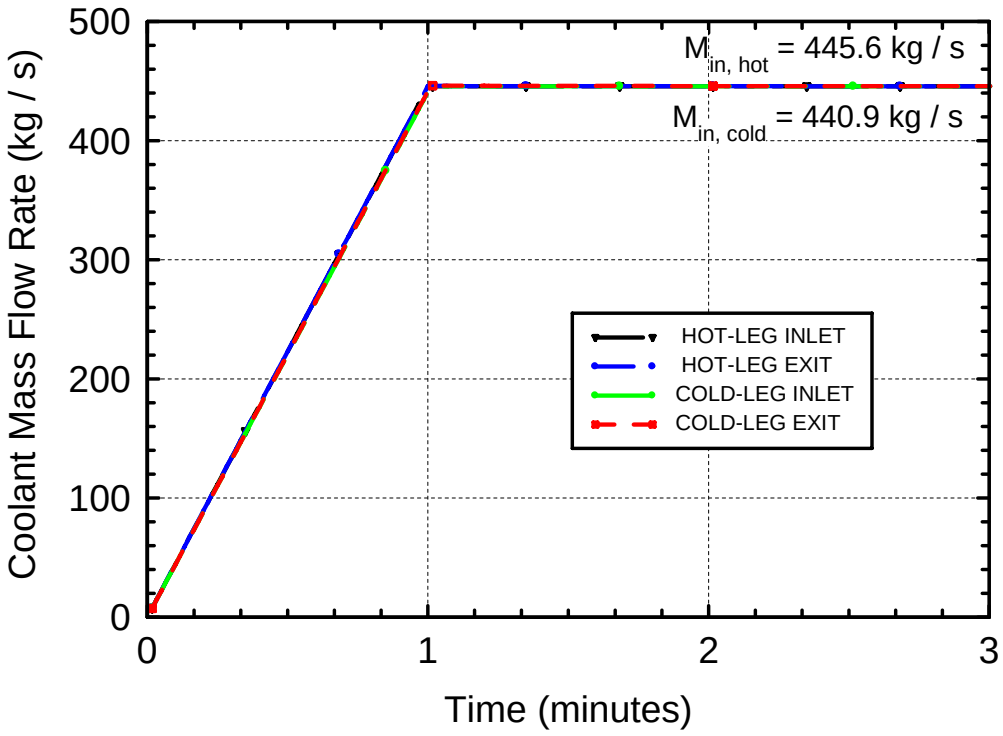

Figure 4-37. Coolant mass flow rates in the He/He recuperator.

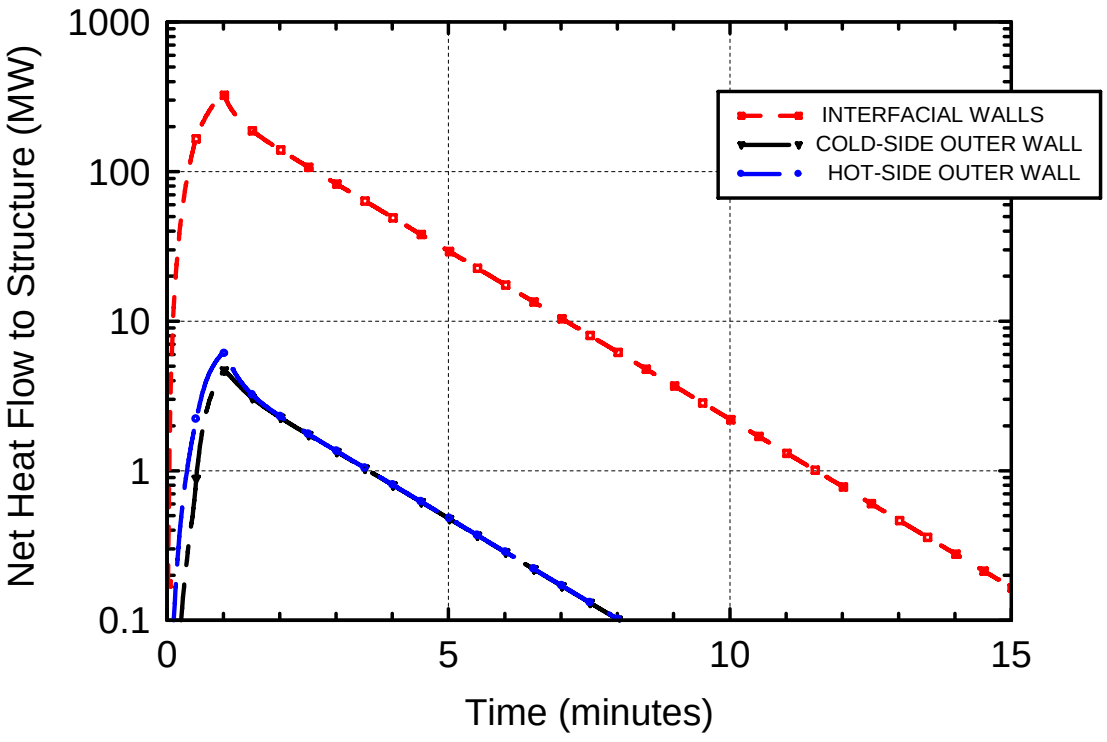

Figure 4-38. Net heat flow to structural walls of the He/He recuperator.

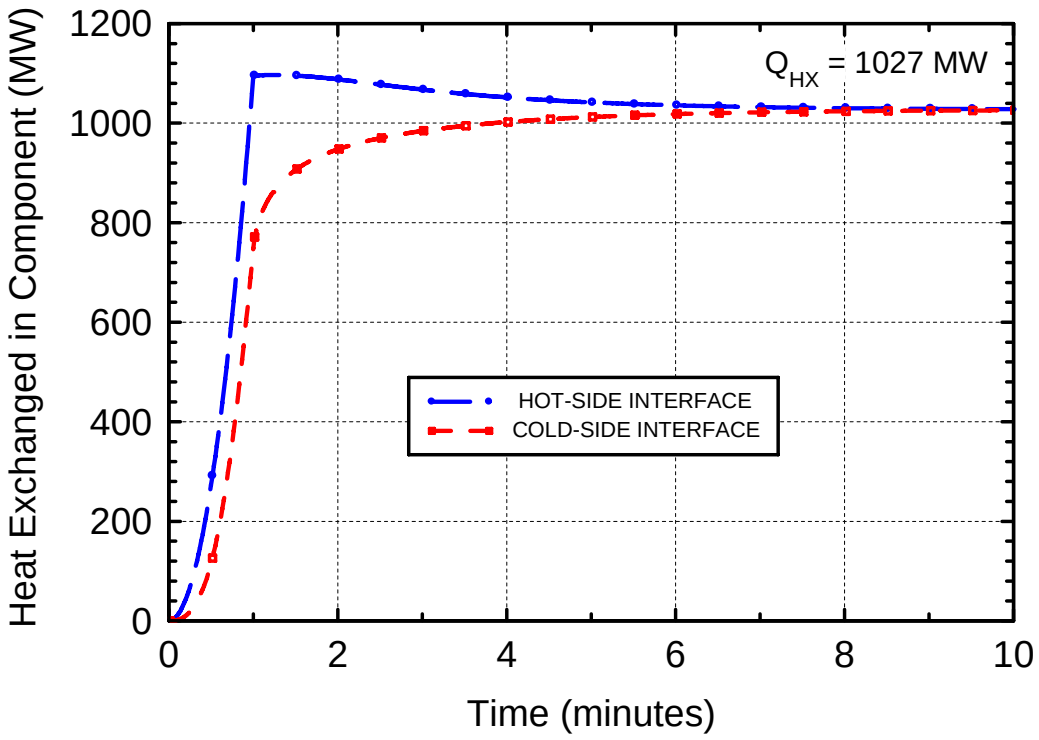

Figure 4-39. Heat exchanged between coolants in the He/He recuperator.

After 60 seconds into the transient, the nominal inlet conditions (mass flow rate and temperature) are established in the recuperator. The rate of thermal energy storage in the structural walls of the pre-cooler (300,000 kg of stainless steel) then decreases rapidly with time (Figure 4-38), and steady state operating conditions are nearly established after about 10 minutes (Figures 4-36 and 4-39). The recuperator then exchanges 1027 MW of thermal energy between the hot and cold helium legs (Figure 4-39).

The temperature and pressure distributions in the recuperator at steady state are shown in Figures 4-40 and 4-41. These distributions are typical of those in a recuperator with a counter-current flow arrangement. The flow direction is indicated in Figure 4-40. At steady-state, the pressure losses in the hot- and cold-leg channels amount to 50 kPa and 25 kPa, respectively (Figure 4-41).

The distributions of the coolant Reynolds numbers, Nusselt numbers, and Darcy friction factors at steady state, calculated using the equations delineated in Section 4.9.3 are also shown in Figures 4-42 through 4-44 for verification purposes.

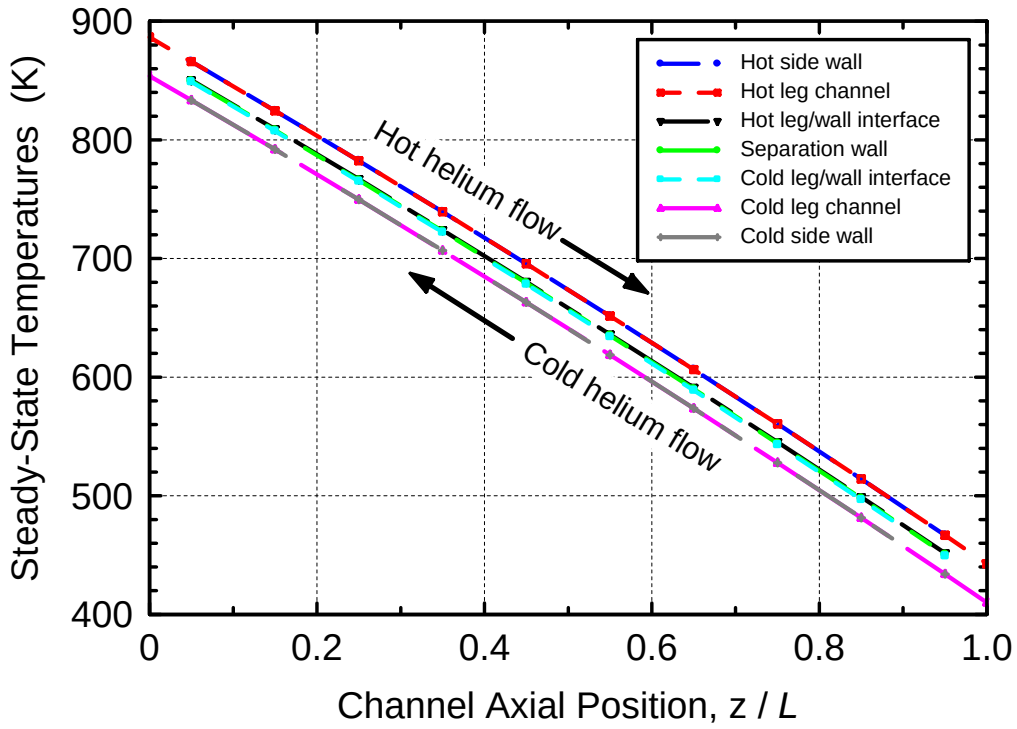

Figure 4-40. Steady state temperature distribution in the He/He recuperator.

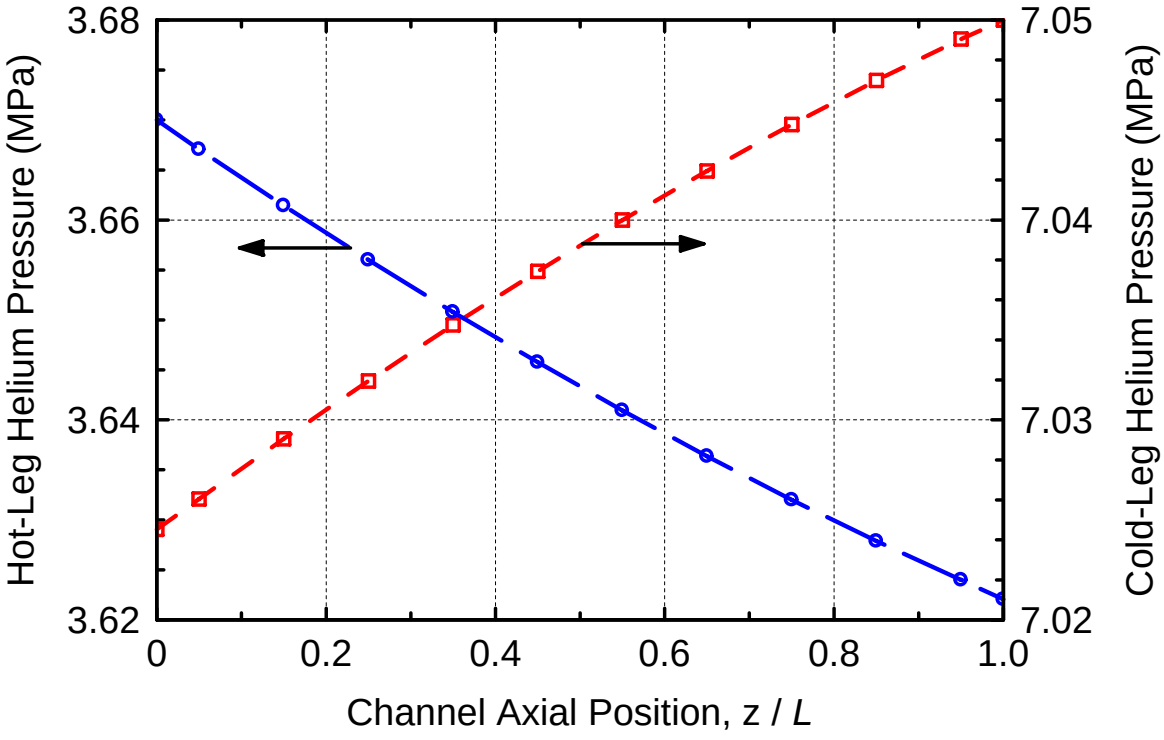

Figure 4-41. Steady state pressure distributions in the He/He recuperator.

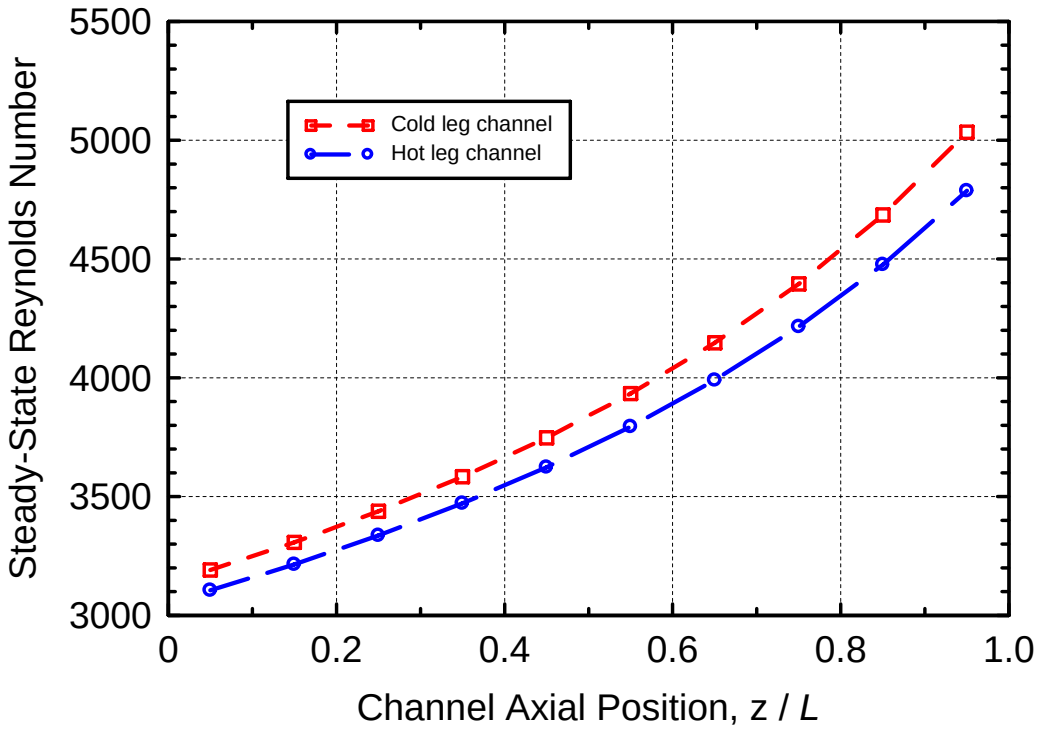

Figure 4-42. Reynolds number in coolant channels of He/He recuperator.

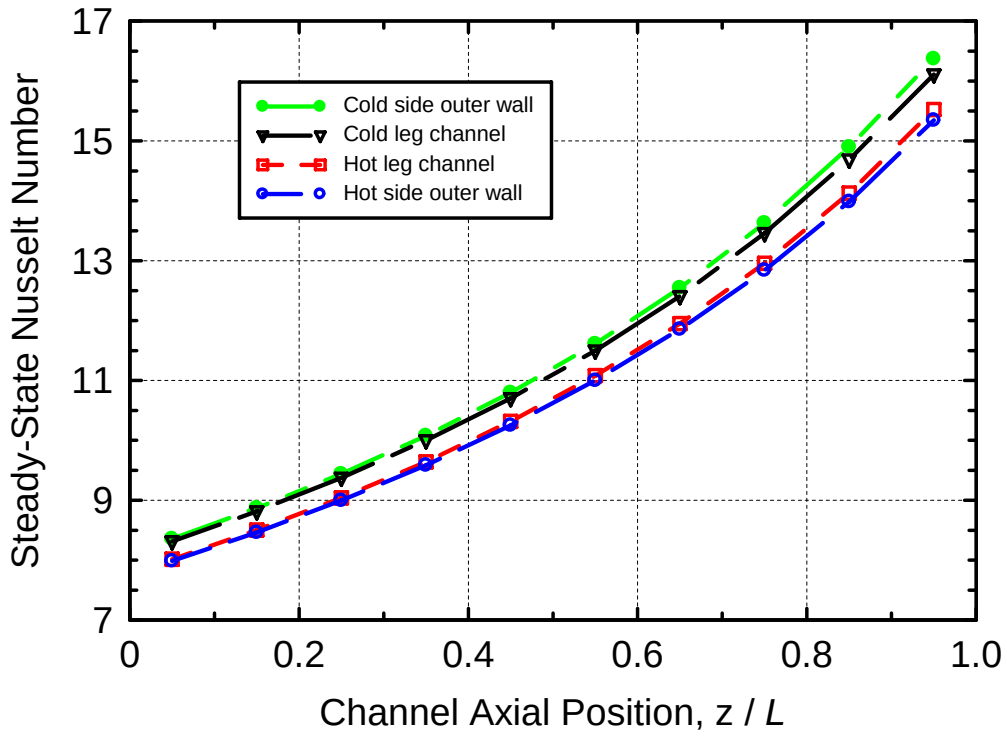

Figure 4-43. Nusselt number in coolant channels of He/He recuperator.

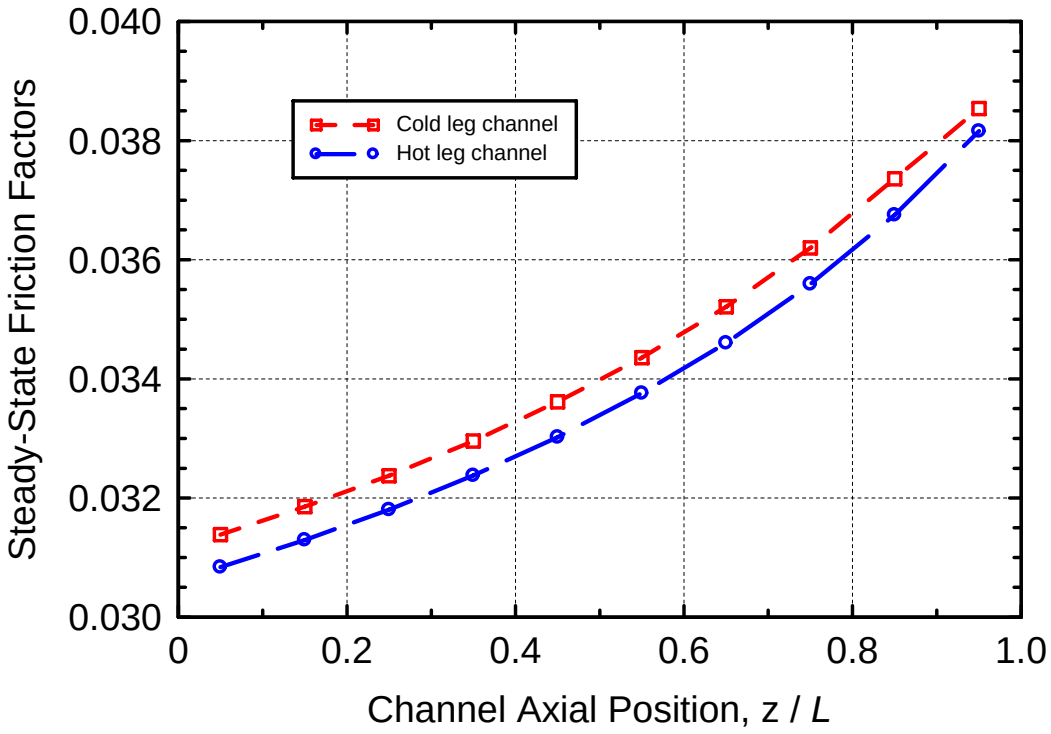

Figure 4-44. Darcy friction factor in coolant channels of He/He recuperator.

4.13 Chapter 4 References

Ainley, D. G., and G. C. R. Mathieson, 1951, *A Method of Performance Estimation for Axial-Flow Turbines*, British Aeronautical Research Council, Reports and Memoranda No. 2974, December 1951.

Aungier, R. H., 2003, *Axial-Flow Compressor – A Strategy for Aerodynamic Design and Analysis*, ASME Press, New York, NY, Chapter 6, pp. 118-152.

Aungier, R. H., 2006, *Turbine Aerodynamics – Axial-Flow and Radial-Inflow Turbine Design and Analysis*, ASME Press, New York, NY, pp. 69-79.

Benner, M. W., S. A. Sjolander, and S. H. Moustapha, 2006a, An Empirical Prediction Method for Secondary Losses in Turbines – Part I: A New Loss Breakdown Scheme and Penetration Depth Correlation, *Journal of Turbo-machinery*, Vol. 128, pp. 273-280.

Benner, M. W., S. A. Sjolander, and S. H. Moustapha, 2006b, An Empirical Prediction Method for Secondary Losses in Turbines – Part II: A New Secondary Loss Correlation, *Journal of Turbo-machinery*, Vol. 128, pp. 281-291.

Fielding, L., 2000, *Turbine Design – The Effect on Axial Flow Turbine Performance of Parameter Variation*, ASME Press, New York, NY, pp. 130-132.

Gauntt, R. O., R. K. Cole, C. M. Erickson, R. G. Gido, R. D. Gasser, S. B. Rodriguez, and M. F. Young, 2000, *MELCOR Computer Code Manuals*, Vol. 2: Reference Manuals, Version 1.8.5, May 2000, Report No. NUREG/CR-6119, Vol. 2, Rev. 2, SAND2000-2417/2, Sandia National Laboratories, Albuquerque, NM, October 2000.

Gnielinski, V., 1976, New Equations for Heat and Mass Transfer in Turbulent Pipe and Channel Flow, *International Chemical Engineering*, Vol. 16 (2), pp. 359-368.

Horlock, J. H., 1960, Losses and Efficiencies in Axial-Flow Turbines, *International Journal of Mechanical Science*, 2, 48-75.

Kakaç, S. and H. Liu, 1998, *Heat Exchangers – Selection, Rating and Thermal Design*, CRC Press, New York, NY, Chapter 2, pp. 35-38, Chapters 3 and 4, pp. 73-138.

Koch, C. C., and L. H. Smith, Jr., 1976, Loss Sources and Magnitudes in Axial-Flow Compressors, *Journal of Engineering for Power*, Vol. A98, pp. 411-424.

Lakshminarayana, B., 1970, Predicting the Tip Clearance Flow in Axial Flow Turbo-machinerys, *Journal of Basic Engineering*, Vol. 92, pp. 467-482.

Lieblein, S., 1959, Loss and Stall Analysis in Compressor Cascades, *Journal of Basic Engineering*, Vol. 81 (September 1959), pp. 387-400.

MacDonald, P. E., J. W. Sterbentz, R. L. Sant, P. D. Bayless, R. R. Schultz, H. D. Gougar, R. L. Rodriguez, S. B., R. O. Gauntt, R. Cole et al., 2005, Development of Design and Simulation Model and Safety Study of Large-Scale Hydrogen Production Using Nuclear Power – FY05 Final Letter Report, Sandia National Laboratories, Albuquerque, NM.

Petukhov, B. S., 1970, Heat Transfer and Friction in Turbulent Pipe Flow with Variable Physical Properties, in *Advances in Heat Transfer*, Volume 6, Academic Press, New York, NY, J. P. Hartnett and T. F. Irvine, Jr., Editors, pp. 503-564.

Schlichting, Hermann, 1979, Boundary Layer Theory, 7th Edition, McGraw-Hill Book Company.

Schobeiri, T., and M. Abouelkheir, 1992, Row-by-Row Off-Design Performance Calculation Method for Turbines, *Journal of Propulsion and Power*, 8(4), pp. 823-828.

Takizuka, T., S. Takada, X. Yan, S. Kosugiyama, S. Katanishi, and K. Kunitomi, 2004, R&D on the Power Conversion System for Gas Turbine High Temperature Reactors, *Nuclear Engineering and Design*, Vol. 233, pp. 329-346.

Tournier, J.-M, and M. S. El-Genk, 2006, *Models of Turbine and Compressor Units for MELCOR Secondary System Modules*, Report No. UNM-ISNPS-2-2006, University of New Mexico's Institute for Space and Nuclear Power Studies, Albuquerque, NM; delivered to Salvador Rodriguez (SNL) in August 2006.

van Doormaal, J. P., and G. D. Raithby, 1984, Enhancements of the SIMPLE Method for Predicting Incompressible Fluid Flows, *Numerical Heat Transfer*, Vol. 7, pp. 147-163.

Wilson. D. G., and T. Korakianitis, 1998, *The Design of High-Efficiency Turbomachinery and Gas Turbines*, Prentice Hall, Inc., Upper Saddle River, NJ, Second Edition, p. 468.

Zhu, J., and S. A. Sjolander, 2005, Improved Profile Loss and Deviation Correlations for Axial-Turbine Blade Rows, in *Proceedings of GT2005 ASME Turbo Expo 2005: Power for Land, Sea and Air*, held June 6-9, 2005, in Reno-Tahoe, Nevada, USA, American Society of Mechanical Engineers, New York, NY, Paper No. GT2005-69077, pp. 783-792.

Zhu, J., and S. A. Sjolander, 2005, Improved Profile Loss and Deviation Correlations for Axial-Turbine Blade Rows, in *Proceedings of GT2005 ASME Turbo Expo 2005: Power for Land, Sea and Air*, held June 6-9, 2005, in Reno-Tahoe, Nevada, USA, American Society of Mechanical Engineers, New York, NY, Paper No. GT2005-69077, pp. 783-792.

5. POINT KINETICS AND INTERACTIVE GRAPHICAL USER INTERFACE

5.1 Chapter 5 Highlights

An accurate and fast-running 6-point kinetics model was developed for high-temperature, graphite-moderated and helium-cooled reactors. The model was subsequently incorporated into MELCOR-H2. The model includes (a) An active neutron source for zero-power reactor startup; and (b) Doppler and fuel and graphite temperature reactivity feedbacks. The model, written in FORTRAN 95 standard language, was developed and tested using Compaq Visual FORTRAN Professional Edition 6.5.0 (2000), which provides a superset of the FORTRAN 95 standard with other extensions for compatibility with previous FORTRAN languages and platforms. The developed model uses an extremely efficient exponential matrix technique with a discretization error on the order of $(\Delta t)^3$, in which the exponential matrix is approximated using the 7^{th}-order-accurate Padé(3,3) function. Unlike prompt jump approximation (PJA) methods, the present model is also capable of modeling high reactivity insertion cases, i.e., $\rho / \overline{\beta} >$ \$1.0. Other desirable characteristics of the present model include unconditional stability, and the freedom to use a time step size that is less restrictive than that used by MELCOR's thermal-hydraulics model of the VHTR core. The values of the temperature feedback coefficients were obtained by least-squared fit of the preliminary neutronics calculations performed by INEEL (MacDonald et al., 2003) for the NGNP prismatic reactor.

The developed 6-point kinetics model was successfully benchmarked using the Inhour solution for step reactivity insertions (both positive and negative). In order to test the temperature-feedback reactivity model, the present 6-point kinetics model was coupled to an 84-nodes thermal-hydraulics model of the prismatic NGNP, developed at University of New Mexico-Institute for Space and Nuclear Power Studies (UNM-ISNPS), to simulate the startup of the reactor and its transient behavior during a change in power level. The predictions were consistent with those reported in the literature. In addition, the model was also tested on the SNL VHTR-SI input deck.

The governing equations and boundary conditions of the present 6-point kinetics model are presented in Section 5.3. The temperature-feedback reactivity model developed is described in Section 5.4. The delayed-neutron group data recommended for use in MELCOR-H2, for thermal fission in U^{235}, is collected in Section 5.5. Sections 5.6 and 5.7 describe the exponential matrix solution technique used to solve the 6-point kinetics equations, and the Padé(3,3) approximant of the exponential matrix. The input and output parameters of the subroutine developed in FORTRAN 95 are described in details in Section 5.8, and guidelines for implementing the subroutine into MELCOR-H2 are presented. Finally, the results of a simulation case of the prismatic NGNP operation, obtained by coupling the present 6-point kinetics model to the UNM-ISNPS 84-nodes thermal-hydraulics model of the reactor, are presented in Section 5.9. The VHTR-SI simulation results are included in Chapter 1. The FORTRAN code of the subroutines is in Appendices S through U.

Finally, for overall reporting convenience, Section 5.10 provides a brief discussion of the interactive GUI.

5.2 Chapter 5 Nomenclature

{A}	7 x 7 matrix of 6-point kinetics, linear differential equations
C_i	Concentration of i^{th} group delayed-neutron precursors (atoms / m^3)
f_i	Relative abundance of i^{th} group delayed neutrons, $f_i = \beta_i / \overline{\beta}$
k	Effective multiplication factor of neutron population
M	Location point or vector, [x , y , z]
N, n	Neutron density (n / m^3)
P	Reactor's thermal power (W)
Q_f	Immediate (prompt and delayed) energy released per fission (J), ~ 190 MeV
S	Total neutron source density (n / m^3.s)
[S]	Source vector (7 components)
S_o	Active neutron source density (n / m^3.s)
s'_o	Active neutron source (n / s)
S_o	Rate of thermal power generated by active neutron source (W / s)
t	Time (s)
T	Temperature (K)
$\overline{T}$	Volumetric average temperature (K)
v	One-group neutron speed (m / s)
VOL	Volume of homogenous reactor core (m^3)
Y_i	Fission power generated by i^{th} group delayed-neutron precursors (W)

Greek

α_j	Mass fraction of graphite in zone j
β_i	Effective delayed-neutron yield for the i^{th} group
$\overline{\beta}$	Total effective delayed-neutron yield, $\overline{\beta} = \sum_{i=1}^{6} \beta_i$
Δt	Numerical time step size (s)
θ	Implicit numerical discretization parameter, $0 \leq \theta \leq 1$
Λ	Neutron generation time (s), $\Lambda = (\nu v \Sigma_f)^{-1}$
λ_i	Decay constant for i^{th} delayed-neutron group (s^{-1})
ν	Average number of neutrons produced per thermal fission
ρ	Nuclear reactor reactivity, $\rho = 1 - 1 / k$
Σ_a	Macroscopic absorption cross-section (m^{-1})
Σ_f	Macroscopic fission cross-section (m^{-1})
Φ	Neutron flux (n / m^2.s)
Ψ_1	Fundamental shape mode of neutron flux (dimensionless)
[ψ]	Thermal powers vector (7 components)

Subscript/Superscript

D	Doppler
ext	external reactivity
f	Fuel compact density feedback
G	graphite (moderator and reflector) density feedback
n	Older time step value
n+1	New time step value
o	Initial value at time, $t = 0$

Operators

[S]	Vector (7 components)
{A}	Matrix (7 x 7)
$\{A\}^{-1}$	Inverse of matrix {A} (7 x 7)
{exp(A)}	7 x 7 exponential matrix of matrix {A}
$\{\Im\}$	7 x 7 Identity matrix
•	Matricial and vectorial multiplication operator

5.3 Standard 6-Point Kinetics Equations

The reactor 6-point kinetics equations in the present model are written in terms of the reactor's thermal power, *P*, and the thermal powers generated by the 6 group delayed-neutron precursors, $\{Y_i\}$:

$$\frac{dP}{dt} = \frac{\rho - \overline{\beta}}{\Lambda} \times P + \sum_{i=1}^{6} \lambda_i Y_i + S_o \,, \tag{5-1}$$

$$\frac{dY_i}{dt} = \frac{\beta_i}{\Lambda} \times P - \lambda_i Y_i \,, \; i = 1 \text{ to } 6. \tag{5-2}$$

The total reactivity of the reactor, ρ, is related to the effective multiplication factor, *k*, of the neutron population by:

$$\rho = \frac{k-1}{k} = 1 - \frac{1}{k} \,, \tag{5-3}$$

and $\Lambda = (\nu\nu\Sigma_f)^{-1}$ is the neutron generation time (s). Note that in Equations (5-1) and (5-2):

$$Y_i = Q_f VOL \times \frac{C_i(t)}{\nu\Lambda} \tag{5-4}$$

represents the thermal power (W) generated by the i^{th} group delayed-neutron precursors, and:

$$S_o = Q_f \times \frac{s_o'}{\nu\Lambda}, \tag{5-5}$$

is the rate of thermal power generated by the active neutron source (W/s).

These first-order differential equations are solved subject to the following initial conditions:

$$P_{(t=0)} = P_o \text{ and } Y_{i(t=0)} = Y_i^o, \; i = 1 \text{ to } 6. \tag{5-6}$$

If we assume equilibrium at time $t = 0$, i.e., $dY_i / dt = 0$ for $i = 1$ to 6, and $dP / dt = 0$, then Equation (5-2) gives:

$$Y_{i(t=0)} = Y_i^o = \frac{\beta_i}{\lambda_i \Lambda} P_o, \; i = 1 \text{ to } 6. \tag{5-7}$$

When an active neutron source is present ($s_o' > 0$), a small negative external reactivity, $\rho_o < 0$ must be inserted to ensure equilibrium. Equation (5-1) then gives the following value for this reactivity in terms of the equilibrium reactor's thermal power:

$$\rho_o = -\frac{\Lambda S_o}{P_o} \; . \tag{5-8}$$

When there is no active source present ($s_o' = 0$), then the external reactivity, $\rho_o = 0$, to ensure equilibrium. In this case also, the reactor can be critical at any thermal power value, P_o, and the precursor powers are related to P_o by Equation (5-7).

5.4 Temperature-Feedback Reactivity Model

The reactor's total reactivity is sum of external reactivity, ρ_{ext} (active control), fuel Doppler feedback reactivity, ρ_D, fuel density temperature-feedback reactivity, ρ_f, and graphite density temperature-feedback reactivity, ρ_G:

$$\rho = \rho_{ext} + \rho_D + \rho_f + \rho_G \; . \tag{5-9}$$

The feedback reactivities are obtained by least-squared fit of the preliminary neutronics calculations performed by INEEL and reported by MacDonald et al. (2003) for the NGNP prismatic reactor. Three sets of calculations were reported: (a) Calculations of the effective reactor multiplication factor, *k*, for a constant and uniform fuel temperature, T_f = 1373 K, and a variable but uniform moderator/reflector temperature; (b) Calculations of *k* for a constant and uniform graphite temperature, T_G = 1200 K, and a variable but uniform fuel temperature; and (c) Calculations of *k* for an isothermal core ($T_f = T_G$). Results of these calculations are reported in Figure 5-1. For the prismatic, graphite-moderated NGNP reactor, the temperature-feedback

reactivities are expressed in terms of the volume-averaged fuel and graphite moderator/reflector temperatures, $\overline{T}_f$ and $\overline{T}_G$. The fuel Doppler reactivity is usually well approximated using a logarithmic function, i.e.,

$$\rho_D = \chi_D \ln(\overline{T}_f / T_f^o) \ . \tag{5-10}$$

In order to properly fit the INEEL calculations shown in Figure 5-1, the fuel density feedback reactivity is a 2nd order polynomial of the volume-averaged fuel temperature:

$$\rho_f = \chi_{f,1}(\overline{T}_f - T_f^o) + \chi_{f,2}\left[(\overline{T}_f)^2 - (T_f^o)^2\right], \tag{5-11}$$

and the graphite density feedback reactivity is a 4th-order polynomial of the graphite moderator/reflector volume-averaged temperature:

$$\rho_G = \sum_{m=1}^{4} \chi_{G,m}\left[(\overline{T}_G)^m - (T_G^o)^m\right]. \tag{5-12}$$

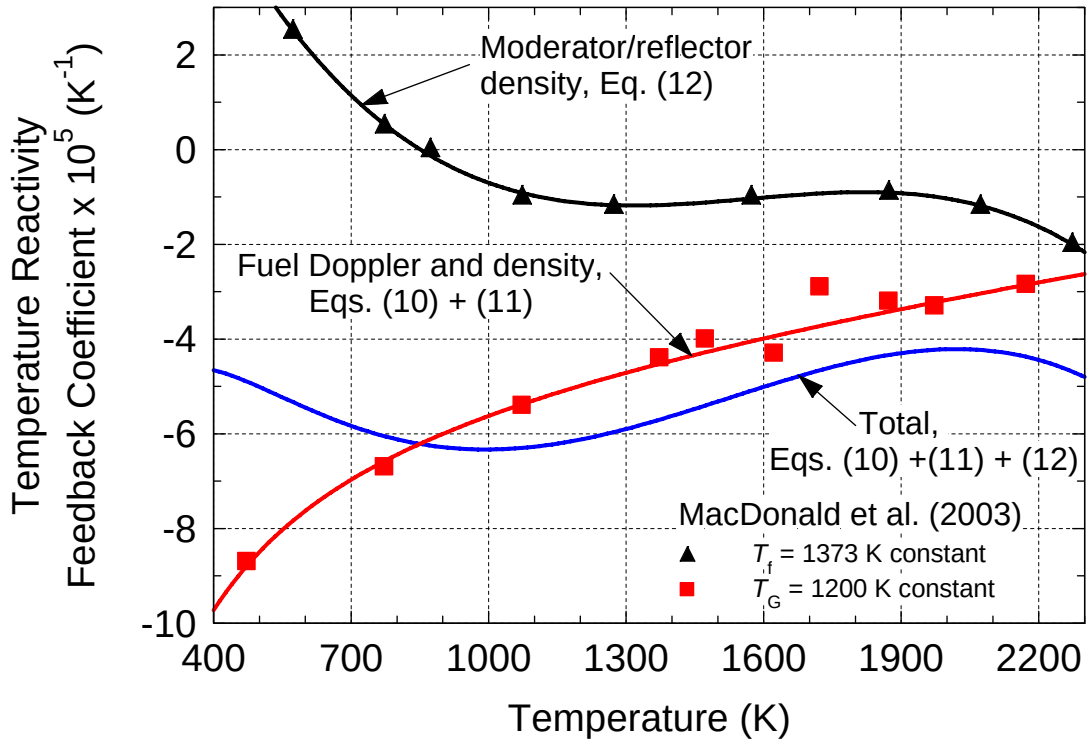

Figure 5-1. Preliminary calculations (MacDonald et al., 2003) and fitting of feedback reactivity coefficients for the prismatic NGNP helium-cooled nuclear reactor.

The values of the feedback coefficients, χ_j are obtained from least-squared fits of Equations (5-10) through (5-12) to the INEEL calculations (Figure 5-1):

$$\chi_D = -0.022, \quad \chi_{f,1} = -4.78 \times 10^{-5}\ (K^{-1}), \quad \chi_{f,2} = +6.75 \times 10^{-9}\ (K^{-2}),$$

$$\chi_{G,1} = +14.834 \times 10^{-5}\ (K^{-1}), \quad \chi_{G,2} = -1.6025 \times 10^{-7}\ (K^{-2}), \qquad (5\text{-}13)$$

$$\chi_{G,3} = +6.9907 \times 10^{-11}\ (K^{-3}), \quad \chi_{G,4} = -1.1142 \times 10^{-14}\ (K^{-4}).$$

The scatter in the numerical results presented in Figure 5-1 is due to a mismatch in the uranium and graphite temperature libraries, and to differences in the MCNP uranium (both ^{235}U and ^{238}U) cross-section libraries (MacDonald et al., 2003). At temperatures below 927 °C, cross-sections were generated using ENDF/B/VI Revision 2 data, and using ENDF/B/VI Revision 5 data above 1000 °C.

The temperatures T_f^o and T_G^o appearing in Equations (5-10) through (5-12) are the volume-averaged temperatures of the fuel and the graphite materials in the reactor, at the initial and steady state conditions when $\rho_D = \rho_f = \rho_G = 0$ and $\rho = \rho_{ext} = \rho_o$ (see Equation (5-8)). These steady state volume-averaged temperatures would be calculated by MELCOR-H2 during the initialization phase of the prismatic NGNP reactor, before starting the transient simulation. Following convergence to steady state, the volume-averaged temperatures T_f^o and T_G^o would be calculated by MELCOR-H2 and supplied to the 6-point kinetics model before initiating the transient iterations. The form of Equations (5-10) through (5-12) ensures that at time $t = 0$, the feedback reactivities calculated by the 6-point kinetics model are nil ($\rho_D = \rho_f = \rho_G = 0$), and that the equilibrium initial conditions, Equations (5-6) through (5-8), are satisfied.

5.5 Delayed-Neutron Group Data

The delayed-neutron group data recommended for use in MELCOR-H2 are those obtained from comprehensive studies carried out at Los Alamos National Laboratory using the bare metal assembly, Godiva (Keepin, 1965, Section 4.1). These measurements dealt with delayed neutrons from fast fission of six nuclides, U^{235}, U^{233}, U^{238}, Pu^{239}, Pu^{240}, and Th^{232}, and from thermal fission of three nuclides, U^{235}, U^{233}, and Pu^{239}. For the prismatic NGNP, helium-cooled and graphite-moderated thermal reactor of interest, the data for delayed neutrons from thermal fission of U^{235} are used. These data, shown in Table 5-1, are taken from Table 4.8 of Keepin (1965). The total, absolute delayed-neutron yield is 0.0158 (Keepin, 1965, Tables 4.8 and 4.12). This is the total number of delayed neutrons produced per fission. Since the average number of neutrons produced per thermal fission in U^{235} is $\nu = 2.432$ (Keepin, 1965, Table 4.14), then $\overline{\beta} = 0.0158/2.432 = 0.0065$. The effective individual group fractions are then calculated using $\beta_i = \overline{\beta} \times f_i$.

Table 5-1. Delayed-Neutron Half-Lives, Decay Constants, and Yields from Thermal Fission of U-235

Group index, i	Half-life, $\tau_{1/2}$ (s)	Decay constant λ_i (1/s)	Relative abundance, f_i	Absolute group yield (%)
1	55.72	0.0124	0.033	0.052
2	22.72	0.0305	0.219	0.346
3	6.22	0.111	0.196	0.310
4	2.30	0.301	0.395	0.624
5	0.610	1.14	0.115	0.182
6	0.230	3.01	0.042	0.066
Sum	-	-	1.000	1.580

5.6 Numerical Solution by Approximation of Exponential Matrix

The fundamental difficulty in devising a stable and accurate numerical solution of the 6-point kinetics equations originates in the exponential nature of the solution. Examination of Equations (5-1) and (5-2) shows that seven different time scales exist of the exponential solution: $\{1/\lambda_i\}$, I = 1 to 6 and $\Lambda/(\rho-\overline{\beta})$. While the shortest time scale of the decay processes, $1/\lambda_6 \approx 1/3$ s, is relatively large, the neutron generation time scale may be several orders of magnitude smaller. In a large, fast-spectrum nuclear reactor, the neutron generation time $\Lambda = (\nu\Sigma_f)^{-1}$ typically ranges between 5×10^{-5} s and 10^{-3} s, while in a thermal-spectrum reactor, Λ is typically 2 orders of magnitude larger, $\sim 10^{-2}$ s. Due to such very short time scales, conventional explicit integration methods such as Euler's method and the higher-order Runge-Kutta techniques (Gill, 1951) require the use of severely restrictive (short) time steps to avoid exponential amplification of the error, requiring an unreasonably large amount of CPU time (Greenspan et al., 1968).

While higher-order corrections to the PJA have been proposed in the literature, such as those of Goldstein and Shotkin (1969), to predict the transient behavior of fast-spectrum reactors, the accuracy of such models still decreases with increasing neutron generation lifetime, Λ. Therefore, the PJA is not suitable for predicting the transient behavior of thermal-spectrum nuclear reactors, and the full 6-point kinetics equations must be solved simultaneously. The technique developed herein capitalizes on the work of Porsching (1966).

In order to highlight the basis of the numerical technique recommended for use in MELCOR-H2, the 6-point kinetics Equations (5-1) and (5-2) are recast in vectorial form, using the change of variable: $P = \Psi_1$, and $Y_i = \Psi_{i+1}$, for i = 1 to 6. These equations then become:

$$\frac{d\Psi_1}{dt} = \frac{\rho-\overline{\beta}}{\Lambda} \times \Psi_1 + \sum_{i=1}^{6} \lambda_i \Psi_{i+1} + S_o \,, \tag{5-14}$$

$$\frac{d\Psi_{i+1}}{dt} = \frac{\beta_i}{\Lambda} \times \Psi_1 - \lambda_i \Psi_{i+1}, \; i = 1 \text{ to } 6, \tag{5-15}$$

which may be written in matricial form as:

$$\frac{d}{dt}[\Psi] = \{A\} \bullet [\Psi] + [S], \text{ with } [\Psi] = [\Psi_o] \text{ at } t = 0, \tag{5-16}$$

where the vectors $[\Psi]$ and $[S]$ are given by $[\Psi] = [\Psi_1 \quad \Psi_2 \quad \Psi_3 \quad \Psi_4 \quad \Psi_5 \quad \Psi_6 \quad \Psi_7]^T$ and $[S] = [S_o \quad 0 \quad 0 \quad 0 \quad 0 \quad 0 \quad 0]^T$, and the 7×7 matrix $\{A\}$ has the form:

$$\{A\} = \begin{bmatrix} A_{11} & ..... & A_{17} \\ A_{21} & ..... & A_{27} \\ .... & ..... & .... \\ .... & ..... & .... \\ A_{71} & ..... & A_{77} \end{bmatrix} = \begin{bmatrix} (\rho - \bar{\beta})/\Lambda & \lambda_1 & \lambda_2 & ..... & \lambda_6 \\ \beta_1/\Lambda & -\lambda_1 & 0 & ..... & 0 \\ \beta_2/\Lambda & 0 & -\lambda_2 & ..... & 0 \\ ..... & ..... & ..... & ..... & ..... \\ \beta_6/\Lambda & 0 & 0 & ..... & -\lambda_6 \end{bmatrix}. \tag{5-17}$$

Note that the coefficient A_{11} is the only time-dependent coefficient of the matrix $\{A\}$, through control actions of the reactor and Doppler and temperature feedback effects. For a moment, let us assume that the total reactivity ρ and the active source term S_o are constants independent of time, and let us derive the analytical solution of Equation (5-16). A solution of the homogeneous equation (with [S] = 0) is $\{\exp(At)\} \bullet [\Phi]$, where $[\Phi]$ is an arbitrary constant vector. For an arbitrary matrix $\{M\}$, the power series $\{\Im\} + \{M\} + \{M\}^2/2! + \{M\}^3/3! + ...$ converges to a matrix called the exponential of $\{M\}$, which is denoted $\{\exp(M)\}$. An obvious particular solution of Equation (5-16a) is the constant vector (independent of time): $(-\{A\}^{-1} \bullet [S])$. Therefore, the solution of Equation (5-16a) can be written:

$$[\Psi] = \{\exp(At)\} \bullet [\Phi] - \{A\}^{-1} \bullet [S]. \tag{5-18}$$

The unknown vector $[\Phi]$ is obtained from satisfying the initial condition, Equation (5-16b):

$$[\Psi_o] = \{\Im\} \bullet [\Phi] - \{A\}^{-1} \bullet [S], \tag{5-19}$$

where $\{\Im\}$ is the Identity matrix, which gives:

$$[\Phi] = [\Psi_o] + \{A\}^{-1} \bullet [S]. \tag{5-20}$$

Finally, the exact solution of Equations (5-16) for constant reactivity and source term is:

$$[\Psi] = \{\exp(At)\} \bullet \left([\Psi_o] + \{A\}^{-1} \bullet [S] \right) - \{A\}^{-1} \bullet [S]. \tag{5-21}$$

The form of Equation (5-21) suggests the following algorithm to advance the numerical solution in time (Porsching, 1966). Let us assume that the solution $[\Psi]_n$ is known at time t_n. Then, the solution is advanced to time ($t_{n+1} = t_n + \Delta t$) using:

$$[\Psi]_{n+1} = \{\exp(\mathrm{A}\,\Delta t)\} \bullet \left([\Psi]_n + \{\mathrm{A}\}^{-1} \bullet [\mathrm{S}]\right) - \{\mathrm{A}\}^{-1} \bullet [\mathrm{S}]. \tag{5-22}$$

Since in practice the total reactivity and active source term change over the interval [t_n , t_{n+1}], "average" values of the A_{11} and S_o coefficients are used during this time step, i.e.,

$$\mathrm{A}_{11} = \frac{\theta\rho_{n+1} + (1-\theta)\rho_n - \overline{\beta}}{\Lambda} \text{ and } S_o = \theta(S_o)_{n+1} + (1-\theta)(S_o)_n, \tag{5-23}$$

where $0 \leq \theta \leq 1$. A value of θ = 0.5 provides the best accuracy in time. Porsching (1966) has shown that the local discretization error of the method defined by Equation (5-22) is of the order $(\Delta t)^3$. That is, the method is 3rd-order accurate in time. The advantages of the present method are that it preserves the original form of the kinetics equations, and it captures the exponential behavior of the solution if a suitable approximation to the exponential matrix $\exp\{\mathrm{A} \times \Delta t\}$ is used.

The accurate evaluation of the exponential matrix is in itself a difficult problem. Unless the time step is uncomfortably small, the power series defining the exponential converges too slowly for practical use. In other words, any method based on the truncation of the exponential power series would yield highly inaccurate results, unless the time step is severely restricted. For example, using the first two terms of the series, i.e., $\exp\{\mathrm{M}\} \approx \{\Im\} + \{\mathrm{M}\}$, is equivalent to using the Euler's approximation method to solve the kinetics equations. Similarly, the simplified Runge-Kutta approximation method is equivalent to approximating the exponential matrix using the first three terms of the series, i.e., $\exp\{\mathrm{M}\} \approx \{\Im\} + \{\mathrm{M}\} + \{\mathrm{M}\}^2 / 2$. When applied to the solution of the kinetics equations, both of these methods require the use of unreasonably small time steps to avoid exponential growth of the error and to ensure stability of the solution (Porsching, 1966; Greenspan et al., 1968).

5.7 Padé Approximants of the Exponential Matrix

Porsching (1966) has suggested the use of rational matrix functions to approximate the exponential matrix for solving the kinetics equations, and proposed different approximations of various accuracy. Of particular interest in Porsching's work was the consideration of the Padé(0,1) and Padé(1,2) rational functions.

The Padé(p,q) rational function or "approximant" of a function is the ratio of two polynomials, of degrees p in the numerator and q in the denominator, which approximates a particular function F(x) to an order of O(x^{p+q+1}) (Baker, 1975). The coefficients of the polynomials are constructed from the coefficients of the Taylor series expansion of the function. An advantage of the Padé approximants is that they are capable of providing bounded and stable values over a much wider domain than the conventional Taylor series approximation, which diverges quickly away from the chosen expansion point. Some of the ground work on the Padé approximants was established

early in the 19th century by Cauchy, Jacobi and Forbenius, before Padé's thesis was even published. Padé seemed to have been unaware of this previous work, but was the first investigator to emphasize the importance of displaying the functions in tabular form, and to study the structure of this table (Baker, 1975). A fragment of Padé approximants to the exponential function exp(x) is shown in Table 5-2 (Baker, 1975, p. 11). A few of these approximants are also plotted in Figure 5-2, and compared with the exponential function. It is clear on this figure that the range over which the approximant is an accurate representation of the function exp(x) increases with increasing (p+q) values.

Various Padé approximants of the exponential matrix, i.e., Padé(0,1), (1,2), (2,2) and (3,3), were studied in this work, and the Padé(3,3) function was chosen based on the accuracy of the method. The accuracy of the present numerical solution was evaluated by comparison with the exact Inhour solution for the case of a step reactivity insertion. Delayed-neutron group data, such as decay constants and yields were those from thermal fission of U^{235} (Table 5-1). The neutron generation time was taken as $\Lambda = 10^{-2}$ s, a value that is representative of a commercial graphite-moderated, thermal spectrum reactor.

Table 5-2. Padé(p,q) Approximations to the Exponential Function, exp(x) (Baker, 1975, p. 11)

p	$q = 0$	$q = 1$	$q = 2$	$q = 3$
0	$\frac{1}{1}$	$\frac{1}{1-x}$	$\frac{2}{2-2x+x^2}$	$\frac{6}{6-6x+3x^2-x^3}$
1	$\frac{1+x}{1}$	$\frac{2+x}{2-x}$	$\frac{6+2x}{6-4x+x^2}$	$\frac{24+6x}{24-18x+6x^2-x^3}$
2	$\frac{2+2x+x^2}{2}$	$\frac{6+4x+x^2}{6-2x}$	$\frac{12+6x+x^2}{12-6x+x^2}$	$\frac{60+24x+3x^2}{60-36x+9x^2-x^3}$
3	$\frac{6+6x+3x^2+x^3}{6}$	$\frac{24+18x+16x^2+x^3}{24-6x}$	$\frac{60+36x+9x^2+x^3}{60-24x+3x^2}$	$\frac{120+60x+12x^2+x^3}{120-60x+12x^2-x^3}$

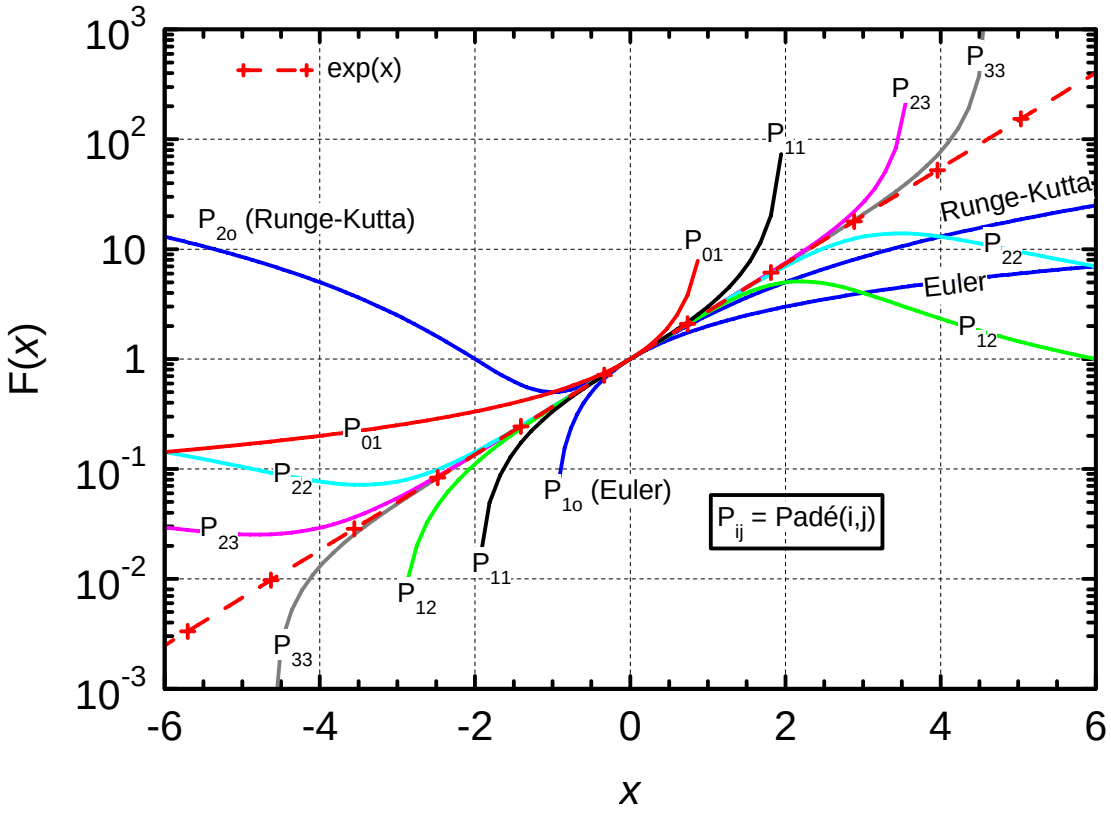

Figure 5-2. Padé approximants of the exponential function.

In order to appreciate the stability and accuracy of the proposed numerical technique, a constant reactivity value of \$1.0 was chosen, for which the reactor's thermal power increases by one order of magnitude in 8 s, by 2 orders of magnitude in 16 s, and 4 orders of magnitude in only 32 s. Results for this test case (a step input reactivity of $\rho / \bar{\beta}$ = 1.0 dollar, no active neutron source, $S_o = 0$, and $\Lambda = 10^{-2}$ s) are shown in Figure 5-3. When using a fixed time step, $\Delta t = 4$ s, the errors in the thermal power after 40 s into the transient (at which time the power has increased by a factor ~ 10^5) are 28%, 2.3%, and 0.019% for the Padé(1,2), Padé(2,2), and Padé(3,3) approximants, respectively. That is, the error is divided by a factor ~ 12 for each order of accuracy increase in the approximant function. The Padé(1,2) approximant is accurate to the order $O(x^4)$, while Padé(2,2) is accurate to the order $O(x^5)$, and Padé(3,3) to the order $O(x^7)$. Note that from the point of view of CPU time, all the exponential matrix numerical techniques with Padé approximant perform nearly identically since they all require the solution of two 7×7 linear systems of equations by Gauss elimination at each time step and/or internal iteration to resolve the change in the total reactivity of the reactor by feedback effects. In case of the absence of an active neutron source, only one Gauss elimination is required per step.

As expected, the error of the present numerical technique increases with increasing time step (Figure 5-3). For a relatively large time step of 2 s, the error is less than 0.001% at time $t = 40$ s, after which the reactor's thermal power has increased by a factor 10^5. This calculation required only 20 time steps. Doubling the time step to $\Delta t = 4$ s caused the error to increase to 0.02% after $t = 40$ s. Even with an unreasonably large time step of 8 s, the local discretization error at each

time step is only ~ 0.3%. Since the reactor's thermal power increases tenfold between each time step (when Δt = 8 s), this very low discretization error shows very clearly the tremendous ability of the Padé(3,3) approximant to capture the exponential behavior of the solution of the kinetics equations. Because of such good stability and accuracy of the present numerical technique, it was not necessary to consider any higher order approximants.

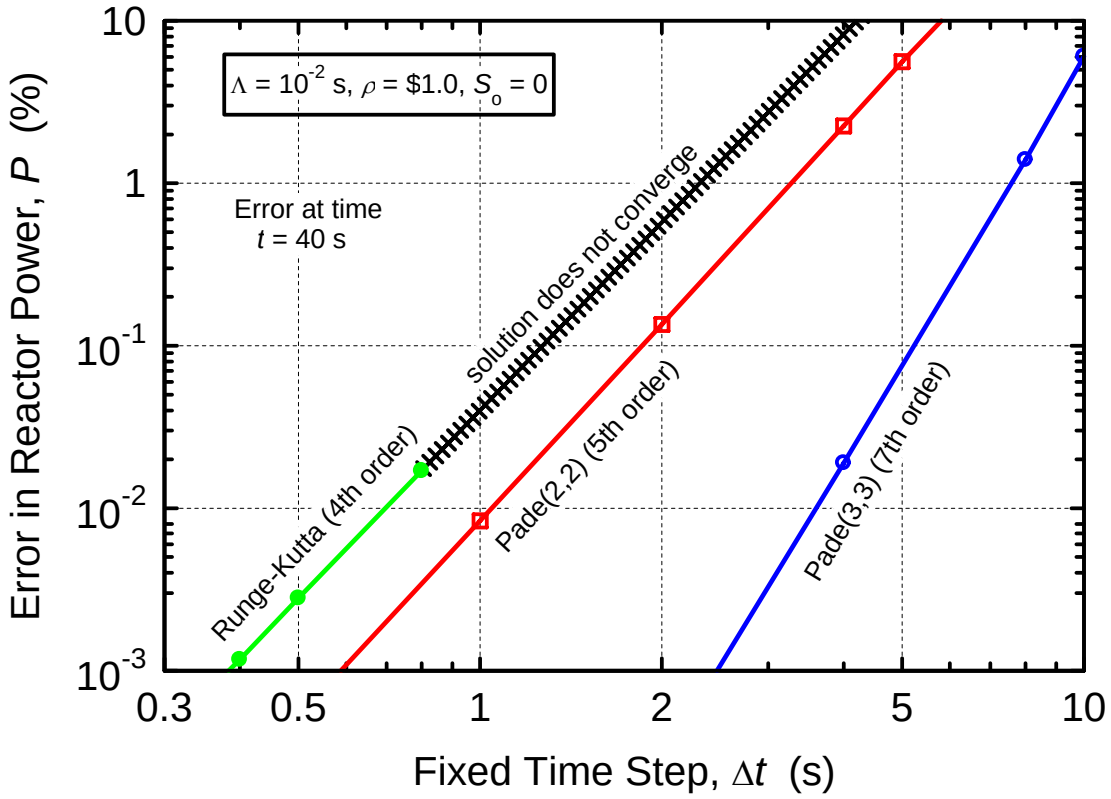

Figure 5-3. Effect of fixed time step size on accuracy of numerical solution of 6-point kinetics equation, for $1.0 step reactivity insertion.

Results obtained using the well-known 4th-order Runge-Kutta numerical integration technique (Gill, 1951) are also shown in Figure 5-3. This solution technique did not converge for time steps > 0.8 s. Incidentally, the present exponential matrix method with the Padé(3,3) approximant, which is 7th-order accurate, may use a time step that is one order of magnitude larger than that of the 4th-order Runge-Kutta technique, for the same discretization error (Figure 5-3).

In practice, the total reactivity of the reactor would not exceed $1.0, and since the increasing reactor thermal power would increase the fuel and moderator temperatures, the total reactivity would be reduced by feedback effects (the reactor is designed with negative temperature reactivity coefficients for safety; see Figure 5-1). Thus, the reactor period would always be longer than for the prompt critical case, and the accuracy of the Padé(3,3) exponential matrix numerical technique is established and suitable for all practical transients of interest. Furthermore, when the 6-point kinetics equations are coupled to the thermal model of the nuclear

reactor, through the temperature feedback coefficients, the maximum time step of the numerical model in MELCOR-H2 will not be restricted. The numerical technique developed herein is stable and accurate even for a ten-fold increase in thermal power per time step. Thus, the solution of the point kinetics equations is not Δt limited; rather, the limit on the time step will be that imposed by the thermal-hydraulics model of the reactor in MELCOR-H2.

The numerical solution of the 6-point kinetics equations, developed for incorporation into MELCOR-H2, uses the Padé(3,3) approximant of the exponential matrix, and is implemented as follows. Once the coefficients A_{11} and S_o have been updated using Equations (5-23), the solution computes the vector of dimension 7:

$$[\mathrm{B}] = \{\mathrm{A}\}^{-1} \bullet [\mathrm{S}] \tag{5-24}$$

using Gauss elimination with partial pivoting and row normalization (Golub and van Loan, 1984). The solution then calculates the vector [C] and the 7×7 matrix {X}:

$$[\mathrm{C}] = [\Psi]_n + [\mathrm{B}] \text{ and } \{\mathrm{X}\} = \{\mathrm{A}\} \times \Delta t \,. \tag{5-25}$$

The exponential matrix is then approximated by the Padé(3,3) rational function (see Table 5-2):

$$\{\exp(\mathrm{X})\} \cong \left\{ \Im - \frac{\mathrm{X}}{2} + \frac{\mathrm{X}^2}{10} - \frac{\mathrm{X}^3}{120} \right\}^{-1} \bullet \left\{ \Im + \frac{\mathrm{X}}{2} + \frac{\mathrm{X}^2}{10} + \frac{\mathrm{X}^3}{120} \right\}, \tag{5-26}$$

and Equation (5-22) becomes:

$$[\Psi]_{n+1} = \left\{ \Im - \frac{\mathrm{X}}{2} + \frac{\mathrm{X}^2}{10} - \frac{\mathrm{X}^3}{120} \right\}^{-1} \bullet \left\{ \Im + \frac{\mathrm{X}}{2} + \frac{\mathrm{X}^2}{10} + \frac{\mathrm{X}^3}{120} \right\} \bullet [\mathrm{C}] - [\mathrm{B}]. \tag{5-27}$$

This linear system of equations is easily solved by computing the vector:

$$[\mathrm{E}] = \left\{ \Im + \frac{\mathrm{X}}{2} + \frac{\mathrm{X}^2}{10} + \frac{\mathrm{X}^3}{120} \right\} \bullet [\mathrm{C}], \tag{5-28}$$

and solving the (7×7) linear system:

$$[\mathrm{D}] = \left\{ \Im - \frac{\mathrm{X}}{2} + \frac{\mathrm{X}^2}{10} - \frac{\mathrm{X}^3}{120} \right\}^{-1} \bullet [\mathrm{E}] \tag{5-29}$$

for the vector [D], using Gauss elimination with partial pivoting and row normalization (see subroutines GAUSSB and UPPERB in Appendices T and U). The solution vector is then advanced in time as:

$$[\Psi]_{n+1} = [\mathrm{D}] - [\mathrm{B}]. \tag{5-30}$$

A FORTRAN subroutine of the present model is developed and tested using Compaq Visual FORTRAN Professional Edition 6.5.0 (2000), which provides a superset of the FORTRAN 95 standard with other extensions for compatibility with previous FORTRAN languages and platforms. All the coding instructions used in the present model are compatible with Standard Fortran 77, except that two advanced capabilities of the Fortran 95 set are used for matrix computation: (a) the subroutine uses the generic intrinsic function MATMUL(**A**,**B**) for multiplication of matrices (or vectors) **A** and **B**; and (b) the assignment instruction for matrices and vectors; for example, if **A** is a vector, the instruction (**A** = 10) assigns the value 10 to each component of the vector. Similarly, if **A** and **B** are vectors of same dimension **N**, the assignment instruction (**A** = **B**) is equivalent to **A**(*i*) = **B**(*i*), for *i* = 1 to **N**. These advanced matrix instructions can easily be replaced with equivalent DO loops if they are not available in the MELCOR-H2 FORTRAN compiler.

The FORTRAN code of the subroutine UNM_KINETICS is given in Appendix S. The solution of the 7 × 7 linear systems of equations is obtained by Gauss elimination with partial pivoting and row normalization (Golub and van Loan, 1984), and performed by the subroutine GAUSSB (see Appendix T). This routine in turn calls the subroutine UPPERB (see Appendix U) to obtain the solution of the resulting 7 × 7 upper-triangular linear system. These three subroutines are available on the CD-ROM included with this manual. The next section describes the input and output parameters of the subroutine UNM_KINETICS, and provides guidelines for its proper implementation in MELCOR-H2.

5.8 Input and Output Variables of Subroutine UNM_Kinetics

This section describes in details the input and output variables of the subroutine UNM_KINETICS. For clarity, all variable names used in the program are typed in **BOLD** in this section. Typically, the parameters that change with time during transient operation of the nuclear reactor (such as average temperatures, reactivities and thermal powers) are passed between MELCOR-H2 and the subroutine UNM_KINETICS through the argument list (the variables in parentheses following the name of the subroutine). Other parameters used by the 6-point kinetics model, such as the nuclear data of the delayed-neutron groups and the temperature-feedback reactivity coefficients χ_i (see Equations (5-11) through (5-13)), are supplied to the subroutine UNM_KINETICS by MELCOR-H2's user interface through the COMMON /KINETICS/. This COMMON must also appear in MELCOR-H2 main program unit and user interface subroutine.

The subroutine UNM_KINETICS can operate in two different modes (initialization, or normal). The mode of operation is controlled by the parameter **iFLAG** in the argument list. Each transient simulation of MELCOR-H2/UNM-KINETICS should proceed as follows. For a specified, initial reactor's thermal power P_o, MELCOR-H2 must be run to convergence to calculate the steady state, equilibrium temperatures at the nodes in the prismatic NGNP reactor. Once convergence is established, MELCOR-H2 must calculate the average fuel compact (T_f^o in Equations (5-10) and (5-11), variable **Tf_INIT**) and graphite (T_G^o in Equation (5-12), variable **Tg_INIT**) temperatures in the reactor, set the value of the flag to 1 (**iFLAG** = 1), and call the subroutine UNM_KINETICS for the first time. The subroutine then calculates the initial,

equilibrium values of the precursor powers, Y_i^o (Equation (5-7)), and initializes the constant coefficients of the matrix {A} (variable **A_KIN**) and vector [S] (variable **S_KIN**) (Equations (5-16) and (5-17)). Once this initialization phase is completed, MELCOR-H2 must set the value of the flag to 0 (**iFLAG** = 0), and can then start the transient calculation. During the time step iterations, MELCOR-H2 must call the subroutine UNM_KINETICS to calculate the thermal power of the reactor. This power can then be used in the thermal-hydraulics model of the gas-cooled reactor to calculate the change in the fuel and graphite temperatures. The next subsection describes in details the input parameters passed to the subroutine UNM_KINETICS through the argument list.

5.8.1 Input Parameters Passed to the Subroutine Through the Argument List

The following parameters of the argument list are passed to the subroutine UNM_KINETICS, independently of the mode of operation:

IO UNIT number of output file "KINETICS.OUT" written by the subroutine;
This file is OPENED by the subroutine the first time it is called (**iFLAG** = 1)

iFLAG Flag to identify the first time that this subroutine is called.
Before the subroutine is called, MELCOR-H2 must be used
to calculate the steady state, equilibrium temperatures at the nodes in the prismatic NGNP reactor, at the desired initial reactor's thermal power.
Once convergence is established, MELCOR-H2 calculates the volume-averaged fuel compact (**Tf_INIT**) and graphite (**Tg_INIT**) temperatures in the reactor, sets the value of the flag to 1 (**iFLAG** = 1), and calls the subroutine UNM_KINETICS

→ When **iFLAG** = 1, MELCOR-H2 supplies the following input parameters to the subroutine:

Tf_OLD Average fuel compact temperature at equilibrium, **Tf_INIT** (K)

Tg_OLD Average graphite temperature at equilibrium, **Tg_INIT** (K)

Q_OLD(1) Equilibrium reactor's thermal power, P_o (W)
The subroutine, in turns, initializes and returns the thermal powers generated by the precursors: **Q_OLD(2)**, **Q_OLD(3)**,..., **Q_OLD(7)** (W), at equilibrium.
The subroutine also calculates:
BETA(*i*) = Effective fraction for i^{th} delayed-neutron group, and calculates the constant coefficients of the 7×7 matrix **A_KIN** and vector **S_KIN** (all coefficients except coefficients **A_KIN(1,1)** and **S_KIN(1)**)

When iFLAG is different (<>) than 1, the thermal power of the reactor is calculated by the kinetics model (normal mode of operation) and MELCOR-H2 must supply the following input parameters to the subroutine through the ARGUMENT list:

→ When **iFLAG** <> 1, MELCOR-H2 supplies the following input parameters to the subroutine:

IO	UNIT number of output file "KINETICS.OUT" written by the subroutine; This file is opened by the subroutine the first time it is called (**iFLAG** = 1)
TIME0	Previous time value (s)
TAU	Discretization time step size to advance the solution (s)
CONTROL_OLD	External reactivity at previous time (**TIME0**)
CONTROL_NEW	External reactivity at new time (**TIME0** + **TAU**) If **THETA** = 0, the variable **CONTROL_NEW** is not "used" by the routine
Tf_OLD	Average fuel compact temperature at previous time (**TIME0**) (K)
Tf_NEW	Average fuel compact temperature at new time (**TIME0** + **TAU**) (K) If **THETA** = 0, the variable **Tf_NEW** is not "used" by the subroutine
Tg_OLD	Average graphite temperature at previous time (**TIME0**) (K)
Tg_NEW	Average graphite temperature at new time (**TIME0** + **TAU**) (K) If **THETA** = 0, the variable **Tg_NEW** is not "used" by the subroutine
Q_OLD(1)	Thermal power of reactor at previous time (**TIME0**) (W)
Q_OLD(*i*)	Thermal power of precursors at previous time (**TIME0**), (*i*=2 to 7) (W) (these values were calculated by UNM_KINETICS at the previous step)
S_OLD	Neutron source term at previous time (**TIME0**) (W/s)
S_NEW	Neutron source term at new time (**TIME0** + **TAU**) (W/s) If **THETA** = 0, the variable **S_NEW** is not "used" by the subroutine

5.8.2 Output Parameters Passed to MELCOR-H2 Through the Argument List

---

→ When **iFLAG** = 1, UNM_KINETICS returns the following parameters to MELCOR-H2:

The subroutine initializes and returns the thermal powers generated by the precursors, Y_i^o : **Q_OLD(2)**, **Q_OLD(3)**,..., **Q_OLD(7)** (W) at equilibrium (Equation (5-7)).

→ When **iFLAG** <> 1, UNM_KINETICS returns the following parameters to MELCOR-H2:

Because the external reactivity, neutron source term and fuel and graphite temperatures change between time **TIME0** and time (**TIME0** + **TAU**), the subroutine uses values of these quantities at the intermediate time: (**TIME0** + **THETA*****TAU**). For best accuracy, a value **THETA** = 0.5

is used. Since the temperatures at the new time are not known a priori, internal iterations are required at each time step, between MELCOR-H2 reactor thermal-hydraulics model and the 6-point kinetics model, until convergence of the temperatures, total reactivity, and thermal powers is achieved. Alternatively, if the time step size **TAU** is sufficiently small for the transient operation of interest, the thermal-hydraulics model of the gas-cooled reactor in MELCOR-H2 and the 6-point kinetics model UNM_KINETICS can be decoupled using **THETA** = 0. In such case, UNM_KINETICS uses the previous time values of the average fuel and graphite temperatures and of the external reactivity to calculate the reactor's thermal power at the new time.

When **iFLAG** is different than 1, the subroutine returns the following OUTPUT parameters through the ARGUMENT list:

CONTROL_TIL	External reactivity at intermediate time (**TIME0** + **THETA*****TAU**)
RK_FBACK_TIL	Feedback reactivity at intermediate time (**TIME0** + **THETA*****TAU**)
RKTIL	Total reactivity at intermediate time (**TIME0** + **THETA*****TAU**)
Tf_TIL	Average fuel compact temperature at intermediate time (K) If **THETA** = 0, the variable **Tf_TIL = Tf_OLD**
Tg_TIL	Average graphite temperature at intermediate time (K) If **THETA** = 0, the variable **Tg_TIL = Tg_OLD**
S_TIL	Neutron source term at intermediate time (W/s) If **THETA** = 0, the variable **S_TIL = S_OLD**
Q_NEW(1)	Thermal power of reactor at new time (**TIME0** + **TAU**) (W)
Q_TIL(1)	Thermal power of reactor at intermediate time (W) If THETA = 0, the variable Q_TIL(1) = Q_OLD(1)
Q_NEW(*i*)	Thermal powers of precursors at new time (*i*=2 to 7) (W)
Q_TIL(*i*)	Thermal powers of precursors at intermediate time (*i*=2 to 7) (W) If **THETA** = 0, the variables **Q_TIL(*i*) = Q_OLD(*i*)** (*i*=2 to 7)

5.8.3 Parameters of Common/Kinetics

The **COMMON /KINETICS/** in the subroutine UNM_KINETICS is used to supply the subroutine with the values of the fixed, input constants of the kinetics model, such as the nuclear data of the delayed-neutron groups and the temperature-feedback reactivity coefficients, χ_i (see Equations (5-11) through (5-13)). These parameters would normally be supplied by the user through MELCOR-H2's input deck. Consequently, this COMMON must also appear in MELCOR-H2 main program unit and user interface subroutine. Alternatively, the default values of these parameters may be used by un-commenting (activating) the **DATA** STATEMENTS in the subroutine UNM_KINETICS, to simplify (and accelerate) the incorporation of UNM_KINETICS into MELCOR-H2. Nonetheless, even if the **DATA** STATEMENTS in the subroutine UNM_KINETICS are activated, the input deck of MELCOR-H2 still needs to supply a transient profile of the external (control) reactivity to UNM_KINETICS, through the variables **CONTROL_OLD** and **CONTROL_NEW**. The **DATA** STATEMENTS in question are:

(a) Default values of delayed-neutrons data for thermal fissions in U-235 (Keepin, 1965, Tables 4.8, 4.12 and 4.14) (see Table 5-1):

```
DATA XLprompt    /0.01D0/
DATA LAMBDA      /0.0124D0, 0.0305D0, 0.111D0, 0.301D0, 1.14D0, 3.01D0/
DATA F           /0.033D0, 0.219D0, 0.196D0, 0.395D0, 0.115D0, 0.042D0/
DATA BETA_SUM    /0.0065D0/
```

These parameters are:

XLprompt	Prompt neutron generation time, Λ (s)
LAMBDA(*i*)	Decay constant for ith delayed-neutron group, λ_i (1/s)
F(*i*)	Relative abundance of ith delayed-neutron group, f_i
BETA_SUM	Total effective delayed-neutron fraction, $\overline{\beta}$

In addition, the subroutine UNM_KINETICS calculates the effective fraction of ith delayed-neutron group, **BETA(*i*)** = $f_i \times \overline{\beta}$ during the initialization phase (**iFLAG** = 1).

(b) Default values of the temperature-feedback reactivity coefficients (MacDonald et al., 2003); see Equations (5-10) through (5-13) of this manual:

```
DATA RK_D     /-2.200D-2/
DATA RK_F1    /-4.780D-5/
DATA RK_F2    / 6.750D-9/
DATA RK_G1    /14.834D-5/
DATA RK_G2    /-1.6025D-7/
DATA RK_G3    / 6.991D-11/
DATA RK_G4    /-1.114D-14/
```

These parameters are:

RK_D	Core Doppler temperature reactivity coefficient, χ_D
RK_F1	Fuel expansion temperature reactivity coefficient, χ_{f1} (K^{-1})
RK_F2	Fuel expansion temperature reactivity coefficient, χ_{f2} (K^{-2})
RK_G1	Graphite expansion temperature reactivity coefficient, χ_{G1} (K^{-1})
RK_G2	Graphite expansion temperature reactivity coefficient, χ_{G2} (K^{-2})
RK_G3	Graphite expansion temperature reactivity coefficient, χ_{G3} (K^{-3})
RK_G4	Graphite expansion temperature reactivity coefficient, χ_{G4} (K^{-4})

(c) Default value of implicit/explicit discretization parameter for highest temporal accuracy:

```
DATA THETA    /0.50D0/
```

Any **THETA** value GREATER THAN ZERO (**THETA** > 0) requires internal iterations between the GCR thermal-hydraulics model and the 6-point kinetics model, to resolve the dependence of the total reactivity on the advanced-time fuel and graphite temperatures. If the user wishes to run

the MELCOR-H2 thermal-hydraulics model of the GCR decoupled from the 6-point kinetics model, then **THETA** = 0.D0 should be used. In this case, no internal iterations are performed to resolve the dependence of the total reactivity on the advanced-time fuel and graphite temperatures; this means that the temperature-feedback and control reactivities are accounted for explicitly in the model (since they are calculated at the previous time step).

The **COMMON /KINETICS/** also stores values of parameters that do not change between time steps, such as the initial (reference) values of the average fuel and graphite temperatures (T_j^o, variable **Tf_INIT**, and T_G^o, variable **Tg_INIT**) used in Equations (5-10) through (5-12), and the constant coefficients of the matrix {A} (variable **A_KIN**) and vector [S] (variable **S_KIN**), which are calculated by the UNM_KINETICS subroutine the first time it is called (**iFLAG** = 1).

The following parameters are stored in the **COMMON /KINETICS/** the first time that this subroutine is called (when **iFLAG** = 1). These parameters must be available to the subroutine when it is called subsequently (**iFLAG** <> 1).

Tf_INIT Average fuel compact temperature at time = 0 (steady-state) (K)
Tg_INIT Average graphite temperature at time = 0 (steady-state) (K)

The following parameters are calculated by the UNM-KINETICS subroutine and stored in the **COMMON /KINETICS/**:

A_KIN (7 × 7) matrix {A} for solution of 6-point kinetics equations (Equation (5-17)).
S_KIN Source vector [S] for solution of 6-point kinetics equations (Equations (5-16) and (5-17)); the (7 × 7) **A_KIN** matrix and **S_KIN** vector must be available to the subroutine when it is called. They are initialized the first time that the subroutine is called (when **iFLAG** = 1), except for **A_KIN**(1,1) and **S_KIN**(1) that are time-dependent
B_KIN, **C_KIN**, **D_KIN**, **E_KIN** = Vectors of dimension 7 used in the numerical solution (see Equations (5-24), (5-25a), (5-28), and (5-29)
X_KIN (7 × 7) matrix {X}, **X_KIN** = **TAU** * **A_KIN** (Equation (5-25b))
X2_KIN Square of (7 × 7) matrix **X_KIN**, $\{X\}^2$
X3_KIN Cube of (7 × 7) matrix **X_KIN**, $\{X\}^3$
Z_KIN Intermediate (7 × 7) matrix used in the numerical solution

In the next section, a simulation case of the prismatic NGNP operation obtained by coupling the present 6-point kinetics model with the UNM-ISNPS 84-nodes thermal-hydraulics model is presented to test the subroutine and illustrate the effects of temperature-feedback effects on the transient response of the prismatic NGNP reactor. The transient simulates a reactor thermal power change between 600 MW and 506 MW, over a period of 1000 s, following by restoration of the original power level within another 1000 s time period. Figures showing the changes in average fuel and graphite temperatures, reactivities, and reactor's thermal power as functions of time are presented, and the data files of the calculated transient are included on the CD-ROM accompanying this manual.

5.9 Test Case to Illustrate Feedback Reactivity Model

In order to test the temperature-feedback reactivity model and provide a benchmark test to verify the proper implementation of the present 6-point kinetics model (subroutine UNM_KINETICS) into MELCOR-H2, the kinetics model was coupled to an 84-nodes thermal-hydraulic model of the prismatic NGNP reactor, developed at UNM-ISNPS, to simulate the startup of the reactor and its transient behavior during a change in power level.

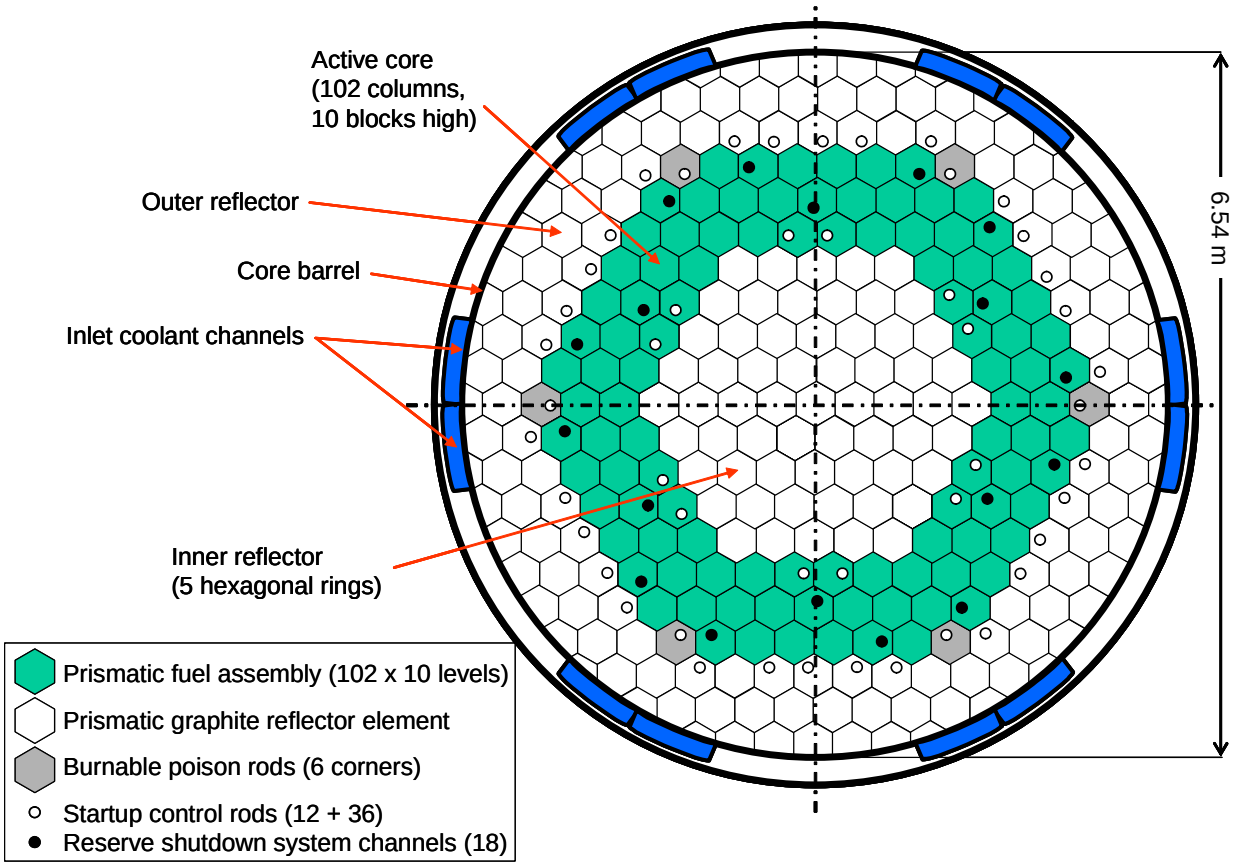

Figure 5-4. Cross-section view of GT-MHR/NGNP prismatic reactor.

Horizontal and elevation cross-sections of the GT-MHR/NGNP prismatic reactor (IAEA, 2001; MacDonald et al., 2003 and 2004) are shown in Figures 5-4 and 5-5. The reactor consists of an arrangement of hexahedral assemblies that are 80 cm high, with a flat-to-flat distance of 36.2 cm. The inner graphite reflector, which occupies the five innermost rings of the reactor, consists of 61 graphite assembly columns of 10 assemblies each, and weights about 99 metric tons. The annular, active core zone occupies rings 6, 7 and 8, and consists of 102 fuel assembly columns of 10 assemblies each (Figures 5-4 and 5-5). Each fuel assembly level in the core is penetrated with a total of 10,626 vertical coolant channels that are 16 mm in diameter, and a total of 20,700 TRISO fuel compact "rods" (pellets stack) that are 12.5 mm in diameter. The gas channels and fuel rod penetrations (12.7 mm in diameter) are essentially drilled into the graphite moderator assemblies. The total mass of graphite moderator in the active core zone is 97.8 metric tons.

The outer graphite reflector, which occupies the three outermost rings of the reactor, extends to a maximum diameter of 6.54 m, and consists of approximately 131 graphite assemblies stacked on 10 levels. This outer reflector, the largest graphitic component of the reactor, weights 212.4 metric tons, and comprises 42.6 w% of the total amount of graphite present in the reactor (Figure 5-5).

The upper (level 12) and lower (level 1) graphite reflectors are arranged above and below the fuel assembly levels (2 to 11), and weigh 44.5 tons each (Figure 5-5). The masses of the graphitic components in the reactor are calculated based on the reported geometry and assuming a nuclear graphite density of 1.778 kg/m^3 (a volume porosity of 21%).

The helium gas coolant enters the reactor at the bottom, through six pairs of annular flow channels placed on the outside surface of the core barrel (Figure 5-4), and flows upward to the upper plenum (Figure 5-5). The gas flow then reverses direction and flows downward through the 10,626 coolant channels penetrating the fuel assemblies. It then mixes in the bottom plenum and exits the reactor.

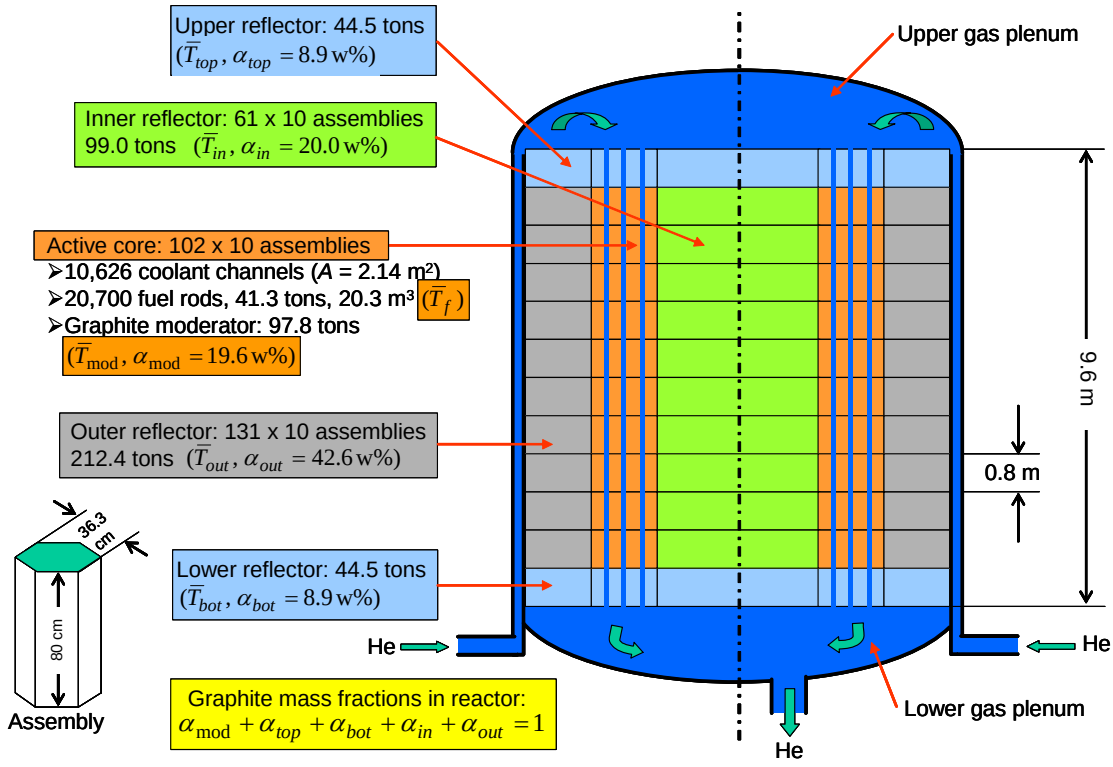

Figure 5-5. Elevation view of GT-MHR/NGNP prismatic reactor.

In order to test the temperature feedback reactivity model of the NGNP reactor (Figures 5-4 and 5-5), a transient thermal-hydraulics model of the reactor was developed at UNM-ISNPS. The model divides the volume of the reactor into 12 levels and 7 zones in each level, for a total of $12 \times 7 = 84$ temperature nodes. The energy conservation in each zone and the thermal conductances between zones are written such that the nodal temperature values represent the volume-averaged temperatures of each zone when a steady state condition is achieved. The

seven zones in each level are: (a) TRISO fuel compact rods (or graphite plugs in the upper and lower reflectors); (b) graphite moderator in fuel assemblies; (c) helium gas in circular coolant channels through the fuel assembly columns; (d) inner reflector zone; (e) outer reflector zone; (f) metallic reactor vessel; and (g) helium gas in the annular flow channels outside of the core barrel (Figure 5-5). The transient thermal-hydraulics model of the NGNP prismatic reactor accounts for thermal energy storage in the different modeled zones, axial conduction and radial conduction between the different zones, convective heat transfer between solid structures and gas coolant, and radiative heat transfer through the transparent gas in the upper and lower plenums.

The thermal-hydraulics model is coupled to the 6-point kinetics model developed in the present task, through the temperature-feedback reactivity model, Equations (5-9) through (5-12). The volume-averaged temperatures of the fuel compact ($\overline{T}_f$), inner reflector ($\overline{T}_{in}$), fuel assembly moderator ($\overline{T}_{\mathrm{mod}}$), and outer reflector ($\overline{T}_{out}$) are computed by the thermal-hydraulics model using a simple average of the 10 nodal temperatures associated with each zone. The volume-averaged temperatures of the upper ($\overline{T}_{top}$) and lower ($\overline{T}_{bot}$) reflectors are computed by properly averaging the nodal temperatures at assembly levels 12 and 1, respectively. Finally, the mass-averaged (or volume-averaged) temperature of the graphite in the reactor is computed based on the mass fraction of each graphitic component (Figure 5-5), i.e.,

$$\overline{T}_G = \alpha_{in}\overline{T}_{in} + \alpha_{\mathrm{mod}}\overline{T}_{\mathrm{mod}} + \alpha_{out}\overline{T}_{out} + \alpha_{top}\overline{T}_{top} + \alpha_{bot}\overline{T}_{bot} \ . \tag{5-31}$$

Obviously, we have by construction (Figure 5-5):

$$\alpha_{in} + \alpha_{\mathrm{mod}} + \alpha_{out} + \alpha_{top} + \alpha_{bot} = 1 \, . \tag{5-32}$$

The external reactivity profile of the power change transient is illustrated in Figure 5-6. Initially, the reactor is operating at steady state, at a nominal thermal power of 600 MW ($S_o = 0$, $\rho_o = 0$). UNM's thermal-hydraulic model predicts average fuel and graphite temperatures of T_f^o = 1160 K and T_G^o = 1127.4 K, respectively. These values are in close agreement with those reported by MacDonald et al. (2003), 1164 K and 1114 K, respectively, for the same thermal power level, coolant mass flow rate (226.6 kg/s), and inlet temperature (763 K). During the transient, which is initiated at time, t_1 = 100 s (Figure 5-6), the coolant inlet temperature and mass flow rate through the reactor are kept constant. At time t_1, 50 cents of negative reactivity are inserted into the reactor, at a steady rate and over a period of 5 minutes (τ = 300 s). The movement of the control rods is then stopped for a period of 10 minutes (600 s), during which time a quasi-steady equilibrium is established. At time t_2 = 1000 s, 50 cents of positive reactivity are inserted back into the reactor, following the exact reverse process (Figure 5-6).

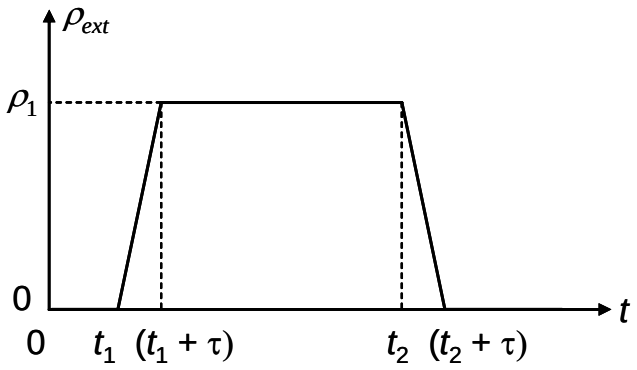

(ρ_1 = – \$0.5, t_1 = 100 s, t_2 = 1000 s, τ = 300 s)

Figure 5-6. External reactivity profile for transient test case.

Results of the transient calculation are shown in Figures 5-7 through 5-10. These calculations illustrate the usual characteristics of a reactor with negative temperature-feedback reactivity coefficient (Figure 5-1), with inherent stability. For example, upon insertion of negative reactivity in the reactor, due to the movement of control rods, the total reactivity becomes negative (Figure 5-8) and the thermal power of the reactor starts dropping (Figure 5-9). As a result, the average fuel and graphite temperatures in the reactor start to drop (Figure 5-10), generating a positive reactivity change by feedback effect, which opposes the external negative reactivity (Figure 5-7). Such a scenario is allowed to develop because of the difference in time periods of the neutronics and heat transfer processes. While the neutron population responds almost immediately to a change in external reactivity, the temperatures in the reactor, and consequently the feedback-temperature reactivity, respond much more slowly, due to the thermal inertia of the system. The effect of the very large mass and thermal inertia of graphite in the gas-cooled, prismatic NGNP reactor is well illustrated in Figure 5-10. While the fuel temperature responds rather quickly to a change in thermal power, decreasing by about 60 K over the reactivity insertion period of 300 s, the average graphite temperature changes much more slowly, decreasing by only about 13 K over the same period of time.

Approximately 2 minutes after the control rods have stopped (time ~ 520 s), a quasi-steady state equilibrium is established, at constant thermal power of 506 MW, fuel average temperature of 1100 K, and helium exit temperature of 1195.2 K (Figures 5-8 through 5-10). The graphite temperature; however, has not reached equilibrium yet, because of the large thermal inertia of graphite in the reactor. Its average temperature decreases slowly, at a rate of ~ 0.2 K/minute (Figure 5-10).

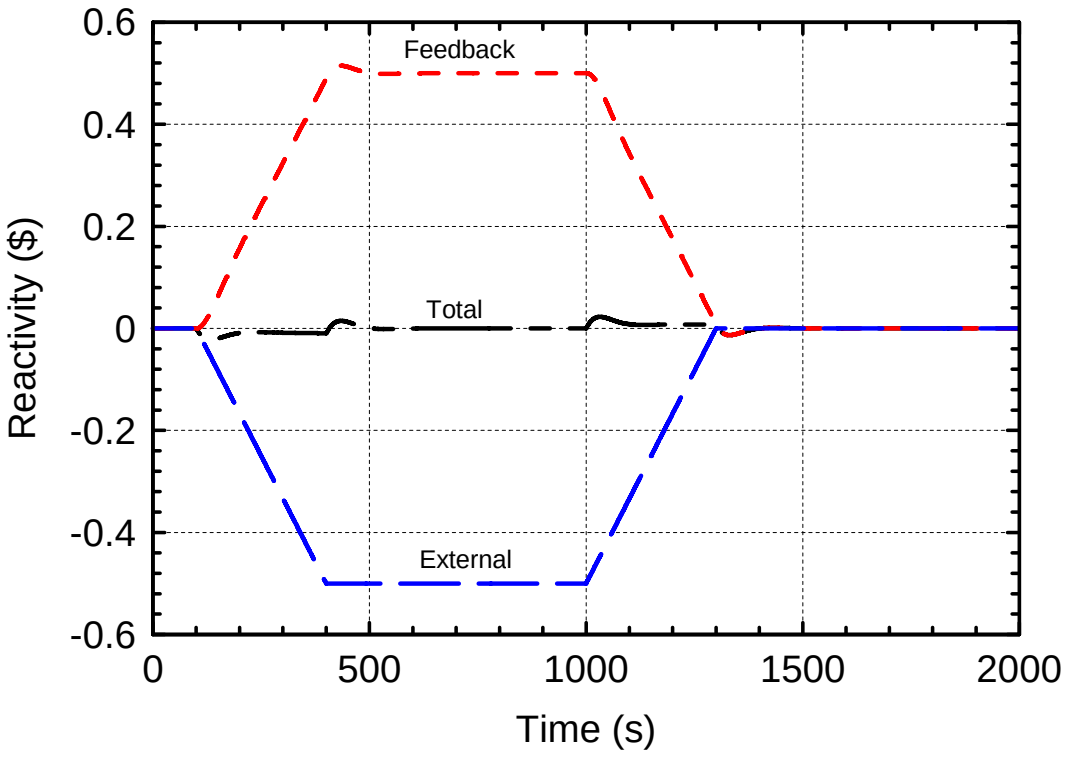

Figure 5-7. External and feedback reactivities of reactor during transient test case.

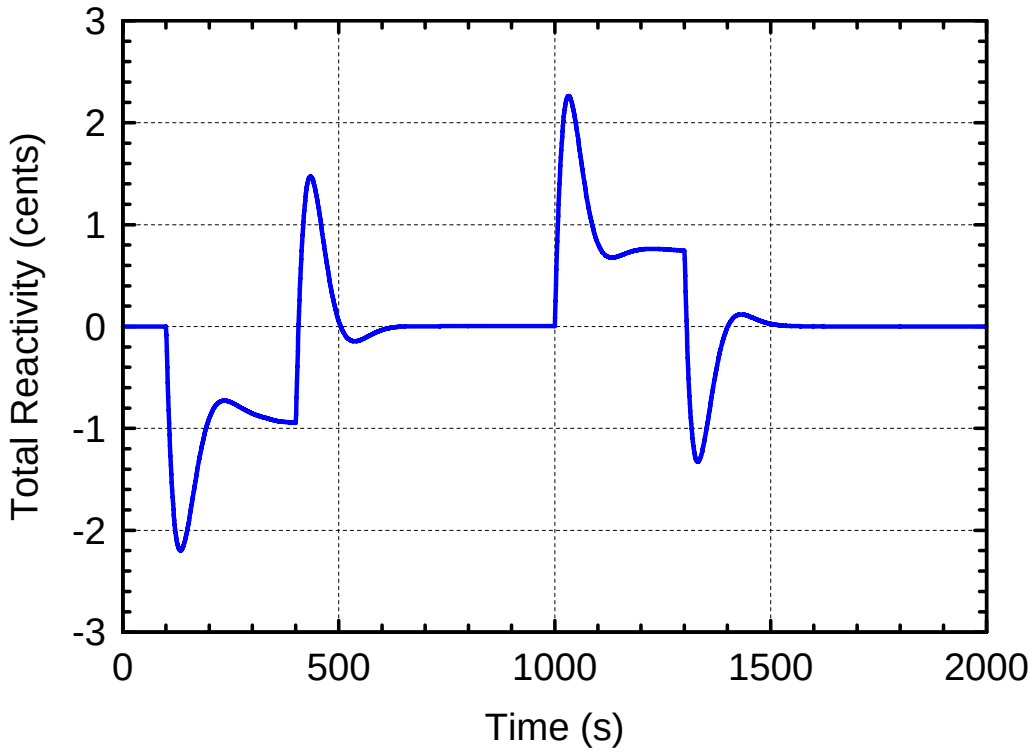

Figure 5-8. Total reactivity of reactor during transient test case.

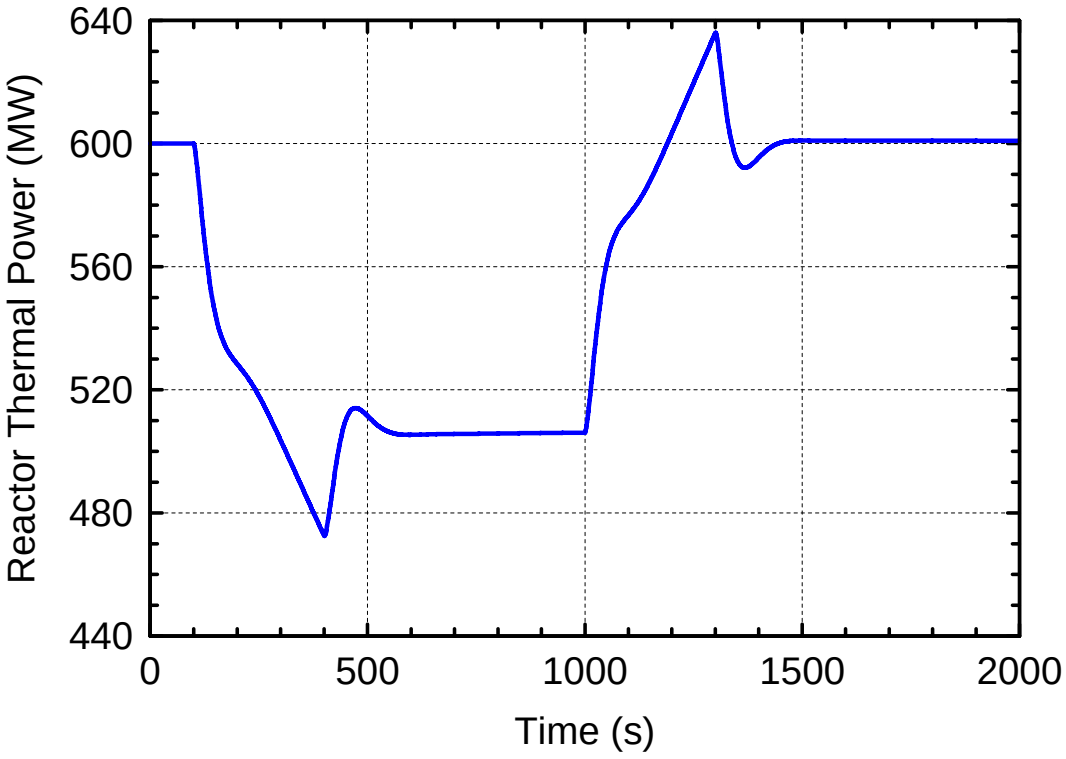

Figure 5-9. Thermal power of NGNP reactor during the transient test case.

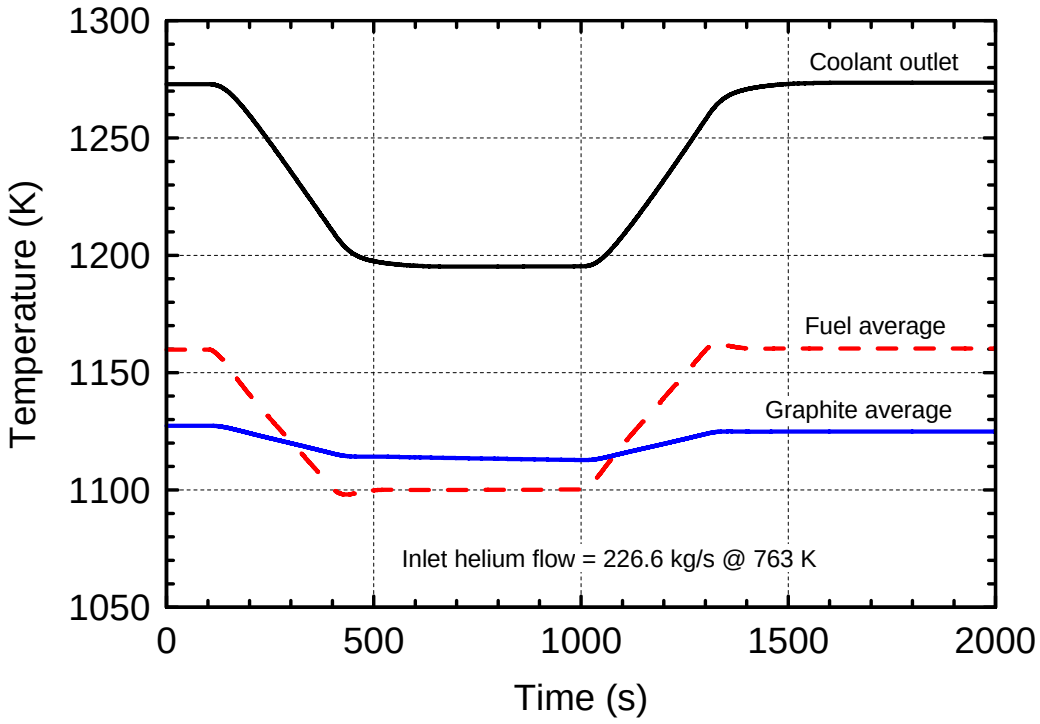

Figure 5-10. Average fuel and graphite temperatures during transient test case.

During the second phase of the transient (time $\geq$ 1000 s), when the position of the control rods is restored to their original position (Figure 5-6), the changes in the reactivities, reactor thermal power, and temperatures are mirror images of their variation during the first period of the transient (time < 1000 s). After 2000 s into the transient, the helium exit temperature is 1273.6 K (compared to 1272.9 K at time zero) and the reactor thermal power is 600.9 MW (compared to 600 MW at time zero). The average fuel temperature has reached its initial value of 1160 K; however, the average graphite temperature, 1125 K, is lower than its initial, equilibrium value of 1127.4 K. The slower response of the graphite temperature is caused by the large thermal inertia of this material, and it will be several hours before thermal equilibrium is established again, at which time the slight increase in the average graphite temperature will amount to a negative feedback reactivity effect that lowers the reactor thermal power back to its original equilibrium value of 600 MW.

The values of reactivities, average temperatures, and reactor thermal power, calculated by the UNM-ISNPS thermal-hydraulics model coupled to the 6-point kinetics model (UNM_KINETICS) and presented in Figures 5-7 through 5-10, are provided on the CD-ROM included with this manual. This transient test case can be used to test the proper implementation and good working of the subroutine UNM_KINETICS after coupling with MELCOR-H2. During this test, the average fuel and graphite temperatures calculated by UNM and provided on the CD-ROM can be fed to the UNM-KINETICS subroutine, and the reactor thermal power and feedback and total reactivities calculated by MELCOR-H2 / UNM_KINETICS can be compared with the values provided on the CD-ROM.

The transient calculations of the presented test case were obtained using a fixed time step size of Δt = 1 s and an implicit/explicit discretization parameter, θ = 0.50. A sensitivity analysis showed that for the present slow transient of interest, this solution was of very high accuracy. Different adaptive time step algorithms were tested, and their accuracy was evaluated by comparison with the above solution.

An adaptive step size technique similar to that proposed by Keepin and Cox (1960) for solving the 6-point kinetics equations was used in the present, coupled UNM-ISNPS thermal-hydraulics/UNM_KINETICS model. Because peaks in reactor thermal power and temperature do not occur simultaneously (see Figures 5-8 through 5-10), the quantity chosen to evaluate the suitability of the time step size must include the relative change in reactor's thermal power and that in fuel average temperature, both:

$$\delta = \mathbf{DMAX1}\left(\frac{\left| P_{n+1} - P_n \right|}{P_n},\ 10 \times \frac{\left| (\overline{T}_f)_{n+1} - (\overline{T}_f)_n \right|}{(\overline{T}_f)_n} \right), \tag{5-33}$$

where the subscript n refers to the value at old (previous) time, and the subscript (n+1) refers to the value calculated at the new time. The dimensionless parameter δ was chosen as an indicator to dictate the change in the time step size, Δt. After the new-time solution has been computed using the previous time step size, the following tests are performed:

(a) If $\delta < F_1$, the time step size is increased by a factor $\gamma > 1$;

(b) If $F_1 \le \delta < F_2$, the solution is advanced and the time step remains unchanged. This is the preferred range of change in thermal power and temperature; and

(c) If $F_2 \le \delta$, the time step size is decreased by the factor $\gamma > 1$.

In addition to these conditions, the model imposes minimum and maximum values of the time step size, which should not be exceeded. A factor $\gamma = 1.2$ was selected, and provided good results.

The transient test case described earlier was calculated using the following parameters:

(a) $F_1 = 0.05\%$, $F_2 = 0.5\%$, and $\theta = 0.5$;

(b) $F_1 = 0.10\%$, $F_2 = 1.0\%$, and $\theta = 0.5$;

(c) $F_1 = 0.05\%$, $F_2 = 0.5\%$, and $\theta = 0.0$;

(d) $F_1 = 0.10\%$, $F_2 = 1.0\%$, and $\theta = 0.0$;

Comparison with the solution obtained with $\Delta t = 1$ s, and an implicit/explicit discretization parameter, $\theta = 0.50$, showed that the maximum error in the calculated reactor thermal power over the 2000 s long transient was 0.1 MW, 0.3 MW, 0.6 MW, and 0.6 MW for cases (a), (b), (c), and (d), respectively (the time step size was always > 1 s in all these cases). These results show that the MELCOR-H2 thermal-hydraulics model and the 6-point kinetics model (UNM_KINETICS) can be decoupled ($\theta = 0.0$) with minimum error for the presented test case. A fiducial factor F_2 of 0.5% or 1% also gives reasonable accuracy. The parameters of case (c) can then be used initially in MELCOR-H2 to simplify and facilitate the implementation of the UNM_KINETICS subroutine, so that transient calculations can be developed quickly with the new model. When using a parameter value of $\theta = 0.0$, the MELCOR-H2 thermal-hydraulics model of the gas-cooled reactor is effectively decoupled from the 6-point kinetics model. This means that no internal iterations are performed to resolve the dependence of the total reactivity on the advanced-time fuel and graphite temperatures, and that the temperature-feedback and control reactivities are accounted for explicitly in the model (since they are calculated at the previous time step).

5.10 Interactive Graphical User Interface

MELCOR-H2 computes the system's transient variables and displays them on the screen in real time using a GUI. Figure 5-11 shows the sulfuric acid decomposition, hydrogen production, secondary system pressure, and the pressure of the sulfuric acid as it is decomposed. If desired, the analyst/designer may change input during a simulation to see how the calculated parameters respond (see green arrows in Figure 5-12). The figure shows the effect of changing the convective heat transfer coefficient after the calculation had started.

The GUI enables the MELCOR-H2 user to efficiently view the key nuclear/hydrogen plant variables, and to quickly determine their impact on overall hydrogen and electrical output.

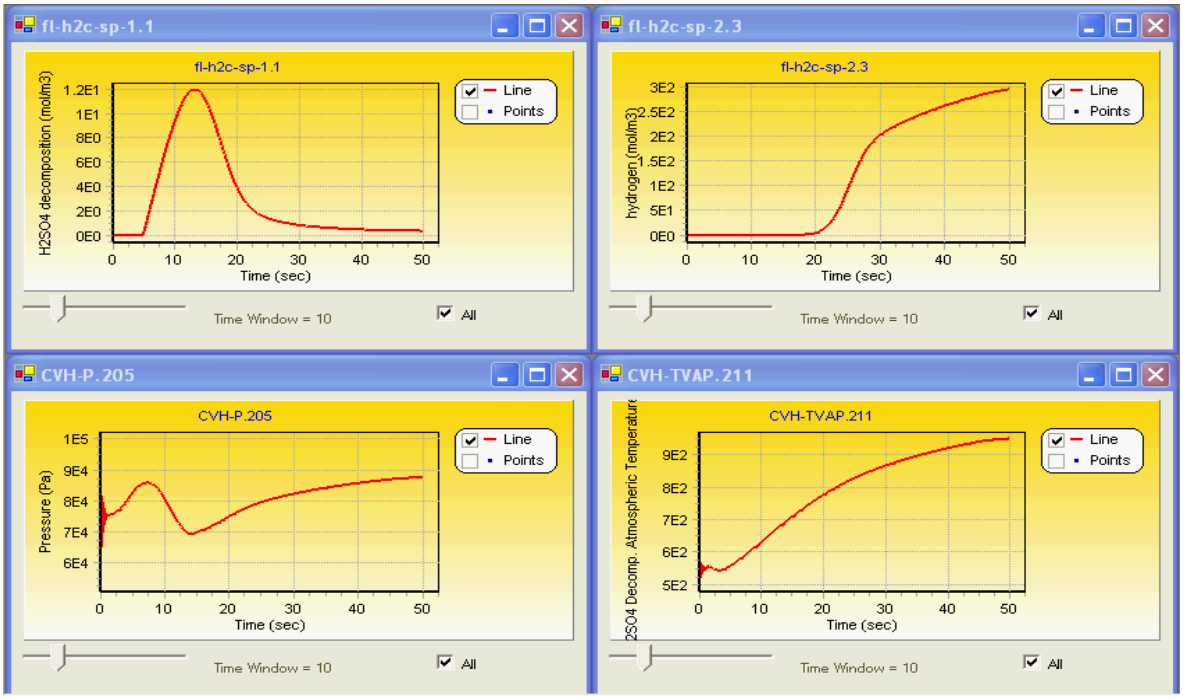

Figure 5-11. GUI output of a nuclear/hydrogen plant.

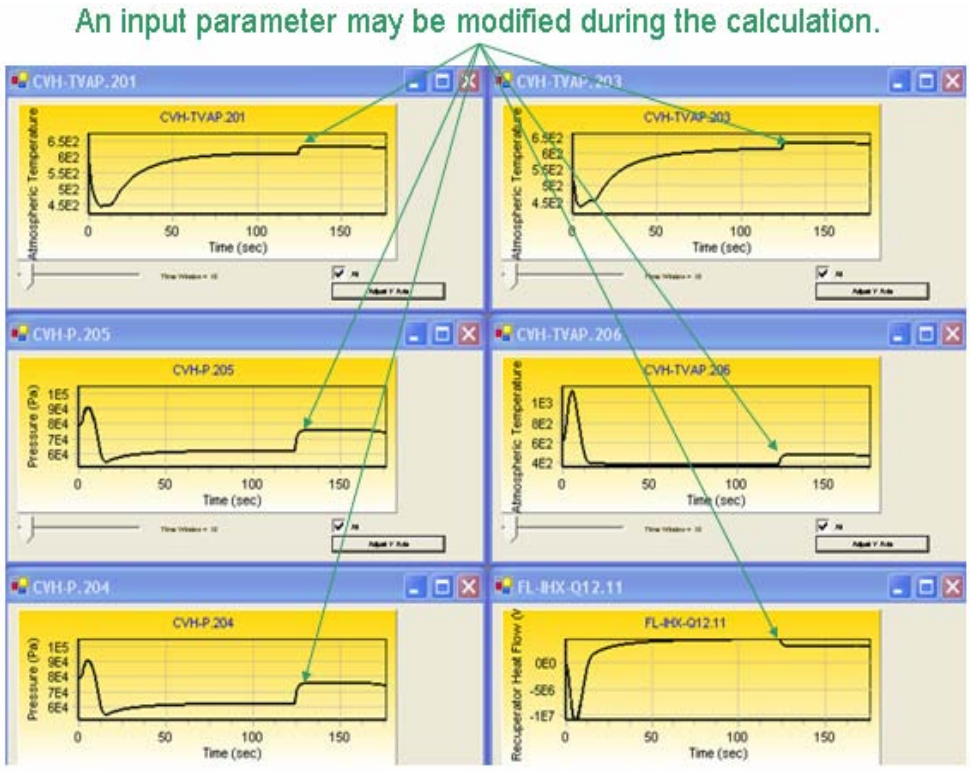

Figure 5-12. Modification of a system parameter during the transient simulation.

5.11 Chapter 5 References

Baker, G. A., Jr., 1975, *Essentials of Padé Approximants*, Academic Press, Inc., New York, NY, Chapter 1, pp. 3-12, and Chapter 14, pp. 193-205.

Gauntt, R. O., R. K. Cole, C. M. Erickson, R. G. Gido, R. D. Gasser, S. B. Rodriguez, and M. F. Young, 2000, *MELCOR Computer Code Manuals*, Vol. 2: Reference Manuals, Version 1.8.5, May 2000, Report No. NUREG/CR-6119, Vol. 2, Rev. 2, SAND2000-2417/2, Sandia National Laboratories, Albuquerque, NM, October 2000.

Gill, S., 1951, A Process for the Step-by-Step Integration of Differential Equations in an Automatic Digital Computing Machine, *Proceedings of the Cambridge Philosophical Society*, Cambridge University Press, Vol. 47, pp. 96-108.

Goldstein R., and L. M. Shotkin, 1969, Use of the Prompt-Jump Approximation in Fast-Reactor Kinetics, *Nuclear Science and Engineering*, **38**, pp. 94-103.

Golub, G. H., and C. F. van Loan, 1984, *Matrix Computations*, 2nd Edition, The Johns Hopkins University Press, Baltimore and London.

Greenspan, H., C. N. Kelber and D. Okrent, Eds., 1968, *Computing Methods in Reactor Physics*, Gordon and Breach Science Publishers, Inc., New York, NY, Chapter 6, pp. 444-506.

IAEA, 2001, *Current Status and Future Development of Modular High Temperature Gas Cooled Reactor Technology*, International Atomic Energy Agency, Vienna, Austria, Report No. IAEA-TECDOC-1198, February 2001.

Keepin, G. R., and C. W. Cox, 1960, General Solution of the Reactor Kinetic Equations, *Nuclear Science and Engineering*, **8**, pp. 670-690.

Keepin, G. R., 1965, *Physics of Nuclear Kinetics*, Addison-Wesley Publishing Company, Inc., Reading, Massachusetts, Chapter 4, pp. 73-129.

MacDonald, P. E., J. W. Sterbentz, R. L. Sant, P. D. Bayless, R. R. Schultz, H. D. Gougar, R. L. Moore, A. M. Ougouag and W. K. Terry, 2003, *NGNP Preliminary Point Design – Results of the Initial Neutronics and Thermal-Hydraulic Assessments during FY-2003*, Idaho National Engineering and Environmental Laboratory, Idaho Falls, Idaho, Report No. INEEL/EXT-03-00870, Revision 1, September 2003.

MacDonald, P. E., P. D. Bayless, H. D. Gougar, R. L. Moore, A. M. Ougouag, R. L. Sant, J. W. Sterbentz, and W. K. Terry, 2004, The Next Generation Nuclear Plant – Insights Gained from the INEEL Point Design Studies, *2004 International Congress on Advances in Nuclear Power Plants (ICAPP '04), Embedded International Topical Meeting, 2004 American Nuclear Society Annual Meeting*, held in Pittsburgh, PA, June 13-14, 2004, Paper 3405.

MatLab, 2004, "MATLAB® 7.0.1," http://www.mathworks.com/products/matlab, accessed September 2004.

Porsching, T. A., 1966, Numerical Solution of the Reactor Kinetics Equations by Approximate Exponentials, *Nuclear Science and Engineering*, **25**, pp. 183-188.

Rodriguez, S. B., R. O. Gauntt, R. Cole, et al., 2005, Development of Design and Simulation Model and Safety Study of Large-Scale Hydrogen Production Using Nuclear Power – FY05 Final Letter Report, Sandia National Laboratories, Albuquerque, NM.

Shampine, L. F. and M. W. Reichelt, 1997, The MATLAB ODE Suite, *SIAM Journal on Scientific Computing*, **18** (1), pp. 1-22.

Shampine, L. F., M. W. Reichelt, and J. A. Kierzenka, 1999, Solving Index–I DAEs in MATLAB and Simulink, *SIAM Review*, **41** (3), pp. 538-552.

Simulink, 2004, "SIMULINK® 6.1," http://www.mathworks.com/products/simulink, accessed September 2004.

Van Loan, C., 1977, "On the Limitation and Application of Padé Approximation to the Matrix Exponential," in *Padé and Rational Approximation – Theory and Applications*, E. B. Saff and R. S. Varga, Eds., Academic Press, Inc., New York, NY, 1977, pp. 439-448.

Ward, R. C., 1977, Statistical Roundoff Error Analysis of a Padé Algorithm for Computing the Matrix Exponential, in *Padé and Rational Approximation – Theory and Applications*, E. B. Saff and R. S. Varga, Eds., Academic Press, Inc., New York, NY, 1977, pp. 449-460.

APPENDIX A: MELCOR-H2 BENCHMARKING OF THE SNL TRANSIENT SULFURIC ACID DECOMPOSITION EXPERIMENTS

Sal B. Rodriguez[1], David Louie[2], Randall O. Gauntt[1], Fred Gelbard[1], Paul Pickard[1], Randy Cole[1], Katherine McFadden[1], Tom Drennen[1], Billy Martin[1], Louis Archuleta[2], Shripad T. Revankar[3], Karen Vierow[4], Mohamed El-Genk[5], and Jean Michel Tournier[5]
P.O. Box 5800, MS 0748, Albuquerque, NM 87185-0748, sbrodri@sandia.gov
Sandia National Laboratories[1]
OMICRON Safety and Risk [2]
Purdue University[3]
University of Texas A & M[4]
University of New Mexico[5]

Abstract

MELCOR is a world-renowned nuclear reactor safety analysis code that is used to simulate both light water and gas-cooled reactors. MELCOR-H2 is an extension of MELCOR that can model detailed nuclear reactors that are fully coupled with modular secondary-system components and the sulfur iodine (SI) thermochemical cycle for the generation of hydrogen and electricity. The models are applicable to both steady state and transient calculations. Previous work has shown that the hydrogen generation rate calculated by MELCOR-H2 for the SI cycle was within the expected theoretical yield, thus providing a macroscopic confirmation that MELCOR-H2's computational approach is reasonable. However, in order to better quantify its adequacy, benchmarking of the code with experimental data is required.

Sulfuric acid decomposition experiments were conducted during late 2006 at Sandia National Laboratories, and MELCOR-H2 was used to simulate them. We developed an input deck based on the experiment's geometry, as well as the initial and boundary conditions, and then proceeded to compare the experimental acid conversion efficiency and SO_2 production data with the code output. The comparison showed that the simulation output was typically within less than 10% of experimental data, and that key experimental data trends such as acid conversion efficiency, molar acid flow rate, and solution mole % were computed adequately by the MELCOR-H2.

[a]Sandia is a multiprogram laboratory operated by Sandia Corporation, a Lockheed Martin Company, for the United States Department of Energy's National Nuclear Security Administration under Contract DE-AC04-94AL85000.

Introduction

Large-scale production of hydrogen through nuclear/thermochemical plants is the subject of much recent interest. This is particularly so of the sulfur iodine (SI) cycle and the secondary systems interconnected to it [1-3]. Other important thermochemical cycles such as the Westinghouse Hybrid Sulfur (HyS) and adiabatic UT-3 cycles are being considered [1, 3]. It is significant that both the SI and Westinghouse cycles share the same sulfur chemistry, so advances in one naturally lead to advances in the other. A literature search shows many recent efforts to model SI and HyS chemistry that is coupled to secondary systems, but these employ primarily steady-state models, and/or are not coupled to a fully-detailed nuclear plant [1-4]. Fully-coupled, dynamic modeling is important, as current research shows that there is a complex, dynamic interdependent behavior of the subsystems, and this affects hydrogen and electrical output, safety, and overall plant behavior.

MELCOR has been used to adequately simulate numerous types of nuclear reactors, including high-temperature gas-cooled reactors [5-7]. MELCOR-H2 is an extended version of MELCOR designed to fully couple detailed models of nuclear reactors with modular secondary-system components and thermochemical cycles for the generation of hydrogen and electricity [8-13].

Whereas previous MELCOR-H2 work has shown that it can yield hydrogen in amounts corresponding to expected theoretical yields [14, 15], the next step is to show that the MELCOR-H2 SI transient chemistry models can adequately simulate experimental data. To that effect, we simulated the sulfur decomposition experiments that were conducted at Sandia National Laboratories (SNL) recently [16, 17]. This paper briefly discusses the experiments, and then continues with a description of the MELCOR-H2 models, how the simulations were conducted, and the results of the simulations.

Brief Experiment Description

SNL is currently advancing the production of hydrogen for the SI cycle by investigating the decomposition of sulfuric acid. In the first series of experiments, a half scale decomposer experiment was fabricated. It consists of a bayonet that is made up of three vertical concentric silicon carbide (SiC) tubes, as shown schematically in Figures A-1 and A-2. The cross sectional dimensions are shown; the length of the tube was 27”. Ceramic materials such as SiC were used to construct the experiment because of its resistance to corrosion by acid. However, the tubing is difficult to fabricate and brittle. This makes it somewhat difficult to add thermocouples and other instruments in order to acquire more detailed data for numerical analysis.

The acid solution entered at the bottom of the bayonet in the Teflon manifold and flowed up along the outer annulus of the tubes. The inlet temperature was set at 30 ºC. While the liquid acid solution was flowing up, the recuperation of the heat from the downward flow of the outgoing products and un-reacted acid solution and the external electric heater were sufficient to bring the upward flow of the acid solution to boil and to dissociate the sulfuric acid into sulfur trioxide and water vapor. The temperature of the incoming solution reached about 850 ºC, and thus became a superheated acid vapor, before entering the catalyst bed.

The catalyst was about a third of the length of the entire assembly, was made of a quartz baffle that held up the rows of the catalyst platinum pellets, and had a porosity of 50%. The sulfur trioxide was decomposed into sulfur dioxide and oxygen gases as it flowed through the catalyst. Any un-reacted sulfur trioxide combined with water to form back the acid while the flow was cooled down by the recuperation process in the inner annulus of the tubes. The expected exit temperature of the products and un-reacted acid solution was about 180 ºC.

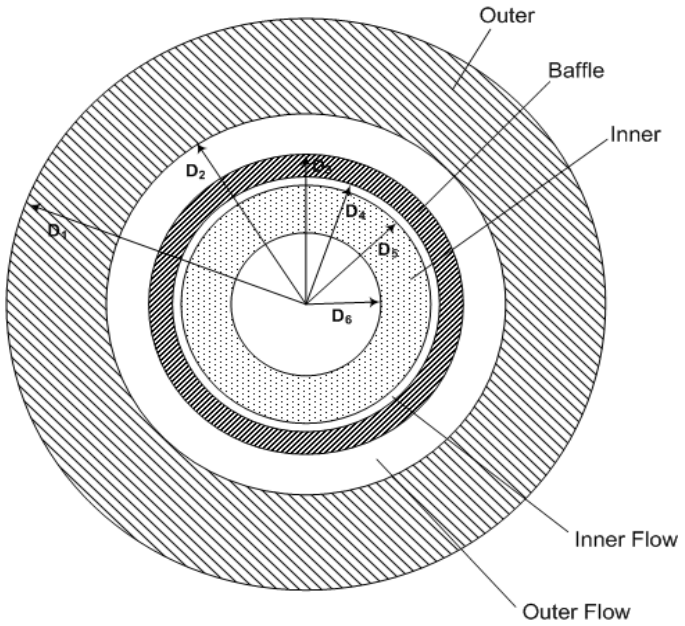

Outer:	OD	38.1 mm (D_1)
	ID	25.4 mm (D_2)
Baffle:	OD	20 mm (D_3)
	ID	17 mm (D_4)
Inner:	OD	15.875 mm (D_5)
	ID	9.525 mm (D_6)

Outer Flow Annulus	$D_{o1} = D_2$
	$D_{i1} = D_3$
Inner Flow Annulus	$D_{o2} = D_4$
	$D_{i2} = D_5$

Figure A-1. Dimensions for the bayonet section.

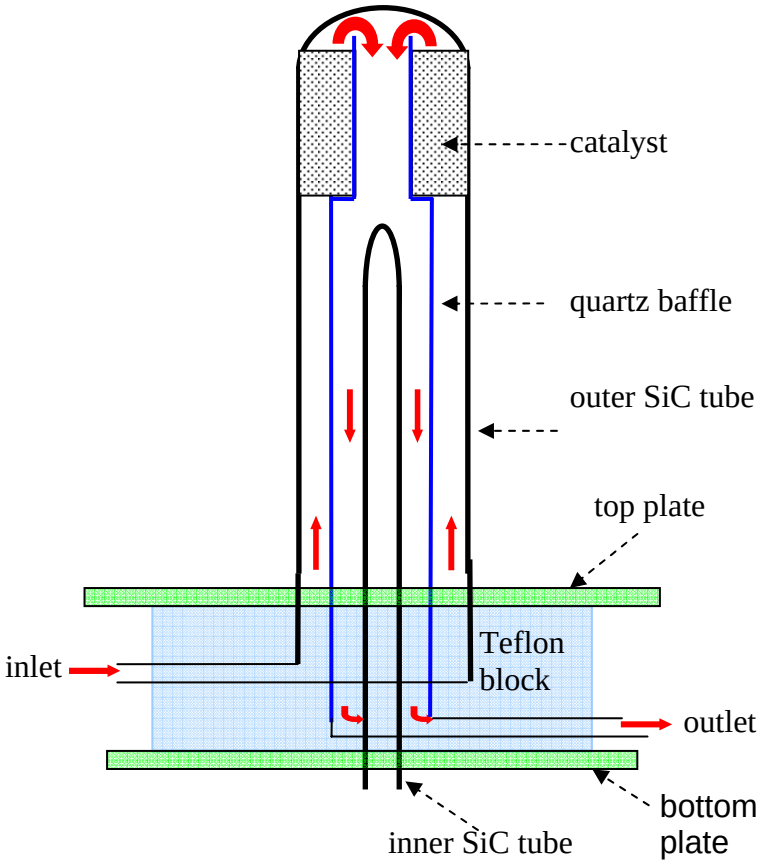

Figure A-2. Bayonet schematic.

Based on the dimension of the tubes in Figure A-1, the upward flow volume of the bayonet was about 123 cm^3, and the downward flow volume was about 43.6 cm^3. Thus, the total flow volume in the bayonet was about 166.6 cm^3.

A series of test runs for the half scale experiment were conducted at 850 ºC, ambient pressure, with inlet acid solutions of 19, 38, 42, and 53 mole %. Note that the data for 53 mole % were not simulated, as they appeared to be atypical from the 19, 38, and 42 mole % experiments; more investigation is needed to determine what variables may have contributed to such behavior. A wide range of solution molar rates were considered, and can be found in references [16, 17]. A more thorough description of the experiment is outside the scope of this paper; however, interested readers are referred to references [16, 17].

Modeling

The chemical reaction for the decomposition of the sulfuric acid is given below:

$$H_2SO_4 \Rightarrow SO_2 + \tfrac{1}{2}O_2 + H_2O \qquad \text{(A-1)}$$

Equation (A-1) considers the stoichiometric reaction because 1 mole of H_2SO_4 will yield 1 mole of SO_2, a half mole of O_2, and 1 mole of H_2O. There are two principle reactions that contribute to Equation (A-1):

$$H_2SO_4 \Leftrightarrow SO_3 + H_2O \tag{A-2}$$

The dissociation of H_2SO_4 as shown in Equation (A-2) takes place above 337 °C. If the temperature decreased below this value, the formation of H_2SO_4 from SO_3 and H_2O will take place. In most cases, this reaction occurs instantaneously. If the temperature continued to rise, and with the help of the catalyst (in a catalyst bed), the decomposition of SO_3 will occur:

$$SO_3 \Rightarrow SO_2 + \tfrac{1}{2}O_2 \tag{A-3}$$

Once the SO_3 decomposes as shown in Equation (3), the reaction is usually irreversible. The desired reaction temperature is about 850 °C, which would yield a high conversion efficiency. Thus, the determining reaction for the decomposition of the sulfuric acid depends on Equation (A-3). The rate constant for Equation (A-3) is usually given in the Arrhenius form as given below. MELCOR-H2 version 1 models the decomposition of H_2SO_4, using the reaction rate constant, which is given as follows,

$$k = A \cdot e^{\frac{-E}{R \cdot T}} \tag{A-4}$$

where A is a pre-exponential or frequency factor (s^{-1}), E is the activation energy (J/mole), R is the gas constant (8.314 J/mole-K), and T is the reaction temperature (K). E is given as 7.31×10^4 J/mole-K. The value of A is taken to be 6.8×10^4 s^{-1}, which is based on the decomposition rate of SO_3 into SO_2 and O_2, and with the assumption of instantaneous conversion of H_2SO_4 to H_2O and SO_3 [18]. Thus the efficiency for this conversion is simply given by the following equation:

$$\eta = 100\% \times (1 - e^{-k \cdot t_r}) \tag{A-5}$$

where η is the efficiency (%), k is given in Equation (A-4), and t_r is the residence time (s) of the acid that contacts the catalyst bed where the decomposition is promoted. The equations show that the reaction rate is strongly dependent on the reaction temperature—the higher the reaction temperature, the higher the conversion efficiency.

To simulate the half scale bayonet experiment, MELCOR-H2 was modified to include a model for a flow system of the chemical species, rather than using single point "chemistry nodes". The principal equations for modeling this experiment are briefly described below.

For a given inlet acid solution flow rate, $\dot{M}_{inlet}$ with f_1 (the mole fraction of H_2SO_4), the H_2O and acid inlet flow rate are given, respectively, as:

$$\dot{M}_{H_2O} = \dot{M}_{inlet}(1\text{-}f_1) \tag{A-6}$$

$$\dot{M}_{acid} = \dot{M}_{inlet} \times f_1 \tag{A-7}$$

Let $M_{acid,r}$ be the number of moles of acid actually decomposed, and according to Equation (A-1), the number of moles for the products is given as

$$M_{SO_2} = M_{acid,r} \cdot 1$$

$$M_{O_2} = M_{acid,r} \cdot 0.5 \qquad \text{(A-8)}$$

$$M_{H_2O} = M_{acid,r} \cdot 1$$

Thus, for each mole of H_2SO_4 that is decomposed, 2½ moles of products are created. The conversion efficiency (%), is defined as

$$\eta_{acid} = \frac{M_{acid,r}}{f_1 \times \dot{M}_{inlet} \times t_r} \times 100\% \qquad \text{(A-9)}$$

Note that both Equations (A-5) and (A-9) calculate the conversion efficiency. When the residence time t_r is known, the amount of acid decomposed can be calculated easily for a given temperature.

Once the amount of products is calculated, the outlet flow rate of the products, including any un-reacted acid is given by the following relations:

$$\dot{M}_{acid,unreacted} = \dot{M}_{acid} \times (1-\eta_{acid}) \qquad \text{(A-10)}$$

$$\dot{M}_{SO_2} = \dot{M}_{acid} \times \eta_{acid} \qquad \text{(A-11)}$$

$$\dot{M}_{O_2} = \dot{M}_{acid} \times \eta_{acid} \times \frac{1}{2} \qquad \text{(A-12)}$$

$$\dot{M}_{H_2O}^{(outlet)} = \dot{M}_{inlet}(1-f_1) + \dot{M}_{acid} \times \eta_{acid} \qquad \text{(A-13)}$$

Note that Equation (A-13) includes both inlet H_2O and the amount of H_2O produced. Thus the total outlet flow rate is the sum of Equations (A-10) through (A-13).

In terms of energy, the upward flow of the inlet acid solution will heat up from 30 ºC to the reaction temperature (maximum of 850 ºC). Both the sensible heat for the acid and water were calculated, starting from their liquid state to the final gas state. At the catalyst location, an additional energy term is estimated for the reaction (dissociation energy). As the reaction products, the un-reacted acid, and water vapor flow downward to the exit, the recuperation process will transfer heat from the incoming fluid as shown in Figure A-2. This transfer is also captured in MELCOR-H2.

Note that the primary goal for the SNL experiment was to advance the technology for producing larger quantities of hydrogen, as opposed to providing a fully-instrumented experiment for the purpose of code validation. As such, then, the full nature of the fluid entering the catalyst was

not recorded experimentally; in particular, it was unclear if it was completely gaseous, or if it consisted of two phases (liquid and gas). This information was required in order to better estimate the fluid t_r as it traveled through the catalyst. We decided to use the Ergun equation as a first-cut approximation [19],

$$\left[\frac{(P_0-P_L)\rho}{G_0^2}\right]\left(\frac{D_p}{L}\right)\left(\frac{\varepsilon^3}{1-\varepsilon}\right) = 150\left(\frac{1-\varepsilon}{D_p G_0/\mu}\right)+\frac{7}{4}, \qquad \text{(A-14)}$$

where P is the pressure at a given position, ρ is the density, D_p is the pellet diameter, G_0 is the mass flux, L is the catalyst length, μ is the fluid viscosity, and ε is the catalyst porosity. By employing the Ergun equation, we obtained an approximate value for t_r, which we then corroborated by running a MELCOR-H2 simulation and then backtracking t_r. The two were found to be consistent. Then, once t_r was estimated for a given run, t_r for the remaining experimental runs was prorated as follows,

$$t_{r,new} = t_{r,max}\left(\frac{\dot{M}_{max}}{\dot{M}_{new}}\right) \qquad \text{(A-15)}$$

where the subscript "max" indicates that the molar flow rate was the maximum used in the experiment and t_r corresponded to that molar flow rate. This is a first-cut approximation to t_r, but sufficient, given the amount of experimental data that was available. In short, the simulation of each experimental run employed a unique t_r because each was conducted at a different molar flow rate.

For each experimental run, the measured inlet acid solution in mole % of H_2SO_4 was included in the input deck. Beginning with MELCOR-H2 version 1, the code permits the modeling of the flow system, such as the experiment described above. Thus, the required input for two chemical species was needed: H_2SO_4, and H_2O. For a given acid inlet flow rate ($\dot{M}_{H_2SO_4}$), the corresponding water component flow rate ($\dot{M}_{H_2O}$) in the acid solution was computed according to the following equation:

$$\dot{M}_{H_2O} = \frac{\dot{M}_{H_2SO_4}\times(1-f_1)}{f_1} \qquad \text{(A-16)}$$

where f_1 is the mole fraction of the acid solution. For example, suppose there is an acid inlet flow rate of 3.1 mole/hr (8.61×10^{-4} mole/s), than a 38 mole% solution has 5.06 mole/hr of water (1.40×10^{-3} mole/s). These flow rates are included as input, along with the temperatures of the experiment. The inlet temperature is taken to be 30 °C. The reaction temperature was input for the desired temperature of 850 °C, although the code recalculates the reaction temperature based on the heat transfer characteristics and flow rates. The outlet temperature was taken to be at 180 °C. The volume of the bayonet was not needed, since the rate constant for this reaction was independent of volume. If desired, this volume may be used as part of an alternative estimation for t_r. Additional inputs are required to model the outlet flow conditions, beside the outlet

temperature given above. Because this is a flow system with no accumulation, any material that goes in should come out from the bayonet. Therefore, the outlet flow rates of the reactants and products were modeled according to the given inlet condition, and the assumption of 100% reaction completion: that is, for 1 mole of H_2SO_4 decomposed, there should be 1 mole of SO_2, 1 mole of H_2O, and 0.5 mole of O_2. Then, for example, a stoichiometric balance for 3.1 mole/hr of H_2SO_4 flowing in should result in the production of 3.1 mole/hr of SO_2, 3.1 mole/hr of H_2O, and 1.55 mole/hr for O_2. For the total H_2O flow out (sum of what is flowing in and what is produced), the molar flow rate is 8.16 mole/hr (3.1 mole/hr production + 5.06 mole/hr inlet).

Whereas MELCOR-H2 can simulate both sulfuric and hydriodic (HI) acid decomposition, as well as the Bunsen reaction, only the sulfuric acid section was modeled, as the SNL experiments did not include the latter two. In the future, we will simulate those sections, as experimental data becomes available.

The simulations were run for 100 transient seconds, by which time the calculation had reached an asymptotic state. The simulations required only about 4 minutes of CPU time to run to completion, and proved to be robust, as no calculations aborted once a converged time step was used. The time step chosen was 0.001 s, which was sufficiently small such that temporal convergence was reached.

Comparison Between Experimental Data and Code Simulations

As shown in Table A-3, the simulation output compared favorably with data for the nine simulations—the code output was within 1 to 14% error, with eight of the nine showing less than 10% error. Because the experimental data has not yet been released, and because there is an ongoing analysis of the data, this paper includes the normalized SO_2 production rates and a comparison between experimental and calculated SO_2 production efficiencies. Nevertheless, these comparisons provide a useful canon by which to gauge MELCOR-H2 performance with the experimental data. Readers interested in the explicit data are referred to the relevant papers [16, 17].

The simulations showed that for a given molar flow rate, the higher the solution mole %, the higher the conversion efficiency. This trend was also reflected in the data, as shown in Table A-3. Additionally, the simulations indicated that the acid conversion efficiency dropped as the molar flow rate increased. This is reasonable because faster molar flow rates should result in shorter fluid t_r within the catalyst, thus decreasing the amount of reaction. An observation of Table A-3 shows that the data also captured this trend.

Finally, Figure A-3 shows the normalized SO_2 production rate, which provides a direct indication of the expected production of H_2. The agreement between the simulations and data is very good.

Table A-3. Comparison Between Experimental Data and Simulation Output

Solution Mole %	Normalized Acid Flow Rate	Conversion Efficiency: Difference Between Experimental Data and MELCOR-H2 Output (%)
19	0.28	3.6
19	0.53	-2.0
19	1.00	-1.6
38	0.26	6.5
38	0.46	6.6
38	0.49	1.6
42	0.27	8.7
42	0.44	0.92
42	0.99	-14.3

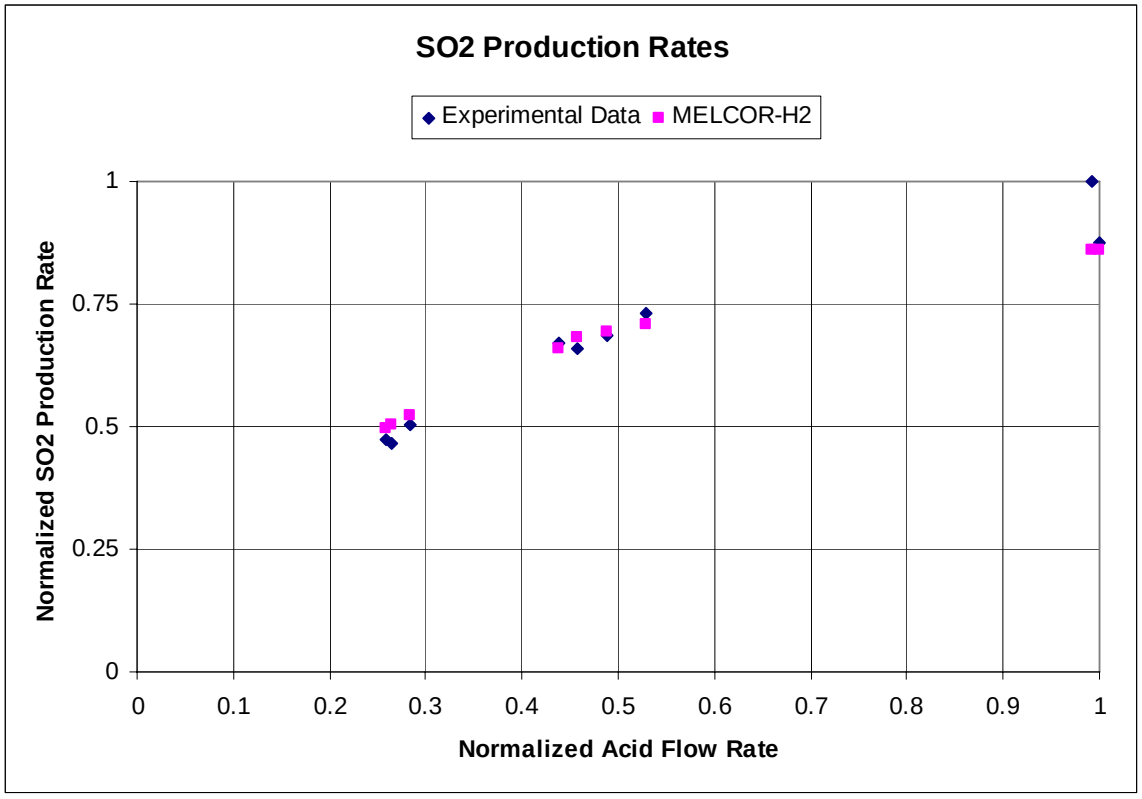

Figure A-3. Normalized experimental and computed SO_2 production rates.

Conclusion

Sulfuric acid decomposition experiments conducted at SNL were simulated using MELCOR-H2. The code output agreed quite well with experimental data. In addition, observed trends in the simulations were reflected by the experimental data; this included the relationship between solution mole % and conversion efficiency, as well as the relationship between molar flow rate and efficiency.

References

1. Brown, L. C., G. E. Besenbruch, R. D. Lentsch, et al., 2003, *High Efficiency Generation of Hydrogen Fuels Using Nuclear Power*, General Atomics, GA-A24285, Rev. 1, December 2003.

2. Nariaki Sakaba, Seiji Kasahara, Hirofumi Ohashi, *et al*, "Hydrogen Production by Thermochemical Water-Splitting IS Process Utilizing Heat from High-Temperature Reactor HTTR." World Hydrogen Energy Conference, Lyon, France (June 2006).

3. Mohamed S. El-Genk and Jean-Michel Tournier, "Thermo-Chemical Generation of Hydrogen Using High Temperature Gas Power Cycle Modeling Recommendation in MELCOR," Institute for Space and Nuclear Power Studies and the Chemical and Nuclear Engineering Department, University of New Mexico (February 2006).

4. Oh, C. H., C. Davis, S. Shermal, et al, "International Nuclear Engineering Research Initiative Project at INL, ANL, and KAERI," ANS Thermal Hydraulics Division Newsletter, Research Briefs (Spring 2006).

5. Gauntt, R. O., J. E. Cash, R. K. Cole, et al, "MELCOR Computer Code Manuals. Vol. 1: Primer and Users' Guide Version 1.8.6," Sandia National Laboratories (September 2005).

6. Hogan, Kevin J., Karen Vierow, Shripad T. Revankar, et al, "Assessment of PBMR Analysis Using the MELCOR Code," ANS 2006 Annual Meeting, Reno, Nevada (June 2006).

7. MacDonald, Philip E., "Advanced Reactor, Fuel Cycle, and Energy Products Workshop for Universitie," http://neri.inel.gov/universities_workshop/proceedings/pdfs/ngnp.pdf, Idaho National Engineering and Environmental Laboratory (March 4-5, 2004).

8. Rodriguez, Sal B., Randall O. Gauntt, Randy Cole, et al, "MELCOR Extensions for Simulation of Modular Power Cycles and Thermochemical Cycles for the Generation of Hydrogen via Nuclear Reactors," World Hydrogen Energy Conference, Lyon, France (June 2006).

9. Rodriguez, Sal B., Randall O. Gauntt, Randy Cole, et al, "Development of Design and Simulation Model and Safety Study of Large-Scale Hydrogen Production Using Nuclear Power," AIChE, Columbus, Ohio (November 2005).

10. Rodriguez, Sal B., Randall O. Gauntt, Randy Cole, et al, "MELCOR Modification for

Large-Scale Hydrogen Production Using Nuclear Thermochemical Cycles," ANS (November 2005).

11. Revankar, Shripad T., Seungmin Oh, Sal Rodriguez, "Simplified Model to Couple SI Cycle to Nuclear Heat Transport System," ANS 2006 Annual Meeting, Reno, Nevada (June 2006).

12. Revankar, Shripad T. and Seungmin Oh, "Simplified Sulfur Iodine Chemical Water Splitting Process and Heat Exchanger Equations for Implementation in MELCOR Interface," Purdue University (December 19, 2005).

13. Louie, David, Sal B. Rodriguez, Randy Cole, et al, "Report on Implementing the SI Chemistry Model into MELCOR for the Sandia Hydrogen Generation Project," Omicron Safety and Risk Technologies (April 17, 2006).

14. Rodriguez, Sal, Randall O. Gauntt, Randy Cole, et al, "MELCOR-H2: A Modular, Generalized Tool for the Dynamic Simulation and Design of Fully-Coupled Nuclear Reactor/Hydrogen Production Plants," 2006 ANS Winter Meeting, Albuquerque, NM.

15. Rodriguez, Sal, Randall O. Gauntt, Randy Cole, et al, "Modeling of a Z-IFE Hydrogen Plant Using MELCOR-H2," November 2006 TOFE, Albuquerque, NM.

16. Gelbard, Fred, Robert Moore, Edward Parma, et al, "Sulfuric Acid Decomposition Experiments for Thermochemical Hydrogen Production from Nuclear Power," 2007 American Nuclear Society Annual Meeting, Boston.

17. Gelbard, Fred, Robert Moore, Edward Parma, et al, "Sulfuric Acid Decomposition Experiments," Sandia National Laboratories, February 2007.

18. Huang, C. and A. T-Raissi, 2005, Analysis of Sulfur-Iodine Thermochemical Cycle for Solar Hydrogen Production. Part I: Decomposition of Sulfuric Acid, *Solar Energy 2005*, 78:632-646.

19. S. Ergun, "Fluid Flow Through Packed Columns," Chem. Eng. Prog., 1952, 48:89-94.

APPENDIX B: PRESSURE LOSS COEFFICIENT IN TURBINE BLADES

Over the past 50 years, a number of turbine mean-line loss models have been described in the open literature. Perhaps the best known and most completely documented model is that of Ainley and Mathieson published in 1951. This model includes correlations for all loss components, i.e., profile losses, secondary losses, trailing edge losses and tip clearance (leakage) losses. It is a testimony to the soundness of the Ainley and Mathieson (AM) approach that it has become the foundation for a number of subsequent refinements, most notably those by Dunham and Came (1970), Kacker and Okapuu (1982), and Benner et al. (2006a and 2006b). The present model capitalizes on the latest refinements proposed by Benner, et al. (2006a and 2006b) for modern, subsonic axial turbines with highly-loaded airfoils. Their model relies heavily on the improvements proposed by Kacker and Okapuu (1982), and on the foundation work of Ainley and Mathieson (1951).

In the following, all parameters (such as Reynolds and Mach numbers) are evaluated using the relative gas flow velocities, unless otherwise specified. The total pressure loss coefficient is the sum of the coefficients for profile losses, secondary losses, trailing edge losses and tip clearance (leakage) losses:

$$Y = (Y_p + Y_s) + Y_{TE} + Y_{TC} \ . \tag{B-1}$$

The major contribution of Benner et al. (2006a and 2006b) has been the description of the profile and the secondary losses in a more physical and accurate way. One of the physically unsatisfactory assumptions done in the previous conventional loss schemes was the uniformity of the loss generated in the airfoil surface boundary layer across the span, which produces erroneous values of the secondary loss component. Benner et al. (2006a and 2006) proposed a new loss scheme, which requires a correlation for the spanwise penetration depth of the passage vortex separation line ($Z_{TE} \leq H/2$) at the trailing edge:

$$(Y_p + Y_s) = (1 - Z_{TE} / H) \times Y'_p + Y'_s \ . \tag{B-2}$$

The profile loss coefficient is an improvement over that by Kacker and Okapuu (1982), based on more recent turbine cascade data (Zhu and Sjolander, 2005):

$$Y'_p = 0.914 \times \left[K_{in} Y'_{p,AM} K_p + Y_{shock} \right] \times \left(\frac{\mathrm{Re}_{2C}}{2 \times 10^5} \right)^{K_{\mathrm{Re}}} , \tag{B-3}$$

where

K_{in} = 0.825 for axial entry nozzles,

K_{in} = 2/3 for reaction blades, and

K_{Re} = - 0.575 for $\mathrm{Re}_{2C} = (\rho_2 W_2 C) / \mu_2 < 2 \times 10^5$.

The Mach number correction factor in Equation (B-3) is calculated as (Kacker and Okapuu 1982):

$$K_p = 1 - K_2 \times (1 - K_1) \tag{B-4a}$$

where

$$K_1 = 1 \text{ for } \mathrm{Ma}_2 \leq 0.2, \tag{B-4b}$$

$$K_1 = 1 - 1.25 \times (Ma_2 - 0.2) \text{ for } \mathrm{Ma}_2 > 0.2 \text{ , and} \tag{B-4c}$$

$$K_2 = (Ma_1 / Ma_2)^2 . \tag{B-4d}$$

The profile loss coefficient, $Y'_{p,AM}$, introduced by Ainley and Mathieson (1951) is an interpolation between the results of two special sets of cascade tests ($\beta_1 = 0$, and $\beta_1 = \phi_2$):

$$Y'_{p,AM} = \left\{ Y_{p,AM}^{(\beta_1=0)} + \left|\frac{\beta_1}{\phi_2}\right| \left(\frac{\beta_1}{\phi_2}\right) \left[Y_{p,AM}^{(\beta_1=\alpha_2)} - Y_{p,AM}^{(\beta_1=0)} \right] \right\} \times \left(\frac{t_{\max} / C}{0.2} \right)^{K_m \beta_1 / \phi_2} \tag{B-5a}$$

where

$$K_m = +1 \quad \text{for } t_{\max} / C \leq 0.2, \tag{B-5b}$$

$$K_m = -1 \quad \text{for } t_{\max} / C > 0.2 \ . \tag{B-5c}$$

The results reported by Ainley and Mathieson (1951) for cascades with $\beta_1 = 0$ and $t_{\max} / C = 0.2$ are well correlated by (see Figure B-1):

$$Y_{p,AM}^{(\beta_1=0)} = 0.13 + \frac{S}{C}\left[A + \frac{S}{C}\left(B + C \times \frac{S}{C} \right) \right], \tag{B-6a}$$

where the coefficients *A*, *B*, and *C* are function of the TE relative gas flow angle:

$$A = -0.275862 - 0.0173298 \times \cos\left(7.49775 \times \phi_2 - 285.4\right), \tag{B-6b}$$

$$\begin{aligned} B = {} & -4.28277 \times 10^{-7} \times \phi_2^4 + 1.11388 \times 10^{-4} \times \phi_2^3 - 1.02971 \times 10^{-2} \times \phi_2^2 \\ & + 0.401733 \times \phi_2 - 5.38018 , \end{aligned} \tag{B-6c}$$

$$\begin{aligned} C = {} & 2.31562 \times 10^{-7} \times \phi_2^4 - 6.25296 \times 10^{-5} \times \phi_2^3 + 5.9553 \times 10^{-3} \times \phi_2^2 \\ & - 0.237718 \times \phi_2 + 3.32301. \end{aligned} \tag{B-6d}$$

The results of Ainley and Mathieson (1951), for a cascade with $\beta_1 = \phi_2$ and $t_{max} / C = 0.2$, are also well correlated by (see Figure B-2):

$$Y_{p,AM}^{(\beta_1=\alpha_2)} = 0.31 + \frac{S}{C}\left[-0.776 + \frac{S}{C}\left(B + C \times \frac{S}{C}\right)\right], \qquad \text{(B-7a)}$$

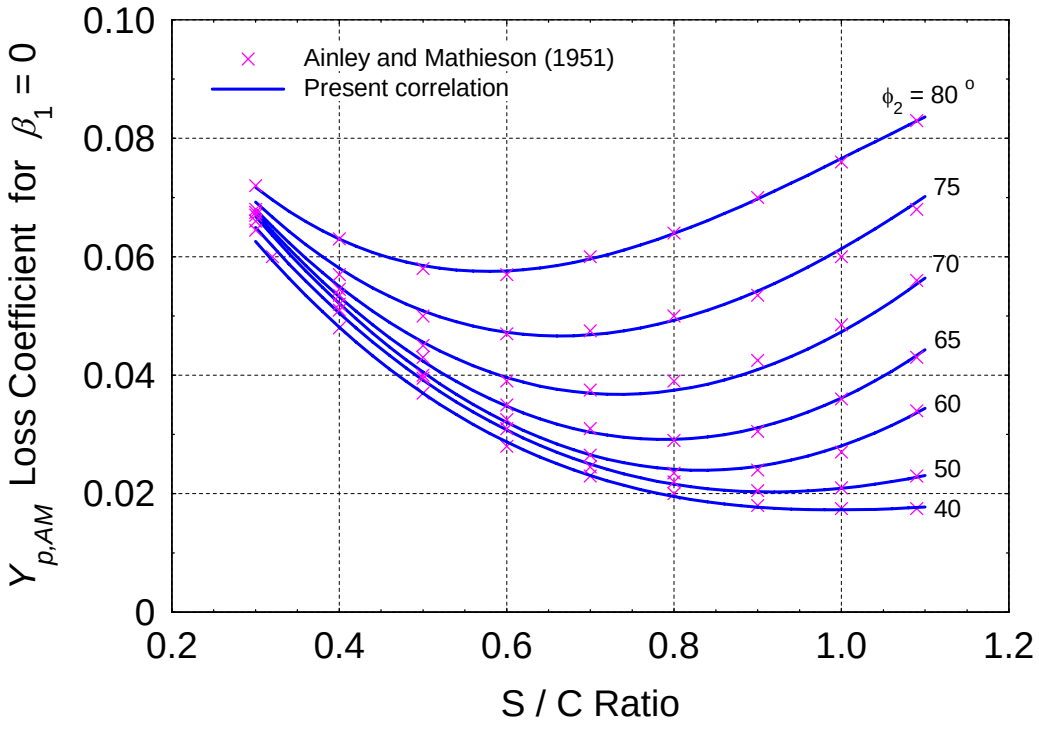

Figure B-1. Profile loss coefficient for $\beta_1 = 0$ and $t_{max}/C = 0.2$ (Ainley and Mathieson, 1951).

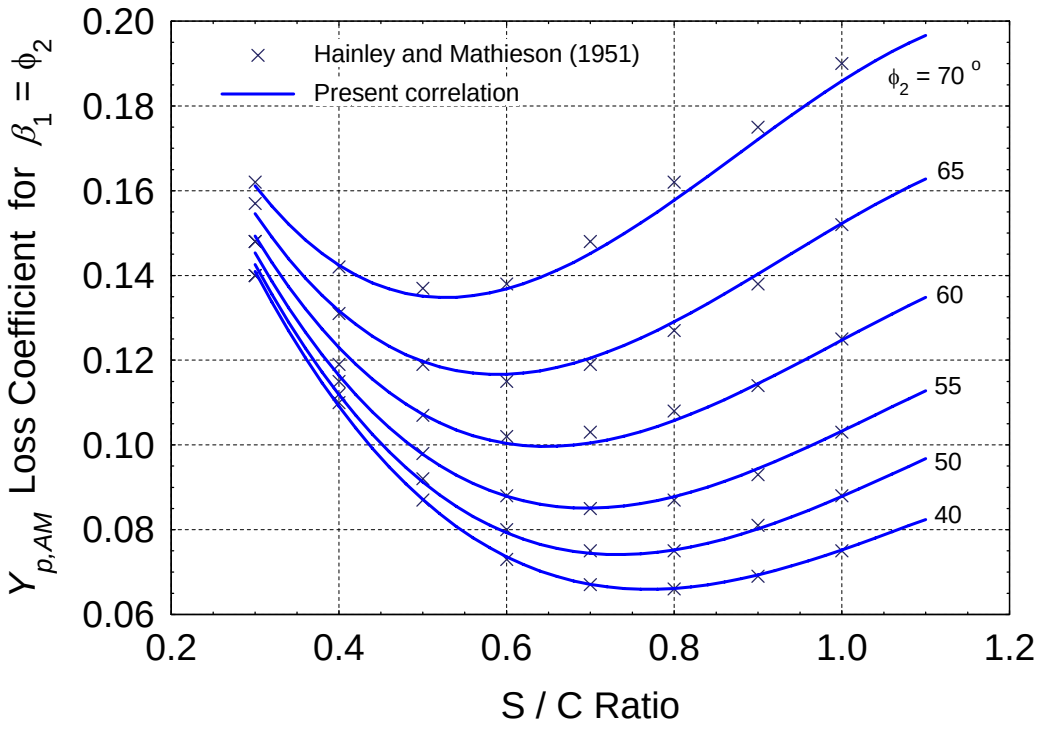

Figure B-2. Profile loss coefficient for $\beta_1 = \phi_2$ and $t_{max}/C = 0.2$ (Ainley and Mathieson, 1951).

where the coefficients B and C are function of the TE relative gas flow angle:

$$B = 3.52951\times10^{-4}\times\phi_2^2 - 2.9723\times10^{-2}\times\phi_2 + 1.40393\ , \tag{B-7b}$$

$$C = -2.31614\times10^{-4}\times\phi_2^2 + 2.00615\times10^{-2}\times\phi_2 - 0.670492\ . \tag{B-7c}$$

These results for cascades with a maximum blade thickness, $t_{max} / C = 0.2$ are corrected for different thicknesses using the last factor on the right side of Equation (B-5a). Note that all the angles in these formulas are in degrees.

Cascade tests in the decades following the publication of the Ainley and Mathieson loss model have revealed that the profile loss coefficient is generally dependent on the Mach number, even in the subsonic flow regime. Compressibility can affect Y_p in two ways, by causing shocks at blade leading edges and by affecting the flow acceleration within blade channels (the correction factor K_p in Equation (B-3)). The shock losses can occur at relatively low average inlet Mach numbers, due to the local flow acceleration adjacent to the highly curved leading edges. These losses, appearing in Equation (B-3), are calculated as (Kacker and Okapuu, 1982):

$$Y_{shock} = \frac{\rho_1 W_1^2}{\rho_2 W_2^2}\times\frac{r_{hub}}{r_{tip}}\times\frac{3}{4}\left(Ma_1^{hub} - 0.4\right)^{1.75} \text{ when } Ma_1^{hub} > 0.4, \tag{B-8a}$$

$$Y_{shock} = 0 \text{ when } Ma_1^{hub} \leq 0.4. \tag{B-8b}$$

Due to the radial variation in the gas flow and pressure, necessary for the flow to be in equilibrium, the incident Mach number, always higher at the hub radius than at the midspan radius, is related to the mean incident Mach number by (Kacker and Okapuu, 1982) (see Figure B-3):

$$\frac{Ma_1^{hub}}{Ma_1} = \begin{cases} 5.71579 \times \left(\frac{r_{hub}}{r_{tip}}\right)^2 - 10.8509 \times \left(\frac{r_{hub}}{r_{tip}}\right) + 6.15292, & \frac{r_{hub}}{r_{tip}} \leq 0.95 \\ 1.0, & \frac{r_{hub}}{r_{tip}} > 0.95 \end{cases} \tag{B-9a}$$

for a reaction stage (rotor), and

$$\frac{Ma_1^{hub}}{Ma_1} = \begin{cases} 4.07224 \times \left(\frac{r_{hub}}{r_{tip}}\right)^2 - 6.64366 \times \left(\frac{r_{hub}}{r_{tip}}\right) + 3.70492, & \frac{r_{hub}}{r_{tip}} \leq 0.8 \\ 1.0, & \frac{r_{hub}}{r_{tip}} > 0.8 \end{cases} \tag{B-9b}$$

for a nozzle (stator).

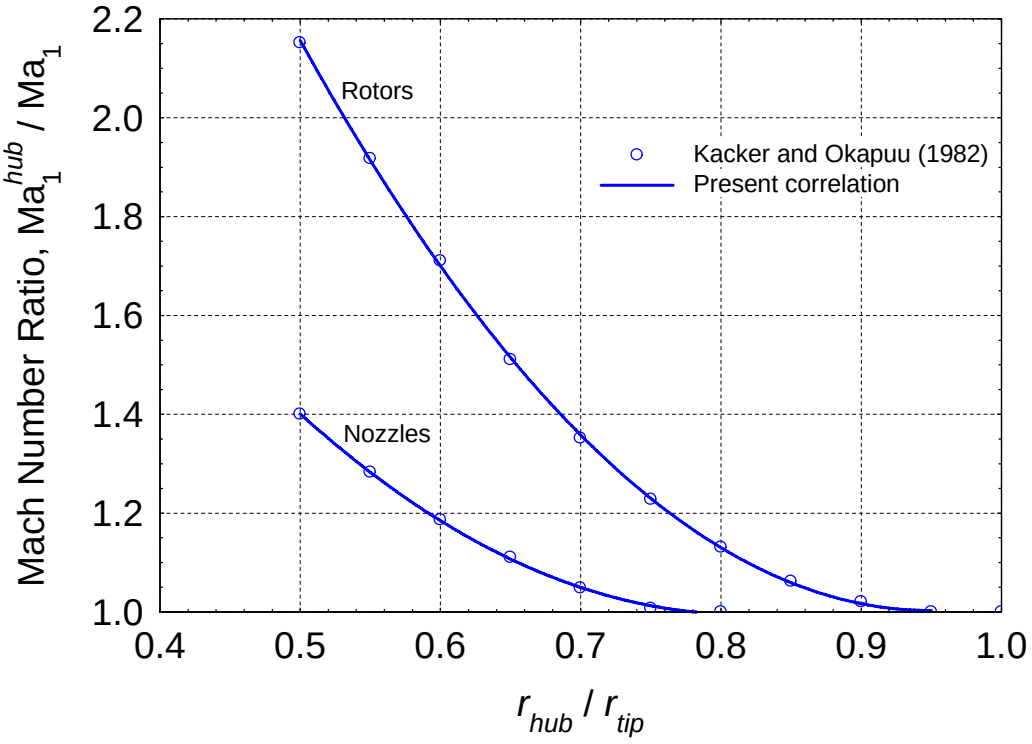

Figure B-3. Inlet mach number ratio for turbine blades (Kacker and Okapuu, 1982).

The spanwise penetration depth (Z_{TE}) of the separation line between the primary and the secondary loss regions, appearing in Equation (B-2), is given by (Benner et al., 2006a):

$$\frac{Z_{TE}}{H} = \frac{0.10(F_t)^{0.79}}{\sqrt{\mathrm{CR}} \times (H/C)^{0.55}} + 32.7\left(\frac{\delta^*}{H}\right)^2 \tag{B-10}$$

where the tangential loading parameter, F_t is given by:

$$F_t = 2\frac{S}{C_x} \times \cos^2(\phi_m) \times \left[\tan(\phi_1) + \tan(\phi_2)\right], \tag{B-11}$$

and the mean velocity vector angle is given by:

$$\tan(\phi_m) = \frac{1}{2}\left[\tan(\phi_1) - \tan(\phi_2)\right] . \tag{B-12}$$

The convergence ratio in Equation (B-10) is given as $\mathrm{CR} = \cos\phi_1 / \cos\phi_2$.

The boundary layer displacement thickness at the inlet endwall, δ^*, in Equation (B-10), is given by (Schlichting, 1979):

$$\delta^* = \frac{\delta}{8} = \frac{0.0463x}{(\rho_1 W_1 x / \mu_1)^{0.2}}, \tag{B-13}$$

assuming a power-law turbulent velocity profile with an exponent of 1/7. The reference length, x, in Equation (B-13) is taken as half the blade axial chord, i.e., $x = C_x / 2$.

The secondary losses coefficient in Equation (B-2) is given by (Benner et al., 2006b):

$$Y_s' = \frac{0.038 + 0.41 \times \tanh(1.2\delta^*/H)}{\sqrt{\cos\Phi} \times \mathrm{CR} \times (H/C)^{0.55} \times (C\cos\phi_2 / C_x)^{0.55}} \text{ when } H/C \le 2.0, \tag{B-14a}$$

$$Y_s' = \frac{0.052 + 0.56 \times \tanh(1.2\delta^*/H)}{\sqrt{\cos\Phi} \times \mathrm{CR} \times (H/C) \times (C\cos\phi_2 / C_x)^{0.55}} \text{ when } H/C > 2.0. \tag{B-14b}$$

Again, all the angles in these formulas are in degrees.

The trailing edge losses, representing the pressure losses due to TE blockage, are expressed in terms of the blockage itself, i.e., the ratio of trailing edge thickness to the throat opening of the cascade itself. Kacker and Okapuu (1982) expressed these losses in terms of the kinetic energy loss coefficient, $\Delta\Phi_{TE}$, for axial entry nozzles ($\beta_1 = 0$) and impulse blades ($\beta_1 = \phi_2$), as shown in Figure B-4. The difference lies in the thicknesses of the profile boundary layers at the trailing edges of blades: impulse blades, with their thick boundary layers, have lower trailing edge losses. The trailing edge thickness contributes significantly to the drag of highly accelerating cascades. For blades other than the two types shown in Figure B-3, the loss coefficient for the

trailing edge kinetic energy losses is interpolated in a manner similar to Equation (B-5a), as (Kacker and Okapuu, 1982):

$$\Delta\Phi_{TE} = \Delta\Phi_{TE}^{(\beta_1=0)} + \left|\frac{\beta_1}{\phi_2}\right|\left(\frac{\beta_1}{\phi_2}\right)\left[\Delta\Phi_{TE}^{(\beta_1=\alpha_2)} - \Delta\Phi_{TE}^{(\beta_1=0)}\right], \tag{B-15a}$$

where

$$\Delta\Phi_{TE}^{(\beta_1=0)} = 0.595628\times\left(\frac{t_{TE}}{O}\right)^2 + 0.122642\times\left(\frac{t_{TE}}{O}\right) - 2.27958\times10^{-3} \tag{B-15b}$$

for an axial entry nozzle (Figure B-4), and

$$\Delta\Phi_{TE}^{(\beta_1=\alpha_2)} = 0.310658\times\left(\frac{t_{TE}}{O}\right)^2 + 0.0656168\times\left(\frac{t_{TE}}{O}\right) - 1.43176\times10^{-3} \tag{B-15c}$$

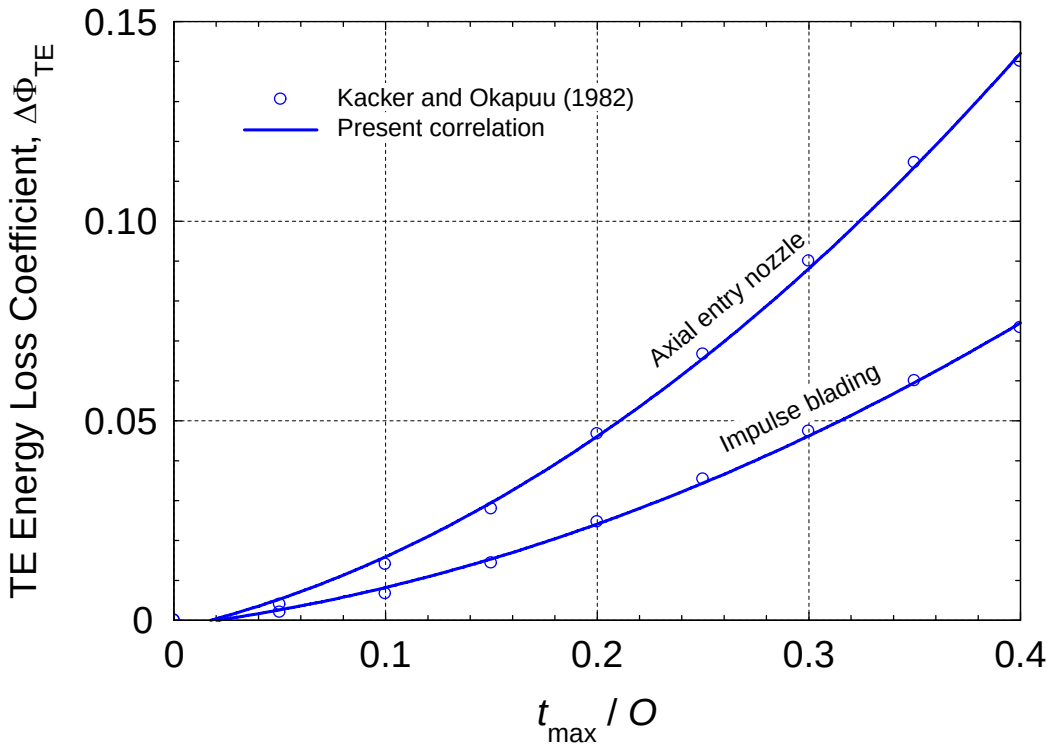

Figure B-4. Loss coefficient for trailing edge losses after Kacker and Okapuu (1982).

for an impulse blading (Figure B-4). The kinetic energy loss coefficient, $\Delta\Phi_{TE}$, is converted to a pressure loss coefficient using the following relationship:

$$Y_{TE} = \frac{\left\{1-\frac{\gamma-1}{2}Ma_2^2\left(\frac{1}{1-\Delta\Phi_{TE}}-1\right)\right\}^{-\gamma/(\gamma-1)}-1}{1-\left(1+\frac{\gamma-1}{2}Ma_2^2\right)^{-\gamma/(\gamma-1)}}. \qquad \text{(B-15d)}$$

Because a turbine operates with some clearance between the tips of the rotor blades and the casing, a fraction of the fluid leaks across the tips, causing a reduction in turbine work output. Yaras and Sjolander (1992) and Matsunuma (2006) reviewed existing methods for predicting the tip-leakage losses in the light of detailed studies conducted recently in turbine cascades. The improved model proposed by Yaras and Sjolander (1992) is used herein, which states:

$$Y_{TC} = Y_{tip} + Y_{gap} \ , \qquad \text{(B-16a)}$$

where the tip leakage losses are given by:

$$Y_{tip} = 1.4K_E \frac{C}{S}\times\frac{\tau}{H}\times\frac{\cos^2\phi_2}{\cos^3\phi_m}\times C_L^{1.5}, \qquad \text{(B-16b)}$$

and the gap losses, contributing a smaller amount to the overall end loss, are given by:

$$Y_{gap} = 0.0049K_G \frac{C}{S}\times\frac{C}{H}\times\frac{\sqrt{C_L}}{\cos\phi_m}. \qquad \text{(B-16c)}$$

The blade lift coefficient, C_L, is given by Ainley and Mathieson (1952) as:

$$C_L = 2\frac{S}{C}\times\cos(\phi_m)\times\left[\tan(\phi_1)+\tan(\phi_2)\right]. \qquad \text{(B-17)}$$

For mid-loaded blades, K_E = 0.5 and K_G = 1.0, and for front- or aft-loaded blades, K_E = 0.566 and K_G = 0.943 (Yaras and Sjolander, 1992).

References

Ainley, D. G., and G. C. R. Mathieson, 1951, *A Method of Performance Estimation for Axial-Flow Turbines*, British Aeronautical Research Council, Reports and Memoranda No. 2974, December 1951.

Benner, M. W., S. A. Sjolander, and S. H. Moustapha, 2006a, An Empirical Prediction Method for Secondary Losses in Turbines – Part I: A New Loss Breakdown Scheme and Penetration Depth Correlation, *Journal of Turbo-machinery*, Vol. 128, pp. 273-280.

Benner, M. W., S. A. Sjolander, and S. H. Moustapha, 2006b, An Empirical Prediction Method for Secondary Losses in Turbines – Part II: A New Secondary Loss Correlation, *Journal of Turbo-machinery,* Vol. 128, pp. 281-291.

Dunham, J., and P. M. Came, 1970, Improvements to the Ainley-Mathieson Method of Turbine Performance Prediction, *Journal of Engineering for Power*, Vol. 92, pp. 252-256.

Kacker, S. C., and U. Okapuu, 1982, A Mean Line Prediction Method for Axial Flow Turbine Efficiency, *Journal of Engineering for Power*, Vol. 104, pp. 111-119 (January 1982).

Lieblein, S., 1959, Loss and Stall Analysis in Compressor Cascades, *Journal of Basic Engineering*, Vol. 81 (September 1959), pp. 387-400.

Matsunuma, T., 2006, Effects of Reynolds Number and Freestream Turbulence on Turbine Tip Clearance Flow, *Journal of Turbo-machinery*, Vol. 128, pp. 166-177.

Schlichting, Hermann, 1979, *Boundary Layer Theory*, 7th Edition, McGraw-Hill Book Company.

Yaras, M. I., and S. A. Sjolander, 1992, Prediction of Tip-Leakage Losses in Axial Turbines, *Journal of Turbo-machinery*, Vol. 114, pp. 204-210.

Zhu, J., and S. A. Sjolander, 2005, Improved Profile Loss and Deviation Correlations for Axial-Turbine Blade Rows, in *Proceedings of GT2005 ASME Turbo Expo 2005: Power for Land, Sea and Air*, held June 6-9, 2005, in Reno-Tahoe, Nevada, USA, American Society of Mechanical Engineers, New York, NY, Paper No. GT2005-69077, pp. 783-792.

APPENDIX C: PRESSURE LOSS COEFFICIENT IN COMPRESSOR BLADES

In the following, all parameters (such as Reynolds and Mach numbers) are evaluated using the relative gas flow velocities, unless otherwise specified. The total pressure loss coefficient is the sum of coefficients for profile losses and tip clearance (leakage) losses:

$$Z = Z_p + Z_{TC}\,. \tag{C-1}$$

The secondary losses and end-wall losses are not accounted for in this work for the axial compressor cascades. In the 1950s, investigators like W. R. Hawthorne and L. H. Smith (Horlock and Denton, 2005) had made substantial progress in understanding fluid mechanics of secondary flow in axial compressors, but attempts to integrate this work into design methods were not very successful. The challenges of modeling secondary and clearance losses were dominant then, and indeed remain so to this day (Horlock and Denton, 2005). In compressors, the classical secondary flow is not as strong as in axial turbines, because the gas turning angle is much smaller in the former. A small gas turning angle is used in compressors to avoid separation of the boundary layer in a positive pressure gradient field.

The profile loss coefficient, Z_p is determined using the approach of Koch and Smith (1976). Their model, an improvement to that proposed by Lieblein (1959), is still regarded as one of the most comprehensive (Wilson, 1984; Boyer and O'Brien, 2003). It accounts for the actual momentum thickness and trailing edge shape factor of the fully turbulent boundary layer, and for the effects of flow area contraction, Reynolds number, and Mach number on these parameters.

Lieblein (1959) had shown that the losses around the blade profile appear as a boundary-layer momentum thickness, θ_{TE}, at the trailing edge, and in the wake, θ_2 ($\theta_2 > \theta_{TE}$ in highly loaded blades because there is a mixing loss as the suction-surface and pressure-surface boundary layers join to form the wake). Leiblein (1959) also showed that as the aerodynamic loading on a compressor blade increased, the diffusion on the suction surface increased, but that on the pressure surface stayed approximately constant. This prompted this investigator to define an "equivalent diffusion ratio" D_{eq}, as:

$$D_{eq} = \frac{\text{Peak relative velocity on the suction surface}}{\text{Outlet relative velocity}, W_2} > 1\,, \tag{C-2}$$

and to propose a correlation for this ratio, as a function of blade solidity and inlet and outlet flow angles ϕ_1 and ϕ_2. Koch and Smith (1976) introduced additional factors correlating the airfoil maximum thickness ratio, t_{max} / C, and the streamtube contraction ratio, A_2 / A_1. These authors also used cascades data with boundary layers of higher turbulence levels than those of Lieblein, more representative of the conditions encountered in a modern compressor. Based on their work, Koch and Smith (1976) correlated the equivalent diffusion ratio as:

$$D_{eq} = \frac{W_1}{W_2} \times \left[1 + K_3 \frac{t_{\max}}{C} + K_4 \Gamma^*\right] \times \sqrt{\left(\sin\phi_1 - K_1 \frac{C}{S}\Gamma^*\right)^2 + \left(\frac{\cos\phi_1}{A^*_{throat} \times \rho_{throat} / \rho_1}\right)^2} \tag{C-3}$$

where the contraction ratio is given by:

$$A^*_{throat} = \left[1.0 - \frac{K_2 \dfrac{C}{S}\left(\dfrac{t_{\max}}{C}\right)}{\cos\left(0.5(\phi_1 + \phi_1)\right)}\right] \frac{A_{throat}}{A_1} \ . \tag{C-4a}$$

The cascade throat area is assumed to occur at one-third of the axial chord:

$$A_{throat} = A_1 - \tfrac{1}{3}\left(A_1 - A_2\right) . \tag{C-4b}$$

The gas density at the throat is calculated as:

$$\frac{\rho_{throat}}{\rho_1} = 1 - \frac{\mathrm{Ma}^2_{x_1}}{1 - \mathrm{Ma}^2_{x_1}}\left(1 - A^*_{throat} - K_1 \frac{\tan\phi_1}{\cos\phi_1}\frac{C}{S}\Gamma^*\right), \tag{C-4c}$$

and the square of the axial Mach number at the inlet as:

$$\mathrm{Ma}^2_{x_1} = \frac{W^2_{x_1}}{\gamma R T_1} = \frac{\left(W_1 \cos\phi_1\right)^2}{\gamma\, R T_1} \ . \tag{C-4d}$$

Koch and Smith (1976) obtained the values of the constants in these equations from their experimental data: $K_1 = 0.2445$, $K_2 = 0.4458$, $K_3 = 0.7688$, and $K_4 = 0.6024$. The dimensionless blade circulation parameter in Equations (C-3) and (C-4c) is given by:

$$\Gamma^* = \frac{r_{1m} V_{\theta 1} - r_{2m} V_{\theta 2}}{\left(\dfrac{r_{1m} + r_{2m}}{2}\right)\dfrac{C}{S} \times W_1} = \frac{r_{1m} V_1 \sin\alpha_1 + r_{2m} V_2 \sin\alpha_2}{\left(\dfrac{r_{1m} + r_{2m}}{2}\right)\dfrac{C}{S} \times W_1} . \tag{C-5}$$

Note that the absolute gas velocities are used in the numerator of Equation (C-5), <u>not</u> the relative velocities.

Based on Koch and Smith's experimental data at $\mathrm{Re}_1 = 10^6$, the boundary-layer momentum thickness at the blade outlet is correlated in this work as (Figure C-1):

$$\frac{\theta^o_2}{C} = \left[0.0072 \times D_{eq} - 0.0032\right] \times \left[1.0 + 0.2234 \times \left(D_{eq} - 1.0\right)^6\right]. \tag{C-6}$$

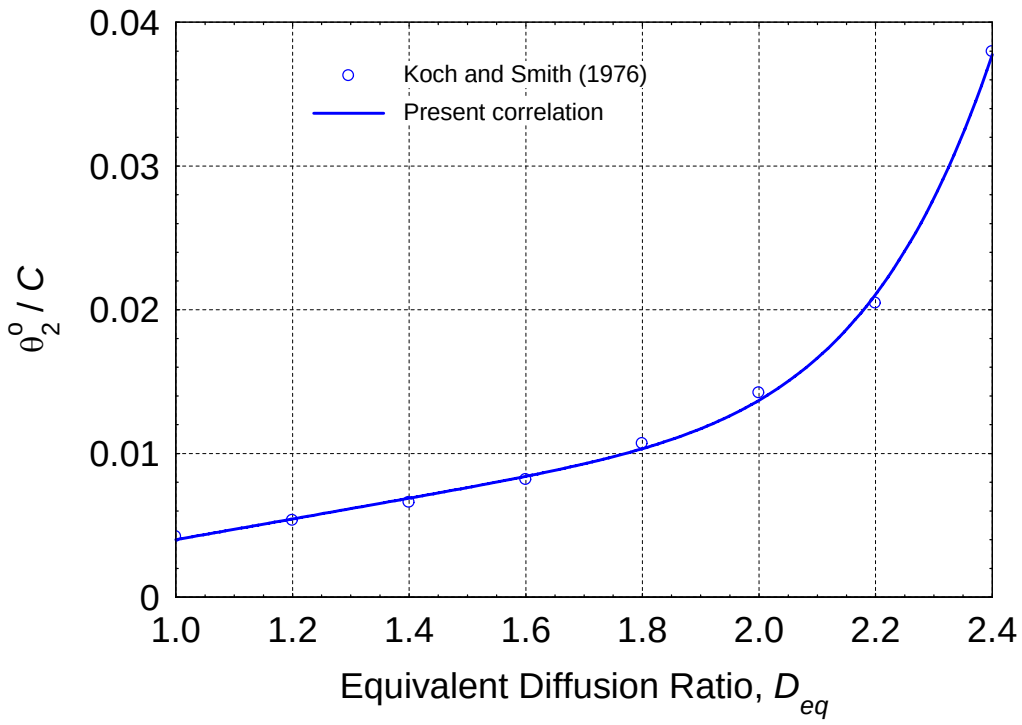

Figure C-1. Boundary-layer momentum thickness at blade outlet, $Re_1 = 10^6$ (Koch and Smith, 1976).

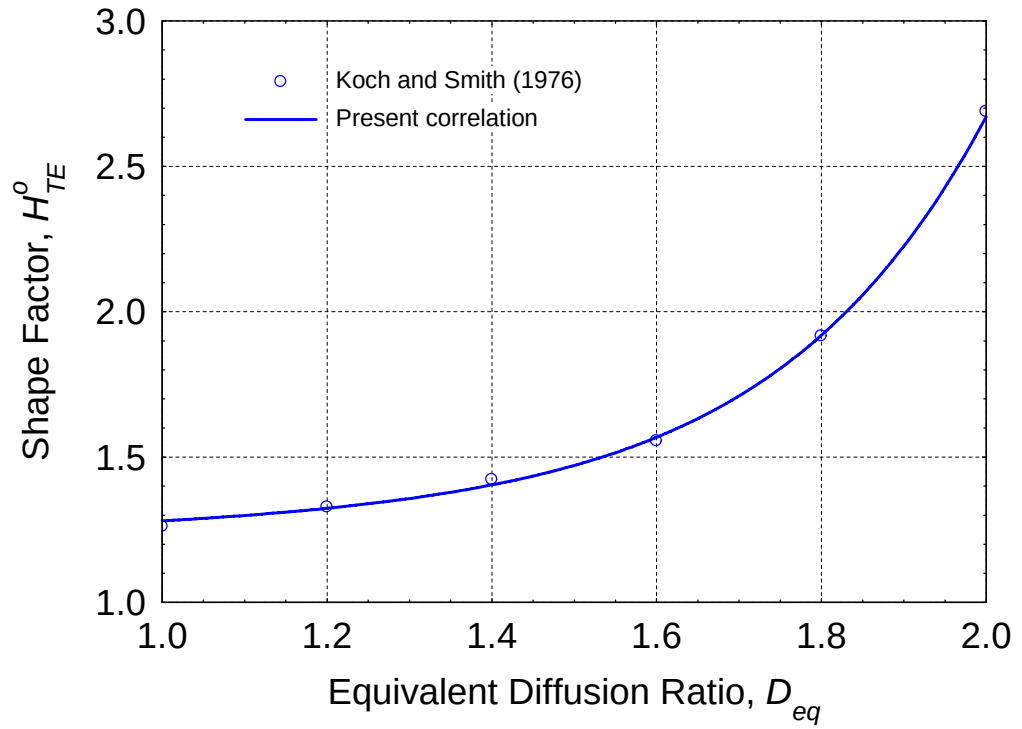

Figure C-2. Trailing-edge boundary-layer shape factor, $Re_1 = 10^6$ (Koch and Smith, 1976).

The boundary layer trailing-edge shape factor, the ratio of the boundary layer displacement thickness, δ^* to the momentum thickness, θ_2, is also correlated as (Figure C-2):

$$H_{TE}^{o} = \frac{\delta_{TE}^{*}}{\theta_2^{o}} = 1.231 + D_{eq}^{3} \times \left(0.0476 + 0.00207 \times D_{eq}^{6}\right). \tag{C-7}$$

The values of θ_2^o and H_{TE}^o are obtained for the following nominal conditions:

b. No contraction of the flow annulus height, *h*;
c. An inlet Reynolds number of $\mathrm{Re}_1 = \rho_1 W_1 C / \mu_1 = 10^6$; and
d. Hydraulically smooth blades.

Koch and Smith (1976) gave correction factors for conditions other than nominal. For the boundary-layer momentum thickness, they proposed:

$$\frac{\theta_2}{C} = \left(\frac{\theta_2^o}{C}\right) \times \zeta_M \times \zeta_H \times \zeta_{\mathrm{Re}} \ . \tag{C-8a}$$

The correction factor for inlet Mach number (Figure C-3) is correlated as:

$$\zeta_M = 1.0 + \left(0.117569 - 0.169832 \times D_{eq}\right) \times \mathrm{Ma}_1^{n} \tag{C-8b}$$

with an exponent:

$$n = 2.8532 + D_{eq}\left(-0.977474 + 0.194771 \times D_{eq}\right). \tag{C-8c}$$

The correction factor for flow area contraction (Figure C-4) is a linear function given by:

$$\zeta_H = 0.53 \frac{H_1}{H_2} + 0.47, \tag{C-8d}$$

and the correction factor for inlet Reynolds number is given by:

$$\zeta_{\mathrm{Re}} = \begin{cases} \left(\dfrac{10^6}{\mathrm{Re}_1}\right)^{0.166}, & \mathrm{Re}_1 \geq 2 \times 10^5, \\ 1.30626 \times \left(\dfrac{2 \times 10^5}{\mathrm{Re}_1}\right)^{0.5}, & \mathrm{Re}_1 < 2 \times 10^5 \ . \end{cases} \tag{C-8e}$$

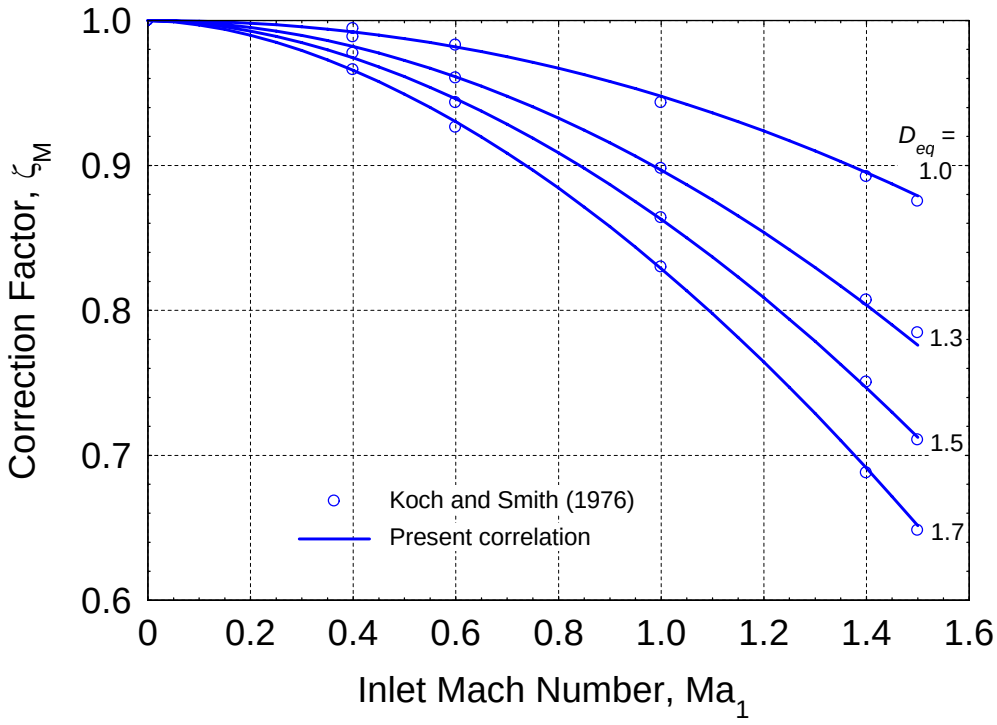

Figure C-3. Correction factor for effect of Mach number on boundary-layer momentum thickness (Koch and Smith, 1976).

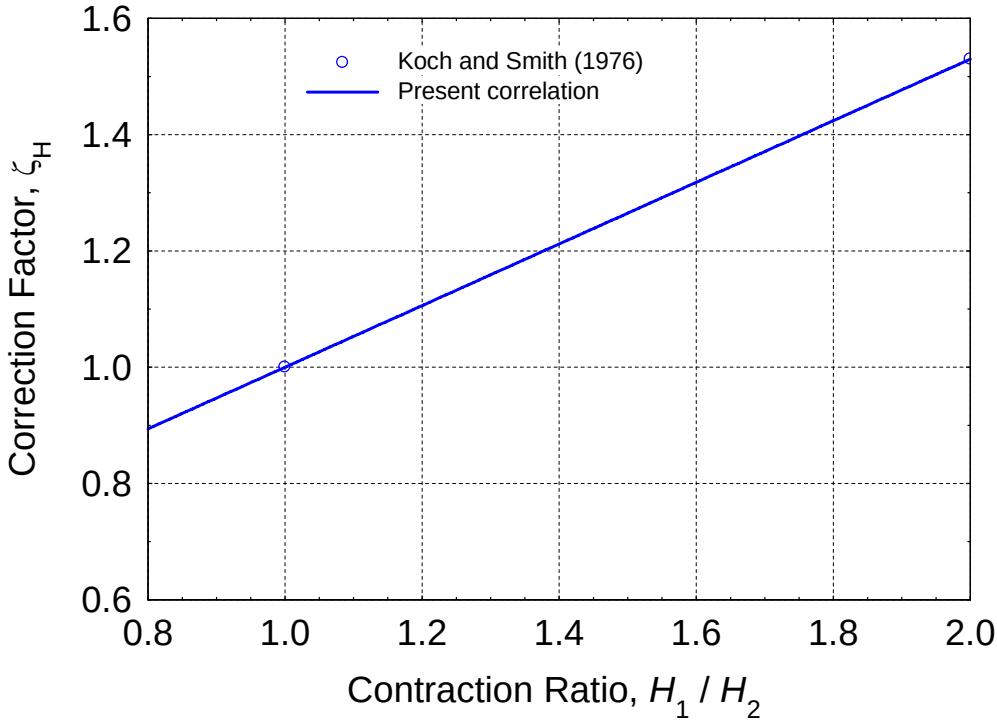

Figure C-4. Correction factor for effect of flow area contraction on boundary-layer momentum thickness (Koch and Smith, 1976).

Similarly, Koch and Smith (1976) corrected the trailing edge boundary-layer shape factor as:

$$H_{TE} = H_{TE}^{o} \times \xi_M \times \xi_H \times \xi_{\mathrm{Re}} \ . \tag{C-9a}$$

The correction factor for inlet Mach number (Figure C-5) is given by:

$$\xi_M = 1.0 + \left[1.07247 + D_{eq} \times \left(-0.867098 + 0.180425 \times D_{eq}\right)\right] \times \mathrm{Ma}_1^{1.8} . \tag{C-9b}$$

The correction factor for the flow area contraction (Figure C-6) is calculated as:

$$\xi_H = 1.0 + \left(\frac{H_1}{H_2} - 1.0\right) \times \left(0.0026 \times {D_{eq}}^{8} - 0.024\right), \tag{C-9c}$$

and the correction factor for inlet Reynolds number is given by:

$$\xi_{\mathrm{Re}} = \left(\frac{10^6}{\mathrm{Re}_1}\right)^{0.06} . \tag{C-9d}$$

The values of θ_2 and H_{TE}, obtained from Equations (C-8a) and (C-9a) for each blade row, can be used in the following relation, due to Leiblein (1959), to obtain the blade-profile total pressure loss coefficient:

$$Z_p = \frac{\Delta \hat{P}_{loss}}{\rho_1 \dfrac{{W_1}^2}{2}} = 2\left(\frac{\theta_2}{C}\right) \times \frac{C}{S \cos\phi_2} \times \left(\frac{\cos\phi_1}{\cos\phi_2}\right)^2 \times \left(\frac{2H_{TE}}{3H_{TE} - 1}\right) \times \left[1 - \left(\frac{\theta_2}{C}\right)\frac{C}{S}\frac{H_{TE}}{\cos\phi_2}\right]^{-3} . \tag{C-10}$$

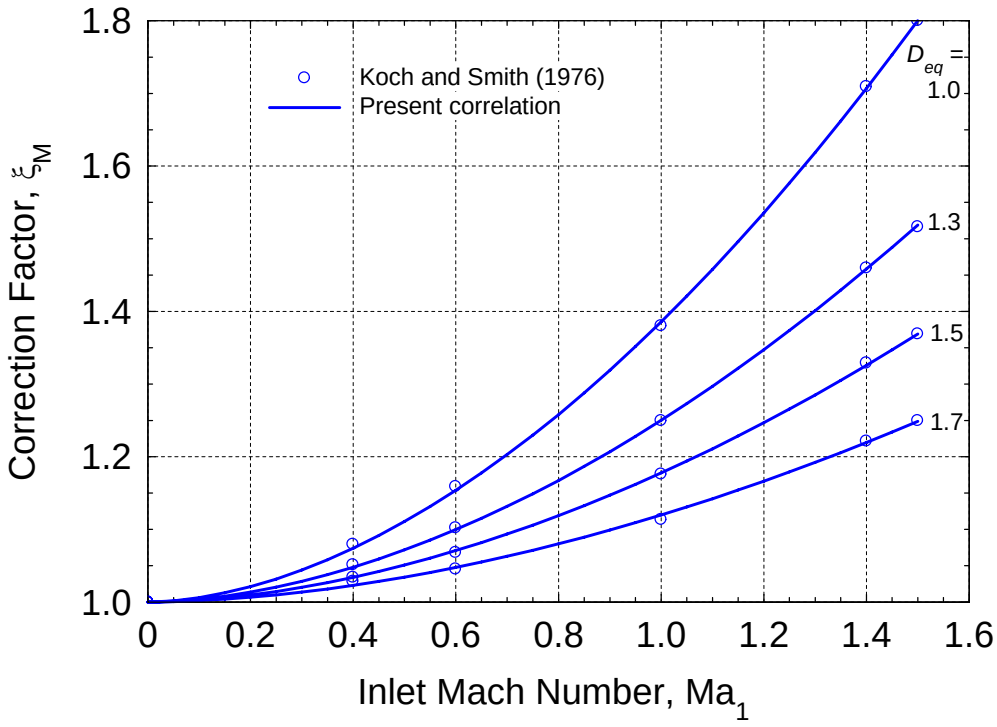

Figure C-5. Correction factor for effect of Mach number on trailing-edge boundary-layer shape factor (Koch and Smith, 1976).

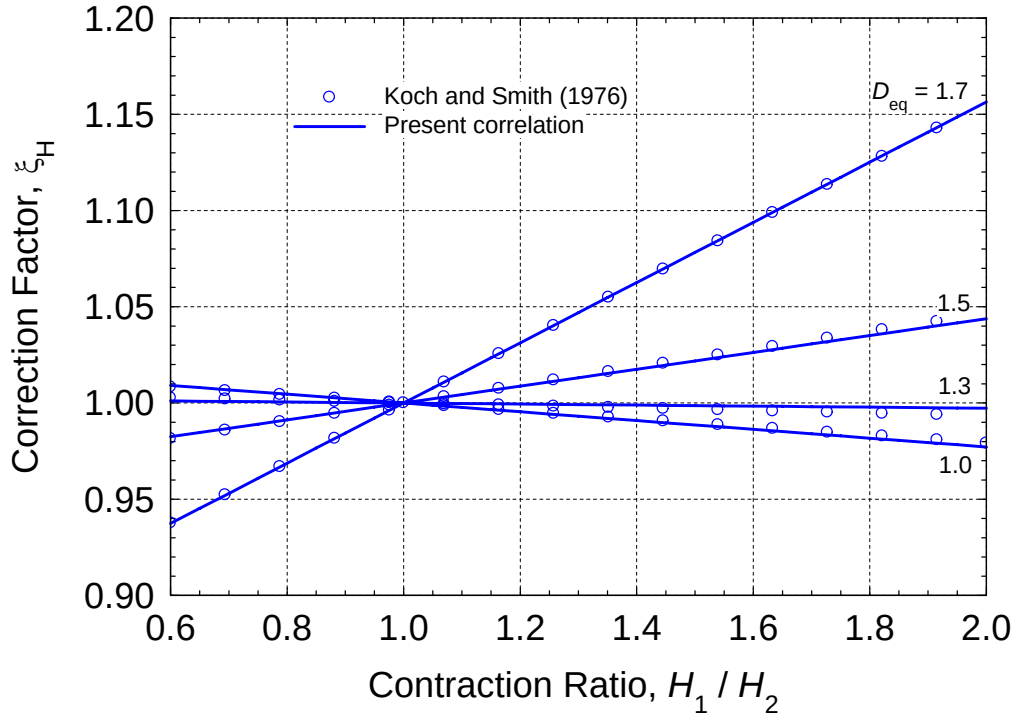

Figure C-6. Correction factor for effect of flow area contraction on trailing-edge boundary-layer shape factor (Koch and Smith, 1976).

References

Boyer, K. M., and W. F. O'Brien, 2003, An Improved Streamline Curvature Approach for Off-Design Analysis of Transonic Axial Compression Systems, *Journal of Turbo-machinery*, Vol. 125, pp. 475-481.

Horlock, J. H., and J. D. Denton, 2005, A Review of Some Early Design Practice Using Computational Fluid Dynamics and a Current Perspective, *Journal of Turbo-machinery*, Vol. 127, pp. 5-13.

Koch, C. C., and L. H. Smith, Jr., 1976, Loss Sources and Magnitudes in Axial-Flow Compressors, *Journal of Engineering for Power*, Vol. A98, pp. 411-424.

Lieblein, S., 1959, Loss and Stall Analysis in Compressor Cascades, *Journal of Basic Engineering*, Vol. 81 (September 1959), pp. 387-400.

Wilson, D. G., 1984, *The Design of High-Efficiency Turbo-machinery and Gas Turbines*, The Massachusetts Institute of Technology (MIT) Press, Cambridge, Massachusetts, Chapter 7, pp. 239-278, and Chapter 8, pp. 282-328.

APPENDIX D: INPUT FILE "TURBINE.INP"

```
****** INPUT FILE of the MULTISTAGE, AXIAL-FLOW TURBINE FORTRAN MODEL         *
 * JAERI, 6-STAGE AXIAL-FLOW TURBINE OF THE GTHTR300 (TAKIZUKA ET AL. 2004)    *
 ******************************************************************************

 ******************************************************************************
 * Operating parameters of PRIMARY LOOP                                       *
 ******************************************************************************
    1.00  *     x_He  = Molar fraction of helium in He-Xe gas mixture         *
 1123.0D0 *     Tin   = Gas Temperature at inlet of turbine             (K)   *
  6.88D6  *     Pin   = Gas Pressure   at  Inlet of turbine            (Pa)   *
  441.8D0 *   FLRATE  = Gas mass flow rate through  turbine          (kg/s)   *
 ******************************************************************************
  3600.D0 *   Nshaft  = Shaft rotational speed (rpm)                           *
 ******************************************************************************

 ******************************************************************************
 * GEOMETRICAL PARAMETERS OF THE MULTISTAGE, AXIAL-FLOW GAS TURBINE           *
 ******************************************************************************
    6     * Nstages   = Number of rotor stages of axial-flow turbine          *
  1.100D0 * Rcas_in   = Inner radius of turbine casing at  inlet        (m)   *
  1.100D0 * Rcas_ex   = Inner radius of turbine casing at outlet        (m)   *
 0.9480D0 * Rhub_in   = Hub   radius at turbine  inlet                  (m)   *
 0.8424D0 * Rhub_ex   = Hub   radius at turbine outlet                  (m)   *
 ******************************************************************************
 1.6760D0 * XLturbine = Axial length of turbine rotor                   (m)   *
 0.0040D0 * THICKcas  = Thickness of metallic casing                    (m)   *
 0.3000D0 * EMISScas  = Radiative emissivity of metallic casing                *
  300.0D0 * Tair      = Ambient air temperature                         (K)   *
 0.0020D0 * deltaDisk = Clearance between housing and end-disks         (m)   *
 ******************************************************************************

 ******************************************************************************
 * GEOMETRICAL PARAMETERS OF THE STATOR SECTIONS, INCLUDING Exit Guide Vanes   *
 ******************************************************************************
 * beta1(i) = Stator blades angle at Leading  Edge (degrees)                  *
    0.0D0    3.0D0    3.0D0    3.0D0    3.0D0    3.0D0   30.0D0
 ******************************************************************************
 * beta2(i) = Stator blades angle at Trailing Edge (degrees)                  *
   70.5D0   70.5D0   70.5D0   70.5D0   70.5D0   70.5D0    0.0D0
 ******************************************************************************
 *     C(i) = True chord length of stator blades         (m)                  *
    0.07D0   0.07D0   0.07D0   0.07D0   0.07D0   0.07D0   0.07D0
 ******************************************************************************
 *     N(i) = Number of stator blades in cascade                              *
     82       82       82       82       82       82       80
 ******************************************************************************
 * stagger  = Stagger angle of stator blades       (degrees) (< 0 IF UNKNOWN)  *
   -1.0D0   -1.0D0   -1.0D0   -1.0D0   -1.0D0   -1.0D0   -1.0D0
 ******************************************************************************
 *     Z(i) = Location of maximum camber                 (m) (< 0 IF UNKNOWN)  *
   -1.0D0   -1.0D0   -1.0D0   -1.0D0   -1.0D0   -1.0D0    3.0D-2
 ******************************************************************************
 *     O(i) = Throat opening of stator cascade           (m) (< 0 IF UNKNOWN)  *
   -1.0D0   -1.0D0   -1.0D0   -1.0D0   -1.0D0   -1.0D0   -1.0D0
 ******************************************************************************
 *  tmax(i) = Maximum thickness of stator blades         (m) (<0 IF UNKNOWN)   *
   -1.0D0   -1.0D0   -1.0D0   -1.0D0   -1.0D0   -1.0D0   -1.0D0
 ******************************************************************************
 *   tTE(i) = Blade thickness at trailing edge           (m)                   *
   5.0D-3   5.0D-3   5.0D-3   5.0D-3   5.0D-3   5.0D-3   5.0D-3
```

```
*****************************************************************************
*   tau(i) = Blade tip clearance to shroud              (m)                 *
   1.0D-3   1.0D-3   1.0D-3   1.0D-3   1.0D-3   1.0D-3   1.0D-3
*****************************************************************************

*****************************************************************************
* GEOMETRICAL PARAMETERS OF THE ROTOR SECTIONS                               *
*****************************************************************************
* beta1(i) = Rotor  blades angle at Leading  Edge (degrees)                  *
    3.0D0    3.0D0    3.0D0    3.0D0    3.0D0    3.0D0
*****************************************************************************
* beta2(i) = Rotor  blades angle at Trailing Edge (degrees)                  *
   70.5D0   70.5D0   70.5D0   70.5D0   70.5D0   70.5D0
*****************************************************************************
*     C(i) = True chord length of rotor  blades         (m)                  *
    0.07D0   0.07D0   0.07D0   0.07D0   0.07D0   0.07D0
*****************************************************************************
*     N(i) = Number of rotor  blades in cascade                              *
     80       80       80       80       80       80
*****************************************************************************
* stagger  = Stagger angle of rotor  blades       (degrees) (< 0 IF UNKNOWN)  *
   -1.0D0   -1.0D0   -1.0D0   -1.0D0   -1.0D0   -1.0D0
*****************************************************************************
*     Z(i) = Location of maximum camber                 (m) (< 0 IF UNKNOWN)  *
   -1.0D0   -1.0D0   -1.0D0   -1.0D0   -1.0D0   -1.0D0
*****************************************************************************
*     O(i) = Throat opening of rotor  cascades          (m) (< 0 IF UNKNOWN)  *
   -1.0D0   -1.0D0   -1.0D0   -1.0D0   -1.0D0   -1.0D0
*****************************************************************************
*  tmax(i) = Maximum thickness of rotor  blades         (m) (<0 IF UNKNOWN)   *
   -1.0D0   -1.0D0   -1.0D0   -1.0D0   -1.0D0   -1.0D0
*****************************************************************************
*   tTE(i) = Blade thickness at trailing edge           (m)                   *
   5.0D-3   5.0D-3   5.0D-3   5.0D-3   5.0D-3   5.0D-3
*****************************************************************************
*   tau(i) = Blade tip clearance to shroud              (m)                   *
   1.0D-3   1.0D-3   1.0D-3   1.0D-3   1.0D-3   1.0D-3
*****************************************************************************
```

APPENDIX E: SUBROUTINE TURBINE_INPUT

Please contact Sal Rodriguez at (505) 284-2808 (e-mail: sbrodri@sandia.gov), or Randall O. Gauntt at (505) 284-3989 (e-mail: rogaunt@sandia.gov), or Gary Rochau at (505) 845-7543 (e-mail: gerocha@sandia.gov) for a request to use the FORTRAN subroutines.

APPENDIX F: SUBROUTINE AXIAL_TURBINE

Please contact Sal Rodriguez at (505) 284-2808 (e-mail: sbrodri@sandia.gov), or Randall O. Gauntt at (505) 284-3989 (e-mail: rogaunt@sandia.gov), or Gary Rochau at (505) 845-7543 (e-mail: gerocha@sandia.gov) for a request to use the FORTRAN subroutines.

APPENDIX G: INPUT FILE “COMPRESSOR.INP”

```
****** INPUT FILE of the MULTISTAGE, AXIAL-FLOW COMPRESSOR FORTRAN MODEL      *
* JAERI, 20-STAGE AXIAL-FLOW COMPRESSOR OF THE GTHTR300 (TAKIZUKA ET AL. 2004)*
*****************************************************************************

*****************************************************************************
* Operating parameters of PRIMARY LOOP                                       *
*****************************************************************************
    1.00  *     x_He  = Molar fraction of helium in He-Xe gas mixture         *
  301.0D0 *     Tin   = Gas Temperature at inlet of compressor          (K)   *
  3.52D6  *     Pin   = Gas Pressure   at  Inlet of compressor         (Pa)   *
  449.7D0 *   FLRATE  = Gas mass flow rate through  compressor       (kg/s)   *
*****************************************************************************
  3600.D0 *   Nshaft  = Shaft rotational speed (rpm)                           *
*****************************************************************************

*****************************************************************************
* GEOMETRICAL PARAMETERS OF THE MULTISTAGE, AXIAL-FLOW GAS COMPRESSOR         *
*****************************************************************************
   20     * Nstages   = Number of rotor stages of axial-flow compressor       *
  0.837D0 * Rcas_in   = Inner radius of compressor casing at  inlet     (m)   *
  0.837D0 * Rcas_ex   = Inner radius of compressor casing at outlet     (m)   *
 0.7329D0 * Rhub_in   = Hub   radius at compressor  inlet               (m)   *
 0.7649D0 * Rhub_ex   = Hub   radius at compressor outlet              (m)   *
*****************************************************************************
 2.7240D0 * XLcompres = Axial length of compressor rotor               (m)   *
 0.0040D0 * THICKcas  = Thickness of metallic casing                   (m)   *
 0.3000D0 * EMISScas  = Radiative emissivity of metallic casing               *
  300.0D0 * Tair      = Ambient air temperature                        (K)   *
 0.0020D0 * deltaDisk = Clearance between housing and end-disks        (m)   *
*****************************************************************************

*****************************************************************************
* GEOMETRICAL PARAMETERS OF THE STATOR SECTIONS, INCLUDING Exit Guide Vanes   *
*****************************************************************************
* beta1(i) = Stator blades angle at Leading  Edge (degrees)                  *
    0.0D0   58.0D0   58.0D0   58.0D0   58.0D0   58.0D0   58.0D0
   58.0D0   58.0D0   58.0D0   58.0D0   58.0D0   58.0D0   58.0D0
   58.0D0   58.0D0   58.0D0   58.0D0   58.0D0   58.0D0   85.0D0
*****************************************************************************
* beta2(i) = Stator blades angle at Trailing Edge (degrees)                  *
   48.0D0   48.0D0   48.0D0   48.0D0   48.0D0   48.0D0   48.0D0
   48.0D0   48.0D0   48.0D0   48.0D0   48.0D0   48.0D0   48.0D0
   48.0D0   48.0D0   48.0D0   48.0D0   48.0D0   48.0D0    0.0D0
*****************************************************************************
*     C(i) = True chord length of stator blades         (m)                  *
    0.06D0   0.06D0   0.06D0   0.06D0   0.06D0   0.06D0   0.06D0
    0.06D0   0.06D0   0.06D0   0.06D0   0.06D0   0.06D0   0.06D0
    0.06D0   0.06D0   0.06D0   0.06D0   0.06D0   0.06D0   0.06D0
*****************************************************************************
*     N(i) = Number of stator blades in cascade                              *
     94       94       94       94       94       94       94
     94       94       94       94       94       94       94
     94       94       94       94       94       94       94
*****************************************************************************
* stagger  = Stagger angle of stator blades       (degrees) (< 0 IF UNKNOWN)  *
   -1.0D0   -1.0D0   -1.0D0   -1.0D0   -1.0D0   -1.0D0   -1.0D0
   -1.0D0   -1.0D0   -1.0D0   -1.0D0   -1.0D0   -1.0D0   -1.0D0
   -1.0D0   -1.0D0   -1.0D0   -1.0D0   -1.0D0   -1.0D0   -1.0D0
*****************************************************************************
```

```
*     Z(i) = Location of maximum camber                (m) (< 0 IF UNKNOWN)  *
    0.036D0   0.024D0   0.024D0   0.024D0   0.024D0   0.024D0    0.024D0
    0.024D0   0.024D0   0.024D0   0.024D0   0.024D0   0.024D0    0.024D0
    0.024D0   0.024D0   0.024D0   0.024D0   0.024D0   0.024D0    0.024D0
*************************************************************************
*     O(i) = Throat opening of stator cascade          (m) (< 0 IF UNKNOWN)  *
   -1.0D0   -1.0D0   -1.0D0   -1.0D0   -1.0D0   -1.0D0   -1.0D0
   -1.0D0   -1.0D0   -1.0D0   -1.0D0   -1.0D0   -1.0D0   -1.0D0
   -1.0D0   -1.0D0   -1.0D0   -1.0D0   -1.0D0   -1.0D0   -1.0D0
*************************************************************************
*  tmax(i) = Maximum thickness of stator blades        (m) (<0 IF UNKNOWN)   *
   -1.0D0   -1.0D0   -1.0D0   -1.0D0   -1.0D0   -1.0D0   -1.0D0
   -1.0D0   -1.0D0   -1.0D0   -1.0D0   -1.0D0   -1.0D0   -1.0D0
   -1.0D0   -1.0D0   -1.0D0   -1.0D0   -1.0D0   -1.0D0   -1.0D0
*************************************************************************
*   tTE(i) = Blade thickness at trailing edge          (m)                  *
   4.0D-3   4.0D-3   4.0D-3   4.0D-3   4.0D-3   4.0D-3   4.0D-3
   4.0D-3   4.0D-3   4.0D-3   4.0D-3   4.0D-3   4.0D-3   4.0D-3
   4.0D-3   4.0D-3   4.0D-3   4.0D-3   4.0D-3   4.0D-3   4.0D-3
*************************************************************************
*   tau(i) = Blade tip clearance to shroud             (m)                  *
   1.0D-3   1.0D-3   1.0D-3   1.0D-3   1.0D-3   1.0D-3   1.0D-3
   1.0D-3   1.0D-3   1.0D-3   1.0D-3   1.0D-3   1.0D-3   1.0D-3
   1.0D-3   1.0D-3   1.0D-3   1.0D-3   1.0D-3   1.0D-3   1.0D-3
*************************************************************************

*************************************************************************
* GEOMETRICAL PARAMETERS OF THE ROTOR SECTIONS                           *
*************************************************************************
* beta1(i) = Rotor  blades angle at Leading  Edge (degrees)              *
   42.0D0   42.0D0   42.0D0   42.0D0   42.0D0   42.0D0   42.0D0
   42.0D0   42.0D0   42.0D0   42.0D0   42.0D0   42.0D0   42.0D0
   42.0D0   42.0D0   42.0D0   42.0D0   42.0D0   42.0D0
*************************************************************************
* beta2(i) = Rotor  blades angle at Trailing Edge (degrees)              *
   10.0D0   10.0D0   10.0D0   10.0D0   10.0D0   10.0D0   10.0D0
   10.0D0   10.0D0   10.0D0   10.0D0   10.0D0   10.0D0   10.0D0
   10.0D0   10.0D0   10.0D0   10.0D0   10.0D0   10.0D0
*************************************************************************
*     C(i) = True chord length of rotor  blades          (m)              *
    0.078D0   0.078D0   0.078D0   0.078D0   0.078D0   0.078D0   0.078D0
    0.078D0   0.078D0   0.078D0   0.078D0   0.078D0   0.078D0   0.078D0
    0.078D0   0.078D0   0.078D0   0.078D0   0.078D0   0.078D0
*************************************************************************
*     N(i) = Number of rotor  blades in cascade                          *
     72        72        72        72        72        72        72
     72        72        72        72        72        72        72
     72        72        72        72        72        72
*************************************************************************
* stagger  = Stagger angle of rotor  blades       (degrees) (< 0 IF UNKNOWN)  *
   -1.0D0   -1.0D0   -1.0D0   -1.0D0   -1.0D0   -1.0D0    -1.0D0
   -1.0D0   -1.0D0   -1.0D0   -1.0D0   -1.0D0   -1.0D0    -1.0D0
   -1.0D0   -1.0D0   -1.0D0   -1.0D0   -1.0D0   -1.0D0
*************************************************************************
*     Z(i) = Location of maximum camber                (m) (< 0 IF UNKNOWN)  *
    3.12D-2   3.12D-2   3.12D-2   3.12D-2   3.12D-2   3.12D-2   3.12D-2
    3.12D-2   3.12D-2   3.12D-2   3.12D-2   3.12D-2   3.12D-2   3.12D-2
    3.12D-2   3.12D-2   3.12D-2   3.12D-2   3.12D-2   3.12D-2
*************************************************************************
*     O(i) = Throat opening of rotor  cascades         (m) (< 0 IF UNKNOWN)  *
   -1.0D0   -1.0D0   -1.0D0   -1.0D0   -1.0D0   -1.0D0    -1.0D0
   -1.0D0   -1.0D0   -1.0D0   -1.0D0   -1.0D0   -1.0D0    -1.0D0
   -1.0D0   -1.0D0   -1.0D0   -1.0D0   -1.0D0   -1.0D0
```

```
*******************************************************************************
*  tmax(i) = Maximum thickness of rotor  blades         (m) (<0 IF UNKNOWN)   *
   -1.0D0   -1.0D0   -1.0D0   -1.0D0   -1.0D0   -1.0D0    -1.0D0
   -1.0D0   -1.0D0   -1.0D0   -1.0D0   -1.0D0   -1.0D0    -1.0D0
   -1.0D0   -1.0D0   -1.0D0   -1.0D0   -1.0D0   -1.0D0
*******************************************************************************
*   tTE(i) = Blade thickness at trailing edge           (m)                   *
   4.0D-3   4.0D-3   4.0D-3   4.0D-3   4.0D-3   4.0D-3   4.0D-3
   4.0D-3   4.0D-3   4.0D-3   4.0D-3   4.0D-3   4.0D-3   4.0D-3
   4.0D-3   4.0D-3   4.0D-3   4.0D-3   4.0D-3   4.0D-3
*******************************************************************************
*   tau(i) = Blade tip clearance to shroud              (m)                   *
   1.0D-3   1.0D-3   1.0D-3   1.0D-3   1.0D-3   1.0D-3   1.0D-3
   1.0D-3   1.0D-3   1.0D-3   1.0D-3   1.0D-3   1.0D-3   1.0D-3
   1.0D-3   1.0D-3   1.0D-3   1.0D-3   1.0D-3   1.0D-3
*******************************************************************************
```

APPENDIX H: SUBROUTINE COMPRESSOR_INPUT

Please contact Sal Rodriguez at (505) 284-2808 (e-mail: sbrodri@sandia.gov), or Randall O. Gauntt at (505) 284-3989 (e-mail: rogaunt@sandia.gov), or Gary Rochau at (505) 845-7543 (e-mail: gerocha@sandia.gov) for a request to use the FORTRAN subroutines.

APPENDIX I: SUBROUTINE AXIAL_COMPRESSOR

Please contact Sal Rodriguez at (505) 284-2808 (e-mail: sbrodri@sandia.gov), or Randall O. Gauntt at (505) 284-3989 (e-mail: rogaunt@sandia.gov), or Gary Rochau at (505) 845-7543 (e-mail: gerocha@sandia.gov) for a request to use the FORTRAN subroutines.

APPENDIX J: SUBROUTINE HE_XE

Please contact Sal Rodriguez at (505) 284-2808 (e-mail: sbrodri@sandia.gov), or Randall O. Gauntt at (505) 284-3989 (e-mail: rogaunt@sandia.gov), or Gary Rochau at (505) 845-7543 (e-mail: gerocha@sandia.gov) for a request to use the FORTRAN subroutines.

APPENDIX K: INPUT FILE "HX.INP" FOR HE/WATER PRECOLLER

```
**** INPUT FILE OF THE GENERIC HEAT EXCHANGER MODEL  ************************
* Test of a helium gas / liquid water pre-cooler heat exchanger                *
*******************************************************************************

*******************************************************************************
   1      * IFLAG13=1 : GENERATE COMPLETE FILES "*.OUT" FOR DEBUGGING          *
*******************************************************************************
    1     * iCOOLANT2 : FLAG FOR SELECTING  HOT-LEG COOLANT (1=HELIUM)         *
    2     * iCOOLANT4 : FLAG FOR SELECTING COLD-LEG COOLANT (1=HELIUM, 2=H2O) *
    1     * iWALL     : FLAG FOR STRUCTURAL MATERIAL        (1=SS-304/316)    *
*******************************************************************************

*******************************************************************************
* GEOMETRICAL PARAMETERS OF GENERIC HEAT EXCHANGER                             *
*******************************************************************************
    1     * iCURRENT: 1=COUNTER-CURRENT, <>1 = PARALLEL FLOW HEAT EXCHANGER   *
   2.70D0 * XL      : TOTAL LENGTH OF THE FLOW CHANNELS                   (m) *
 4.4121D0 * AFLOW2  : FLOW AREA OF            HOT-LEG COOLANT CHANNELS   (m2) *
  3.66D-3 * Dequ2   : EQUIVALENT DIAMETER OF  HOT-LEG COOLANT CHANNELS    (m) *
 0.9651D0 * AFLOW4  : FLOW AREA OF           COLD-LEG COOLANT CHANNELS   (m2) *
  8.00D-3 * Dequ4   : EQUIVALENT DIAMETER OF COLD-LEG COOLANT CHANNELS    (m) *
*******************************************************************************
 10.003D3 * XMASSw1 : MASS OF HOT-LEG OUTER  WALLS                       (kg) *
 40.227D3 * XMASSw3 : MASS OF HEAT-EXCHANGE  WALLS                       (kg) *
 100.0D0  * XMASSw5 : MASS OF COLD-LEG OUTER WALLS                       (kg) *
  8.00D-3 * DR1     : THICKNESS OF  HOT-LEG OUTER WALLS                    (m) *
  1.50D-3 * DR3     : THICKNESS OF SEPARATION WALLS BETWEEN COOLANT LEGS   (m) *
  8.00D-3 * DR5     : THICKNESS OF COLD-LEG OUTER WALLS                    (m) *
*******************************************************************************
 1.7915D3 * Sun2    : UNFINNED, TOTAL HEAT-EXCHANGE AREA ON  HOT SIDE     (m2) *
 11.085D3 * Sfin2   :   FINNED, TOTAL HEAT-EXCHANGE AREA ON  HOT SIDE     (m2) *
    2     * iFIN2   :  HOT FINS TYPE (1=STACKED MATRICES, 2=ADIABATIC TIP)    *
 4.455D-3 * XLfin2  :  LENGTH OF    HOT-SIDE FINS                         (m) *
  0.50D-3 * dFIN2   : THICKNESS OF  HOT-SIDE FINS (RECTANGULAR FINS)      (m) *
*******************************************************************************
 1.3029D3 * Sun4    : UNFINNED, TOTAL HEAT-EXCHANGE AREA ON COLD SIDE     (m2) *
   0.0D0  * Sfin4   :   FINNED, TOTAL HEAT-EXCHANGE AREA ON COLD SIDE     (m2) *
    2     * iFIN4   : COLD FINS TYPE (1=STACKED MATRICES, 2=ADIABATIC TIP)    *
   1.0D-2 * XLfin4  :  LENGTH OF   COLD-SIDE FINS                         (m) *
   0.8D-3 * dFIN4   : THICKNESS OF COLD-SIDE FINS (RECTANGULAR FINS)      (m) *
*******************************************************************************
    10    * Nz      : NUMBER of DISCRETIZATION NODES ALONG FLOW CHANNELS       *
*******************************************************************************

**** NUMERICAL SOLUTION PARAMETERS ******************************************
*  TYPE OF MOMENTUM CONSERVATION EQUATION APPROXIMATION                        *
  1      * iSIMPLE : 0=SIMPLE     1=SIMPLEC APPROXIMATION                     *
*******************************************************************************
   30     * IOKMAX = NUMBER OF TEMPERATURE-COUPLING INTERNAL ITERATIONS       *
   1.D-12 * CVGSIMPL = max|M'| FOR CONVERGENCE OF SIMPLEC INTERNAL ITERATIONS *
    3     * INTERMAX = MAXIMUM NUMBER OF SIMPLEC INTERNAL ITERATIONS          *
   1.0D2  * CVGenth  = max|Sh| FOR CONVERGENCE OF ENERGY  INTERNAL ITERATIONS
    3     * ITERhMAX = MAXIMUM NUMBER OF ENERGY  INTERNAL ITERATIONS          *
*******************************************************************************

*******************************************************************************
* ELEMENTARY CHECK-UP OF HEAT EXCHANGER GEOMETRY (DO NOT FILL IN THIS PART)   *
*******************************************************************************
```

```
          * TOTAL NUMBER of CELLS in the TRANSVERSE DIRECTION                *
          * TOTAL NUMBER of CELLS in the AXIAL      DIRECTION                 *
*****************************************************************************
* CELLS TRANSVERSE POSITION (START FROM HOT LEG WALL) [DIMENSIONS in METER m] *
*****************************************************************************
* CELLS  AXIAL POSITION (START FROM HOT LEG ENTRANCE) [DIMENSIONS in METER m] *
*****************************************************************************

*****************************************************************************
* PARAMETERS FOR OUTPUT DISPLAY                                             *
*****************************************************************************
    1     * iPRINT  (STORAGE IN "#####.TIME" FILES EVERY iPRINT ITERATIONS)   *
**** COLD-LEG PRESSURE VARIATION WITH TIME ***********************************
    4     * iLpress = i-COORDINATE OF THE POSITION CONSIDERED  (PRESS.TIME)   *
    1     * jLpress = j-COORDINATE OF THE POSITION CONSIDERED                 *
**** HOT-LEG  PRESSURE VARIATION WITH TIME ***********************************
    2     * iVpress = i-COORDINATE OF THE POSITION CONSIDERED  (PRESS.TIME)   *
   10     * jVpress = j-COORDINATE OF THE POSITION CONSIDERED                 *
**** TEMPERATURE VARIATION WITH TIME *****************************************
    4     * iTEMP  = i-COORDINATE OF THE POSITION CONSIDERED   (TEMP.TIME)    *
    1     * jTEMP  = j-COORDINATE OF THE POSITION CONSIDERED                  *
****  AXIAL VELOCITY VARIATION WITH TIME ************************************
    2     * iUz    = i-COORDINATE OF THE POSITION CONSIDERED  (GAXIAL.TIME)   *
   10     * jUz    = j-COORDINATE OF THE POSITION CONSIDERED                  *
*****************************************************************************
```

APPENDIX L: INPUT FILE "HX.INP" FOR HE/HE RECUPERATOR

```
**** INPUT FILE OF THE GENERIC HEAT EXCHANGER MODEL  ************************
* Test of a helium/helium  plate-fin recuperator (triangular stacked matrices)*
*****************************************************************************

*****************************************************************************
   1      * IFLAG13=1 : GENERATE COMPLETE FILES "*.OUT" FOR DEBUGGING         *
*****************************************************************************
    1     * iCOOLANT2 : FLAG FOR SELECTING  HOT-LEG COOLANT (1=HELIUM)        *
    1     * iCOOLANT4 : FLAG FOR SELECTING COLD-LEG COOLANT (1=HELIUM, 2=H2O) *
    1     * iWALL     : FLAG FOR STRUCTURAL MATERIAL        (1=SS-304/316)    *
*****************************************************************************

*****************************************************************************
* GEOMETRICAL PARAMETERS OF GENERIC HEAT EXCHANGER                           *
*****************************************************************************
    1     * iCURRENT: 1=COUNTER-CURRENT, <>1 = PARALLEL FLOW HEAT EXCHANGER   *
   3.90D0 * XL      : TOTAL LENGTH OF THE FLOW CHANNELS                  (m) *
 6.9995D0 * AFLOW2  : FLOW AREA OF            HOT-LEG COOLANT CHANNELS   (m2) *
  2.04D-3 * Dequ2   : EQUIVALENT DIAMETER OF  HOT-LEG COOLANT CHANNELS    (m) *
 6.9995D0 * AFLOW4  : FLOW AREA OF           COLD-LEG COOLANT CHANNELS   (m2) *
  2.04D-3 * Dequ4   : EQUIVALENT DIAMETER OF COLD-LEG COOLANT CHANNELS    (m) *
*****************************************************************************
  4.530D3 * XMASSw1 : MASS OF HOT-LEG OUTER  WALLS                      (kg) *
 289.89D3 * XMASSw3 : MASS OF HEAT-EXCHANGE  WALLS                      (kg) *
  4.530D3 * XMASSw5 : MASS OF COLD-LEG OUTER WALLS                      (kg) *
  2.00D-3 * DR1     : THICKNESS OF  HOT-LEG OUTER WALLS                  (m) *
  0.80D-3 * DR3     : THICKNESS OF SEPARATION WALLS BETWEEN COOLANT LEGS  (m) *
  2.00D-3 * DR5     : THICKNESS OF COLD-LEG OUTER WALLS                  (m) *
*****************************************************************************
 20.909D3 * Sun2    : UNFINNED, TOTAL HEAT-EXCHANGE AREA ON  HOT SIDE    (m2) *
 32.529D3 * Sfin2   :   FINNED, TOTAL HEAT-EXCHANGE AREA ON  HOT SIDE    (m2) *
    1     * iFIN2   :  HOT FINS TYPE (1=STACKED MATRICES, 2=ADIABATIC TIP)    *
 3.409D-3 * XLfin2  :  LENGTH OF    HOT-SIDE FINS                        (m) *
  0.50D-3 * dFIN2   : THICKNESS OF  HOT-SIDE FINS (RECTANGULAR FINS)      (m) *
*****************************************************************************
 20.909D3 * Sun4    : UNFINNED, TOTAL HEAT-EXCHANGE AREA ON COLD SIDE    (m2) *
 32.529D3 * Sfin4   :   FINNED, TOTAL HEAT-EXCHANGE AREA ON COLD SIDE    (m2) *
    1     * iFIN4   : COLD FINS TYPE (1=STACKED MATRICES, 2=ADIABATIC TIP)    *
 3.409D-3 * XLfin4  :  LENGTH OF   COLD-SIDE FINS                        (m) *
  0.50D-3 * dFIN4   : THICKNESS OF COLD-SIDE FINS (RECTANGULAR FINS)      (m) *
*****************************************************************************
  10      * Nz      : NUMBER of DISCRETIZATION NODES ALONG FLOW CHANNELS      *
*****************************************************************************

**** NUMERICAL SOLUTION PARAMETERS ****************************************
*  TYPE OF MOMENTUM CONSERVATION EQUATION APPROXIMATION                      *
  1       * iSIMPLE : 0=SIMPLE     1=SIMPLEC APPROXIMATION                   *
*****************************************************************************
   30     * IOKMAX = NUMBER OF TEMPERATURE-COUPLING INTERNAL ITERATIONS       *
   1.D-12 * CVGSIMPL = max|M'| FOR CONVERGENCE OF SIMPLEC INTERNAL ITERATIONS *
    3     * INTERMAX = MAXIMUM NUMBER OF SIMPLEC INTERNAL ITERATIONS         *
   1.0D2  * CVGenth  = max|Sh| FOR CONVERGENCE OF ENTHALPY INTERNAL ITERATIONS
    3     * ITERhMAX = MAXIMUM NUMBER OF ENTHALPY INTERNAL ITERATIONS        *
*****************************************************************************

*****************************************************************************
* ELEMENTARY CHECK-UP OF HEAT EXCHANGER GEOMETRY (DO NOT FILL IN THIS PART)  *
*****************************************************************************
```

```
          * TOTAL NUMBER of CELLS in the TRANSVERSE DIRECTION                *
          * TOTAL NUMBER of CELLS in the AXIAL      DIRECTION                 *
*****************************************************************************
* CELLS TRANSVERSE POSITION (START FROM HOT LEG WALL) [DIMENSIONS in METER m] *
*****************************************************************************
* CELLS  AXIAL POSITION (START FROM HOT LEG ENTRANCE) [DIMENSIONS in METER m] *
*****************************************************************************

*****************************************************************************
* PARAMETERS FOR OUTPUT DISPLAY                                             *
*****************************************************************************
    2     * iPRINT  (STORAGE IN "#####.TIME" FILES EVERY iPRINT ITERATIONS)   *
**** COLD-LEG PRESSURE VARIATION WITH TIME ***********************************
    4     * iLpress = i-COORDINATE OF THE POSITION CONSIDERED  (PRESS.TIME)   *
   10     * jLpress = j-COORDINATE OF THE POSITION CONSIDERED                 *
**** HOT-LEG  PRESSURE VARIATION WITH TIME ***********************************
    2     * iVpress = i-COORDINATE OF THE POSITION CONSIDERED  (PRESS.TIME)   *
    1     * jVpress = j-COORDINATE OF THE POSITION CONSIDERED                 *
**** TEMPERATURE VARIATION WITH TIME *****************************************
    3     * iTEMP  = i-COORDINATE OF THE POSITION CONSIDERED   (TEMP.TIME)    *
    5     * jTEMP  = j-COORDINATE OF THE POSITION CONSIDERED                  *
****  AXIAL VELOCITY VARIATION WITH TIME ************************************
    4     * iUz    = i-COORDINATE OF THE POSITION CONSIDERED  (GAXIAL.TIME)   *
    1     * jUz    = j-COORDINATE OF THE POSITION CONSIDERED                  *
*****************************************************************************
```

APPENDIX M: SUBROUTINE HX_INPUT

Please contact Sal Rodriguez at (505) 284-2808 (e-mail: sbrodri@sandia.gov), or Randall O. Gauntt at (505) 284-3989 (e-mail: rogaunt@sandia.gov), or Gary Rochau at (505) 845-7543 (e-mail: gerocha@sandia.gov) for a request to use the FORTRAN subroutines.

APPENDIX N: SUBROUTINE INITIALIZE

Please contact Sal Rodriguez at (505) 284-2808 (e-mail: sbrodri@sandia.gov), or Randall O. Gauntt at (505) 284-3989 (e-mail: rogaunt@sandia.gov), or Gary Rochau at (505) 845-7543 (e-mail: gerocha@sandia.gov) for a request to use the FORTRAN subroutines.

APPENDIX O: SUBROUTINE HEAT_EXCHANGER

Please contact Sal Rodriguez at (505) 284-2808 (e-mail: sbrodri@sandia.gov), or Randall O. Gauntt at (505) 284-3989 (e-mail: rogaunt@sandia.gov), or Gary Rochau at (505) 845-7543 (e-mail: gerocha@sandia.gov) for a request to use the FORTRAN subroutines.

APPENDIX P: SUBROUTINE COOLANT_PROPERTIES

Please contact Sal Rodriguez at (505) 284-2808 (e-mail: sbrodri@sandia.gov), or Randall O. Gauntt at (505) 284-3989 (e-mail: rogaunt@sandia.gov), or Gary Rochau at (505) 845-7543 (e-mail: gerocha@sandia.gov) for a request to use the FORTRAN subroutines.

APPENDIX Q: SUBROUTINE WALL_PROPERTIES

Please contact Sal Rodriguez at (505) 284-2808 (e-mail: sbrodri@sandia.gov), or Randall O. Gauntt at (505) 284-3989 (e-mail: rogaunt@sandia.gov), or Gary Rochau at (505) 845-7543 (e-mail: gerocha@sandia.gov) for a request to use the FORTRAN subroutines.

APPENDIX R: SUBROUTINE NUSSELT_NUMBER

Please contact Sal Rodriguez at (505) 284-2808 (e-mail: sbrodri@sandia.gov), or Randall O. Gauntt at (505) 284-3989 (e-mail: rogaunt@sandia.gov), or Gary Rochau at (505) 845-7543 (e-mail: gerocha@sandia.gov) for a request to use the FORTRAN subroutines.

APPENDIX S: SUBROUTINE UNM_KINETICS

Please contact Sal Rodriguez at (505) 284-2808 (e-mail: sbrodri@sandia.gov), or Randall O. Gauntt at (505) 284-3989 (e-mail: rogaunt@sandia.gov), or Gary Rochau at (505) 845-7543 (e-mail: gerocha@sandia.gov) for a request to use the FORTRAN subroutines.

APPENDIX T: SUBROUTINE GAUSSB

```
C +++
**********************************************************************
C +++ *      SOLUTION OF A BANDED LINEAR SYSTEM [A]*[X]=[B]
*
C +++ *      USING THE GAUSS ELIMINATION WITH OPTIONAL PARTIAL PIVOTING
*
C +++
**********************************************************************
      SUBROUTINE GAUSSB(IO,A,NN,B,X,N,p,IPIVOT,NORMROW,
     &                  EPS,ISTATUS,NPERMUT)
      IMPLICIT DOUBLE PRECISION(A-H,O-Z) , INTEGER(I-N)
      PARAMETER(Mcd=100)
C
      DIMENSION A(NN,1) , B(1) , X(1)
C
      INTEGER p,p1,jMAX(Mcd),iMAX(Mcd) , q
C
C
C ++++++++++++++++++++++++++++++++++++++++++++++++++++++++++++++++++++
C +++ ===> INPUT PARAMETERS <=======================================
C ++++++++++++++++++++++++++++++++++++++++++++++++++++++++++++++++++++
C +++ IO  : UNIT number of output file 'KINETICS.OUT'
C +++ [A] : BAND STORAGE OF A SQUARED-MATRIX OF DIMENSION N
C +++ [B] : VECTOR SOURCE  OF DIMENSION N
C
C +++ NN : NUMBER OF ROWS OF [A] AS SPECIFIED IN THE MAIN PROGRAM
C +++      (INSTRUCTION "DIMENSION")
C +++ p  : UPPER & LOWER BANDWIDTH OF MATRIX [A]
C
C +++ IPIVOT = 1  : PARTIAL PIVOTING (ROW PERMUTATION) ALLOWED
C +++ IPIVOT = 0  : NO PIVOTING ALLOWED
C
C +++ NORMROW = 1 : ROW NORMALIZATION
C +++ NORMROW = 0 : NO  NORMALIZATION
C
C +++ EPS  : ZERO PRECISION (EVERY NUMBER BELOW EPS IS CONSIDERED NUL)
C
C ++++++++++++++++++++++++++++++++++++++++++++++++++++++++++++++++++++
C +++ ===> OUTPUT PARAMETERS <======================================
C ++++++++++++++++++++++++++++++++++++++++++++++++++++++++++++++++++++
C +++ [X]  : VECTOR SOLUTION  (DIMENSION N, CELL NUMEROTATION)
C
C +++ NPERMUT : NUMBER OF PERMUTATIONS IF PARTIAL PIVOTING ALLOWED
C
C +++ ISTATUS =  0 : SOLUTION COMPLETED
C +++ ISTATUS = -i : PIVOT BANDii IS NUL (SOLUTION NOT COMPLETED)
C ++++++++++++++++++++++++++++++++++++++++++++++++++++++++++++++++++++
C
C +++ Normally, the parameter iFLAG13 = 0:
      iFLAG13 = 0
C +++ In the debugging mode, set iFLAG13 = 1 for more detailed printout
C
      IF (iFLAG13.EQ.1) THEN
```

```
        WRITE(IO,*) ' @@@@@@@ SUBROUTINE GAUSS @@@@@@@@@'
        WRITE(IO,*) ' IPIVOT=',IPIVOT,'     NORMROW=',NORMROW
        WRITE(IO,*) ' EPS=',SNGL(EPS)
        WRITE(IO,*) ' NN =',NN,'  N =',N,'    p =',p
        WRITE(IO,*) '   '
      ENDIF
C
      p1 = p+1
      NPERMUT = 0
C
C +++ INITIALIZATION OF jMAX() & iMAX() ******************************
      DO 10 i=1,N
        jMAX(i) = MIN0( i+p,N)
        iMAX(i) = jMAX(i)
 10   CONTINUE
C
C
C +++ MAIN ITERATIONS ************************************************
      DO 20 i=1,N-1
C
      PMAX = DABS(A(i,p1))
C
      IF (IPIVOT.EQ.1)  THEN
C +++ SEARCH OF PIVOT ON COLUMN BELOW PIVOT ========================>
        ip1 = i+p1
        KMAX = i
        DO 30 k=i+1,iMAX(i)
          PkMAX = DABS(A(k,ip1-k))
          IF (PkMAX.GT.PMAX) THEN
                             KMAX = k
                             PMAX = PkMAX
                             ENDIF
 30     CONTINUE
C
        IF (KMAX.NE.i) THEN
C +++   ====> PERMUTATION OF THE LINES KMAX and i
          NPERMUT = NPERMUT+1
          imKMAX = i-KMAX
      IF (iFLAG13.EQ.1)
     & WRITE(IO,*) '!!!!! PERMUT i=',i,'   with k=',KMAX
          DO 40 j=p1,MAX0( jMAX(i) , jMAX(KMAX) ) - i + p1
            store     = A(i,j)
            A(i,j)    = A(KMAX,j+imKMAX)
            A(KMAX,j+imKMAX) = store
 40       CONTINUE
C
          store   = B(i)
          B(i)    = B(KMAX)
          B(KMAX) = store
C
          jstore     = jMAX(i)
          jMAX(i)    = jMAX(KMAX)
          jMAX(KMAX) = jstore
        ENDIF
C +++   ====> END OF PERMUTATION OF THE LINES KMAX and i
C
      ENDIF
```

```
C +++ END OF THE LOOP IPIVOT = 1 <===================================
C
C
      IF (PMAX.LE.EPS) THEN
C +++ ====> THE PIVOT IS NUL ====> ERROR STATUS
                        ISTATUS = -i
                        WRITE(IO,*) '!!!!! kSTATUS=',ISTATUS
                        RETURN
      ENDIF
C
      IF (NORMROW.EQ.1) THEN
C +++ DIVIDE LINE i BY THE PIVOT A(i,p+1) ====>
        t = 1.D0/A(i,p1)
        B(i) = B(i)*t
C
        DO 50 j=p1,jMAX(i)-i+p1
          A(i,j) = A(i,j)*t
 50     CONTINUE
      ENDIF
C
C
C +++ GAUSS ELIMINATION ===========================================>
      DO 60 k=i+1,iMAX(i)
        imk = i-k
        t = -A(k,imk+p1) / A(i,p1)
        IF (DABS(t).GT.EPS)  THEN
C +++ SUBSTRACT Aki * ROWi  FROM  ROWk :  Lk = Lk - Aki*Li ====>
        B(k) = B(k) + t*B(i)
        jMAX(k) = MAX0( jMAX(k) , jMAX(i) )
C
        DO 70 j=imk+p1+1 , jMAX(i)+p1-k
          A(k,j) = A(k,j) + t*A(i,j-imk)
 70     CONTINUE
C +++   NOTE : THERE IS NO NEED TO PUT EXPLICITLY A(k,i) = 0.
        ENDIF
 60   CONTINUE
C
C
C +++ END OF THE MAIN ITERATIONS ************************************
 20   CONTINUE
C
C
      PMAX = DABS(A(N,p1))
      IF (PMAX.LE.EPS) THEN
C +++ ====> THE PIVOT IS NUL ====> ERROR STATUS
                        ISTATUS = -N
                        WRITE(IO,*) '!!!!! kSTATUS=',ISTATUS
                        RETURN
      ENDIF
C
      IF (NORMROW.EQ.1) THEN
C +++ DIVIDE LINE N BY THE PIVOT A(N,p+1) ====>
        B(N)    = B(N)/A(N,p1)
        A(N,p1) = 1.D0
      ENDIF
C
C
```

```
C +++ ====>  SOLUTION OF THE RESULTING UPPER TRIANGULAR SYSTEM  <====
      ISTATUS = 0
      IF (NPERMUT.GE.1) THEN
                        q = 2*p
                        ELSE
                        q = p
      ENDIF
C
      CALL UPPERB(A,NN,B,X,N,p,q)
C
      IF (ISTATUS.LT.0) THEN
        WRITE(IO,*) ' @@@@@@@ SUBROUTINE GAUSS @@@@@@@@@'
        WRITE(IO,*) ' ====> kSTATUS=',ISTATUS
      ENDIF
C
      RETURN
      END
C +++ ***************************************************************
C +++ * END OF THE SOLUTION OF A BANDED LINEAR SYSTEM [A]*[X]=[B]    *
C +++ *  USING THE GAUSS ELIMINATION WITH OPTIONAL PARTIAL PIVOT     *
C +++ ***************************************************************
```

APPENDIX U: SUBROUTINE UPPERB

```
C +++ ****************************************************************
C +++ * SOLUTION OF AN UPPER-TRIANGULAR LINEAR SYSTEM [A]*[X]=[B]    *
C +++ * (THE MATRIX A as LOWER & UPPER BAND WIDTHS p & q)            *
C +++ ****************************************************************
      SUBROUTINE UPPERB(A,NN,B,X,N,p,q)
      IMPLICIT DOUBLE PRECISION(A-H,O-Z) , INTEGER(I-N)
      DIMENSION A(NN,1) , B(1) , X(1)
      INTEGER p,q,  p1
C
C
      p1 = p+1
      X(N) = B(N)/A(N,p1)
C
      DO 10 i=N-1,1,-1
        imp1 = i-p1
        S = 0.D0
        DO 20 j=i+1,MIN0(i+q,N)
          S = S + A(i,j-imp1)*X(j)
 20     CONTINUE
        X(i) = ( B(i) - S ) / A(i,p1)
 10   CONTINUE
C
      RETURN
      END
C +++ ****************************************************************
C +++ * END OF THE SOLUTION OF AN UPPER-TRIANGULAR LINEAR SYSTEM     *
C +++ ****************************************************************
```

DISTRIBUTION

1	MS9018	Central Technical Files, 8944 (electronic copy)
11	MS0748	Salvador Rodriguez, 6763
1	MS0123	Donna L. Chavez, 1011
1	MS4536	Technical Library, 9536 (electronic copy)